

DOCTORAL THESIS

**Finite-element-based limit analysis for strength predictions  
of wood at different scales of observation and a novel  
algorithm for adaptive implementation of velocity  
discontinuities in upper bound approaches**

submitted in satisfaction of the requirements for the degree  
Doctor of Science in Civil Engineering  
of the Vienna University of Technology, Faculty of Civil Engineering

DISSERTATION

**Finite-Elemente-basierte Traglastanalyse für  
Festigkeitsvorhersagen von Holz auf unterschiedlichen  
Betrachtungsebenen und ein neuartiger Algorithmus zur  
adaptiven Implementierung von Diskontinuitäten in  
kinematischen Traglastansätzen**

ausgeführt zum Zwecke der Erlangung des akademischen Grades eines  
Doktors der technischen Wissenschaften  
eingereicht an der Technischen Universität Wien, Fakultät für Bauingenieurwesen

von

M.Sc. **Mingjing Li**

Matrikelnr.: 1428781

Mooslackengasse 21/509, 1190 Wien, Österreich

Betreuer:

Univ. Prof. Dipl.-Ing. Dr. techn. DDr.h.c. **Josef Eberhardsteiner**

Assistant Prof. Dipl.-Ing. Dr. techn. **Josef Füssl**

Institut für Mechanik der Werkstoffe und Strukturen

Technische Universität Wien

Gutachter:

Prof. BE DPhil **Chris M. Martin**

Department of Engineering Science

University of Oxford

Univ. Prof. Dipl.-Ing. Dr. techn. **Christian Hellmich**

Institut für Mechanik der Werkstoffe und Strukturen

Technische Universität Wien

Wien, im Juni 2018

.....

# Acknowledgements

This thesis is based on the work performed during my employment as a research assistant at Institute for Mechanics of Materials and Structures (IMWS), Vienna University of Technology (TU Wien). It would not have been possible without the help of numerous people of whom I would like to address the most important ones in the following.

First and foremost, I would like to express my deepest gratitude to Dr. Josef Füssl, for opening up the opportunity to pursue a PhD thesis at IMWS and for his constant and tremendous supervision throughout my PhD work. His academical guidance and emotional encouragement have been incredibly valuable supporting me through the rough road to finish this thesis. I really appreciate and will miss our insightful discussions of various topics which have always kept me in the right path. Also, his advice on research as well as on my career are greatly appreciated.

I am indebted to Prof. Josef Eberhardsteiner, Vice Rector of TU Wien and former head of the IMWS, for taking me on board, for his support and help in strategic decisions, for his contributions in our publications, and for always having a door open when needed. Also, my deepest gratitude goes to Prof. Chris M. Martin (University of Oxford) for his valuable contributions in our publications, for the kind hospitality during my short visit at University of Oxford, and for agreeing to be a co-examiner of this thesis.

I would like to thank Prof. Christian Hellmich, current head of the institute, for creating the positive and encouraging work environment at IMWS and for serving as a co-examiner of this thesis. IMWS has been a source of friendships as well as good advices and collaborations for both my live and work during past years. My special thanks go to Dr. Markus Lukacevic for interesting scientific and non-scientific discussions and his contributions in our publications. Also, I am thankful for my current and former colleagues, Dr. Mehdi Aminbaghai, DI Maximilian Autengruber, Dr. Guiseppe Balduzzi, DI Eva Binder, Petr Dohnalik, DI Pedro Godinho, Dr. Herwig Hengl, Dr. Georg Hochreiner, Dr. Muhammad Irfan-ul-Hassan, Dr. Xin Jia, M.Sc. Zijie Jiang, M.Sc. Nabor Jimenez Segura, Dr. Georg Kandler, DI Hawraa Kariem, DI Thomas Kiefer, Dr. Markus Königsberger, DI Wolfgang Lederer, DI Sebastian Pech, Prof. Bernhard Pichler, DI Robert Plachy, Dr. Stefan Scheiner, Dr. Vítězslav Štembera, Dr. Michael Schweigler, Dr. Viktória Vass, Dr. Leopold Wagner, M.Sc. Hui Wang, DI Luis Zelaya-Lainez and Dr. Jiaolong Zhang. Meanwhile, Gabriele Ostrowski, Mag.(FH) Martina Pöll and Astrid Schuh are thanked for the smooth and quick handling of all administrative issues, and David Kaufmann is thanked for his great job as system administrator.

Financial support of this work in the framework of the PhD School DokInHolz funded by the Austrian Federal Ministry of Science, Research and Economy and the Austrian Association of Wood Industries is gratefully acknowledged. We also gratefully acknowledge the financial support of this work by the Austrian Science Fund (FWF) through the Erwin Schrödinger Fellowship J3748-N30. TU Wien is acknowledged as well for the financial support during the last year of this work.

Finally, I would like to thank my family and friends for their support during my stay in Vienna in last years. Especially, I would like to express my deepest gratitude to my wife and parents for their understanding and support without reservation which was invaluable for me to make it through during the most difficult times in my PhD work.

# Abstract

Numerical limit analysis belongs to the field of computational plasticity and is mainly used to predict load bearing capacities of engineering structures. In contrast to conventional elastoplastic analysis methods, limit analysis exclusively focuses on the time instant of structural collapse, and thus the whole load history up to this point doesn't need to be examined. Especially, finite-element-based limit analysis formulations have evolved to powerful tools, able to solve complex large-scale problems efficiently and robustly. Within this thesis, existing finite-element-based limit analysis formulations are discussed in detail and, subsequently, systematically adapted and extended to be applicable to orthotropic materials. The performance of the proposed formulations is assessed by means of different engineering problems. The whole thesis addresses two main tasks and thus has been organised into two parts accordingly.

The first part of the thesis is dedicated to the implementation of numerical limit analysis approaches for strength predictions of wood and wood-based products. Since wood is undergoing a revival and has recaptured market shares in recent years, a reliable and efficient strength prediction tool is urgently needed in timber engineering. However, due to the intrinsic hierarchical structure of wood, a sophisticated and realistic numerical description of its strength behaviour is only possible by means of multiscale considerations. For this reason, numerical limit analysis formulations are proposed for two different scales of observation, the annual ring scale and the clear wood scale. At each scale, effective failure surfaces and distinct failure modes at various stress states could be obtained, and a validation by means of biaxial tests at the clear wood scale has rendered this numerical approach as a powerful tool providing sufficient and reliable information to investigate failure mechanisms of wood at different scales. Furthermore, a comparison between the proposed numerical method with two other computational methods, the extended finite element method and an elastic limit approach in the framework of continuum micromechanics, was performed, showing their strengths and weaknesses on predicting wooden strengths. The numerical limit analysis approaches can, on the one hand, capture basic characteristics of failure modes and the overall strength behaviours correctly and, on the other hand, fulfil the requirement of simplicity and efficiency for being applicable in engineering practice. To assess the applicability in engineering problems, the proposed numerical limit analysis approaches are implemented to predict the load bearing capacity of wood-based products. According to a validation by means of experimental results, this numerical method can provide reliable predictions on bending capacities of cross-laminated timber plates and allows for stochastic studies, taking inhomogeneities and uncertainties of the material into account. In summary, numerical limit analysis can be expected to play an important role for fast strength predictions of wood and wood-based products in the future.

The second part of the thesis is dedicated to the development of new finite-element-based upper bound formulations, allowing for an efficient description of localised failure mechanisms in combine with the consideration of orthotropic strength behaviours. Adaptive mesh refinement is commonly used in numerical upper bound approaches to handle localised failure mechanisms, which normally leads to the use of very fine meshes in failure regions and thus requires high computational effort. Alternatively, by introducing velocity discontinuities (as additional degrees of freedom) in discretised structures and arranging them in a sensible way, localised failure mechanisms can be

---

captured accurately and efficiently by velocity jumps across these discontinuities. To guarantee a consistent orthotropic strength behaviour within solid elements and across discontinuities, an algorithm is derived projecting the stress-based yield function into a traction-based yield function with respect to the plane of plastic flow localisation. Then, to automatically arrange velocity discontinuities in a sensible way, an adaptive strategy is developed to iteratively introduce new velocity discontinuities and adjust orientations of existing ones within the discretised structures. For selected examples, the adaptively-arranged velocity discontinuities can play dominant roles in the resulting upper bound failure modes and thus the plastic strain-rate within solid elements is reduced to a minimum, making adaptive mesh refinement for these examples obsolete.



# Contents

<b>Introduction</b>	<b>1</b>
Motivation . . . . .	3
Research objectives and outline of the thesis . . . . .	5
Contribution of the author . . . . .	6
<b>1 Strength predictions of clear wood at multiple scales using numerical limit analysis approaches (Li et al., 2018c)</b>	<b>7</b>
1.1 Introduction . . . . .	8
1.1.1 Prediction tools for the ultimate strength of wood . . . . .	8
1.1.2 Numerical limit analysis . . . . .	10
1.1.3 Objective of the paper . . . . .	11
1.2 FEM formulation of limit analysis . . . . .	12
1.2.1 Lower bound formulation . . . . .	12
1.2.1.1 Equilibrium within elements . . . . .	13
1.2.1.2 Equilibrium between elements . . . . .	13
1.2.1.3 Periodic boundary conditions . . . . .	13
1.2.1.4 Failure criteria . . . . .	14
1.2.1.5 Discretised lower bound optimisation problem . . . . .	16
1.2.2 Upper bound formulation . . . . .	16
1.2.2.1 Compatibility between velocity and strain-rate field . . . . .	17
1.2.2.2 Periodic boundary conditions . . . . .	18
1.2.2.3 Plastic flow rule . . . . .	18
1.2.2.4 Discretised upper bound optimisation problem . . . . .	19
1.3 Application to wood . . . . .	20
1.3.1 Application of limit analysis at the annual ring scale . . . . .	22
1.3.1.1 Determination of effective failure surfaces . . . . .	24
1.3.1.2 Failure mechanisms of wood cells . . . . .	26

1.3.1.3	Earlywood . . . . .	26
1.3.1.4	Latewood . . . . .	28
1.3.2	Application of limit analysis at clear wood scale . . . . .	28
1.3.2.1	Determination of effective failure surfaces . . . . .	31
1.4	Summary and conclusions . . . . .	32
1.A	Second-order cone programming . . . . .	33
1.B	Matrix representation of the limit analysis formulation . . . . .	34
<b>2</b>	<b>Comparison of unit cell-based computational methods for predicting the strength of wood (Füssl et al., 2017)</b>	<b>37</b>
2.1	Introduction . . . . .	38
2.2	Methods and theory . . . . .	41
2.2.1	Extended finite element method (XFEM) . . . . .	44
2.2.2	Limit analysis (LA) . . . . .	46
2.2.2.1	Numerical upper bound formulation . . . . .	46
2.2.2.2	Numerical lower bound formulation . . . . .	48
2.2.3	Elastic limit (EL) approach . . . . .	49
2.2.3.1	Continuum micromechanics . . . . .	50
2.2.3.2	Unit cell homogenisation . . . . .	50
2.2.3.3	Elastic Limit estimates . . . . .	51
2.3	Material . . . . .	52
2.3.1	Morphology . . . . .	52
2.3.2	Mechanical behaviour . . . . .	53
2.4	Calculations and results . . . . .	58
2.4.1	Annual ring scale . . . . .	58
2.4.2	Clear wood scale . . . . .	60
2.5	Conclusions . . . . .	64
<b>3</b>	<b>Bending strength predictions of cross-laminated timber plates subjected to concentrated loading using 3D finite-element-based limit analysis approaches (Li et al., 2018d)</b>	<b>67</b>
3.1	Introduction . . . . .	68
3.2	Numerical limit analysis formulations . . . . .	71
3.2.1	Lower bound formulation . . . . .	71
3.2.1.1	Equilibrium within elements . . . . .	72

3.2.1.2	Equilibrium between elements . . . . .	72
3.2.1.3	Static boundary conditions . . . . .	72
3.2.1.4	Plastic failure criteria . . . . .	73
3.2.1.5	Discretised lower bound optimisation problem . . . . .	73
3.2.2	Upper bound formulation . . . . .	74
3.2.2.1	Weak equilibrium . . . . .	76
3.2.2.2	Plastic yield function . . . . .	77
3.2.2.3	Assembly . . . . .	78
3.3	Application to CLT plates . . . . .	78
3.3.1	CLT plate bending test . . . . .	78
3.3.2	Application using strength profiles . . . . .	83
3.4	Summary and conclusions . . . . .	89
<b>4</b>	<b>A numerical upper bound formulation with sensibly-arranged velocity discontinuities and orthotropic material strength behaviour (Li et al., 2018b)</b>	<b>92</b>
4.1	Introduction . . . . .	93
4.1.1	Numerical limit analysis . . . . .	93
4.1.2	Objective of the paper . . . . .	94
4.2	Upper bound approaches . . . . .	95
4.3	Numerical results . . . . .	98
4.3.1	Rigid strip footing . . . . .	99
4.3.2	Block with asymmetric holes . . . . .	101
4.3.2.1	Mohr-Coulomb failure criterion . . . . .	101
4.3.2.2	Tsai-Wu failure criterion . . . . .	104
4.3.3	Shear test on block . . . . .	106
4.4	Summary and conclusions . . . . .	107
<b>5</b>	<b>An algorithm for adaptive introduction and arrangement of velocity discontinuities within 3D finite-element-based upper bound limit analysis approaches (Li et al., 2018a)</b>	<b>111</b>
5.1	Introduction . . . . .	112
5.2	Kinematic theorem . . . . .	115
5.3	Traction-based plastic yield function . . . . .	117
5.3.1	Projection algorithm . . . . .	117
5.3.2	Numerical verification . . . . .	119
5.4	Associated plastic flow rule . . . . .	122

---

5.5	Finite-element-based upper bound formulation . . . . .	124
5.5.1	Primal formulations . . . . .	124
5.5.2	Dual formulations . . . . .	128
5.6	Adaptive arrangement of the velocity discontinuity . . . . .	129
5.6.1	Determination of planes of plastic flow localisation . . . . .	130
5.6.2	Adaptive introduction and adjustment of velocity discontinuities . . . . .	132
5.7	Numerical results . . . . .	135
5.7.1	Block with thin symmetric notches . . . . .	136
5.7.2	Block with symmetric rectangular holes . . . . .	140
5.7.3	Examples with orthotropic strength behaviours . . . . .	143
5.7.4	3D cylinder with central circular notch . . . . .	146
5.8	Summary and conclusions . . . . .	149
5.A	Second-order cone programming . . . . .	150
	<b>Conclusions and outlook</b>	<b>152</b>
	<b>Bibliography</b>	<b>168</b>
	<b>Curriculum Vitae</b>	<b>169</b>
	<b>Publications and Conference Contributions</b>	<b>170</b>

# Introduction

## Motivation

Limit analysis is a computational method widely applied to predict load bearing capacities of engineering structures exhibiting elastoplastic material response. Normally, a complete elastoplastic analysis requires an iterative procedure considering the whole loading history, which can become very expensive and difficult for certain problems. Alternatively, belonging to a group known as direct method, limit analysis exclusively focuses on the critical work rate at the time instant of structural collapse, when structures lose the capability to store any further external work as recoverable internal energy. With a quite simple solution procedure and a small set of input parameters, limit analysis can provide robust and efficient predictions on collapse loads of structures in a direct manner.

Based on the assumption of rigid and perfectly plastic material response, the fundamental problem of limit analysis can be stated as: *Find the kinematically admissible velocity field which minimises the external work rate over the set of all statically admissible stress fields which maximise the internal dissipation rate.* Unfortunately, the resulting saddle-point problem can be solved exactly only for simple geometric and loading situations as well as for simple material behaviours. For more complex situations, the plastic flow compatibility in the static lower bound principal and the plastic admissibility in the kinematic upper bound principle may be relaxed, providing lower and upper bounds for the collapse load.

The first complete formulations of limit analysis theorems were established in the early-1950s (Drucker et al., 1951, 1952, Hill, 1951), and their analytical solutions have been applied to provide useful bounds for engineering problems, e.g. in soil mechanics (Chen, 2013) and concrete plasticity (Nielsen and Hoang, 2016). However, since analytical solutions of limit analysis are normally limited to simple problems, starting from the early-1970s (Anderheggen and Knöpfel, 1972, Lysmer, 1970, Maier et al., 1972), intensive research efforts have been invested globally to implement limit analysis theorems into well-developed numerical formulations for more general applications from simple two-dimensional benchmark examples to complicated three-dimensional engineering problems. Thanks to the rapid evolution of computer technology and development in mathematical programming, the so-defined numerical limit analysis approaches have been proven a reliable and efficient tool for strength prediction of materials and safety assessment of structures used in engineering applications, e.g. in geotechnical engineering (Martin and White, 2012, Sloan, 2013), masonry engineering (Milani et al., 2006a,b) and concrete engineering (Domenico et al., 2014, Pisano et al., 2015).

Due to developments and increasing applications of anisotropic engineering materials, e.g. laminated and reinforced composites, the implementation of orthotropic yield functions into numerical limit analysis formulations has been investigated in several previous works (Capsoni et al., 2001a,b, Corradi et al., 2006, Li, 2011, Pisano et al., 2012, Pisano and Fuschi, 2007). However, numerical limit analysis has never been applied to wood. As a naturally-grown material, wood exhibits quite complex and variable mechanical behaviours, which have restricted deeper understanding of the mechanical processes within the material and more efficient utilisations in engineering applications. Especially with respect to the strength behaviours of wood, on the one hand, experimental investigations are normally difficult as well as expensive, and on the other hand, none of the existing numerical prediction tools is universally accepted by the wood community.

Since the strength behaviours of wood is strongly influenced by the underlying complex hierarchical material system, a multiscale approach has been developed based on the framework of micromechanics (Bader et al., 2010, Hofstetter et al., 2008, Lukacevic and Füssl, 2016, Lukacevic et al., 2014b, 2017), where strength prediction tools are applied to unit cell models representing the structural characteristics of wood at different scales of observation. Subjected to this multiscale concept, the application of the conventional finite element method at each length scale leads to very high computational cost and probably to an unnecessarily high complexity of the overall model. For this reason, taking benefit from its simplicity and efficiency, numerical limit analysis can serve as a powerful alternative strength prediction tool for wood and wood-based products.

The performance of numerical limit analysis formulations heavily relies on the discretisation strategy and the mathematical programming method applied to solve the underlying optimisation problem. For the discretisation of limit analysis formulations, although several methods using high-order interpolation functions have been developed during recent years, in order to get rigorous bounds, the finite-element-based method is still the most robust and reliable one, using piecewise linear stress elements (Lyamin and Sloan, 2002a, Makrodimopoulos and Martin, 2006) for lower bound calculations and constant strain elements (Lyamin and Sloan, 2002b) or simplex strain elements (Makrodimopoulos and Martin, 2007) for upper bound calculations. Regarding the underlying optimisation problem, second-order cone programming is the state-of-the-art algorithm which allows for the formulation of most commonly-used nonlinear yield functions in their native form, as second-order cone constraints, and can provide robust and efficient solutions for large scale problems.

Since plastic failure often occurs very localised, the application of adaptive mesh refinement in numerical limit analysis approaches has been intensively investigated. However, in such approaches, the heavily refined mesh in the critical plastic failure regions normally leads to a significant increase in number of elements and thus still demands very high computational effort. For this reason, in numerical upper bound formulations velocity discontinuities have been implemented, which allow velocity jumps across all element interface as additional degrees of freedom measuring plastic failure. Velocity discontinuities have been proven powerful in overcoming locking effects and increasing the quality of upper bound solutions when constant strain elements are used (Krabbenhøft et al., 2005, Makrodimopoulos and Martin, 2008, Sloan and Kleeman, 1995), but their capability in modelling localised failure mechanisms has rarely been investigated so far, especially when orthotropic strength behaviours are considered. Since well-arranged ve-

locity discontinuities play a dominant role in corresponding upper bound failure modes according to Smith and Gilbert (2007) and Milani and Lourenço (2009), an efficient and robust algorithm, which can arrange velocity discontinuities automatically into layouts with good agreement to localised failure modes, will provide an alternative approach to adaptive mesh refinement and prevent the use of fine meshes in numerical upper bound calculations.

## Research objectives and outline of the thesis

The main objective of this thesis has been the development of new finite-element-based limit analysis approaches / concepts, serving as strength prediction tools with sufficient efficiency and robustness to be applied to engineering problems. Accordingly, this thesis has been structured into two parts, with them and the related tasks defined in the following:

- (a) Assessing the applicability of numerical limit analysis for strength predictions of orthotropic materials and proposing a concept for the implementation of this numerical method to wood and wood-based products.
  - Implementing finite-element-based limit analysis formulations for strength predictions of wood, considering the intrinsic hierarchical structure at different scales of observation (Publication 1).
  - Comparing the performance of the implemented numerical limit analysis approaches with two existing methods, the extended finite element method and an elastic limit approach (Publication 2).
  - Applying the new formulations to predict the load bearing capacity of cross-laminated timber plates, considering strength variations and imperfections in wooden boards using a stochastic approach (Publication 3).
- (b) Developing an alternative strategy to the commonly-used adaptive mesh refinement in numerical limit analysis approaches, allowing for more efficient description of localised plastic failure mechanisms.
  - Presenting a concept for a sensible arrangement of velocity discontinuities in finite-element-based limit analysis formulations, including materials with orthotropic strength behaviours (Publication 4).
  - Developing a new algorithm for an automated implementation of velocity discontinuities into a sensible arrangement (Publication 5).

These tasks were addressed in five peer-reviewed publications. In the following, the outline of this thesis is summarised according to these publications.

**Publication 1** aims at a new numerical method to understand failure mechanisms and to predict strength behaviours of wood. By enriching finite-element-based limit analysis formulations with orthotropic yield functions and periodic boundary conditions, the numerical limit analysis approaches are applied for the first time to predict the strength behaviours of clear wood. The intrinsic hierarchical material structure is considered following a multiscale concept including two scales of observation, the annual ring scale

exhibiting a periodic honeycomb-like structure and the clear wood scale represented by a laminated annual ring structure. Numerical lower bound and upper bound calculations are applied to determine effective failure surfaces and identify various failure modes at different stress states, for earlywood and latewood unit cell models at the annual ring scale and laminated unit cell models at the clear wood scale. Applying a multiscale approach, material strength properties at the clear wood scale are defined according to numerical results obtained at the annual ring scale. To validate the present numerical limit analysis approaches, effective failure surfaces obtained at the clear wood scale are compared with biaxial loading test results on Norway spruce clear wood.

In **Publication 2**, the numerical limit analysis are compared with the extended finite element method and an elastic limit approach regarding their capacities for efficient and reliable predictions on effective strength properties of clear wood. The extended finite element method is powerful and allows for a very realistic description of strength-governing processes, but its complexity and high computational effort prevent widespread use in the engineering field. The elastic limit approach is efficient due to the analytical solution basis and elegant since material properties of difference phases can be linked across several scales of observation, but stress and strain averages over material phases are perhaps not able to capture all failure-triggering processes. The numerical limit analysis, comparable to the extended finite element method, can provide reliable predictions on basic characteristics of failure modes and the overall strength behaviours, and, like the elastic limit approach, exhibits high computational efficiency and robustness allowing for rapid strength predictions within engineering design processes. Similar to Publication 1, all these three methods are applied to the annual ring scale and the clear wood scale, and their strength predictions are compared with each other as well as with experimental results to evaluate their applicability to wood.

**Publication 3** is dedicated to the application of three-dimensional finite-element-based limit analysis formulations to solve engineering problems, i.e. the load-bearing capacities of cross-laminated timber plates. Cross-laminated timber is an innovative wood product with excellent in-plane and out-of-plane performances and earning global popularity in timber engineering. It is well-known that, the orthotropic and inhomogeneous strength properties of wooden boards have a strong influence on the load bearing capacities of cross-laminated timber plates, especially when the complex wood fibre distributions due to randomly occurring knots are considered. For this reason, combining recent advances in numerical limit analysis and a knot reconstruction algorithm, the bending strength of cross-laminated timber plates under concentrated loading is predicted using the numerical limit analysis approaches, and the scatter of strength properties resulting from the material's homogeneities is investigated using a stochastic approach. For the latter, data collected during the grading process of wooden boards is condensed into so-called strength profiles for individual wooden boards, and the cross-laminated timber plates are assembled using wooden boards with strength profiles randomly-chosen from the database. Numerical results are compared to experimental observations, with respect to magnitude as well as scatter of bending capacities of cross-laminated plates.

**Publication 4** presents the implementation of sensibly-arranged velocity discontinuities in three-dimensional finite-element-based upper bound formulations for orthotropic material strength behaviours. In the formulations, the description of the unknown velocity field can be extended by introducing velocity discontinuities between finite elements as additional degrees of freedom. To allow orthotropic yield functions within



finite elements as well as across velocity discontinuities, the concept of “projecting” the stress-based orthotropic yield function onto a certain discontinuity is briefly presented, giving a traction-based yield function which allows for a consistent description of the material strength behaviour. Instead of mesh refinement, a concept of sensible arrangement of velocity discontinuities is proposed, allowing for a more efficient and accurate description of localised plastic failure modes. The present implementations are verified by means of several selected examples under plane strain conditions.

**Publication 5** focuses on an adaptive algorithm implementing velocity discontinuities into three-dimensional finite-element-based upper bound formulations, in order to achieve more reliable and efficient numerical upper bound solutions. As outlined in Publication 4, velocity discontinuities can be very powerful if they are sensibly arranged. To allow a general application of this approach, an adaptive algorithm is presented to implement velocity discontinuities into the optimal layout by iteratively introducing new and adjusting existing discontinuities according to possible planes of plastic flow localisation determined at each strain-rate evaluation node. To guarantee consistent strength behaviours throughout the whole discretised structure, traction-based yield functions defining the plastic flow across discontinuities are derived from their stress-based counterparts. This procedure is outlined in detail and the obtained traction-based yield functions are verified numerically for orthotropic strength behaviours. By means of three different examples, considering either isotropic or orthotropic strength behaviours, the performance of the proposed strategy is investigated, and upper bound collapse loads as well as failure modes are compared to reference solutions.

## Contribution of the author

This thesis is a cumulative work consisting of five publications in peer-reviewed scientific journals. The author’s contributions to the respective publications are as follows:

- **Publication 1:** *Strength predictions of clear wood at multiple scales using numerical limit analysis approaches* (Li et al., 2018c)

The author contributed to the development and implementation of the numerical approach, performed all numerical calculations and data analysis, and prepared most of the manuscript.

- **Publication 2:** *Comparison of unit cell-based computational methods for predicting the strength of wood* (Füssl et al., 2017)

The author contributed to a part of the numerical approaches, performed a part of numerical calculations and data analysis, and prepared a part of the manuscript.

- **Publication 3:** *Bending strength predictions of cross-laminated timber plates subjected to concentrated loading using 3D finite-element-based limit analysis approaches* (Li et al., 2018d)

The author contributed to the extension of the numerical approach and the development of the stochastic approach, performed all numerical calculations and most data analysis, and prepared most of the manuscript.

- **Publication 4:** *A numerical upper bound formulation with sensible-arranged velocity discontinuities and orthotropic material strength behaviour* (Li et al., 2018b)

The author contributed to the development of the new numerical upper bound concept, performed all numerical calculations and data analysis, and prepared most of the manuscript.

- **Publication 5:** *An algorithm for adaptive introduction and arrangement of velocity discontinuities within 3D finite-element-based upper bound limit analysis approaches* (Li et al., 2018a)

The author contributed to the development of the new adaptive strategy for upper bound calculations and the derivation of relevant algorithms, performed all numerical calculations and data analysis, and prepared most of the manuscript.

## Strength predictions of clear wood at multiple scales using numerical limit analysis approaches (Li et al., 2018c)

Authored by Mingjing Li, Josef Füssl, Markus Lukacevic, Josef Eberhardsteiner & Chris M. Martin

Published in *Computers and Structures*, 196:200-216, 2018

The final publication is available at:

<https://www.sciencedirect.com/science/article/pii/S0045794917311550>

**Abstract:** This work aims at a new approach for understanding failure mechanisms and predicting wood strengths, which are strongly influenced by the complex hierarchical material system of wood. Thus, a mechanical concept, where different microstructural characteristics are incorporated, appears to be necessary, based on the division of wood into meaningful scales of observation. At each scale, effective strength properties are to be determined and a multiscale approach needs to be applied, for which conventional numerical methods appear to be inefficient. In this work, numerical limit analysis approaches are further developed and applied for the first time to wood, complementing conventional methods successfully at certain scales of observation in a multiscale ‘damage’ approach.

Limit analysis belongs to the group of direct plastic analysis methods, focusing exclusively on the time instant of structural collapse, and delivering the ultimate strength. Compared with conventional numerical approaches that have previously been applied to wood, limit analysis approaches are much more stable and efficient.

In this work, orthotropic failure criteria and periodic boundary conditions are implemented into both lower bound and upper bound numerical limit analysis formulations. As numerical results, effective failure surfaces are obtained at both annual ring scale and clear wood scale. A validation at clear wood scale indicates that this new approach

is very promising.

**Keywords:** strength prediction of wood, numerical limit analysis approaches, different length scales, orthotropic failure criteria, periodic boundary conditions.

## 1.1 Introduction

In recent years, wood, as a building material, has undergone a revival. This can be attributed to its excellent mechanical and physical properties on one hand and the fact that it is an environmentally sustainable material with a pleasant appearance on the other hand. Also, due to continuous extensions and improvements in building codes throughout Europe, allowing higher and more complex timber constructions, its share of the building market is constantly increasing and the volume of consumption is experiencing enormous growth rates. In the course of this, however, demands on timber constructions are increasing constantly. In order to meet these demands and allow the use of wood in complex applications, prediction tools for the mechanical performance of wood are gaining importance. A wider repertoire of advanced prediction tools should facilitate a better utilisation of wood and wood-based products, increasing their competitiveness compared with other building materials. Especially for predicting the ultimate strength of wood, very few reliable and promising methods exist so far. A brief overview of some existing methods for predicting/modelling structural failure at the wooden board level is given in the following.

### 1.1.1 Prediction tools for the ultimate strength of wood

The first group of approaches avoids the direct description of failure mechanisms and instead uses so-called *mean stress concepts* (Masuda, 1988), where averaged stresses over a finite small area are assumed to indicate failure. These areas can be adjusted to typical features of wood, such as structural characteristics of wood fibres (Aicher et al., 2002). Serrano and Gustafsson (2007), Sjödin and Serrano (2008) and Sjödin et al. (2008) applied this approach in combination with findings of linear elastic fracture mechanics. They investigated single and multiple dowel connections, where the size of the finite area was governed by the fracture properties of the material. The suitability of different area definitions, over which the stresses are averaged, and also the efficiency of various failure criteria, were compared by Guindos (2011). Lukacevic and Füssl (2014) presented a physically-based structural failure criterion, where it was assumed that in wooden boards with knots, global failure can be related to a stress transfer mechanism, which is identifiable by evaluating averaged stress fields in the vicinity of knots. Either way, such models are mostly dependent on empirical parameters and the true failure mechanisms cannot be identified. This can be overcome by directly modelling failure processes.

The most sophisticated approaches for this are based on multi-surface plasticity/failure criteria, as described in Mackenzie-Helnwein et al. (2003) and Schmidt and Kaliske (2006). Thereby, orthotropic yield surfaces are defined describing the onset of plastic deformation, whereas failure surfaces indicate stress states where cracks are to be expected. Cracking is normally modelled with so-called cohesive elements, including an anisotropic traction separation law for wood. Applications of this model show promising

results regarding the estimation of load carrying behaviour (Schmidt and Kaliske, 2007, 2009). Danielsson and Gustafsson (2014) also used a cohesive zone model based on plasticity theory for parameter studies of a glued laminated timber beam with a hole.

These approaches work well for a homogeneous fibre orientation and if the location of the crack path is known in advance. The weak point of these methods is the influence on the failure mechanism by specifying the crack direction. As wood is a naturally grown material, usually complex stress states prevail, especially in the presence of knots and other defects, meaning that such an approach is difficult to apply. In such cases additional strategies are required, like the approach in Jenkel and Kaliske (2014), where cohesive interface elements are aligned with predetermined fibre directions around knots.

In recent years, Lukacevic and Füssl (2014, 2016), Lukacevic et al. (2014a, 2017) have established the basis for a crack initiation and propagation criterion in the framework of the extended finite element method (XFEM), which has been implemented into a numerical simulation tool for wooden boards. The implementation of such an approach poses two questions: (i) which stress states cause the initiation of a crack? and (ii) what is the corresponding crack direction at the wooden board scale? These questions can only be answered by looking deeper into the microscopic hierarchical structure of wood, and taking several structural features at different length scales into account. Therefore, to obtain reliable failure surfaces and reliable crack directions at the wooden board scale, a multiscale ‘damage’ approach is pursued. For such an approach, failure mechanisms at different length scales of wood need to be analysed numerically. Doing this exclusively by applying the concept of multi-surface plasticity/failure criteria in combination with XFEM, at each length scale, leads to very high computational cost and probably to an unnecessarily high complexity of the overall model.

For this reason, an additional numerical method is to be introduced, namely *numerical limit analysis*. This method, a so-called ‘direct method’, focuses exclusively on the time instant of failure, and delivers lower and upper bounds for the ultimate strength of the considered material structure. Compared with conventional numerical approaches, where the complete load history has to be considered and, in order to predict correct failure mechanisms, proper regularisation techniques must be used, the limit analysis approach is much more stable and efficient. Moreover, it leads to rigorous bounds on the material strength and, thus, gives a reliable error measure for the prediction. Thus, this method can serve as a useful tool for complementing more complex numerical step-by-step approaches by, for example, identifying critical failure regions in a preliminary simulation procedure, as also suggested in Füssl et al. (2017), Pisano et al. (2015).

Of course, these advantages result from the strict limitations on which these formulations are based, including: (i) the associated plastic flow rule and (ii) the rigid and perfectly plastic (ductile) material behaviour. For wood, these two idealisations are not entirely correct, but the first can be considered as an appropriate assumption, which is made due to a lack of information about the non-associativity, and the second does not exclude that good strength predictions are also possible for strain-softening structures. In Denton and Morley (2000) it is stated: “A structure does not need to exhibit perfect plasticity for the theoretical plastic collapse load based on the peak yield stress of each component to be approached closely. Rather, it is necessary that, at the point when a collapse mechanism forms under a particular loading, all those regions within the structure which are undergoing straining lie very close to the peak yield stress which they can achieve.” Wood definitely has the ductile potential to ‘activate’ the strength of

many points along a potential crack surface before brittle failure occurs. Nevertheless, one might argue that this approach, mainly evolved from and applied in fields dealing with very homogeneous (manmade) materials like steel, is not suitable for application to wood, where failure is often induced by the largest defect (such as knots at the wooden board scale, or cell wall imperfections at an observation scale below). With regard to this, it might be mentioned that the prediction quality of concepts addressing structural failure of a highly heterogeneous material depends on knowledge about the local strength reduction due to defects. Thus, tools which are capable of analysing this influence for a huge number of defect variations within an acceptable timeframe, like numerical limit analysis, might be very useful for fracture models at the macroscopic scale. For this reason, the numerical limit analysis approach seems to be an appropriate method to make a comprehensive multiscale ‘damage’ framework for wood worth pursuing.

### 1.1.2 Numerical limit analysis

Originally, the objective of limit analysis was the determination of the load bearing capacity of structures exhibiting elastoplastic material response. At collapse, the capacity of structures to store any additional external work as recoverable energy is lost. Thus, for a prescribed macroscopic velocity field and a prescribed macroscopic traction field on the boundary, defining the loading situation, limit analysis concentrates on the critical energy dissipation rate at failure of structures or, in this paper, of unit cells for microstructures. The problem may be stated as follows according to Ciria et al. (2008): *Find the kinematically admissible velocity field, which minimises the external energy over the set of all statically admissible stress fields, which maximise the internal dissipated energy.* Unfortunately, the resulting saddle-point problem can be solved exactly only for simple geometric and loading situations, and for simple material behaviour. For more complex situations, the plastic flow compatibility in the static lower bound principle and the plastic admissibility in the kinematic upper bound principle may be relaxed, providing lower and upper bounds for the load bearing capacity (effective strength) of structures.

The first complete formulations of limit analysis theorems were established in the 1950s by Drucker et al. (1951, 1952), Hill (1951), though analytical exact solutions (coincident lower and upper bounds) were limited to very simple problems. Thanks to the rapid evolution of computer technology and developments in mathematical programming, the finite element method (FEM) has proven to be a powerful tool for implementing limit analysis approach, from simple two-dimensional problems to complicated three-dimensional applications. Therefore, more attention has been given to numerical limit analysis formulations within past decades.

Early implementations of limit analysis using the finite element method in conjunction with numerical optimisation were performed by Lysmer (1970) for the lower bound problem, and by Maier et al. (1972) for the upper bound problem. In these works, linear three-noded triangular elements were used for discretisation and the resulting optimisation problems could be solved by linear programming, provided that the adopted failure criteria were linearised.

Many subsequent works can be found focusing on nonlinear optimisation and higher-order triangular elements for the discretisation. Notable contributions with respect

to the use of nonlinear programming have been given by Krabbenhøft and Damkilde (2000), Lyamin and Sloan (2000, 2002a,b), enabling nonlinear failure criteria to be implemented in their native form. However, local smoothing procedures for yield surfaces with singularities, like the Tresca or Mohr-Coulomb criteria, are necessary with this approach.

In general, the efficiency of a numerical limit analysis method depends significantly on the algorithms used for solving the associated optimisation problem. In later studies by Makrodimopoulos and Martin (2006, 2007), Ciria et al. (2008), Portioli et al. (2014), and in Füssl et al. (2008) for composite materials, second-order cone programming (SOCP) has proven to be an excellent alternative method, with sufficient robustness and efficiency to solve large-scale optimisation problems of limit analysis. This method is also applicable to a wide variety of failure criteria, since many commonly-used yield functions can be cast as second-order cones. Therefore, within this work, SOCP is employed for the numerical limit analysis formulation.

### 1.1.3 Objective of the paper

The main objectives driven this work can be formulated as follows:

- The formulation of numerical limit analysis approaches so that they are applicable to certain observation scales of wood. This requires the extension of conventional FEM-based limit analysis formulations to incorporate orthotropic failure criteria and periodic boundary conditions.
- The application of these formulations to selected microstructures at the *annual ring scale* as well as the *clear wood scale* to demonstrate the applicability of the numerical limit analysis method. Moreover, 2D strength data in terms of effective failure surfaces are to be obtained, to show the potential and possible future benefits of such an approach.
- Comparison of the numerically obtained effective failure surfaces at the clear wood scale with experimental results from biaxial testing, to assess the accuracy and capability of the proposed limit analysis concept with respect to the prediction of wood strengths.

The paper is structured as follows. In the next two sections, classical lower bound formulations (Section 2.1) and upper bound formulations (Section 2.2) are recapitulated and the implementation of periodic boundary conditions, for unit cell considerations, as well as orthotropic failure criteria, are presented. The application of these newly derived formulations to wood unit cells at the annual ring scale, and the resulting failure modes and effective failure surfaces, are presented in Section 3.1. Subsequently, in Section 3.2, effective failure surfaces at the clear wood scale are obtained and compared with experimental results. Finally, a brief summary and concluding comments are given in Section 4.

## 1.2 FEM formulation of limit analysis

The lower bound theorem is based on statically admissible stress fields,  $\boldsymbol{\sigma}$ , satisfying the equilibrium equations, the failure criterion and static boundary conditions, while the upper bound theorem is based on kinematically admissible velocity fields,  $\dot{\mathbf{u}}$ , fulfilling the compatibility equation, the associated plastic flow rule and kinematic boundary conditions. Neither of them necessarily gives the exact load multiplier  $\beta^*$  for structural failure, but they provide a lower bound  $\beta^{LB}$  and an upper bound  $\beta^{UB}$ , fulfilling

$$\beta^{LB} \leq \beta^* \leq \beta^{UB}. \quad (1.1)$$

When the bracketing error, defined as the difference between  $\beta^{LB}$  and  $\beta^{UB}$ , is smaller than the required accuracy of the prediction, a sufficient approximation of  $\beta^*$  is obtained, which represents a complete solution satisfying the equilibrium equation, the compatibility equation, and the failure criterion with associated flow.

In this paper, both lower bound and upper bound formulations are developed in 2D and applied to 2D unit cells representing microstructures of wood at different scales of observation. Note that at each scale, the characteristic dimensions of the unit cells in the 2D plane are much smaller than the dimension of the material in the out-of-plane direction. Therefore, the plane strain condition is enforced in all of following formulations.

### 1.2.1 Lower bound formulation

The lower bound theorem states that any load multiplier determined from a statically admissible stress field which is in equilibrium with given external loads is not greater than the exact collapse multiplier  $\beta^*$ . Therefore, for a given discretisation, the best lower bound for the load multiplier,  $\beta^{LB}$ , can be found through the following optimisation problem:

$$\begin{aligned} \beta^{LB} = \max \quad & \beta \\ \text{s.t.} \quad & \mathbf{L}_\sigma \boldsymbol{\sigma} + \beta \mathbf{h} = \mathbf{0} \quad \text{in } V \\ & \mathbf{L}_t \boldsymbol{\sigma} = \beta \mathbf{t} \quad \text{on } \Gamma_t \\ & f(\boldsymbol{\sigma}) \leq 0 \quad \text{in } V \end{aligned} \quad (1.2)$$

where in the first constraint, enforcing equilibrium within the body  $V$ ,  $\mathbf{L}_\sigma$  denotes the divergence operator and  $\mathbf{h}$  the live body force vector. In the static boundary conditions,  $\mathbf{L}_t$  is the traction-stress operator depending on the outward normal vector  $\mathbf{n}$  of the loaded surface  $\Gamma_t$  and  $\mathbf{t}$  represents the prescribed live traction forces. Plastic admissibility, defined by the yield function  $f$ , is enforced by the third constraint.

For the discretisation of the stress field  $\boldsymbol{\sigma}$ , triangular elements with three nodes are used, in which the stress field is approximated with linear shape functions. Each element has its own set of internal stress evaluation nodes, thus multiple nodes from adjacent elements may share the same coordinates. At discontinuities between elements, the continuity of normal and shear stress components is enforced. The discretised version of the optimisation problem in Eq. (1.2), as well as its adaptations for periodic boundary conditions and orthotropic failure criteria, are described step by step in the following.



### 1.2.1.1 Equilibrium within elements

The discretised form of the internal equilibrium equation, first constraint in Eq. (1.2), can be expressed for an element as follows:

$$\mathbf{L}_\sigma^e \mathbf{N}_\sigma^e \mathbf{q}_\sigma^e + \beta \mathbf{h}^e = \mathbf{0}, \quad \forall e \in \{1, \dots, LE\}, \quad \text{with} \quad (1.3)$$

$$\mathbf{L}_\sigma^e = \begin{pmatrix} \frac{\partial}{\partial x} & 0 & \frac{\partial}{\partial y} \\ 0 & \frac{\partial}{\partial y} & \frac{\partial}{\partial x} \end{pmatrix} \in \mathfrak{R}^{2 \times 3}, \quad \text{and} \quad (1.4a)$$

$$\mathbf{h}^e = \begin{pmatrix} h_x^e \\ h_y^e \end{pmatrix} \in \mathfrak{R}^2, \quad (1.4b)$$

denoting the divergence operator and the live body force vector for an element. In this work, no dead or live body forces are taken into account, hence,  $\mathbf{h}^e = \mathbf{0}$ .  $LE$  is the total number of elements,  $\mathbf{N}_\sigma^e \in \mathfrak{R}^{3 \times 9}$  contains linear shape functions interpolating between the nodal stresses  $\mathbf{q}_\sigma^e \in \mathfrak{R}^9$ , containing all three nodal stress vectors  $\mathbf{q}_\sigma^{e,i} = (q_{\sigma,xx}^{e,i}, q_{\sigma,yy}^{e,i}, q_{\sigma,xy}^{e,i})^\top \in \mathfrak{R}^3 (\forall i \in \{1, 2, 3\})$  of an element.

### 1.2.1.2 Equilibrium between elements

Due to the approximation of the stress field within an element using linear shape functions, continuity of the stress field between elements can be ensured by applying constraints to two node pairs of each discontinuity (between elements). Denoting an arbitrary discontinuity as  $dis$  with two pairs of adjacent stress nodes designated  $(1, 1')$  and  $(2, 2')$ , the constraints can be expressed as

$$\begin{pmatrix} \mathbf{L}_t^{dis} & \mathbf{0} & -\mathbf{L}_t^{dis} & \mathbf{0} \\ 0 & \mathbf{L}_t^{dis} & \mathbf{0} & -\mathbf{L}_t^{dis} \end{pmatrix} \begin{pmatrix} \mathbf{q}_\sigma^{dis,1} \\ \mathbf{q}_\sigma^{dis,2} \\ \mathbf{q}_\sigma^{dis,1'} \\ \mathbf{q}_\sigma^{dis,2'} \end{pmatrix} = \mathbf{0}, \quad \forall dis \in \{1, \dots, LD\}, \quad \text{with} \quad (1.5)$$

$$\mathbf{L}_t^{dis} = \begin{pmatrix} \cos \theta^{dis} & 0 & \sin \theta^{dis} \\ 0 & \sin \theta^{dis} & \cos \theta^{dis} \end{pmatrix} \in \mathfrak{R}^{2 \times 3} \quad (1.6)$$

as the 2D rotation operator with  $\theta^{dis}$  denoting the normal to  $dis$  and the  $x$ -axis of the global coordinate system.  $\mathbf{q}_\sigma^{dis,i} = (q_{\sigma,xx}^{dis,i}, q_{\sigma,yy}^{dis,i}, q_{\sigma,xy}^{dis,i})^\top \in \mathfrak{R}^3 (\forall i \in \{1, 2, 1', 2'\})$  are the nodal stress vectors associated with the corresponding discontinuity, and  $LD$  is the total number of discontinuities in the discretised body.

### 1.2.1.3 Periodic boundary conditions

Since we want to investigate unit cells of microstructures of wood, the conventional static boundary conditions, appearing in the second constraint in Eq. (1.2), must be replaced by periodic boundary conditions. Therefore, the relevant portion of the boundary  $\partial\Omega$  of each unit cell is divided into two parts, a positive part  $\partial\Omega^+$  and a negative part  $\partial\Omega^-$  with corresponding nodes  $\mathbf{x}^+ \in \partial\Omega^+$ ,  $\mathbf{x}^- \in \partial\Omega^-$ , associated outward normal

vectors  $\mathbf{n}^+ = -\mathbf{n}^-$  and the relation  $\partial\Omega^+ \cup \partial\Omega^- = \partial\Omega$ . In the lower bound formulation, periodicity of the stress field is then ensured by enforcing an anti-periodic traction field through

$$\mathbf{t}^+ = -\mathbf{t}^-, \quad (1.7)$$

where  $\mathbf{t}^+$  are traction vectors associated with  $\mathbf{x}^+$  and  $\mathbf{t}^-$  are traction vectors associated with  $\mathbf{x}^-$ . It allows for a periodic succession of the unit cell, and leads to stress fields in the unit cell representative of the whole material structure. Moreover, stress fluctuations vanish by volume averaging of the stresses over the unit cell (abbreviated as UC in the following equations) and a meaningful effective (macroscopic) stress state  $\Sigma$  can be obtained as

$$\Sigma = \frac{1}{V_{UC}} \int_{V_{UC}} \boldsymbol{\sigma}(\mathbf{x}) dV. \quad (1.8)$$

The discretised form of the periodic traction constraint for one pair of corresponding stress nodes reads

$$\begin{pmatrix} \mathbf{L}_t^{per} & -\mathbf{L}_t^{per} \end{pmatrix} \begin{pmatrix} \mathbf{q}_\sigma^{per, \mathbf{x}^+} \\ \mathbf{q}_\sigma^{per, \mathbf{x}^-} \end{pmatrix} = \mathbf{0}, \quad \forall per \in \{1, \dots, LP\}, \quad (1.9)$$

where  $LP$  is the number of node pairs for which the periodic boundary conditions are defined,  $\mathbf{L}_t^{per} \in \mathfrak{R}^{2 \times 3}$  is identical to the discontinuity operator  $\mathbf{L}_t^{dis}$ , while  $\mathbf{q}_\sigma^{per, \mathbf{x}^+}$  and  $\mathbf{q}_\sigma^{per, \mathbf{x}^-}$  are the nodal stress vectors for the corresponding node pairs.

It is then sufficient to apply the external loading through the traction at the surface nodes  $\mathbf{x}^+$ . To define an arbitrary 2D effective loading state, the following two sets of constraints, specifying the normal traction components in the  $x$  and  $y$  directions, are necessary:

$$\begin{aligned} T_{n,x}^{\mathbf{x}^+} &= \frac{1}{l_x} \sum_{per}^{LP} \frac{l_{LB}^{per}}{2} \mathbf{l}_{t,x}^{per \top} \mathbf{q}_\sigma^{per, \mathbf{x}^+} = \beta q_{t,x}, \quad \forall per \in \{1, \dots, LP\} \\ T_{n,y}^{\mathbf{x}^+} &= \frac{1}{l_y} \sum_{per}^{LP} \frac{l_{LB}^{per}}{2} \mathbf{l}_{t,y}^{per \top} \mathbf{q}_\sigma^{per, \mathbf{x}^+} = \beta q_{t,y}, \quad \forall per \in \{1, \dots, LP\} \end{aligned} \quad (1.10)$$

with

$$\begin{pmatrix} q_{t,x} \\ q_{t,y} \end{pmatrix} = \mathbf{q}_t \in \mathfrak{R}^2 \quad \text{and} \quad \begin{pmatrix} \mathbf{l}_{t,x}^{per \top} \\ \mathbf{l}_{t,y}^{per \top} \end{pmatrix} = \mathbf{L}_t^{per}, \quad (1.11)$$

where  $\mathbf{l}_{t,x}^{per} \in \mathfrak{R}^3$  and  $\mathbf{l}_{t,y}^{per} \in \mathfrak{R}^3$  are the vectors which map the stress vector  $\mathbf{q}_\sigma^{per, \mathbf{x}^+}$  into the surface traction components  $q_{t,x}^{per, \mathbf{x}^+}$ ,  $q_{t,y}^{per, \mathbf{x}^+}$  of the node  $\mathbf{x}^+$  in  $x$  and  $y$  directions.  $l_{LB}^{per}$  is the element boundary length to which the corresponding node  $\mathbf{x}^+$  belongs,  $l_x$  and  $l_y$  are the total lengths of the boundaries in the  $x$  and  $y$  directions, and  $q_{t,x}$  and  $q_{t,y}$  are prescribed loading components associated with the macroscopic tractions  $\mathbf{T}_{n,x}^{\mathbf{x}^+}$  and  $\mathbf{T}_{n,y}^{\mathbf{x}^+}$ , respectively.

#### 1.2.1.4 Failure criteria

At the wood cell level, both isotropic and anisotropic plastic behaviour of material phases is encountered. Therefore, two failure criteria have been employed, the orthotropic Tsai-Wu failure criterion (Tsai, 1965, Tsai and Wu, 1971), for plane strain reading

$$F_1 \sigma_{x'x'} + F_2 \sigma_{y'y'} + P_{11} \sigma_{x'x'}^2 + P_{22} \sigma_{y'y'}^2 + P_{66} \tau_{x'y'}^2 + 2P_{12} \sigma_{x'x'} \sigma_{y'y'} \leq 1, \quad (1.12)$$

where  $F_i (\forall i \in 1, 2)$  and  $P_{ij} (\forall i, j \in 1, 2, 3)$  denote strength parameters of the material, and the von Mises isotropic failure criterion, for plane strain reading

$$(\sigma_{xx} - \sigma_{yy})^2 + 4\tau_{xy}^2 \leq 4k^2, \quad (1.13)$$

where  $k$  represents the yield strength of the material in pure shear. Note that for orthotropic materials, stress variables  $\boldsymbol{\sigma}' = (\sigma_{x'x'}, \sigma_{y'y'}, \tau_{x'y'})^\top \in \mathfrak{R}^3$  in the yield function, Eq. (1.12), are defined with respect to the local  $x'-y'$  coordinate system in order to take the local principal material orientation into consideration. For isotropic material, no local principal material orientation is required, and the yield function, Eq. (1.13), can be expressed in the global coordinates  $x$  and  $y$ . Since both yield functions, Eqs. (1.12) and Eq. (1.13), are quadratic, they can be transformed into the general form,

$$\mathbf{F}^\top \boldsymbol{\sigma}' + \boldsymbol{\sigma}'^\top \mathbf{P} \boldsymbol{\sigma}' \leq 1, \quad (1.14)$$

where  $\mathbf{P} \in \mathfrak{R}^{3 \times 3}$  and  $\mathbf{F} \in \mathfrak{R}^3$  contain material strength parameters. These have the form

$$\mathbf{F} = \begin{pmatrix} F_1 \\ F_2 \\ F_6 \end{pmatrix}, \quad \mathbf{P} = \begin{pmatrix} P_{11} & P_{12} & 0 \\ P_{21} & P_{22} & 0 \\ 0 & 0 & P_{66} \end{pmatrix} \quad (1.15)$$

for the orthotropic Tsai-Wu failure criterion Eq. (1.12), and

$$\mathbf{F} = \begin{pmatrix} 0 \\ 0 \\ 0 \end{pmatrix}, \quad \mathbf{P} = \frac{1}{4k^2} \begin{pmatrix} 1 & -1 & 0 \\ -1 & 1 & 0 \\ 0 & 0 & 4 \end{pmatrix} \quad (1.16)$$

for the von Mises failure criterion Eq. (1.13). Note that the latter failure criterion is isotropic, and therefore the local stress vector is consistent with the global one  $\boldsymbol{\sigma}' = \boldsymbol{\sigma}$ . When the matrix  $\mathbf{P}$  is symmetric and positive definite or semidefinite symmetric, it can be decomposed as  $\mathbf{P} = \mathbf{D}^\top \mathbf{D}$  with  $\mathbf{D} \in \mathfrak{R}^{3 \times 3}$ . Then the general form of the failure criterion, Eq. (1.14), can be reformulated into a linear constraint and a second-order cone (SOC) constraint, as follows:

$$\begin{aligned} \mathbf{s} &= \mathbf{a} + \mathbf{B} \boldsymbol{\sigma}' \\ \mathbf{s} &\in \mathcal{C} \end{aligned} \quad (1.17)$$

with

$$\mathbf{a} = (1 \ 0 \ 0 \ 0 \ 0)^\top \in \mathfrak{R}^5 \quad \text{and} \quad \mathbf{B} = \begin{pmatrix} -\mathbf{F}^\top/2 \\ \mathbf{D} \\ \mathbf{F}^\top/2 \end{pmatrix} \in \mathfrak{R}^{5 \times 3}. \quad (1.18)$$

The definition of the cone set  $\mathcal{C}$  and a brief introduction to SOCP is given in Appendix A. Based on Eq. (1.17) and Eq. (1.18), the third set of constraints in Eq. (1.2) can now be written in discretised form as

$$\begin{aligned} \mathbf{s}^{e,i} &= \mathbf{a}^e + \mathbf{B}^e \mathbf{q}_\sigma^{e,i} & \forall e \in \{1, \dots, LE\} \\ \mathbf{s}^{e,i} &\in \mathcal{C}_{e,i} & \forall i \in \{1, 2, 3\} \end{aligned} \quad (1.19)$$

with

$$\mathbf{q}_\sigma^{e,i} = \mathbf{R}_\sigma^e \mathbf{q}_\sigma^{e,i}, \quad \text{where} \quad \mathbf{R}_\sigma^e = \begin{pmatrix} (\cos \theta^e)^2 & (\sin \theta^e)^2 & -2 \cos \theta^e \sin \theta^e \\ (\sin \theta^e)^2 & (\cos \theta^e)^2 & 2 \cos \theta^e \sin \theta^e \\ \cos \theta^e \sin \theta^e & -\cos \theta^e \sin \theta^e & (\cos \theta^e)^2 - (\sin \theta^e)^2 \end{pmatrix} \in \mathfrak{R}^{3 \times 3}. \quad (1.20)$$

$\theta^e$  specifies the rotation of the local coordinate system with respect to the global one and  $\mathbf{q}'_{\sigma^{e,i}} \in \mathfrak{R}^3$  is the nodal stress vector with respect to the local coordinate system, obtained through the tensorial rotation operator  $\mathbf{R}_{\sigma}^e$ .

### 1.2.1.5 Discretised lower bound optimisation problem

Assembling the coefficients of the constraints for the whole discretised body of Eq. (1.3) in matrix  $\mathbf{A}_{LB}^{eq} \in \mathfrak{R}^{2LE \times 9LE}$ , of Eq. (1.5) in matrix  $\mathbf{A}_{LB}^{dis} \in \mathfrak{R}^{4LD \times 9LE}$ , of Eq. (1.9) in matrix  $\mathbf{A}_{LB}^{per} \in \mathfrak{R}^{2LP \times 9LE}$ , of Eq. (1.10) in matrix  $\mathbf{B}_{LB}^{per} \in \mathfrak{R}^{2 \times 9LE}$ , and the SOC constraints according to Eq. (1.19), leads to the final form of the lower bound optimisation problem:

$$\begin{aligned} \beta^{LB} = \max \quad & \beta \\ \text{s.t.} \quad & \mathbf{A}_{LB}^{eq} \mathbf{q}_{\sigma} = \mathbf{0} \\ & \mathbf{A}_{LB}^{dis} \mathbf{q}_{\sigma} = \mathbf{0} \\ & \mathbf{A}_{LB}^{per} \mathbf{q}_{\sigma} = \mathbf{0} \\ & \mathbf{B}_{LB}^{per} \mathbf{q}_{\sigma} = \beta \mathbf{q}_{\mathbf{t}} \\ & \mathbf{q}'_{\sigma} = \mathbf{R}_{\sigma} \mathbf{q}_{\sigma} \\ & \mathbf{s}^{soc} = \mathbf{a}^{soc} + \mathbf{B}^{soc} \mathbf{q}'_{\sigma} \\ & \mathbf{s}^{e,i} \in \mathcal{C}_{e,i} \end{aligned} \quad (1.21)$$

with  $\forall e \in \{1, \dots, LE\}$ ,  $\forall i \in \{1, 2, 3\}$ ,  $\mathbf{R}_{\sigma} \in \mathfrak{R}^{9LE \times 9LE}$ ,  $\mathbf{s}^{soc} \in \mathfrak{R}^{15LE}$ ,  $\mathbf{a}^{soc} \in \mathfrak{R}^{15LE}$ , and  $\mathbf{B}^{soc} \in \mathfrak{R}^{15LE \times 9LE}$ . Furthermore,  $\mathbf{q}_{\sigma} \in \mathfrak{R}^{9LE}$  and  $\mathbf{q}'_{\sigma} \in \mathfrak{R}^{9LE}$  assemble all the nodal stress vectors throughout the body with respect to the global and local coordinate systems, respectively.

## 1.2.2 Upper bound formulation

The upper bound theorem states that any external load multiplier determined when the internal work rate  $W_{int}$  under a kinematically admissible velocity field  $\dot{\mathbf{u}}$  equals the external work rate  $W_{ext}$ , is not less than the exact load multiplier  $\beta^*$ . The rate of internal work/dissipation for a body  $\Omega$  reads

$$W_{int}(\boldsymbol{\sigma}, \dot{\mathbf{u}}) = \int_{\Omega} \boldsymbol{\sigma}^{\top} \dot{\boldsymbol{\varepsilon}}(\dot{\mathbf{u}}) dV, \quad (1.22)$$

where  $\dot{\boldsymbol{\varepsilon}}(\dot{\mathbf{u}}) \in \mathfrak{R}^3$  denotes the 2D strain rate field. The rate of external work provided by body forces  $\mathbf{h}$  and surface traction  $\mathbf{t}$  is given by

$$W_{ext}(\dot{\mathbf{u}}) = \int_{\Omega} \mathbf{h}^{\top} \dot{\mathbf{u}} dV + \int_{\Gamma_t} \mathbf{t}^{\top} \dot{\mathbf{u}} dA, \quad (1.23)$$

but no body force is considered within this work, thus,  $\mathbf{h} = \mathbf{0}$ . Therefore, for the given discretisation, the best upper bound load multiplier,  $\beta^{UB}$ , can be found through the following optimisation problem:

$$\begin{aligned} \beta^{UB} = \min \quad & W_{int} \\ \text{s.t.} \quad & \dot{\boldsymbol{\varepsilon}} = \mathbf{L}_{\dot{\mathbf{u}}} \dot{\mathbf{u}} \quad \text{in } V \\ & \dot{\boldsymbol{\varepsilon}} = \dot{\lambda} \frac{\partial f}{\partial \boldsymbol{\sigma}} \quad \text{in } V \\ & \dot{\mathbf{u}} = \dot{\mathbf{u}}_0 \quad \text{on } \Gamma_u \\ & W_{ext}(\dot{\mathbf{u}}) = 1 \quad \text{in } V \end{aligned} \quad (1.24)$$

where  $\mathbf{L}_{\dot{u}} \in \mathfrak{R}^{3 \times 2}$  is the linear compatibility operator, linking the velocity field with the strain rate field. The second constraint enforces associated plastic flow throughout the whole body, with  $\dot{\lambda}$  as a nonnegative plastic multiplier specifying the magnitude of plastic strain rate, and  $f$  denotes the yield function. The kinematic boundary conditions prescribing the velocities  $\dot{\mathbf{u}}_0$  are represented by the third constraint, and the last constraint simply normalises the external work rate.

The dual of the optimisation problem in Eq. (1.24) can be derived as, according to Makrodimopoulos and Martin (2007),

$$\begin{aligned} \beta^{UB} = \max \quad & W_{ext} \\ \text{s.t.} \quad & \int_{\Omega} (\mathbf{L}_{\dot{u}} \dot{\mathbf{u}})^{\top} \boldsymbol{\sigma} dV = \int_{\Omega} \dot{\mathbf{u}}^{\top} \boldsymbol{\beta} p dV \quad \text{in } V \\ & f(\boldsymbol{\sigma}) \leq 0 \quad \text{in } V \end{aligned} \quad (1.25)$$

in which  $\mathbf{p}$  denotes the equivalent nodal loading arising from the (live) body forces  $\mathbf{h}$  and the surface tractions  $\mathbf{t}$ . For the discretisation of the upper bound optimisation problem, 6-node triangular linear strain elements are used, which are capable of providing very accurate results, as shown in Makrodimopoulos and Martin (2007, 2008). Quadratic shape functions for the interpolation of the unknown velocity field are used in Makrodimopoulos and Martin (2005a). According to Makrodimopoulos and Martin (2005b), in the case of unstructured meshes, linear strain elements with no inter-element velocity discontinuities show better performance than constant strain elements with velocity discontinuities. If the vertices of the linear-strain elements are taken as flow-rule enforcement points, the solutions obtained are strict upper bounds on the exact collapse load, since the plastic flow rule is enforced to hold throughout the whole element. The stress field in the dual problem has a linear variation of stress within each element. The discretisation of the optimisation problems in Eqs. (1.24) and (1.25), and their adaptations for periodic boundary conditions and orthotropic plasticity, are given in the following sections.

### 1.2.2.1 Compatibility between velocity and strain-rate field

One basic assumption of limit analysis is that all changes in geometry of the body occurring during collapse are negligible, thus, the compatibility between the velocity field and the strain rate field can be expressed by the following linear relation:

$$\mathbf{q}_{\dot{\boldsymbol{\varepsilon}}}^e = \mathbf{A}_{UB}^e \mathbf{q}_{\dot{\mathbf{u}}}^e \quad \forall e \in \{1, \dots, UE\}, \quad (1.26)$$

where the vector  $\mathbf{q}_{\dot{\mathbf{u}}}^e \in \mathfrak{R}^{12}$  contains all six nodal velocity vectors  $\mathbf{q}_{\dot{\mathbf{u}}}^{e,i} = (q_{\dot{\mathbf{u}},x}^{e,i}, q_{\dot{\mathbf{u}},y}^{e,i}) \in \mathfrak{R}^2$  ( $\forall i \in \{1, \dots, 6\}$ ) of the element, the vector  $\mathbf{q}_{\dot{\boldsymbol{\varepsilon}}}^e \in \mathfrak{R}^9$  contains three nodal strain vectors  $\mathbf{q}_{\dot{\boldsymbol{\varepsilon}}}^{e,i} \in \mathfrak{R}^3$  ( $\forall i \in \{1, 2, 3\}$ ) at the vertex nodes of the element, and

$$\mathbf{A}_{UB}^e = \mathbf{N}_{\sigma}^{e\top} \mathbf{L}_{\dot{\mathbf{u}}}^e \mathbf{N}_{\dot{\mathbf{u}}}^e \in \mathfrak{R}^{9 \times 12} \quad \forall e \in \{1, \dots, UE\} \quad (1.27)$$

with

$$\mathbf{L}_{\dot{\mathbf{u}}}^e = \begin{pmatrix} \frac{\partial}{\partial x} & 0 & \frac{\partial}{\partial y} \\ 0 & \frac{\partial}{\partial y} & \frac{\partial}{\partial x} \end{pmatrix} \in \mathfrak{R}^{2 \times 3}, \quad (1.28)$$

where  $\mathbf{N}_{\sigma}^e \in \mathfrak{R}^{3 \times 9}$  contains the linear shape functions for the stress field,  $\mathbf{N}_{\dot{\mathbf{u}}}^e \in \mathfrak{R}^{2 \times 12}$  is the quadratic interpolation matrix for the velocity field, and  $UE$  is the total number of elements in the upper bound formulation.

### 1.2.2.2 Periodic boundary conditions

In contrast to the lower bound formulation, where an anti-periodic traction field is enforced over the boundary of the unit cell, in the upper bound formulation a periodic velocity field must be ensured. Therefore, the kinematic boundary condition in Eq. (1.24) should be replaced by the following relation:

$$\dot{\mathbf{u}}^+ = \dot{\mathbf{u}}^- + \dot{\mathbf{E}}(\mathbf{x}^+ - \mathbf{x}^-), \quad (1.29)$$

with  $\dot{\mathbf{u}}^+$  as the velocity vector at the surface node  $\mathbf{x}^+$ , associated with the surface part  $\partial\Omega^+$ , and  $\dot{\mathbf{u}}^-$  as the velocity vector at the surface node  $\mathbf{x}^-$ , associated with the opposite surface part  $\partial\Omega^-$ .  $\dot{\mathbf{E}}$  denotes the effective/macroscopic strain rate tensor of the considered unit cell, and is linked to the microscopic strain rate field as follows:

$$\dot{\mathbf{E}} = \frac{1}{V_{UC}} \int_{V_{UC}} \dot{\boldsymbol{\varepsilon}}(\mathbf{x}) dV. \quad (1.30)$$

Considering the periodic boundary conditions, Eqs. (1.7) and (1.29), the rate of external energy dissipation, Eq. (1.23), can be written as,

$$\begin{aligned} W_{ext} &= \int_{\partial\Omega^+} \dot{\mathbf{u}}^{+\top} \mathbf{t}^+ dS + \int_{\partial\Omega^-} \dot{\mathbf{u}}^{-\top} \mathbf{t}^- dS \\ &= \int_{\partial\Omega^+} \dot{\mathbf{u}}^{+\top} \mathbf{t}^+ + (\dot{\mathbf{u}}^+ - \dot{\mathbf{E}}\mathbf{l})^\top (-\mathbf{t}^+) dS = \int_{\partial\Omega^+} (\dot{\mathbf{E}}\mathbf{l})^\top \mathbf{t}^+ dS \end{aligned} \quad (1.31)$$

where  $\mathbf{l}$  defines the distance between corresponding node pairs ( $\mathbf{x}^+ - \mathbf{x}^-$ ).

After discretization, the periodic constraint in Eq. (1.29) reads

$$\mathbf{L}_u^{per} \mathbf{q}_u^{per} = \dot{\mathbf{E}}^{per} \mathbf{l}^{per} \quad \forall per \in \{1, \dots, UP\}, \quad (1.32)$$

where  $UP$  is the number of node pairs to which periodic boundary conditions are applied,  $\dot{\mathbf{E}}^{per} \in \mathfrak{R}^{2 \times 2}$  is again the effective strain rate tensor of the unit cell,  $\mathbf{l}^{per} \in \mathfrak{R}^2$  is the separation of the node pair  $per$ , while  $\mathbf{q}_u^{per} = [\mathbf{q}_u^{per, \mathbf{x}^+}, \mathbf{q}_u^{per, \mathbf{x}^-}]^\top \in \mathfrak{R}^4$  contains the nodal velocity vectors to which periodic boundary conditions are applied, and  $\mathbf{L}_u^{per} = [\mathbf{I}, -\mathbf{I}] \in \mathfrak{R}^{2 \times 4}$  is the operator linking velocity pairs, with  $\mathbf{I} \in \mathfrak{R}^{2 \times 2}$  as the identity matrix.

In the dual form of the optimisation problem, see Eq. (1.25), the periodic boundary constraints appear in the following expression:

$$\sum_{e=1}^{UE} \frac{A^e}{3} (\mathbf{L}_u^e \mathbf{N}_u^e \mathbf{q}_u^e)^\top \mathbf{N}_\sigma^e \mathbf{q}_\sigma^e = \sum_{per=1}^{UP} (\mathbf{L}_u^{per} \mathbf{q}_u^{per})^\top \mathbf{q}_p^{per}, \quad (1.33)$$

where  $A^e$  is the area of the triangle element  $e$ , and  $\mathbf{q}_p^{per} = [\mathbf{q}_p^{per, \mathbf{x}^+}, \mathbf{q}_p^{per, \mathbf{x}^-}]^\top \in \mathfrak{R}^4$  is the equivalent nodal loading vector for the node pair  $\mathbf{x}^+$  and  $\mathbf{x}^-$ .

### 1.2.2.3 Plastic flow rule

It has been discussed by Makrodimopoulos (2010) that, when the yield function can be cast as a SOC, the set of admissible plastic strains (satisfying the associated flow rule

constraint) has the shape of the dual cone. As a result, the plastic flow constraint in Eq. (1.24) can be reformulated into the form of a SOC as,

$$\mathbf{e} \in \mathcal{C}^*, \quad (1.34)$$

where  $\mathcal{C}^*$  is the dual cone of  $\mathcal{C}$ , which is defined in Eq. (1.17).

In order to obtain a strict upper bound, both the primal and dual formulations of the upper bound problem are required to be strictly feasible, and, therefore, the constraint of the duality gap,

$$\mathbf{e}^\top \mathbf{s} = 0 \quad (1.35)$$

is required to be satisfied throughout the whole body, according to Andersen et al. (2003).

Considering Eq. (1.17), the duality gap constraint in Eq. (1.35) can be expressed as

$$\mathbf{e}^\top \mathbf{s} = \mathbf{e}^\top \mathbf{a} + \mathbf{e}^\top \mathbf{B} \boldsymbol{\sigma}' = 0, \quad (1.36)$$

in which the vector  $\mathbf{a}$  corresponds to the yield stress and the vector  $\mathbf{e}$  is related to the rate of the plastic multiplier  $\dot{\lambda}$ . Therefore, the internal energy dissipation can be expressed as

$$W_{int} = \int_{\Omega} \mathbf{e}^\top \mathbf{a} d\Omega = \int_{\Omega} \dot{\boldsymbol{\varepsilon}}^{p\top} \boldsymbol{\sigma} d\Omega, \quad (1.37)$$

leading together with Eq. (1.36) to

$$\dot{\boldsymbol{\varepsilon}}^p = -\mathbf{B}^\top \mathbf{e}, \quad (1.38)$$

as the transformation of the strain rate  $\dot{\boldsymbol{\varepsilon}}^p$  into the form of a SOC. Since the yield function in Eq. (1.17) is defined with respect to the local material coordinate system, the plastic strain rate in Eq. (1.38) is also locally defined.

The discretised formulation of the second constraint for the plastic flow rule in Eq. (1.24) can now be expressed as

$$\begin{aligned} \mathbf{q}'_{\dot{\boldsymbol{\varepsilon}}}{}^{e,i} &= -\mathbf{B}^{e\top} \mathbf{e}^{e,i} \\ \mathbf{e}^{e,i} &\in \mathcal{C}_{e,i}^* \end{aligned} \quad e \in \{1, \dots, UE\} \text{ and } i = \{1, 2, 3\} \quad (1.39)$$

with

$$\mathbf{q}'_{\dot{\boldsymbol{\varepsilon}}}{}^{e,i} = \mathbf{R}_{\dot{\boldsymbol{\varepsilon}}}^e \mathbf{q}_{\dot{\boldsymbol{\varepsilon}}}{}^{e,i} \quad e \in \{1, \dots, UE\} \text{ and } i \in \{1, 2, 3\} \quad (1.40)$$

as the nodal strain rate tensor with respect to the local coordinate system. The nodal strain transformation matrix  $\mathbf{R}_{\dot{\boldsymbol{\varepsilon}}}^e$  is the same as the nodal stress transformation matrix  $\mathbf{R}_{\boldsymbol{\sigma}}^e$  in Eq. (1.20).

#### 1.2.2.4 Discretised upper bound optimisation problem

Assembling the coefficients of the compatibility constraints of Eq. (1.26) for the whole discretised body in matrix  $\mathbf{A}_{UB}^{com} \in \mathfrak{R}^{9UE \times 2UN}$ , with  $UN$  denoting the total number of velocity evaluation nodes in the upper bound formulation, the periodic boundary conditions of Eq. (1.32) in matrices  $\mathbf{A}_{UB}^{per} \in \mathfrak{R}^{UP \times 2UN}$  and  $\dot{\mathbf{E}}_{UB} \mathbf{l}_{UB} \in \mathfrak{R}^{UP}$ , and the

plastic flow rule constraints of Eq. (1.39) by means of vector  $\mathbf{B}^{soc\top} \in \mathfrak{R}^{3UE}$ , the primal version of the upper bound optimisation problem, Eq. (1.24), reads in discretised form:

$$\begin{aligned} \beta^{UB} = \min \quad & W_{int} \\ \text{s.t.} \quad & \mathbf{A}_{UB}^{com} \mathbf{q}_{\dot{u}} = \mathbf{q}_{\dot{\varepsilon}} \\ & \mathbf{A}_{UB}^{per} \mathbf{q}_{\dot{u}} = \dot{\mathbf{E}}_{UB} \mathbf{l}_{UB} \\ & \mathbf{q}'_{\dot{\varepsilon}} = \mathbf{R}_{\dot{\varepsilon}} \mathbf{q}_{\dot{\varepsilon}} \\ & \mathbf{q}'_{\dot{\varepsilon}} = -\mathbf{B}^{soc\top} \mathbf{e}^{soc} \\ & \mathbf{e}^{e,i} \in \mathcal{C}_{e,i}^* \end{aligned} \quad (1.41)$$

where  $e \in \{1, \dots, UE\}$  and  $i \in \{1, 2, 3\}$ . The vectors  $\mathbf{q}_{\dot{u}} \in \mathfrak{R}^{2UE}$ ,  $\mathbf{q}_{\dot{\varepsilon}} \in \mathfrak{R}^{3UE}$ , and  $\mathbf{q}'_{\dot{\varepsilon}} \in \mathfrak{R}^{3UE}$  denote the assembled vectors of the nodal velocities, the nodal strain rates related to the global coordinate system and the nodal strain rates related to the local coordinate system, respectively.

Introducing the definition

$$\hat{\mathbf{x}}^e = \left\{ \frac{A^e}{3} \mathbf{x}^e \right\}_{e=1, \dots, UE} \quad (1.42)$$

where  $\mathbf{x}^e$  represents an arbitrary position vector of the element  $e$ , the dual version of the optimisation problem Eq. (1.41) can be derived from Eq. (1.25), reading

$$\begin{aligned} \beta^{UB} = \max \quad & W_{ext} \\ \text{s.t.} \quad & \mathbf{A}_{UB}^{com\top} \hat{\mathbf{q}}_{\sigma} = \mathbf{A}_{UB}^{per\top} \mathbf{q}_p \\ & \hat{\mathbf{s}} = \hat{\mathbf{a}} + \mathbf{B}^{soc} \hat{\mathbf{q}}'_{\sigma} \\ & \hat{\mathbf{q}}'_{\sigma} = \mathbf{R}_{\sigma} \hat{\mathbf{q}}_{\sigma} \\ & \hat{\mathbf{s}}^{e,i} \in \mathcal{C}_{e,i} \end{aligned} \quad (1.43)$$

where  $e \in \{1, \dots, UE\}$  and  $i \in \{1, \dots, 6\}$ .

The objective functions in the primal upper bound formulation Eq. (1.41) and the dual upper bound formulation Eq. (1.43), respectively, can be defined as follows:

$$W_{int} = (\hat{\mathbf{a}}^{soc})^{\top} \mathbf{e}^{soc} \quad \text{and} \quad (1.44a)$$

$$W_{ext} = (\dot{\mathbf{E}}_{UB} \mathbf{l}_{UB})^{\top} \mathbf{q}_p \quad (1.44b)$$

representing the rates of internal dissipation and external work, respectively.

### 1.3 Application to wood

An increasingly used and promising mechanistic approach is the so-called multiscale description of material behavior, based on the framework of micromechanics, where a material is modelled at different scales of observation (Ghosh et al., 2001, Hautefeuille et al., 2012, Michel et al., 1999, Saavedra Flores et al., 2016b). In recent years, such a model has been developed for wood in Bader et al. (2011), Hofstetter et al. (2005, 2007, 2008), Lukacevic and Füssl (2016), Lukacevic et al. (2014b, 2017) and is currently in elaboration at the IMWS, Vienna University of Technology. Until now, this approach has mainly been developed for the prediction of effective elastic material properties. The extension to strength predictions represents the next big challenge, and the limit analysis formulations presented above are expected to play a major role in this development.



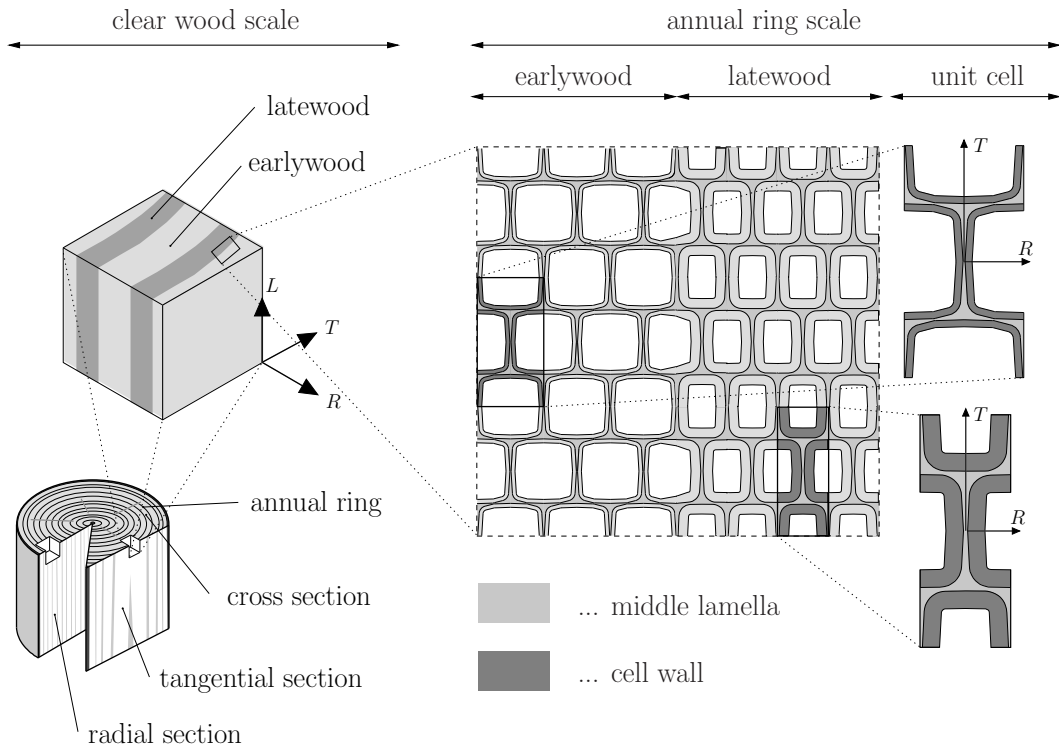


Figure 1.1: The considered hierarchical structure of wood: The clear wood scale (left) and the annual ring scale (right), where earlywood and latewood unit cells are extracted from the honeycomb-like structure.

In this paper, the limit analysis formulations have been applied to selected observation scales as illustrated in Figure 1.1. It shows a flawless (without knots and other defects) wooden log at the macroscopic scale with the adopted cylindrical coordinate system for the longitudinal ( $L$ ), radial ( $R$ ) and tangential ( $T$ ) directions, taking into account the orthotropy of wood at this scale. The layered structure of earlywood and latewood, so-called annual rings, represents the next scale of observation. On a closer look at these layers, a repetitive honeycomb-like structure is revealed, and the morphological characteristics of which have been extensively described by, inter alia, in Fengel and Wegener (1983), Gloimüller et al. (2012), Kollmann (1951). A simplified idealisation of this significantly repetitive structure is illustrated in Figure 1.1, denoted as annual ring scale. This structure can be suitably represented by two unit cells, shown on the right side of Figure 1.1. Failure behaviours of these cells strongly influence the failure modes at all higher observation scales. For this reason, the main focus of this paper will be to analyse failure modes of these cell structures by means of numerical limit analysis. This is explained in more detail in the following subsections. According to the multiscale approach used in Lukacevic et al. (2014a), Milani et al. (2006a,b), failure stress states and corresponding failure modes at the annual ring scale are obtained, which serve as input to the next higher scale of observation, the clear wood scale. Due to the fact that the clear wood structure also exhibits repetitiveness, it is also approximated by unit cells with periodic boundary conditions. Then, the resulting effective failure surfaces are compared with existing experimental data from biaxial-testing published in Eberhardsteiner (1995), as verification for the presented numerical

limit analysis method. In this reference, the biaxial tests were performed on clear wood specimens made of Norway spruce clear wood, thus in this work all unit cell geometries and strength parameters are determined with respect to this wood species.

All computations presented in the following were performed on a Linux desktop machine, with an AMD Phenom(tm) II X6 1090T CPU (6 cores) and 8GB of RAM. While Abaqus was used for the mesh generation and the illustration of results, all other pre- and post-processing tasks as well as the assembly of SOCP optimisation problems were carried out by self-written codes in Fortran. Special focus was laid on sparse matrix manipulations to ensure high efficiency with respect to the variable count and the computational effort. The SOCP optimisation problems themselves were solved by the commercial solver MOSEK ApS (2017), which is based on the conic interior-point algorithm developed by Andersen et al. (2003).

### 1.3.1 Application of limit analysis at the annual ring scale

In the following, the presented limit analysis formulations are applied to the two spruce unit cells illustrated in Figure 1.1, representing two different types of wood cell at the annual ring scale. The overall mechanical behaviour of each unit cell is dominated by two different material layers, the middle lamella and the cell wall layer. The middle lamella is nearly free of cellulose, and thus exhibits isotropic behaviour. In contrast, the cell wall layer, dominated by S2 cell wall material, mainly consists of cellulose microfibrils aligning in a certain dominant direction, and thus exhibits significantly anisotropic behaviour as discussed by Gindl et al. (2004), Gloimüller et al. (2012), Kollmann (1951), Salmen and Burgert (2009). The anisotropic material phase of wood has great similarity with fibre-reinforced composites, and thus it can be appropriately described by an orthotropic Tsai-Wu failure criterion.

The exact geometries of earlywood and latewood cells are adopted from Lukacevic et al. (2014b), where they were chosen according to microscopy images and values found in the literature for spruce. The earlywood unit cell is discretised with 25 196 triangular elements and the latewood unit cell with 25 022. This discretisation and the local material directions ( $r$  and  $t$ ) in the cell wall layer are shown schematically for the earlywood unit cell in Figure 1.2. To all elements in a certain cell wall layer section, as shown in Figure 1.2, the same local coordinate system is assigned. In these sections the global stresses definition  $(\sigma_{RR}, \sigma_{TT}, \tau_{RT})^T$  is replaced by the local ones  $(\sigma_{rr}, \sigma_{tt}, \tau_{rt})^T$ .

Strength parameters assigned to these two material layers are determined on the basis of values found in Bader et al. (2010), Lukacevic et al. (2014b), Schwiedrzik et al. (2016). For the orthotropic Tsai-Wu failure criterion (Eq. (1.15)), describing the plastic behaviour of the cell wall, the adopted parameters are:

$$\begin{aligned} F_1 &= 0 \text{ MPa}^{-1} & F_2 &= 0 \text{ MPa}^{-1} \\ P_{11} &= 4.444 \times 10^{-5} \text{ MPa}^{-2} & P_{22} &= 1.778 \times 10^{-4} \text{ MPa}^{-2} \\ P_{66} &= 5.408 \times 10^{-4} \text{ MPa}^{-2} & P_{12} &= 0 \text{ MPa}^{-2} \end{aligned} \quad (1.45)$$

A value of  $k = 14.3 \text{ MPa}$  is used for the von Mises failure criterion (as shown in Eq. (1.16)) assigned to the middle lamella. The corresponding failure surfaces are plotted in Figure 1.3, with respect to the local coordinates ( $r$  and  $t$ ).

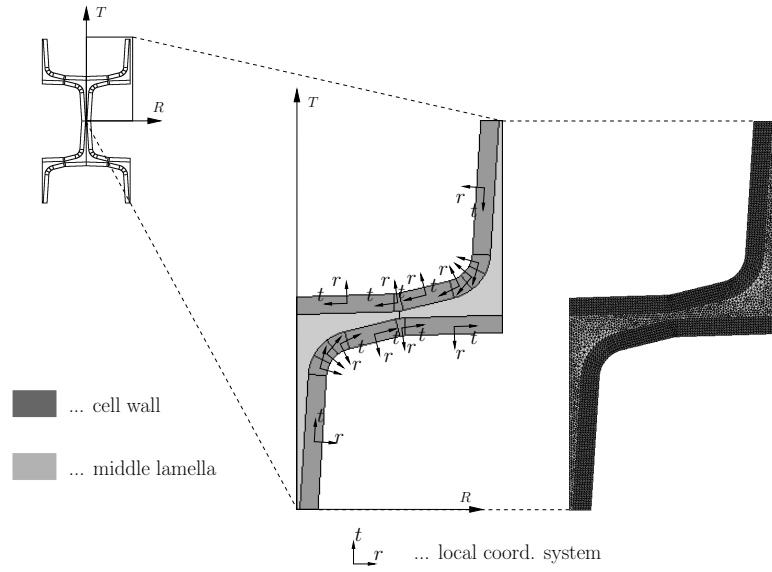


Figure 1.2: Local material directions in the cell wall layer of an earlywood cell and the corresponding discretisation of such a cell.

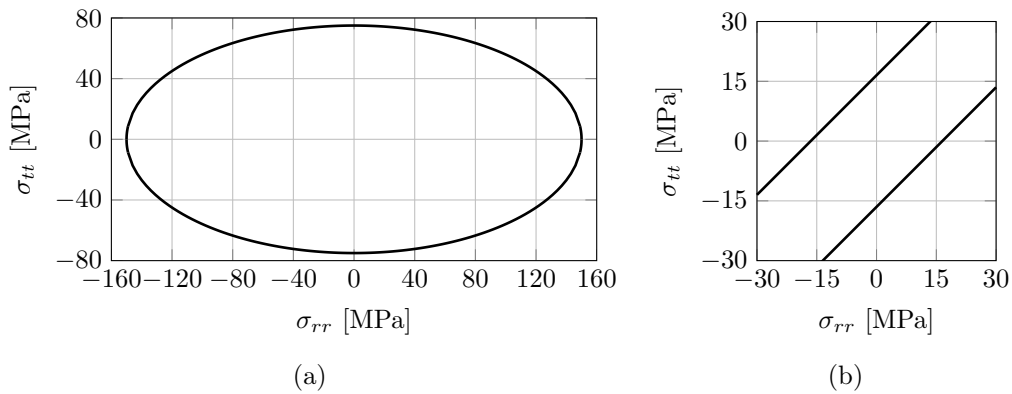


Figure 1.3: Constitutive failure surfaces assigned to (a) the cell wall layers and (b) the middle lamella.

The lower bound formulation, Eq. (1.21), and the dual upper bound formulation, Eq. (1.43), are applied to these wood unit cell models, delivering effective strengths and failure mechanisms under various loading situations. A lower bound result and an upper bound result for the earlywood unit cell under tangential tensile loading are illustrated in Figure 1.4. The required computing time for each of these two simulations was below 2 min. In Figure 1.4, dark and light grey areas indicate the cell wall and the middle lamella, respectively, and the red coloured areas indicate plastic failure. Since in the lower bound formulation only the stress field is considered, no deformation is available from the primal optimisation problem and thus none is displayed in Figure 1.4a. The deformed shape in Figure 1.4b represents the nodal velocity field obtained from the upper bound calculation, whereas the black outline shows the undeformed shape.

The corresponding effective stress states, in this case effective tensile stress states in the  $T$ -direction, are  $\Sigma^{LB} = [0.0, 2.43, 0.0]^T$  from the lower bound and  $\Sigma^{UB} = [0.0, 2.47, 0.0]^T$

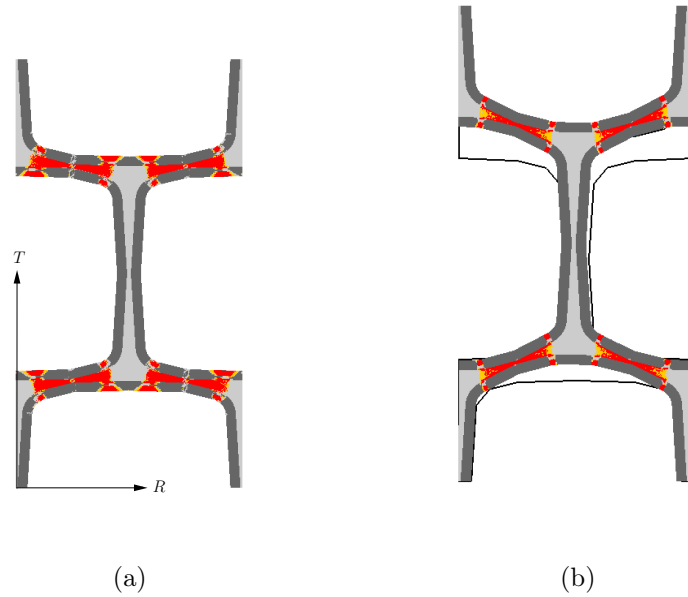


Figure 1.4: Illustrative (a) lower bound failure region with the threshold of the objective function value  $[-3 \times 10^{-2} : 0]$  and (b) upper bound failure region with the threshold  $[-2 \times 10^{-4} : 0]$  (red-coloured areas) for the earlywood unit cell under prescribed tensile loading in the  $T$  direction.

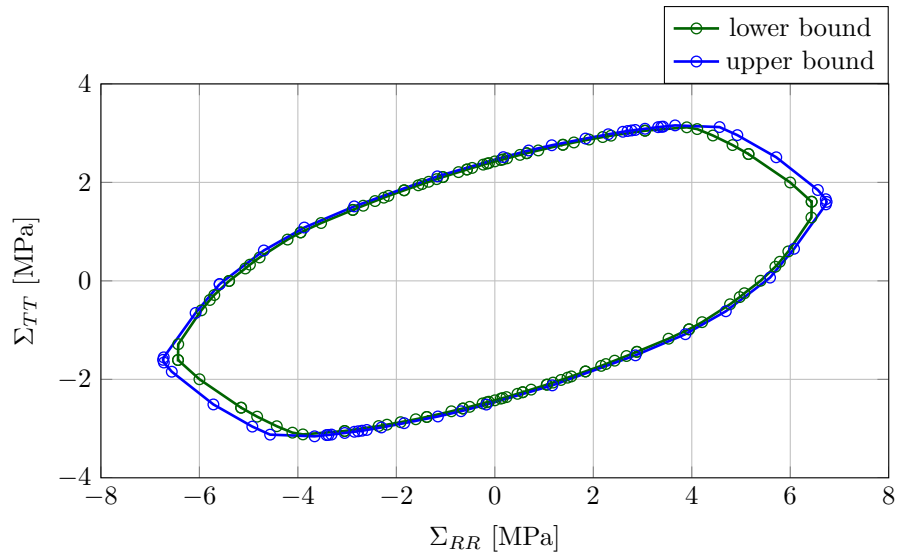
from the upper bound analysis. The resulting normalised bracketing error, defined as  $(\Sigma_T^{UB} - \Sigma_T^{LB}) / (\Sigma_T^{UB} + \Sigma_T^{LB}) = 0.81\%$ , is very small. Also taking into account the good agreement between the plastic failure zones of the lower and upper bound results (see Figure 1.4), the first numerical example using this approach can be regarded as promising.

### 1.3.1.1 Determination of effective failure surfaces

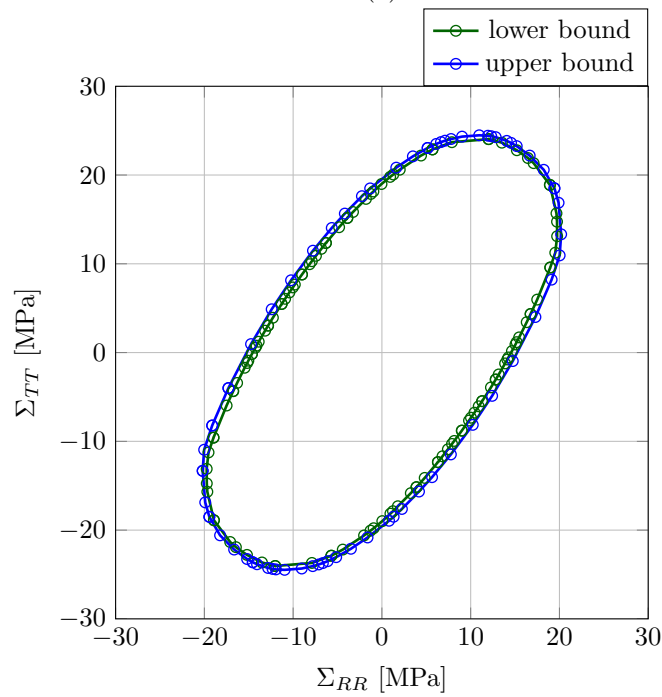
By applying various loading situations (surface tractions in the lower bound formulation and material flow through the boundaries in the upper bound formulation), lower and upper bounds for different effective stress states  $\Sigma$  and the corresponding failure mechanisms are obtained. Each individual effective stress state represents one point on the effective failure surface of the wood unit cell under consideration.

For the earlywood unit cell, 116 individual lower bound simulations with a total computing time of 171.2 min and 54 upper bound simulations with 71.2 min computing time were carried out. The resulting lower and upper bounds of the effective failure surface is shown in Figure 1.5a. The corresponding lower and upper bound for the latewood unit cell is displayed in Figure 1.5b, obtained from 116 and 69 lower and upper bound simulations with computing times of 237.4 min and 144.3 min, respectively.

For each unit cell, the lower and upper bound results lead to an almost identical shape and orientation of the effective failure surface. Moreover, for most regions of the failure surface the bracketing error is tolerably small. The general difference in the magnitude of the obtained effective strengths in the  $RT$ -plane between the earlywood and latewood



(a)



(b)

Figure 1.5: Lower and upper bound effective failure surfaces of (a) the earlywood unit cell and (b) the latewood unit cell.

unit cells seems to be realistic, though unfortunately, no experimental data exists at this scale of observation which could be used for validation.

### 1.3.1.2 Failure mechanisms of wood cells

Next, the failure mechanisms associated with various effective stress states are analysed, and transitions between failure modes are discussed. For this evaluation it is sufficient to focus on upper bound results, since the lower and upper bound analysis provide similar failure modes under similar loading situations, as is shown by the illustrative example in Figure 1.4.

### 1.3.1.3 Earlywood

In Figure 1.6, the effective upper bound failure surface of the earlywood unit cell is plotted once again, including a black velocity vector at each stress point, pointing in the direction of the corresponding effective plastic strain rate. It is interesting to note that the associated plastic flow behaviour (normality) of the underlying cell wall layers remains well preserved at this next higher scale of observation. Considering the shape

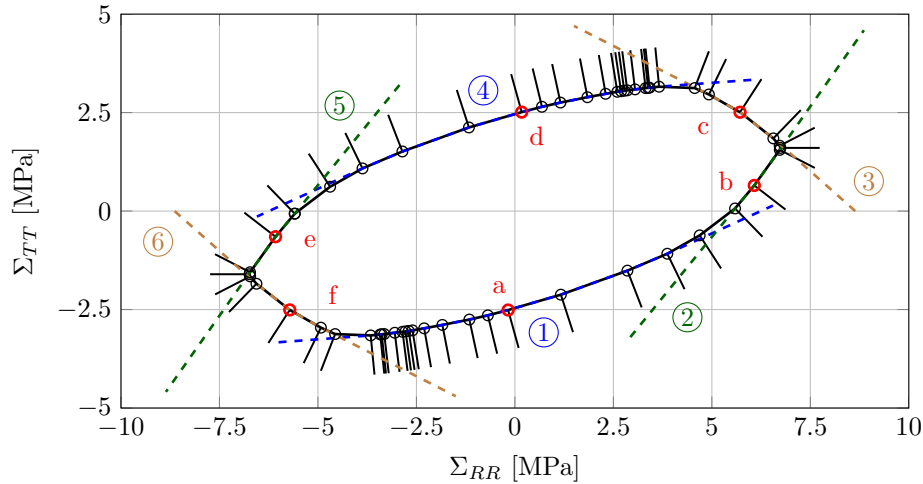


Figure 1.6: The effective upper bound failure surface for the earlywood unit cell, including velocity vectors, pointing in the direction of the related effective plastic strain rate, and dashed curves dividing the failure surface into 6 parts.

of the effective failure surface and the directions of the effective plastic flow vectors, the effective failure surface can be divided into six parts with smoothly pronounced curvature, connected by more sharply curved transition regions. These six surface parts are indicated in Figure 1.6 by dashed curves with circled numbers, and based thereon are selected stress points (red circles), for which the corresponding failure modes are shown in Figure 1.7. To each surface part, a certain collapse mechanism with a distinct failure mode can be assigned. Noting that there are qualitatively similar mechanisms in opposite tension and compression regions, the number of strongly differing mechanisms reduces to three. The identification of mechanisms and modes will be discussed in the following (the referenced mechanisms can be found in Figure 1.7):

1. Failure mechanisms associated with surface parts ① and ④ are mainly affected by loading in the  $T$ -direction, as can be clearly seen in mechanisms (a) and (d), respectively. Failure is characterised by two plastic hinges in each of the four

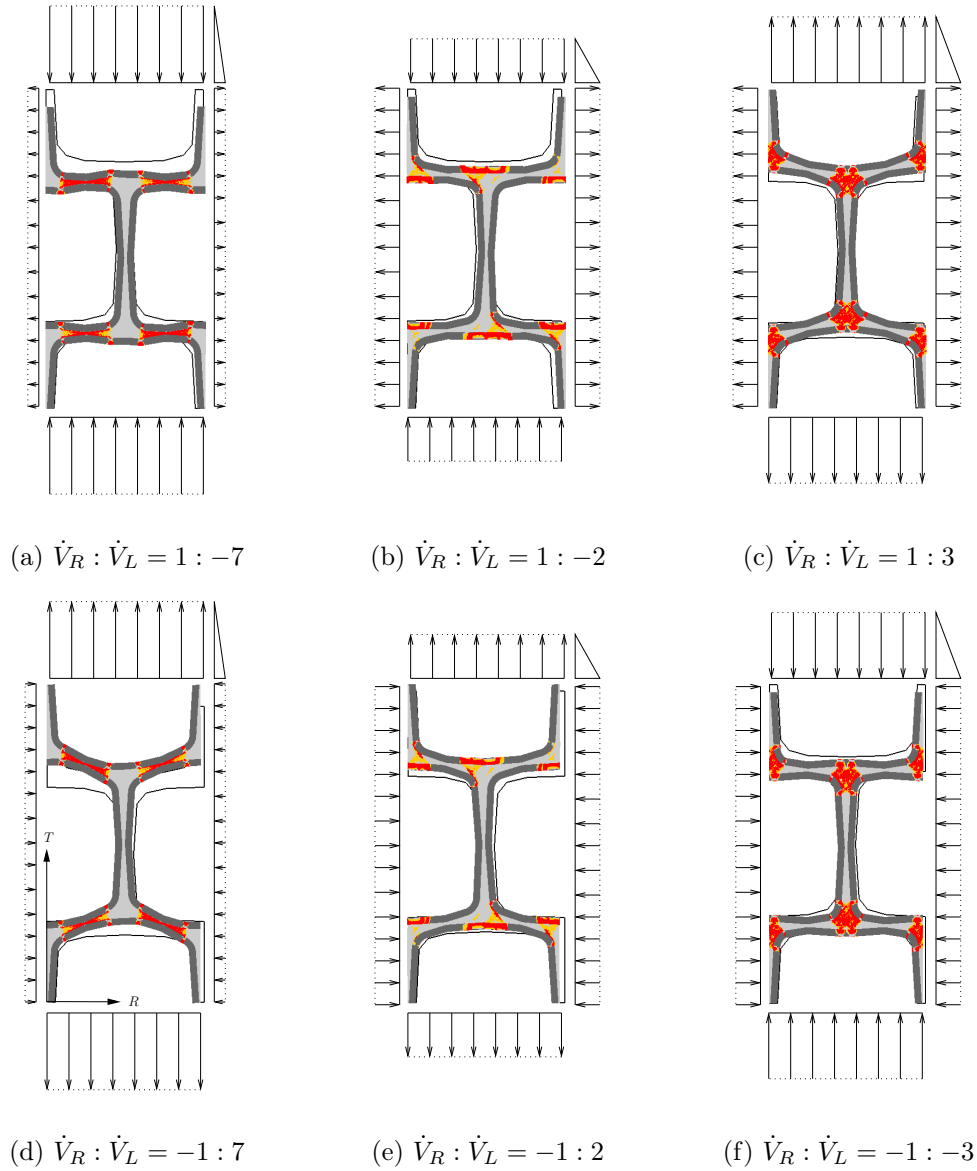


Figure 1.7: Selected failure mechanisms of the earlywood unit cell obtained from the upper bound analysis. Failure modes corresponding to effective stress states marked with red circles in Figure 1.6. Anti-periodic velocity conditions are applied and the velocity field is not constant over each boundary surface indicated as dash line. The loading condition is prescribed as the ratio between  $\dot{V}_R$  and  $\dot{V}_L$ , denoting the area-averaged velocities in  $R$  and  $T$  direction over the corresponding boundary surfaces, which are equivalent to the macroscopic strain rate  $\dot{E}_{RR}$  and  $\dot{E}_{LL}$  (in Eq. (1.30)), respectively.

wooden cell webs running in the  $R$ -direction. Plastification takes place in the middle lamella as well as the cell wall layers. In addition, the middle lamella region in between these two hinges is also plastified, allowing the occurring kinematics.

2. In contrast, failure mechanisms (b) and (e) associated with surface parts ② and

⑤ are mainly characterised by the loading in the  $R$ -direction. Strongly delineated failure regions are initiated in the cell wall layer, and then, penetrating through the middle lamella layer in the  $T$ -direction. The majority of energy is dissipated in the stronger cell wall material, leading to the significantly higher effective strength in the  $R$ -direction.

3. The biaxial character of the loading can be identified in failure mechanisms (c) and (f), associated with surface parts ③ and ⑥. The main plastification occurs in the middle lamella, including small shear failure surfaces running in the  $R$ -direction, accompanied by locally demarcated failure through the cell wall layers.

#### 1.3.1.4 Latewood

In Figure 1.8 the effective upper bound failure surface of the latewood unit cell is plotted once again, also including the directions of the effective plastic strain rates. Similar to the results from the earlywood unit cell, the effective plastic flow vectors for the latewood unit cell reflects the underlying associated flow rule used in the limit analysis. Again, the failure surface can be divided into six parts with different characteristics. The corresponding three independent failure mechanisms are described in the following (the referenced failure mechanisms can be found in Figure 1.9):

1. Failure mechanisms (a) and (d), associated with surface parts ① and ④ are characterised by thin shear bands running diagonally through the middle lamella together with plastic hinges in the cell wall layer. Macroscopic cracks can be expected to run diagonally through the latewood cell structure, as indicated by the shear bands.
2. The similar looking mechanisms (b) and (e) are linked to surface parts ② and ⑤. The difference, compared with the other failure mechanisms, becomes obvious when taking directions of effective/macroscopic plastic strain rates into account, which align almost horizontally. Thus, failure in the  $R$ -direction through the latewood can be expected, including distinct initiation of failure regions in the cell wall layer.
3. The third clearly different mode, seen in failure mechanisms (c) and (f), is associated with surface parts ③ and ⑥. Plastification is dominated by shear failure regions, which extend in a vertical direction through the entire cell wall.

### 1.3.2 Application of limit analysis at clear wood scale

The next higher observation scale, the clear wood scale (see Figure 1.1), also exhibits a repetitive structure, consisting of homogeneous earlywood and latewood layers. Thus, this structure can also be represented by a unit cell with appropriate periodic boundary conditions. At this observation scale, we focus attention on the  $LR$ -plane, as illustrated in Figure 1.1, because experimental data from biaxial tests are available in this plane by Eberhardsteiner (1995). The unit cell at this scale is defined as a layered laminated structure with earlywood and latewood layers aligning in the same orientation, as shown in Figure 1.10. Following the above-mentioned experiments, five different principal



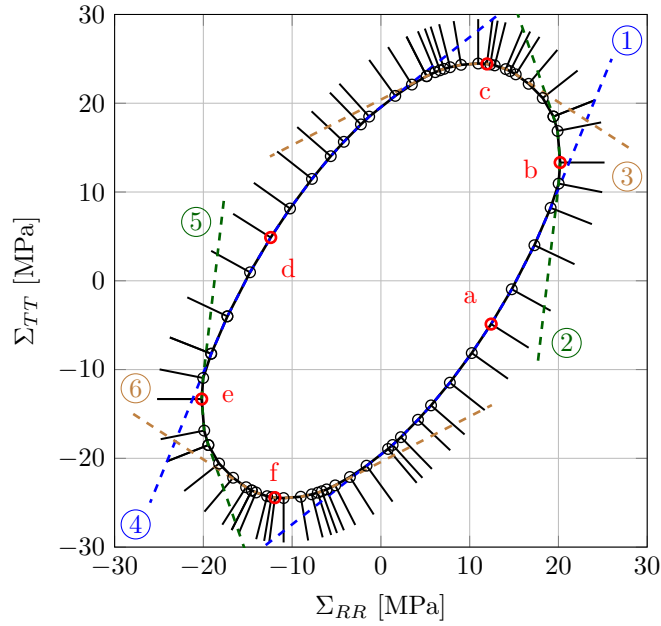


Figure 1.8: The effective upper bound failure surface for the latewood unit cell, including black lines at every stress point, pointing into the direction of the related effective plastic strain rate.

material orientations with respect to principal effective stresses  $\Sigma_1$  and  $\Sigma_2$ , defined by the angle  $\alpha$ , are investigated numerically.

It has been discussed by Eberhardsteiner (1995), and Mackenzie-Helnwein et al. (2003) that the anisotropic strength of clear wood can be approximated by the orthotropic Tsai-Wu failure criterion. Therefore, this criterion is assigned to both the earlywood and latewood layers. Following the idea of upscaling, strength parameters should be determined by results from the previous scale of observation, the annual ring scale.

In this paper, the  $LR$ -plane is considered at the clear wood scale, while the  $RT$ -plane is considered at the annual ring scale. As a result, at the current scale, only effective strengths in the  $R$  direction can be used from the limit analysis simulations at the previous scale (Section 1.3.1). For earlywood and latewood strengths in the  $L$ -direction, experimentally obtained values from Gindl and Teischinger (2002), Sinn et al. (2001) are employed.

Accordingly, the following Tsai-Wu strength parameters are assigned to the earlywood layer:

$$\begin{aligned}
 F_1 &= -0.0116 \text{ MPa}^{-1} & F_2 &= 0 \text{ MPa}^{-1} \\
 P_{11} &= 5.0 \times 10^{-4} \text{ MPa}^{-2} & P_{22} &= 3.38 \times 10^{-2} \text{ MPa}^{-2} \\
 P_{12} &= 0 \text{ MPa}^{-2}
 \end{aligned} \tag{1.46}$$

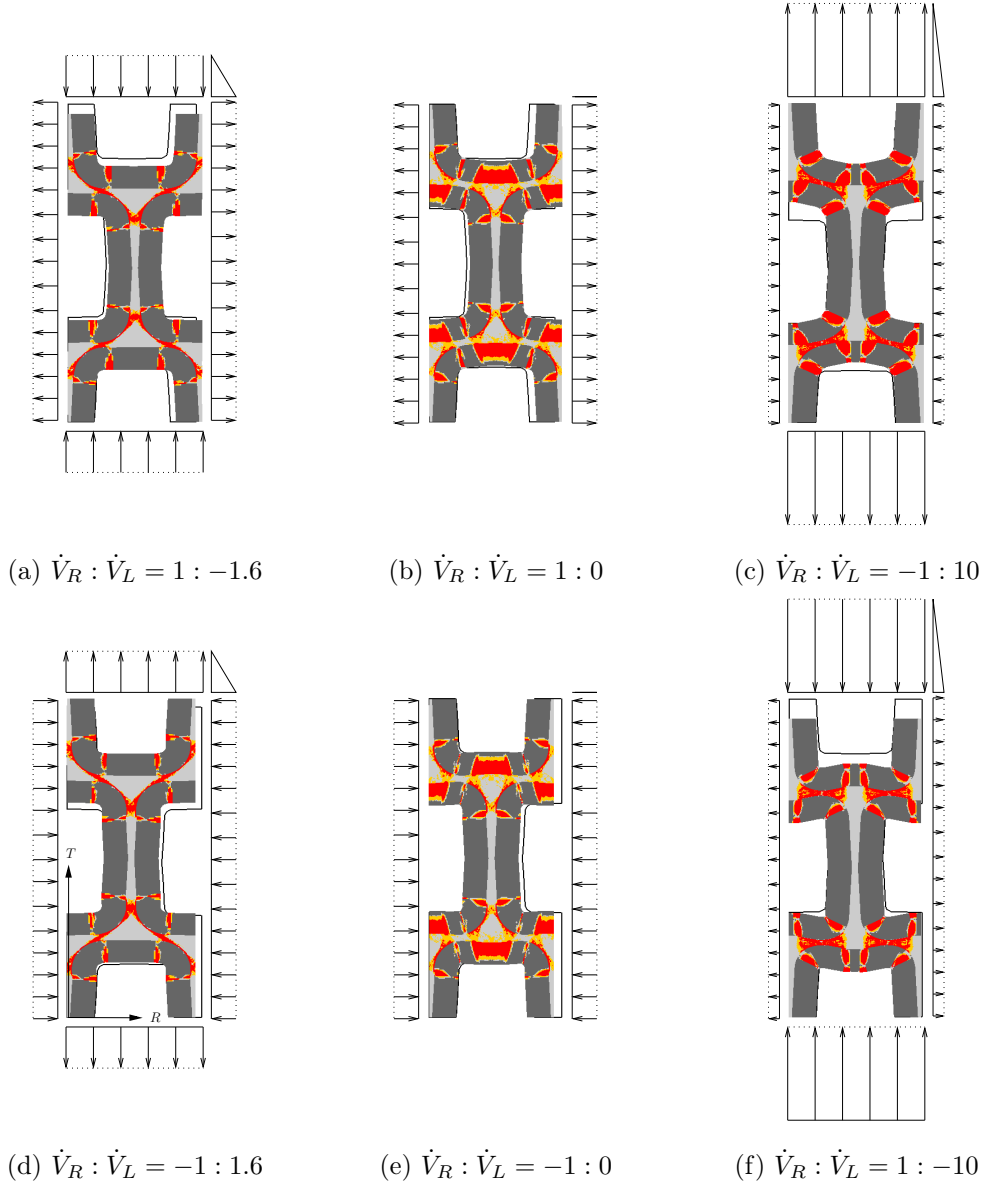
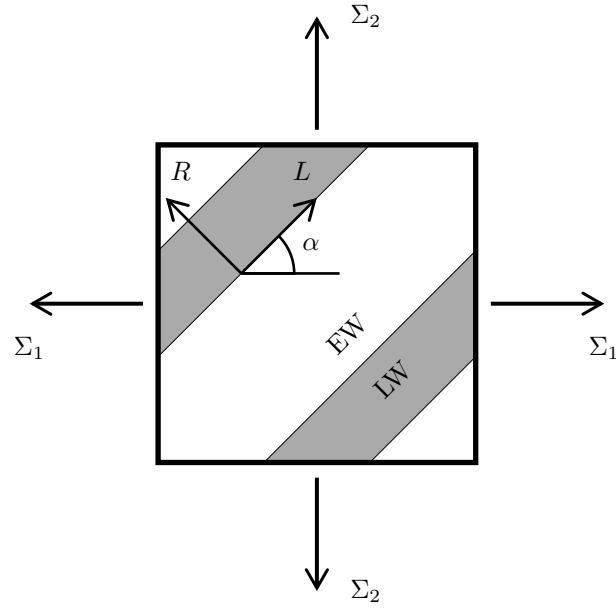


Figure 1.9: Selected failure mechanisms of the latewood unit cell obtained from upper bound simulations. Failure modes belonging to the effective stress states marked with red circles in Figure 1.8. Anti-periodic velocity conditions are applied and the velocity field is not constant over each boundary surface indicated as dash line. The loading condition is prescribed as the ratio between  $\dot{V}_R$  and  $\dot{V}_L$ , denoting the area-averaged velocities in  $R$  and  $T$  direction over the corresponding boundary surfaces, which are equivalent to the macroscopic strain rate  $\dot{E}_{RR}$  and  $\dot{E}_{LL}$  (in Eq. (1.30)), respectively.

and to the latewood layer:

$$\begin{aligned}
 F_1 &= -0.0093 \text{ MPa}^{-1} & F_2 &= 0 \text{ MPa}^{-1} \\
 P_{11} &= 1.0 \times 10^{-4} \text{ MPa}^{-2} & P_{22} &= 4.70 \times 10^{-3} \text{ MPa}^{-2} \\
 P_{12} &= 0 \text{ MPa}^{-2}
 \end{aligned} \tag{1.47}$$



unit cell	1	2	3	4	5
$\alpha$ [°]	0	7.5	15	30	45

Figure 1.10: Representative unit cell for the clear wood scale, consisting of homogeneous earlywood and latewood layers. Five different annual ring orientations, defined by the angle  $\alpha$  have been investigated.

With respect to the shear strength in the  $LR$ -plane, no experimental data, separately for the earlywood and latewood, could be found. Thus, two different approaches were used to estimate suitable values. First, the overall shear strength of clear wood, given in Gindl and Teischinger (2002), is simply assigned to both layers. Second, the clear wood shear strength is linearly scaled based on the considered densities of the earlywood and latewood materials. The resulting Tsai-Wu parameters are listed below:

First approach:

$$P_{66} = 1.35 \times 10^{-2} \text{ MPa}^{-2} \quad \text{for both earlywood and latewood layers}$$

Second approach:

$$P_{66} = 2.44 \times 10^{-2} \text{ MPa}^{-2} \quad \text{for earlywood layer}$$

$$P_{66} = 3.70 \times 10^{-3} \text{ MPa}^{-2} \quad \text{for latewood layer}$$

(1.48)

### 1.3.2.1 Determination of effective failure surfaces

The lower bound formulation, Eq. (1.21), and the dual upper bound formulation, Eq. (1.43), are now applied to the clear wood unit cell models defined in Figure 1.10, delivering effective failure stresses and failure mechanisms under various loading situations. Failure modes obtained from upper bound analysis for three different loading conditions, are shown in Figure 1.11 to illustrate typical patterns of the failure regions and the plastic flow mechanisms. From the corresponding deformation fields, the periodic velocity boundary conditions can be identified very well. However, at this scale

of observation, failure modes are not the main focus and they will not be discussed in detail.

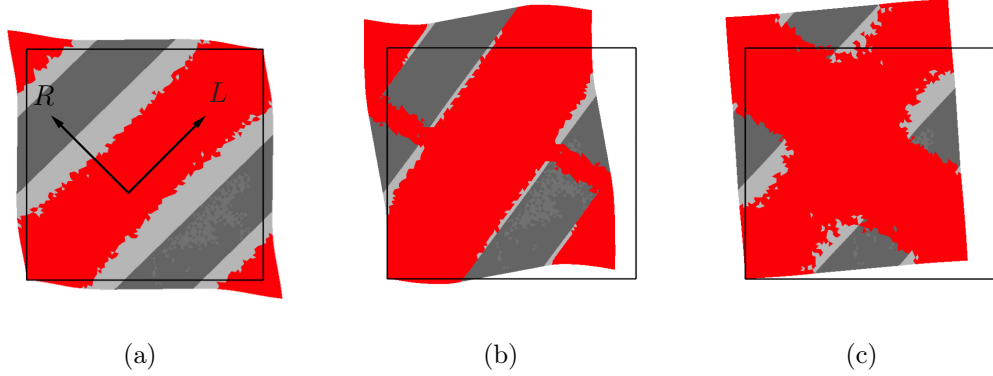


Figure 1.11: Illustrative failure mechanisms of the clear wood unit cell obtained from upper bound simulations for 3 different effective loading ratios  $\dot{E}_1/\dot{E}_2$ : (a) 1.0, (b) -0.8, and (c) -1.0.

Subsequently, similar to the previous scale, numerous loading situations are applied to the clear wood unit cell. The number of simulations and the corresponding (very low) computing times are given in Table 1.1.

unit cell	1	2	3	4	5
number of elements	450	806	622	582	490
number of load situations/simulations	860	660	852	860	860
total computing time [min]	57.7	54.1	74.7	73.1	67.6

Table 1.1: Simulation program at the clear wood scale.

Finally, the effective failure surfaces obtained for the five different annual ring orientations are compared with the experimentally obtained failure stress states for clear wood that were presented in Eberhardsteiner (1995). The result is plotted in Figure 1.12. The numerical limit analysis results agree very well with the experimental results, qualitatively as well as quantitatively. The numerical results tend to overestimate the experimental ones, which is in accordance with the fact that limit analysis is based on an ideal perfectly plastic response of the material, rather than a brittle one. Nevertheless, the results provide meaningful predictions of the clear wood strength, also showing that wood must have some ductile potential, even under tension-dominated loading.

## 1.4 Summary and conclusions

This work shows the first-time application of numerical limit analysis formulations to microstructures of wood. With respect to the three objectives specified in Section 1, the main findings can be summarised as follows:

- The orthotropic Tsai-Wu failure criterion was formulated as a second-order cone constraint, and thus, easily incorporated into numerical limit analysis formulations

that use SOCP. To the authors' knowledge, this failure criterion has not previously been combined for with periodic boundary conditions, as anti-periodic traction fields and periodic velocity fields. These were successfully enforced in lower bound and upper bound formulations, respectively.

- The new limit analysis formulations were successfully applied to unit cells at the annual ring scale and the clear wood scale. Through variation of the applied loading conditions, effective failure surfaces in the macroscopic stress space were obtained very stably and efficiently at both observation scales. For all simulations the small difference between the lower and upper bound results (the bracketing error) was highly satisfactory.
- The comparison between numerically-obtained effective failure surfaces at the clear wood scale and experimental results from biaxial testing of Norway spruce clear wood showed very good agreement, confirming the proposed method as very promising.

Based on these results it can be concluded that, due to its efficiency and simplicity and good prediction quality, the presented limit analysis concept should be able to play an important role in the strength prediction of wood and wood-based products. Future work is being devoted to the extension of this presented approach to the third dimension, as well as applications to the next higher scales of observation, such as the scales of the wooden board and the wood-based product (Hochreiner et al., 2013, 2014). With efficient and stable strength estimates of wooden boards, also stochastic considerations as proposed in Füssl et al. (2016), Kandler et al. (2015a) for elasticity, it should be possible to attempt predictions of the effective strength properties of wood-based products. Even if it is not used to access directly the load bearing capacity of wood, limit analysis seems to be a very well suited method for providing preliminary information on failure mechanisms, for example as input to brittle failure simulations. This could finally provide a conservative design strength for a certain knot group, as it is done in Jenkel and Kaliske (2014) for example. Therein, elastoplastic finite element calculations are performed (which could be replaced by more efficient limit analysis calculations) to gain information about failure zones around/between knots, and this information is used to define the location of cohesive elements, subsequently delivering "brittle" strength estimates. Moreover, to obtain an initial strength evaluation of a defect, or for the identification of critical defects, limit analysis simulations would be sufficient. In parallel, Füssl et al. (2017) have compared the results of the proposed limit analysis concept with results from XFEM simulations and with elastic limit states obtained in the framework of continuum micromechanics in Füssl et al. (2017), showing a very promising and efficient performance of limit analysis with respect to the prediction of failure mechanisms.

## 1.A Second-order cone programming

The definition of the cone set  $\mathcal{C}$  is that,

$$\forall \mathbf{x} \in \mathcal{C} \text{ and } \lambda \geq 0 \iff \lambda \mathbf{x} \in \mathcal{C} \quad (1.49)$$

and then its dual cone  $\mathcal{C}^*$  can be defined as,

$$\mathbf{x}^\top \mathbf{y} \geq 0, \forall \mathbf{x} \in \mathcal{C} \iff \mathbf{y} \in \mathcal{C}^* \quad (1.50)$$

where  $\mathbf{x} \in \mathfrak{R}^n$  and  $\mathbf{y} \in \mathfrak{R}^n$ . If  $\mathcal{C} = \mathcal{C}^*$  holds, the cone is considered as self-dual.

The most common second-order cones is the quadratic cone  $\mathcal{C}$ ,

$$\mathcal{C} = \{\mathbf{x} : x_1 \geq \|\mathbf{x}_{2:d}\|, x_1 \geq 0\} \quad (1.51)$$

and the rotated quadratic cone,

$$\mathcal{C} = \{\mathbf{x} : 2x_1x_2 \geq \|\mathbf{x}_{3:d}\|, x_1 \geq 0, x_2 \geq 0\} \quad (1.52)$$

where  $\mathbf{x}_{m:n} = [x_m \dots x_n]^\top \in \mathfrak{R}^{n-m}$ , and both the two second-order cones are self-dual.

Then the optimization problem of the second-order cone programming (SOCP) can be expressed as

$$\begin{aligned} \min \quad & \mathbf{c}^\top \mathbf{x} \\ \text{s.t.} \quad & \mathbf{A}\mathbf{x} = \mathbf{b} \\ & \mathbf{x} \in \mathcal{C} \end{aligned} \quad (1.53)$$

where  $\mathbf{b} \in \mathfrak{R}^m$ ,  $\mathbf{c} \in \mathfrak{R}^n$ ,  $\mathbf{A} \in \mathfrak{R}^{m \times n}$  and  $\mathcal{C}$  is the second-order cone.

The dual optimization problem is

$$\begin{aligned} \max \quad & \mathbf{b}^\top \mathbf{z} \\ \text{s.t.} \quad & \mathbf{A}^\top \mathbf{z} + \mathbf{y} = \mathbf{c} \\ & \mathbf{y} \in \mathcal{C}^*. \end{aligned} \quad (1.54)$$

where  $\mathbf{z} \in \mathfrak{R}^m$  and  $\mathcal{C}^*$  is the dual cone of  $\mathcal{C}$ .

SOCP can be regarded as a generalization of classical linear programming where the linear constraints are supplemented by specialised nonlinear constraints in the form of the cone constraints. The resulting optimization problem can be solved efficiently with primal-dual algorithms based on the interior-point method.

## 1.B Matrix representation of the limit analysis formulation

To solve the optimization problem, it is very convenient and efficient to use the commercial SOCP solver MOSEK. Therefore, the optimization formulation has to be reformulated in the matrix form suitable for input to MOSEK.

For the lower bound problem, the SOCP formulation in Eq. (1.21) is transformed into

$$\begin{aligned} \max \quad & \beta \\ \text{s.t.} \quad & \begin{matrix} LE \times 2 \\ LD \times 4 \\ LP \times 2 \\ 1 \\ 1 \\ LE \times 9 \\ LE \times 15 \end{matrix} \begin{pmatrix} LE \times 9 & + & LE \times 9 & + & LE \times 15 & + & 1 \\ \mathbf{A}_{LB}^{eq} & \vdots & \mathbf{0} & \vdots & \mathbf{0} & \vdots & \mathbf{0} \\ \mathbf{A}_{LB}^{dis} & \vdots & \mathbf{0} & \vdots & \mathbf{0} & \vdots & \mathbf{0} \\ \mathbf{A}_{LB}^{per} & \vdots & \mathbf{0} & \vdots & \mathbf{0} & \vdots & \mathbf{0} \\ \mathbf{b}_x^{per\top} & \vdots & \mathbf{0} & \vdots & \mathbf{0} & \vdots & -f_{t,x} \\ \mathbf{b}_y^{per\top} & \vdots & \mathbf{0} & \vdots & \mathbf{0} & \vdots & -f_{t,y} \\ -\mathbf{R} & \vdots & \mathbf{I} & \vdots & \mathbf{0} & \vdots & \mathbf{0} \\ \mathbf{0} & \vdots & -\mathbf{B}^{soc} & \vdots & \mathbf{I} & \vdots & \mathbf{0} \end{pmatrix} \begin{pmatrix} \mathbf{q}_\sigma \\ \mathbf{q}'_\sigma \\ \mathbf{s}^{soc} \\ \beta \end{pmatrix} = \begin{pmatrix} \mathbf{0} \\ \mathbf{0} \\ \mathbf{0} \\ \mathbf{0} \\ \mathbf{0} \\ \mathbf{a}^{soc} \end{pmatrix} \end{aligned} \quad (1.55)$$

in which the objective function is the load multiplier  $\beta$ .

Similarly, the upper bound optimization can be derived as the primal form,

$$\begin{aligned}
& \min W_{int} \\
& \text{s.t.} \quad \begin{array}{l} UN \times 2 \quad + \quad UE \times 9 \quad + \quad UE \times 15 \\ UE \times 9 \quad \left( \begin{array}{cccc} \mathbf{A}_{UB}^{eq \top} & \vdots & \mathbf{R}_\sigma^\top & \vdots & \mathbf{0} \\ \mathbf{0} & \vdots & \mathbf{0} & \vdots & -\mathbf{I} \\ UE \times 9 \quad \left( \begin{array}{cccc} \mathbf{0} & \vdots & -\mathbf{I} & \vdots & \mathbf{B}^{soc \top} \\ UP \times 2 \quad \left( \begin{array}{cccc} -\mathbf{A}_{UB}^{per} & \vdots & \mathbf{0} & \vdots & \mathbf{0} \end{array} \right) \end{array} \right) \end{array} \end{array} \end{array} \left( \begin{array}{c} \mathbf{q}_{\dot{u}} \\ -\mathbf{q}'_\varepsilon \\ \mathbf{e}^{soc} \end{array} \right) = \left( \begin{array}{c} \mathbf{0} \\ -\mathbf{e}^{soc} \\ \mathbf{0} \\ \dot{\mathbf{E}}_{UB} \mathbf{l}_{UB} \end{array} \right) \quad (1.56)
\end{aligned}$$

and the dual form,

$$\begin{aligned}
& \max W_{ext} \\
& \text{s.t.} \quad \begin{array}{l} UE \times 9 \quad + \quad UE \times 15 \quad + \quad UE \times 9 \quad + \quad UP \times 2 \\ UN \times 2 \quad \left( \begin{array}{cccc} \mathbf{A}_{UB}^{eq} & \vdots & \mathbf{0} & \vdots & \mathbf{0} & \vdots & -\mathbf{A}_{UB}^{per \top} \\ UE \times 9 \quad \left( \begin{array}{cccc} \mathbf{R}_\sigma & \vdots & \mathbf{0} & \vdots & -\mathbf{I} & \vdots & \mathbf{0} \\ UE \times 15 \quad \left( \begin{array}{cccc} \mathbf{0} & \vdots & -\mathbf{I} & \vdots & \mathbf{B}^{soc} & \vdots & \mathbf{0} \end{array} \right) \end{array} \right) \end{array} \right) \end{array} \end{array} \left( \begin{array}{c} \mathbf{q}_\sigma \\ \mathbf{s}^{soc} \\ \mathbf{q}'_\sigma \\ \mathbf{q}_p \end{array} \right) = \left( \begin{array}{c} \mathbf{0} \\ \mathbf{0} \\ \mathbf{a}^{soc} \end{array} \right) \quad (1.57)
\end{aligned}$$

from Eq. (1.41) and Eq. (1.43) respectively. The duality is clear comparing to the definitions in Eq. (1.53) and Eq. (1.54).

## Acknowledgments

Financial support for this work in the framework of the PhD School DokInHolz funded by the Austrian Federal Ministry of Science, Research and Economy and the Austrian Association of Wood Industries is gratefully acknowledged. We also gratefully acknowledge the financial support of this work by the Austrian Science Fund (FWF) through the Erwin Schrödinger Fellowship J3748-N30.

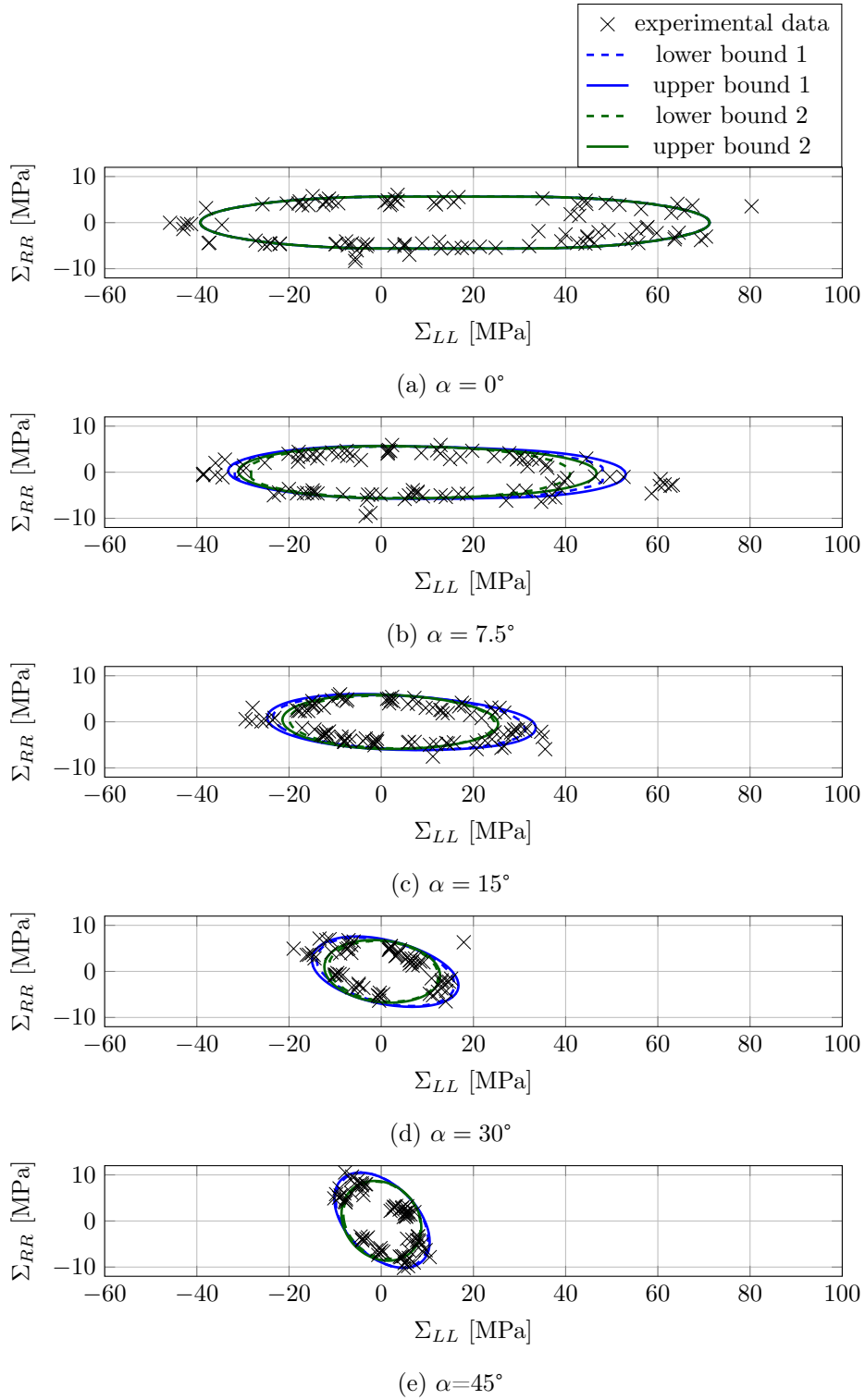


Figure 1.12: Comparison of numerically-obtained lower and upper bound effective failure surfaces of clear wood with experimentally-obtained failure stress states in Eberhardsteiner (1995) for Norway spruce clear wood. Blue curves are obtained with the first approach and green curves with the second approach for the choice of shear strengths (see Eq. (1.48)).



## Comparison of unit cell-based computational methods for predicting the strength of wood (Füssl et al., 2017)

Authored by Josef Füssl, Mingjing Li, Markus Lukacevic, Josef Eberhardsteiner & Chris M. Martin

Published in *Engineering Structures*, 141:427-443, 2017

The final publication is available at:

<https://www.sciencedirect.com/science/article/pii/S0141029617307253>

**Abstract:** Wood, as a naturally-grown material, exhibits a highly anisotropic and inhomogeneous material structure, with a complex wood fibre distribution influenced by randomly occurring knots. Thus, for the prediction of effective strength properties of wood, advanced computational tools are required, which are able to predict as well as consider multidimensional strength information at different scales of observation.

Within this work, three such computational methods will be presented: an extended finite element approach able to describe strong strain-softening and, thus, reproduce brittle failure modes accurately; a newly-developed limit analysis approach, exclusively describing ductile failure; and an elastic limit approach based on continuum micromechanics. All three methods are applied to earlywood and latewood unit cells and to clear wood, finally yielding effective failure surfaces for a range of multidimensional stress states. These failure surfaces are compared with each other and with experimental results from biaxial tests. Based on these comparisons, the strengths and weaknesses of the three computational methods are discussed, and their applicability to wood is evaluated.

The extended finite element method is a powerful technique that allows for a very realistic description of strength-governing processes. Nevertheless, its complexity and high computational effort prevent widespread use in the engineering field. The plastic

limit analysis and elastic limit approaches, however, show good predictive performance compared with the extended finite element method, coupled with excellent efficiency and stability. In this study it is found that together, the latter two approaches are able to enclose the experimentally-obtained failure regions for clear wood almost perfectly, while also delivering new insights with respect to the ductile failure potential of wood.

The conclusion can be drawn that there exist promising computational methods that are capable of delivering reliable multidimensional strength information for wood and, subsequently, will enable effective strength predictions for wooden boards and wood-based products. Finally, this work is intended as a contribution to performance-based optimisation of wooden structures, a necessity for wood to become competitive with respect to other building materials.

**Keywords:** Wood, Strength, XFEM, Limit Analysis, Elastic Limit Estimates.

## 2.1 Introduction

Traditionally, wood as a structural building material has mainly been used in rural areas for one- or two-storey residential buildings or simple halls and stables. Due to the relatively small dimensions of such buildings and the fact that each structural element only appears in a small number, it has not been necessary to exploit the full mechanical potential of wood. Simple design rules combined with practical experience and considerably oversized components have together met all requirements.

In recent years, this situation has changed dramatically. The excellent mechanical and physical properties of wood, combined with the general trend of growing environmental awareness, have put timber structures into the focus of private as well as public building developers – not just to realise small buildings, but to use wooden building elements for highly sophisticated engineering structures. There has already been a nine-storey tower built in London and a 12-storey wooden building is under construction in Bergen, Norway. A 24-storey wooden skyscraper will be completed in Vienna in 2018, which, with a height of 84 m, will be the tallest wooden skyscraper in the world. Another wooden tower, comprising 35 storeys, is planned in Paris, aimed at addressing the French capital's housing challenges in a sustainable, creative and environmentally-friendly manner. Meanwhile, a 34-storey wooden apartment block could be built in Stockholm by 2023 if the planning authorities have their way.

Such projects could, or respectively can, only be realised by the strong initiative of individual responsible authorities, and all of these developers struggle to justify their wooden buildings on economic grounds. Indeed, it is only possible for timber structures to be cost-competitive with steel or concrete structures under ideal planning and executing conditions. A major reason for this is the aforementioned traditional origin of timber constructions, the associated simple design practice, and the resulting conservative dimensioning of wooden structural elements.

This has been the motivation for the present work, which aims at the development and assessment of new computational methods enabling better predictions of the mechanical behaviour of wood. Based on such methods, the great mechanical potential of the 'raw' wooden material should be much better utilised. In this context, simple wooden boards, obtained in sawmills by cutting of logs, are considered as 'raw' material. For use in

construction, these wooden boards are typically assembled into wood-based products like glued-laminated timber (GLT) or cross-laminated timber (CLT). The basic steps of this procedure are shown in Figure 2.1, together with the principal material directions of the flawless wood. The tubular structure of the wooden cells proceeds in the  $L$ -direction

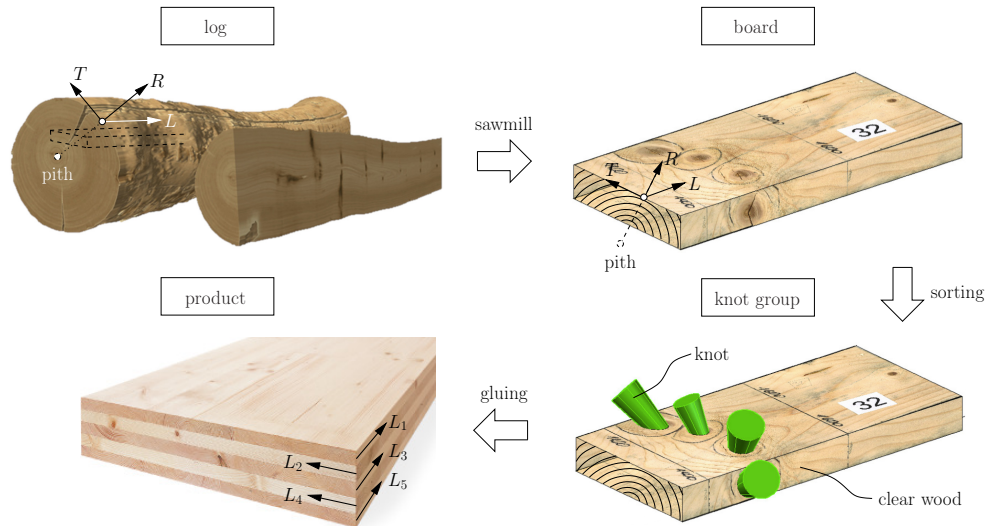


Figure 2.1: Basic steps in wood processing. Wooden boards are obtained in sawmills by cutting logs. These boards are sorted and rated according to characteristics like knots and fibre deviations, before they are glued together to create products (like the CLT board shown).

(longitudinal fibre direction), the  $R$ -direction denotes the radial direction with respect to the central pith, and the  $T$ -direction describes the tangent direction to the circular annual rings. These directions of the flawless wood, which is subsequently referred to as clear wood, are disturbed by randomly occurring knots, forcing the fibres to deviate from the global longitudinal direction. Such knots or knot groups, as illustrated in Figure 2.1, introduce large fluctuations of wooden board properties, and in general board sections with knots exhibit poorer mechanical behaviour than clear wood sections. For this reason, knot-related characteristics are commonly used for sorting and classifying wooden boards. The more accurately this classification procedure works, the more efficiently wooden boards can be used in wood-based products.

Unfortunately, only empirically derived relationships between knot characteristics and certain board properties have been developed and used in the field so far. These do not show very good prediction quality, especially when it comes to strength properties. This is why a growing amount of effort is being put into the development of numerical simulation methods able to describe the influence of knots and knot groups on the effective behaviour of the associated wooden board section. These simulations need to model knots as well as the fibre distribution around them, as shown schematically in Figure 2.2. Suddenly, timber design, which has historically been concerned mostly with beam-like structures, and thus 1D design concepts, has to deal with complex 3D stress and strain fields arising in the vicinity of knots. These stress distributions around knots are often responsible for the initiation of cracks or plastified material zones, and therefore have to be taken into account accurately. This is only possible when a detailed characterisation of the multidimensional strength behaviour of the considered

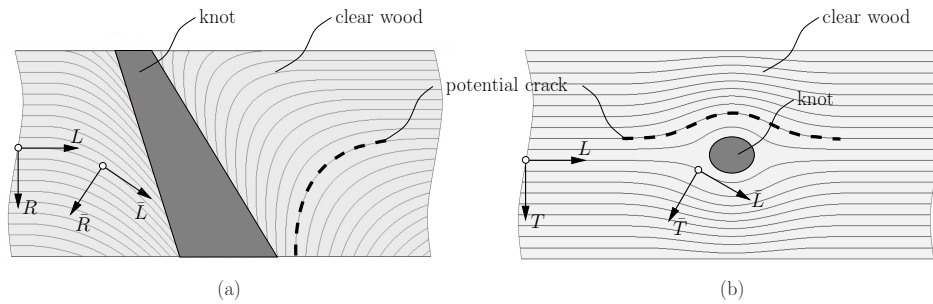


Figure 2.2: Fibre distribution around a knot, illustrated in the (a) longitudinal-radial ( $L$ - $R$ ) plane and (b) longitudinal-tangential ( $L$ - $T$ ) plane, introducing a variety of different 3D stress states into the clear wood.

clear wood is available. This is actually never the case, because the enormous experimental programme that would be required is hardly feasible. Furthermore, it would be virtually impossible to determine experimentally the influence of density fluctuations, different moisture contents, and the different characteristics of several wooden species on the multidimensional strength behaviour.

For this reason, the present work focuses on a new approach for determining 2D and 3D strength information for clear wood. Since failure and plastification is strongly influenced by the complex material system of wood, exhibiting cellular and layered structures on different length scales, a conceptual framework in which these different microstructural characteristics are incorporated appears to be necessary. Since the strength behaviour of the individual components of the wood material can be assumed to be far less complex than that of the overall material system, linking microstructural characteristics to each other and to the macroscopic behaviour, respectively, ultimately leads to a significant reduction of the independent unknown material properties. Moreover, the influence of microstructural changes on the macroscopic behaviour can be identified easily, without performing additional experiments.

Thus, the division of wood into meaningful levels of observation is the first objective of the present work. At each level, failure modes and failure stress states (strength properties) are determined using various computational methods, and the obtained information is transferred – and serves as input – to the next higher level of observation. For this so-called upscaling, a numerical approach based on the extended finite element method has been presented in previous papers of two of the authors (Lukacevic and Füssl, 2016, Lukacevic et al., 2014b). This approach is able to describe failure (even cracking mechanisms) of wood very accurately. For a comprehensive description of the strength behaviour over several levels of observation, however, this method alone seems likely to be insufficient and inefficient. Therefore, within the present work, a plastic limit analysis approach is developed and applied to wood at two levels of observation, contributing successfully to the overall multiscale concept for the prediction of strength properties and failure mechanisms. Moreover, both of these numerical methods are compared with an analytical approach based on continuum micromechanics, originally presented by one of the authors in Hofstetter et al. (2008), delivering elastic limit stresses for given loading states. These stresses refer to ultimate strength in the case of brittle failure, and to elastic limit stresses in the case of ductile failure. Since the extended finite element method is used to describe brittle failure accurately, and limit analysis

is ideally suited for predicting ultimate strength in the case of ductile failure modes, a comprehensive set of complementary methods is available to address the described challenge.

In summary, the objectives of the present work can be formulated as follows:

- Subdividing clear wood into appropriate observation scales and specifying representative unit cells to which the extended finite element method (XFEM), limit analysis (LA) and elastic limit (EL) approaches can be applied.
- Deriving an appropriate LA formulation which is applicable to a unit cell-type homogenisation procedure, similar to the concepts already proposed in Francescato and Pastor (1997), Füssl et al. (2008), Pastor et al. (2010), and applying all three methods to the same clear wood material.
- Comparing the effective strength predictions obtained at the different levels of observation, and evaluating the three methods with respect to their capabilities and efficiency.
- Performance assessment of the three methods with respect to their application to wood, by means of comparisons with experimental results at the clear wood scale.

The paper is structured as follows. In Section 2, the three methods of choice are briefly presented, and the necessary extensions of conventional LA formulations, to be applicable to unit cells of wood microstructures, are given in more detail. Furthermore, an attempt is made to discuss and clarify the fundamental differences between the three methods. Section 3 describes the considered wood species, its microstructure, and the observation scales and representative unit cells derived therefrom. The model geometries and input parameters for all methods are given, and the calculation program is specified. In Section 4, the results of all methods are presented, compared with each other and discussed. Moreover, the results from all three methods at the clear wood scale are plotted against experimental results obtained from biaxial testing. Finally, concluding remarks and a short statement on future work are given in Section 5.

## 2.2 Methods and theory

The failure behaviour of wood is quite complex, being strongly dependent on the type of loading and the level of consideration (observation scale). The majority of the models in the scientific literature focus on the wooden board scale (as illustrated in Figure 2.2), describing the failure behaviour of clear wood and the influence of knots. At this scale, under pressure-dominated stress states, wood behaves in a very ductile manner and strain hardening may even occur. Under tensile- and shear-dominated stress states, a rather brittle failure behaviour can be observed, but with a fracture toughness that can be very different dependent on the wooden structure considered. A brief overview of some existing methods for predicting/modelling structural behaviour at the wooden board level is given in the following.

The first group of approaches avoids any direct description of failure mechanisms, and instead uses *mean stress concepts* (Landelius, 1989, Masuda, 1988), where averaged stresses over a small finite volume are assumed to indicate failure. These volumes

can be adjusted to typical features of wood, such as structural characteristics of wood fibres (Aicher et al., 2002). In Serrano and Gustafsson (2007), Sjödin and Serrano (2008), Sjödin et al. (2008) this approach was applied in combination with findings of linear elastic fracture mechanics. The suitability of different volume definitions, over which the stresses are averaged, and also the effectiveness of various failure criteria, was compared in Guindos (2011). A physically-based structural failure criterion was presented in Lukacevic and Füssl (2014), Lukacevic et al. (2014a), where it was assumed that in wooden boards with knots, global failure can be related to a stress transfer mechanism, which is identifiable by evaluating averaged stress fields in the vicinity of knots. Models based on mean stress concepts are mostly dependent on empirical parameters, and the true failure mechanisms cannot be mapped. This can be overcome by directly modelling failure processes.

The most sophisticated approaches for this are based on multi-surface yield/failure criteria, as described in Mackenzie-Helnwein et al. (2003). In these approaches, orthotropic yield surfaces are defined to describe the onset of ductile failure, whereas orthotropic crack failure surfaces indicate stress states under which cracks are to be expected. Cracking is normally modelled with cohesive elements, including an anisotropic traction separation law for wood. Applications of this model show promising results regarding the estimation of load-carrying behaviour (Schmidt and Kaliske, 2007, 2009). A cohesive zone model based on plasticity theory has also been used for parametric studies of a glued-laminated timber beam with a hole (Danielsson and Gustafsson, 2014).

These approaches work well for a uniform fibre orientation and if the location of the crack path is known in advance. However, due to knots and the fibre deviations around them, as described in Section 1, complex stress states usually prevail, and such an approach becomes impossible to apply. Thus, to be able to assign reliable failure surfaces and corresponding crack directions to clear wood at the wooden board scale, a multiscale approach is pursued. For such an approach, failure mechanisms at different observation scales need to be analysed. This is done here by using three different promising computational methods. The basic characteristics of each method are described in the following, and are qualitatively shown in Figure 2.3. The type of structural response that can be described by each method, in terms of relationships between the effective stress tensor  $\Sigma$  and the effective strain tensor  $\mathbf{E}$ , is illustrated in Figure 2.3(a), where  $\mathbf{C}^{eff}$  denotes the effective elastic stiffness tensor. Figure 2.3(b) shows the corresponding relationships between microscopic stresses  $\sigma(\mathbf{x}_i)$  and microscopic strains  $\varepsilon(\mathbf{x}_i)$ , for a material point  $i$  of the considered structure. The values given therein denote strength and stiffness values of the wood microstructure (see Figure 2.6), which will be explained in detail in Section 3.

The most obvious way to deal with this complex problem, with respect to morphological as well as material behaviour aspects, is to apply the conventional 2D or 3D finite element method. This has been done by the authors recently, see Lukacevic et al. (2014b). Therein, XFEM was applied successfully to representative wood unit cells, delivering effective stress states which cause the initiation of a crack, and simultaneously giving the corresponding effective crack direction. This method is again applied in the present work, leading now to effective strength predictions at two different scales of observation. Nevertheless, even if XFEM, especially in combination with multi-surface plasticity criteria, is a powerful tool allowing for a very realistic description of complex failure mechanisms, its high computational cost and the overall complexity of

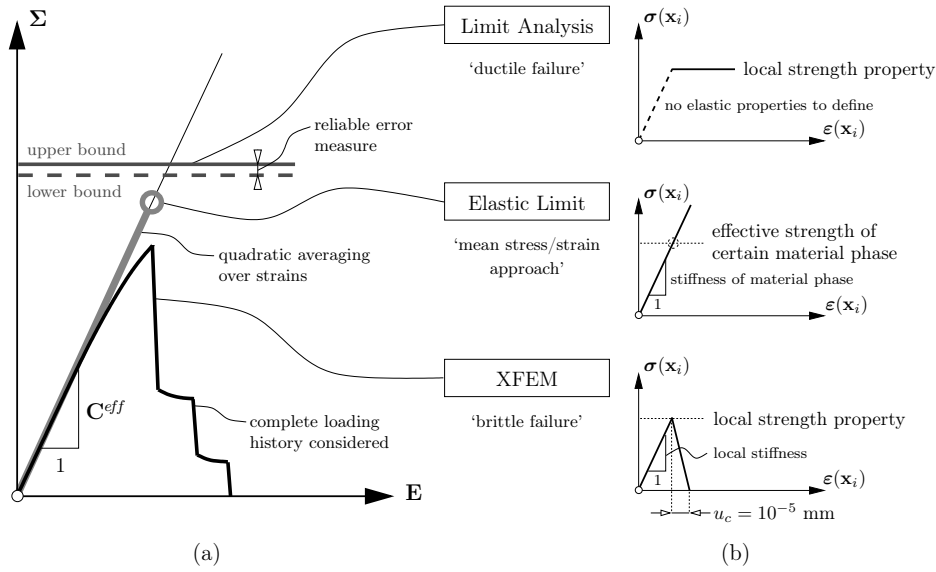


Figure 2.3: Characteristics and qualitative representation of the three methods considered: (a) effective/macroscopic stress-strain response and (b) microscopic stress-strain relationships.

the approach make its use within a multiscale approach rather tedious.

For this reason, additional focus is given to the numerical LA approach and its applicability to microstructures of wood. This method exclusively concentrates on the time instant of failure, and delivers lower and upper bounds for the ultimate strength of the considered material structure. Compared with conventional finite element approaches, where the complete load history has to be considered and, in order to predict the correct failure mechanisms, proper regularisation techniques must be used, the LA approach is much more stable and efficient. Moreover, it leads to rigorous bounds on the material strength, and thus gives a reliable error measure for the prediction. The completely different nature of this so-called direct method, compared with XFEM, becomes obvious in Figure 2.3.

Of course, the efficiency of LA results from the strict assumptions on which this method is based. These include an associated plastic flow rule and ideal plastic (ductile) behaviour of the considered material. Although these two assumptions are not entirely correct for wood, the first is generally made due to a lack of information about the non-associativity, while the second does not exclude the possibility that good strength predictions can also be obtained for strain-softening structures. In Denton and Morley (2000) it is stated: "A structure does not need to exhibit perfect plasticity for the theoretical plastic collapse load based on the peak yield stress of each component to be approached closely. Rather, it is necessary that, at the point when a collapse mechanism forms under a particular loading, all those regions within the structure which are undergoing straining lie very close to the peak yield stress which they can achieve." Wood certainly has the ductile potential to 'activate' the strength of many points along a potential crack surface before brittle failure occurs. It therefore seems that LA could be an appropriate method for determining effective strengths, at least for pressure- and shear-dominated loading states.

The EL approach has been chosen as third method. It is based on continuum micromechanical homogenisation schemes (Suquet, 1997, Zaoui, 2002) characterised by linearly averaging stress and strain fields of material phases to obtain the effective stiffness tensor of the corresponding material system. Higher-order strain averages, in combination with an appropriate failure criterion for the failure-pertinent material phase, can then be used to predict effective strengths. These strengths refer to elastic limit states in case of ductile failure, but represent ultimate strengths in the case of brittle failure. For this reason, the EL approach ideally complements the LA approach, and thus an effective multiscale approach delivering comprehensive failure information for clear wood seems to be possible.

The adopted formulations of the three different computational methods, which are subsequently applied to the wood microstructures, are presented in the following subsections.

### 2.2.1 Extended finite element method (XFEM)

The XFEM, first introduced in Belytschko and Black (1999) and based on the partition of unity method proposed in Melenk and Babuška (1996), allows, through targeted enrichment of the approximation possibilities of the displacement field, the description of singularities and weak or strong discontinuities of the considered field quantity. A field  $u(\mathbf{x})$ , in our case a displacement field, can thereby be approximated by

$$u(\mathbf{x}) \approx \sum_{i=1}^{NN} \mathbf{N}_{u,i}(\mathbf{x}) \left[ \mathbf{q}_{u,i} + \sum_{j=1}^{NG} \mathbf{G}_j(\mathbf{x}) \mathbf{q}_{enr,ij} \right], \quad (2.1)$$

where  $NN$  is the number of nodes of the finite element mesh,  $\mathbf{N}_{u,i}$  represents the conventional element interpolation functions obeying the partition-of-unity property,  $\sum_{i=1}^{NNE} N_i = 1$ , with  $NNE$  as the number of nodes of an element,  $\mathbf{q}_{u,i}$  is the displacement vector, and  $\mathbf{q}_{enr,ij}$  contains the additional degrees of freedom of node  $i$ , representing the amplitude of the  $j$ th extension function  $\mathbf{G}_j(\mathbf{x})$ .  $NG$  is the number of extension functions.

In this work the basic XFEM capability of a commercial finite element package was used, wherein the so-called level set method (Gravouil et al., 2002, Moës et al., 2002, Osher and Sethian, 1988) is applied to describe the location and geometry of discrete moving cracks. Two level set functions ( $\phi$  and  $\psi$ ), which are two almost-orthogonal signed distance functions, are sufficient to describe arbitrary material interfaces and cracks by using conventional finite element interpolation functions:

$$\phi \approx \sum_{i=1}^{NN} N_i \phi_i \quad \text{and} \quad \psi \approx \sum_{i=1}^{NN} N_i \psi_i, \quad (2.2)$$

where  $\phi$  describes the crack surface in a 3D body and  $\psi$  is used to describe the crack front. By combining these two level set functions, an arbitrary evolving crack can be described implicitly as follows (cf. Figure 2.4):

$$\begin{cases} \text{for all } \mathbf{x} \in \text{crack surface,} & \phi(\mathbf{x}) = 0 \quad \text{and} \quad \psi(\mathbf{x}) < 0 \\ \text{for all } \mathbf{x} \in \text{crack tip,} & \phi(\mathbf{x}) = 0 \quad \text{and} \quad \psi(\mathbf{x}) = 0 \end{cases} \quad (2.3)$$



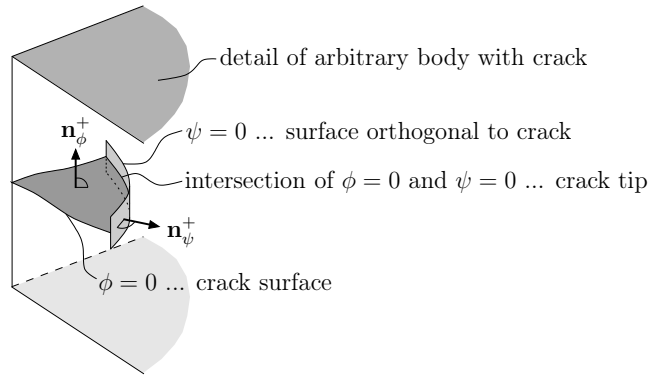


Figure 2.4: Representation of the two iso-zero level sets  $\phi$  and  $\psi$  defining crack geometry and location in the XFEM approach.

Commonly, within the XFEM, singularities caused by crack tips are modelled with extension functions derived in the framework of linear elastic fracture mechanics (Belytschko and Black, 1999). For elements that are completely cut by a crack, the corresponding nodes are enriched by sign or Heaviside functions. In the present work, for describing cracks (strong discontinuities) only the modified Heaviside function (Moës et al., 2002) is used, thus

$$\mathbf{G}_j(\mathbf{x}) = \mathbf{H}(\phi(\mathbf{x})) = \begin{cases} -1 & : \phi(\mathbf{x}) < 0 \\ 1 & : \phi(\mathbf{x}) \geq 0 \end{cases}. \quad (2.4)$$

The simulation of moving cracks is performed using the phantom node method developed in Song et al. (2006) and based on an approach shown in Hansbo and Hansbo (2004). Phantom nodes are superimposed on the original nodes, which are completely tied to the corresponding original nodes for uncut elements. If the element becomes fully cracked, it is represented by two superimposed elements with a combination of phantom and original nodes, which are no longer constrained to each other. The behaviour of the cracked surfaces can now be described by the same methods that are used for cohesive joint elements. The element-by-element propagation of a crack has been successfully used in Song et al. (2006) for several simulations of crack propagation, with only minor mesh dependency. They also noted that, although the crack speed might be overestimated by the element-by-element propagation of a crack, its propagation path is usually in reasonable agreement with experiments.

After crack initiation, perfect brittle damage evolution is assumed, meaning that the transferable stresses drop almost immediately to zero (the displacement from crack initiation to stress-free crack surfaces is set to  $10^{-5}$  mm, see Figure 2.3(b)). To permit subsequent stress transfer over crack surfaces, a node-to-surface contact formulation with finite sliding is used for fully cracked elements.

## 2.2.2 Limit analysis (LA)

As opposed to conventional finite element methods, XFEM included, LA is a ‘direct method’, focusing only on the moment of impending plastic collapse. All deformation up to this point is assumed to be of the same order of magnitude as the elastic deformation, so that the influence of geometry changes on the collapse load can be neglected. In the state of impending plastic collapse, all elastic strain rates in the considered body vanish and it behaves like a rigid–plastic rather than an elastic–plastic body. For this reason, only the strength behaviour of each material phase is required, and the need to specify deformation properties (which are often difficult to determine) can be avoided. This argument was first presented by Drucker et al. (1951), together with the first complete formulations of both the lower bound and upper bound theorems of limit analysis (Drucker et al., 1952), which can be stated informally as follows (Lubliner, 1990): “The loads that are in equilibrium with a stress field that nowhere violates the yield criterion do not exceed the collapse loads, while the loads that do positive work on a kinematically admissible velocity field at a rate equal to the total plastic dissipation are at least equal to the collapse loads.” The required key assumption behind these two theorems is the principle of maximum plastic dissipation, which requires a perfectly plastic material with a convex yield surface and associated plastic flow (normality of incremental plastic strain rates to the yield surface). If the loads resulting from the two theorems are equal to each other, then the true collapse load has been determined. If not, rigorous lower and upper bounds on the exact solution are provided, giving an immediate error indication for the result. Design approaches based on limit analysis represent very efficient methods with a reliability that is often sufficient for many civil and mechanical engineering problems such as structural design and safety assessment, and geotechnical capacity calculations.

In the following, numerical formulations of the bound theorems suitable for application to 2D wood microstructures will be presented.

### 2.2.2.1 Numerical upper bound formulation

An intuitive statement of the upper bound theorem could read: *The considered material structure will collapse under a given loading if an admissible velocity field can be found forming a failure mechanism dissipating less power than the rate of work of the given loading.* A velocity field is considered to be admissible when it obeys, in every point of the material structure, the associated flow rule

$$\dot{\boldsymbol{\epsilon}} = \dot{\lambda} \frac{\partial f}{\partial \boldsymbol{\sigma}} \quad \text{with} \quad \dot{\lambda} \geq 0. \quad (2.5)$$

Here  $f$  denotes a convex yield function specified in terms of the Cauchy stress tensor  $\boldsymbol{\sigma}$ ,  $\dot{\lambda}$  is the plastic multiplier and  $\dot{\boldsymbol{\epsilon}}$  represents the strain rate tensor, which is classically linked to the velocity vector  $\dot{\mathbf{u}}$ , reading

$$\dot{\epsilon}_{ij} = \frac{1}{2} (\dot{u}_{i,j} + \dot{u}_{j,i}) = \mathbf{L}\dot{\mathbf{u}}, \quad (2.6)$$

where  $\mathbf{L}_u \in \mathfrak{R}^{3 \times 2}$  (in 2D) denotes the common differential operator mapping deformations onto strains. In the present work, we are only considering yield functions  $f$  that

can be written down in the following general quadratic form:

$$f = \mathbf{F}^\top \boldsymbol{\sigma} + \boldsymbol{\sigma}^\top \mathbf{P} \boldsymbol{\sigma} \leq 1, \quad (2.7)$$

where  $\mathbf{F} \in \mathfrak{R}^3$  and  $\mathbf{P} \in \mathfrak{R}^{3 \times 3}$  (in 2D) contain coefficients linked to the strength parameters of the considered material phase. When the symmetric matrix  $\mathbf{P}$  is positive definite or semidefinite, the solution set of Equation (2.7) is an ellipsoid, with the square roots of the eigenvalues of  $\mathbf{P}$  giving the semi-axis lengths. It can then be decomposed as  $\mathbf{P} = \mathbf{D}^\top \mathbf{D}$  with  $\mathbf{D} \in \mathfrak{R}^{3 \times 3}$ , and Equation (2.7) can be reformulated into an affine transformation and a cone constraint:

$$\begin{aligned} \mathbf{s} &= \mathbf{a} + \mathbf{B} \boldsymbol{\sigma} \\ \mathbf{s} &\in \mathcal{C} \end{aligned} \quad (2.8)$$

with

$$\mathbf{a} = (1 \ 0 \ 0 \ 0 \ 0)^\top \in \mathfrak{R}^5 \quad \text{and} \quad \mathbf{B} = \begin{pmatrix} -\mathbf{F}^\top/2 \\ \mathbf{D} \\ \mathbf{F}^\top/2 \end{pmatrix} \in \mathfrak{R}^{5 \times 3}, \quad (2.9)$$

and  $\mathcal{C}$  denoting a second-order cone<sup>1</sup>.

Considering Equation (2.8) and following the derivations in Makrodimitopoulos (2010), the flow rule in Equation (2.5) may alternatively be written as

$$\dot{\boldsymbol{\epsilon}} = \dot{\lambda} \frac{\partial f}{\partial \boldsymbol{\sigma}} = -\mathbf{B}^\top \mathbf{y}, \quad (2.13)$$

where  $\mathbf{y} \in \mathfrak{R}^5$  contains terms related to the strain rates.

Finally, in accordance with Makrodimitopoulos (2010), the upper bound optimisation problem takes the form

$$\begin{aligned} \min W_{int} &= \int_V \mathbf{a}^\top \mathbf{y} \, dV \\ \text{s.t.} \quad \mathbf{B}^\top \mathbf{y} + \mathbf{L}_u \dot{\mathbf{u}} &= \mathbf{0} \quad \text{in } V \\ \mathbf{y} &\in \mathcal{C}^* \quad \text{in } V \\ \mathbf{q}^\top \dot{\mathbf{u}} &= 1 \end{aligned} \quad (2.14)$$

where  $\mathcal{C}^*$  is the dual cone to  $\mathcal{C}$  and  $\mathbf{q}$  is the vector of equivalent nodal loads arising from the surface tractions  $\mathbf{t}$ . In this work, since we want to apply the formulation to a unit

<sup>1</sup> A set  $\mathcal{C}$  is called a cone if  $\forall \mathbf{x} \in \mathcal{C}$  and  $\lambda \geq 0$ ,  $\lambda \mathbf{x} \in \mathcal{C}$ . Examples of such cones are

- the nonnegative orthant

$$\mathcal{C} = \mathfrak{R}_+ = \{x : x \geq 0\}, \quad (2.10)$$

- the second-order (or ice-cream) cone

$$\mathcal{C} = \left\{ \mathbf{x} \in \mathfrak{R}^m : \sqrt{\sum_{i=2}^m x_i^2} \leq x_1, x_1 \geq 0 \right\}, \quad (2.11)$$

- and the rotated quadratic cone

$$\mathcal{C} = \left\{ \mathbf{x} \in \mathfrak{R}^m : \sum_{i=3}^m x_i^2 \leq 2x_1x_2, x_1 \geq 0, x_2 \geq 0 \right\}. \quad (2.12)$$

cell, the last line in Equation (2.14), scaling the external work rate to 1, is replaced by periodic boundary conditions formulated in terms of the surface velocities, reading

$$\dot{\mathbf{u}}^+ = \dot{\mathbf{u}}^- + \dot{\mathbf{E}}(\mathbf{x}^+ - \mathbf{x}^-) \quad \text{on } \Omega, \quad (2.15)$$

where  $\dot{\mathbf{u}}^+$  is the velocity vector at the surface node  $\mathbf{x}^+$ , associated with the surface part  $\partial\Omega^+$ , and  $\dot{\mathbf{u}}^-$  is the velocity vector at the surface node  $\mathbf{x}^-$ , associated with the opposite surface part  $\partial\Omega^-$ . The pairs of opposite surfaces  $\partial\Omega^-$  and  $\partial\Omega^+$  are given in Figure 2.6, for the unit cell at the clear wood scale as well as for the two unit cells at the annual ring scale.  $\dot{\mathbf{E}}$  denotes the effective/macroscopic strain rate tensor of the considered unit cell, and is linked to the microscopic strain rate field as follows:

$$\dot{\mathbf{E}} = \frac{1}{V} \int_V \dot{\boldsymbol{\epsilon}}(\mathbf{x}) dV. \quad (2.16)$$

Since the vector  $\mathbf{y}$ , and thus the internal work rate in Equation (2.14) can be written explicitly only for selected yield criteria, the dual form of the optimisation problem in Equation (2.14) is considered subsequently, reading

$$\begin{aligned} \max W_{ext} &= \int_{\partial\Omega^+} \dot{\mathbf{u}}^{+\top} \mathbf{t}^+ dS + \int_{\partial\Omega^-} \dot{\mathbf{u}}^{-\top} \mathbf{t}^- dS = \int_{\partial\Omega^+} (\dot{\mathbf{E}}(\mathbf{x}^+ - \mathbf{x}^-))^{\top} \mathbf{t}^+ dS \\ \text{s.t. } \mathbf{L}_u^{\top} \boldsymbol{\sigma} dV - (\mathbf{t}^+ - \mathbf{t}^-) d\Omega &= \mathbf{0} && \text{in } V \\ \mathbf{s} &= \mathbf{a} + \mathbf{B}\boldsymbol{\sigma} && \text{in } V \\ \mathbf{s} &\in \mathcal{C} && \text{in } V \end{aligned} \quad (2.17)$$

where the dual variables  $\boldsymbol{\sigma}$  represent stress-like quantities,  $dV$  the associated volume on which  $\boldsymbol{\sigma}$  acts, and  $d\Omega$  the surface part relevant to either  $\mathbf{t}^+$  or  $\mathbf{t}^-$ .

The finite element discretisation for the upper bound problem uses the triangular elements depicted in Figure 2.5 (left side). Quadratic shape functions are used to approximate the velocity field, as proposed in Makrodimopoulos and Martin (2005a), resulting in a linear variation of strain rate within the element. If the vertices of the element are used to enforce the flow rule and evaluate the plastic dissipation, the solutions obtained are strict upper bounds on the exact collapse load (Makrodimopoulos and Martin, 2005b, 2007). In the case of unstructured meshes, these linear strain rate elements typically show better performance than the often-used constant strain rate elements with velocity discontinuities (Makrodimopoulos and Martin, 2005b, 2007).

Finally, the discretised form of the dual upper bound optimisation problem in Equation (2.17) can be solved efficiently by an interior point method. In this work, the algorithm outlined in Andersen et al. (2003), which has been implemented in the optimisation software MOSEK ApS (2017), was used.

### 2.2.2.2 Numerical lower bound formulation

An intuitive statement of the lower bound theorem could read: *A body will not collapse under a certain loading if an admissible stress field can be found that is in equilibrium with a loading greater than the considered loading.* A stress field is considered to be admissible when it does not violate the yield criterion, according to Equation (2.7) or (2.8), at any point of the material structure.

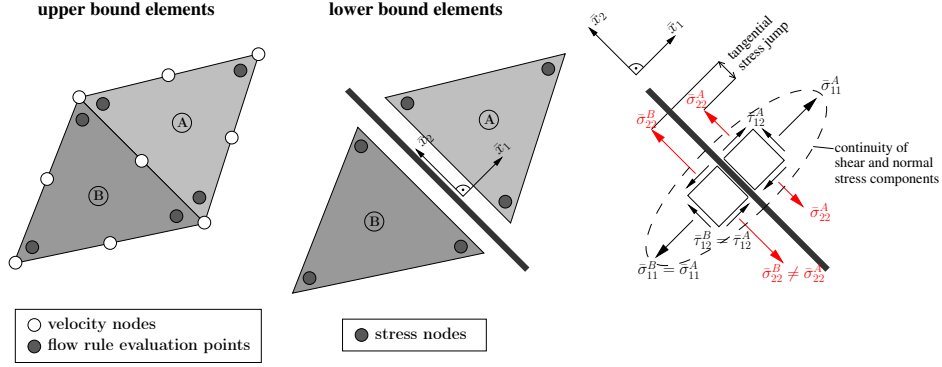


Figure 2.5: Finite elements used in the upper and lower bound LA formulations.

The optimal lower bound solution can be found by solving the following optimisation problem:

$$\begin{aligned}
 \max \quad & \alpha \\
 \text{s.t.} \quad & \mathbf{L}_\sigma \boldsymbol{\sigma} = \mathbf{0} && \text{in } V \\
 & \mathbf{t}^+ + \mathbf{t}^- = \mathbf{L}_t(\boldsymbol{\sigma}^+ + \boldsymbol{\sigma}^-) = \mathbf{0} && \text{on } \Omega \\
 & \frac{1}{\Omega^+} \int_{\Omega^+} \mathbf{L}_t \boldsymbol{\sigma}^+ dS = \alpha \mathbf{t}^+ && \text{on } \Omega^+ \\
 & \mathbf{s} = \mathbf{a} + \mathbf{B}\boldsymbol{\sigma} && \text{in } V \\
 & \mathbf{s} \in \mathcal{C} && \text{in } V
 \end{aligned} \tag{2.18}$$

In the first constraint, which enforces equilibrium within the body  $V$ ,  $\mathbf{L}_\sigma$  denotes the divergence operator. The second constraint represents the static periodic boundary conditions, necessary when applying this formulation to unit cells, with  $\mathbf{t}^+$  as the traction at the surface node  $\mathbf{x}^+$ , associated with the surface part  $\partial\Omega^+$ , and  $\mathbf{t}^-$  as the traction at the surface node  $\mathbf{x}^-$ , associated with the opposite surface part  $\partial\Omega^-$ . The matrix  $\mathbf{L}_t$  depends on the outward normal vector  $\mathbf{n}$  of the surface  $\Omega$  and connects the stresses  $\boldsymbol{\sigma}^+$  and  $\boldsymbol{\sigma}^-$  at the surface to the corresponding tractions. Finally, through  $\mathbf{T}$  the effective traction loading at the surface of the considered unit cell is specified, which is self-equilibrating due to the simultaneously enforced periodic boundary conditions.

To obtain a discretised version of the lower bound optimisation problem in Equation (2.18), the stress field is approximated by a piecewise linear variation using triangular finite elements as shown in Figure 2.5 (middle). Each element has its own set of three internal stress evaluation nodes, thus multiple nodes from adjacent elements may share the same coordinates. At the resulting stress discontinuities between elements, only the continuity of normal and shear stress components needs to be enforced; a jump in the stress component parallel to the discontinuity is allowed (as illustrated in Figure 2.5, right side).

Finally, the discretised form of the lower bound optimisation problem can be solved in a similar way to the dual upper bound problem, using the optimisation software MOSEK ApS (2017).

### 2.2.3 Elastic limit (EL) approach

Unlike the XFEM and LA approaches described before, the EL approach used within this work is solely based on linking the effective stiffness properties of the considered

(loaded) material with the stiffness properties of the underlying material phases. Therefore, depending on the observation scale, either continuum micromechanical schemes (Zaoui, 2002) or analytical solutions for unit cell structures (Suquet, 1987) are employed. Finally, effective stress states of the loaded material structure can be directly related to microscopic strains in an arbitrary material phase. Under the assumption that failure of a certain material phase is responsible for failure of the whole material structure, critical strain states in such a phase can be identified and, subsequently, effective failure stress states of the whole material structure are obtained.

### 2.2.3.1 Continuum micromechanics

Within the framework of continuum micromechanics, a material is seen as a micro-heterogeneous body filling a macro-homogeneous representative volume element (RVE) at different scales of observation. The microstructure within such an RVE can be described by so-called material phases, representing quasi-homogeneous subdomains with known physical characteristics such as volume fractions, characteristic shapes, and mechanical properties. The size of the inhomogeneities defined by the material phases has to be significantly smaller than the characteristic length of the RVE, and the size of the RVE again has to be smaller than the characteristic dimension of the structure built up by the material, or the RVE representing the next higher scale of observation, respectively. In such a way multiscale homogenisation schemes are set up.

In continuum micromechanics, the effective stiffness  $\mathbf{C}^{eff}$  of an RVE can be linked to its microstructure according to Benveniste (1987), Zaoui (2002), based on the solutions in Eshelby (1957), Laws (1977), as follows (Hofstetter et al., 2008):

$$\begin{aligned} \mathbf{C}^{eff} &= \sum_{i=1}^N f_i \mathbf{c}_i : \mathbf{A}_i \quad \text{with} \\ \mathbf{A}_i &= [\mathbf{I} + \mathbf{P}_i^0 : (\mathbf{c}_i - \mathbf{C}^0)]^{-1} : \left\{ \sum_{j=1}^N f_j [\mathbf{I} + \mathbf{P}_j^0 : (\mathbf{c}_j - \mathbf{C}^0)]^{-1} \right\}^{-1}, \end{aligned} \quad (2.19)$$

where  $\mathbf{c}_i$  and  $f_i$  denote the elastic stiffness and the volume fraction of phase  $i$  of total  $N$  material phases, respectively,  $\mathbf{A}_i$  is the concentration tensor of phase  $i$  and  $\mathbf{I}$  is the fourth-order identity tensor.  $\mathbf{C}^{eff}$  relates effective/macroscopic RVE-related stresses  $\boldsymbol{\Sigma}$  to corresponding strains  $\mathbf{E}$ , while  $\mathbf{c}_i$  relates (average) phase stresses  $\boldsymbol{\sigma}_i = (1/V_i) \int_{V_i} \boldsymbol{\sigma}(\mathbf{x}) dV$  to (average) phase strains  $\boldsymbol{\varepsilon}_i = (1/V_i) \int_{V_i} \boldsymbol{\varepsilon}(\mathbf{x}) dV$ .  $\mathbf{x}$  is the location vector for positions inside the RVE,  $\boldsymbol{\sigma}(\mathbf{x})$  and  $\boldsymbol{\varepsilon}(\mathbf{x})$  are the stress and strain fields inside the material phases, and  $V_i$  is the volume of phase domain  $i$  inside the considered RVE. The fourth-order tensor  $\mathbf{P}_i^0$  accounts for the characteristic shape of phase  $i$  in a matrix with stiffness  $\mathbf{C}^0$ . The choice of this stiffness describes the interactions between phases. If  $\mathbf{C}^0$  describes one of the phase stiffnesses, a material with a contiguous matrix with inclusions is represented and Equation (2.19) renders the Mori-Tanaka scheme (Benveniste, 1987), while for  $\mathbf{C}^0 = \mathbf{C}^{eff}$ , a dispersed arrangement of the phases is represented and Equation (2.19) reflects the self-consistent scheme.

### 2.2.3.2 Unit cell homogenisation

If the material microstructure is characterised by the spatial variation of physical quant-

ities which can be represented by a combination of local fluctuations at the level of the elementary cell and a spatial repetition of this elementary cell, a unit cell homogenisation scheme may be employed. The honeycomb structure inherent to wood, presented later, represents such a material microstructure, which can be built up/approximated using identical basic repetitive units. Moreover, the length of these cells is two orders of magnitude larger than their cross-sectional dimensions, justifying the assumption of an infinite extension of the unit cells in the longitudinal direction (i.e., conditions of plane strain). Thus, the unit cell homogenisation methods proposed in Böhm (2004), Suquet (1987) can be applied.

Thereby, the unit cell is subjected to periodic, symmetry, or antisymmetry displacement boundary conditions such that the spatial averages of the corresponding microscopic strains  $\boldsymbol{\varepsilon}(\mathbf{x})$  are equal to the macroscopic strains  $\mathbf{E}$  related to the cellular material. Linking these macroscopic strains to the spatial average of the periodic microstresses they induce, i.e., to the macroscopic stresses  $\boldsymbol{\Sigma}$ , yields the homogenised effective stiffness  $\mathbf{C}^{eff}$  of the cellular material. The effective stiffness expressions, as functions of the unit cell characteristics, and the original application of this method to wood can be found in Hofstetter et al. (2007). In contrast to continuum micromechanics, potential plate-like bending and shear deformations of the cell walls, building up the material structure, can be taken into account with this homogenisation method.

### 2.2.3.3 Elastic Limit estimates

Both of the described methods, continuum micromechanics as well as unit cell homogenisation, can be used, either alone or in combination, to determine the effective stiffness  $\mathbf{C}^{eff}$  of a material structure as a function of its microstructural characteristics.

Let us now assume that the intensity of shear loading of the weakest phase is responsible for failure (an elastic limit state) of our considered material structure. Then, we would need an appropriate stress or strain measure for this material phase and a corresponding failure criterion. In Suquet (1997) such a strain measure is proposed, in fact, quadratic strain averages (second-order moments)  $\bar{\bar{\varepsilon}}_i^d$  are assumed to appropriately represent (failure-causing) local strain peaks in a material phase  $i$ , reading

$$\bar{\bar{\varepsilon}}_i^d = \sqrt{\frac{1}{V_i} \int_{V_i} \frac{1}{2} \boldsymbol{\varepsilon}^d(\mathbf{x}) : \boldsymbol{\varepsilon}^d(\mathbf{x}) dV}, \quad (2.20)$$

where  $\boldsymbol{\varepsilon}^d(\mathbf{x})$  denotes the deviatoric strain field, defined as  $\boldsymbol{\varepsilon}^d(\mathbf{x}) = \boldsymbol{\varepsilon} - (\text{tr } \boldsymbol{\varepsilon}(\mathbf{x})/3)\mathbf{I}$ . According to Hill's lemma (Hill, 1951), the following relationship between microscopic and macroscopic quantities, representing the energy density  $\mathcal{E}$ , is valid:

$$\mathcal{E} = \frac{1}{V_i} \int_{V_i} \frac{1}{2} \boldsymbol{\varepsilon}(\mathbf{x}) : \mathbf{c}_i : \boldsymbol{\varepsilon}(\mathbf{x}) dV = \frac{1}{2} \mathbf{E} : \mathbf{C}^{eff} : \mathbf{E}, \quad (2.21)$$

where  $\mathbf{c}_i = 3k_i\mathbf{J} + 2\mu_i\mathbf{K}$  is the isotropic stiffness of material phase  $i$ , with bulk modulus  $k_i$  and shear modulus  $\mu_i$ , and with  $\mathbf{J}$  and  $\mathbf{K} = \mathbf{I} - \mathbf{J}$  being the volumetric and deviatoric parts of the fourth-order identity tensor  $\mathbf{I}$ . With  $\partial\mathbf{c}_i/\partial\mu_i = 2\mathbf{K}$ , the derivatives of expressions (2.21) with respect to the shear modulus  $\mu_w$  of the weakest phase (with a

volume content of  $f_w$ ) read

$$\frac{\partial \mathcal{E}}{\partial \mu_w} = 2f_w(\bar{\varepsilon}_w^d)^2 = \frac{1}{2} \mathbf{E} : \frac{\partial \mathbf{C}^{eff}}{\partial \mu_w} : \mathbf{E}, \quad (2.22)$$

finally providing an expression for the quadratic strain average of the weakest phase as a function of the effective stiffness and the effective strain, reading

$$\bar{\varepsilon}_w^d = \sqrt{\frac{1}{4f_w} \mathbf{E} : \frac{\partial \mathbf{C}^{eff}}{\partial \mu_w} : \mathbf{E}}. \quad (2.23)$$

In turn, the effective strain is related to the effective stress according to  $\Sigma = \mathbf{C}^{eff} : \mathbf{E}$ . With an appropriate failure criterion for the weakest phase of the considered material structure,

$$F_w(\bar{\varepsilon}_w^d) = 0, \quad (2.24)$$

effective elastic limit stress states  $\Sigma^{EL}$  and, subsequently, an effective failure criterion  $F(\Sigma^{EL}) = 0$  can be obtained.

## 2.3 Material

### 2.3.1 Morphology

The most common wood species used in engineering constructions is spruce, thus, it is a very well investigated material with a large body of experimental data about its microstructural characteristics and the properties of its constituents. For this work, the composition of spruce wood was taken from Hofstetter et al. (2005), in which a comprehensive micromechanical model for the elasticity of wood is presented, and many references to experimental data for the wooden microstructure are given. Those data and similar models were also used in further works, e.g., in Hofstetter et al. (2007), presenting an improved micromechanical model for the elasticity of wood, in Hofstetter et al. (2008), proposing an extension to obtain elastic limit states of wood, and in Bader et al. (2010, 2011), including a poromechanical approach in the micromechanical model.

Based on the underlying data of these models, appropriate observation scales have been defined in the present work, tailored for predicting the effective strength of clear wood based on its microstructural characteristics. The highest observation scale in this multiscale approach, illustrated in Figure 2.6, represents the clear wood scale, consisting of earlywood and latewood layers with a typical thickness between 0.3 and 3.5 mm. Considering the stem cross-section of a tree, the earlywood and latewood layers form a pattern of concentric circles around the pith, known as growth rings.  $T$  indicates the tangential direction and  $R$  the radial direction with respect to these growth rings, while  $L$  shows the longitudinal direction (stem direction).

At the next scale of observation in Figure 2.6, the annual ring scale, the earlywood and latewood layers consist of periodically arranged honeycomb cells, and thus they can be appropriately represented by unit cells. For both the earlywood and latewood layers, two different unit cells have been defined. The less complex ones (upper cells in Figure 2.6) are used within the analytical EL approach, while the ones consisting of two different layers (lower cells in Figure 2.6) serve as the basis for the numerical (XFEM



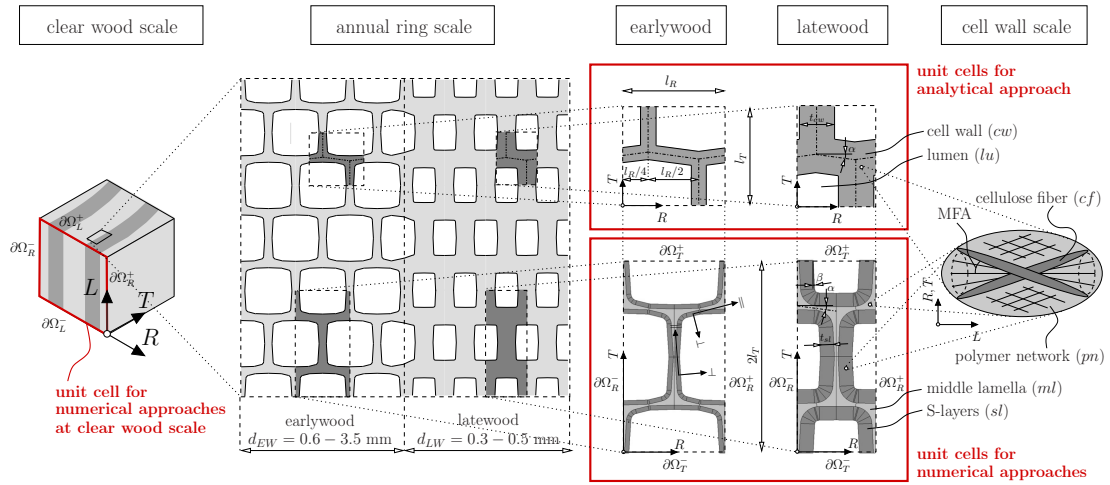


Figure 2.6: Definition of unit cells used for the numerical approaches (XFEM, LA) and the analytical approach (EL) at annual ring scale and clear wood scale for the considered spruce wood (experimentally investigated in Eberhardsteiner (2002)). The 3D unit cells for the XFEM and EL approaches were obtained by simple extrusion of the 2D cross sections shown.

and LA) calculations. Both unit cell types represent the same kind of earlywood and latewood layer, only a different representation of the cell wall has been used, accounting for the possibilities of the particular computational method. In reality, the cell wall consists of five different layers (often referred to as the middle lamella, P, S1, S2, and S3 layers). The volumes of the P, S1 and S3 layers are very small compared with the S2 layer and the middle lamella. For this reason, only two layers are distinguished in the unit cell for the numerical approaches: the middle lamella (ml) and a homogenised layer (sl) representing all S layers and the P layer. The analytical unit cell for the EL approach is completely homogeneous, merging the properties of all five layers into one cell wall material (cw).

Each cell wall layer is itself made up of a non-cellulosic matrix (termed polymer network, pn) in which cellulosic fibres (cf) are embedded, extending spirally at an angle MFA (micro fibril angle) towards the cell axis. The volume contents of these different material phases, at the different observation scales, can be found in Table 2.1.

The parameters defining the geometries of the unit cells in Figure 2.6 are given in Table 2.2.

### 2.3.2 Mechanical behaviour

To obtain the effective elastic behaviour at the cell wall scale (cf. Figure 2.6, right side), Equation (2.19) was applied, with  $\mathbf{C}^0$  as the isotropic stiffness of the polymer network  $\mathbf{c}_{pn}$ , and  $\mathbf{c}_1$  as the anisotropic stiffness of the cellulosic fibres  $\mathbf{c}_{cf}$ . The stiffness tensors

		cell wall scale		unit cells	
		middle lamella ( <i>ml</i> )	S-layers ( <i>sl</i> )	EW	LW
numerical approaches		$f_{pn} = 0.9$	$f_{pn} = 0.6$	$f_{ml} = 0.36$	$f_{ml} = 0.23$
		$f_{cf} = 0.1$	$f_{cf} = 0.4$	$f_{sl} = 0.64$	$f_{sl} = 0.77$
		unit cells		annual ring scale	
		EW	LW	EW	LW
all approaches		$f_{pn} = 0.71$	$f_{pn} = 0.67$	$f_{cw} = 0.24$	$f_{cw} = 0.61$
		$f_{cf} = 0.29$	$f_{cf} = 0.33$	$f_{lu} = 0.76$	$f_{lu} = 0.39$

Table 2.1: Volume content of different material phases at different scales of observation for a typical spruce wood as investigated in Eberhardsteiner (2002) and modelled in Hofstetter et al. (2005). EW = earlywood, LW = latewood. Indices are explained in Figure 2.6.

		shape of unit cells		cell wall geometry			
		$l_R$ [ $\mu\text{m}$ ]	$l_T$ [ $\mu\text{m}$ ]	$\alpha$ [ $^\circ$ ]	$\beta$ [ $^\circ$ ]	$t_{ml}$ [ $\mu\text{m}$ ]	$t_{sl}$ [ $\mu\text{m}$ ]
‘numerical’ unit cell	EW	34	33	8.0	3.5	1.5	1.5
	LW	26	33	8.0	3.0	2.0	4.7
		$l_T/l_R$ [-]		$\alpha$ [ $^\circ$ ]	$t_{cw}/l_R$ [-]		
‘analytical’ unit cell	EW	0.97		8.0	0.13		
	LW	1.27		8.0	0.43		

Table 2.2: Parameters defining the geometry and dimensions of the earlywood (EW) and latewood (LW) unit cells illustrated in Figure 2.6, for a typical spruce wood as investigated in Eberhardsteiner (2002) and modelled in Hofstetter et al. (2005).

$\mathbf{c}_{pn}$  and  $\mathbf{c}_{cf}$  were calculated according to the model in Bader et al. (2010), yielding

$$\mathbf{c}_{cf} = \begin{bmatrix} 16779 & 5626 & 2390 & & & \\ & 16779 & 2390 & & & \\ & & 113123 & & & \\ & & & 7532 & & \\ & \text{sym.} & & & 7532 & \\ & & & & & 11153 \end{bmatrix} \quad \text{and} \quad (2.25)$$

$$\mathbf{c}_{pn} = \begin{bmatrix} 4011 & 1496 & 1496 & & & \\ & 4011 & 1496 & & & \\ & & 4011 & & & \\ & & & 2515 & & \\ & \text{sym.} & & & 2515 & \\ & & & & & 2515 \end{bmatrix} [\text{MPa}]. \quad (2.26)$$

The cellulosic fibres are modelled as cylindrical inclusions, defined through the concentration tensor  $\mathbf{P}_{cf}^0$ , which can be found in Zaoui (2002). The volume content of the cellulosic fibre phase  $f_{cf}$  is given in Table 2.1. The resulting effective cell wall layer stiffnesses define the elastic behaviour of the wood unit cells at the annual ring scale, and thus serve as input to the XFEM simulations as well as to the unit cell homogenisation within the EL approach. No elastic material properties are required for the LA approaches.

The strength behaviour assigned to the wood cell structures is explained in the following. In the course of the EL approach in Bader et al. (2010), lignin is assumed to be the weakest phase in the wood material structure, failing in shear once a certain threshold is achieved (Zimmermann et al., 1994). Thus, an appropriate failure criterion for use in Equation (2.24) reads

$$F_w(\bar{\varepsilon}_w^d) \hat{=} F_{lignin}(\bar{\varepsilon}_{lignin}^d) = (2\mu_{lignin}\bar{\varepsilon}_{lignin}^d)^2 - (\tau_{lignin})^2, \quad (2.27)$$

where  $\tau_{lignin}$  denotes the lignin shear strength, assumed to be 14.3 MPa according to Bader et al. (2010), Lukacevic et al. (2014b). Since it can be assumed that failure of the middle lamella is primarily caused by failure of its main constituent lignin, the shear strength of lignin (and the Von Mises-type failure criterion in Equation (2.27)) was also assigned to the middle lamella of the unit cells for the numerical approaches,  $\tau_{ml} \approx \tau_{lignin} = 14.3$  MPa (see also Table 2.3).

	middle lamella ( <i>ml</i> )	S-layers ( <i>sl</i> )			
	$\tau_{ml}$ [MPa]	$\sigma_{  }^{sl}$ [MPa]	$\sigma_{\perp}^{sl}$ [MPa]	$\tau_{  \perp}^{sl} = \tau_{  L}^{sl}$ [MPa]	$\sigma_L^{sl}$ [MPa]
<b>XFEM</b>	14.3	75	$\infty$	43	175
<b>Limit Analysis</b>	14.3	75	150 / $\infty$	43	-
<b>Elastic Limit</b>	$\tau_{ml} \approx \tau_{lignin} = 14.3$	$\infty$	$\infty$	$\infty$	$\infty$

Table 2.3: Strength values assigned to middle lamella and S-layers of the earlywood and latewood unit cells, for the three different methods. Normal failure stresses  $\sigma^{sl}$  represent absolute values, valid for compression as well as tension. Indices are explained in Figure 2.6.

In contrast to the EL approach, for the numerical approaches the strength behaviour of the explicitly modelled S-layer also needs to be defined. This layer resembles a

unidirectional fibre-reinforced composite, a material for which several failure criteria have been developed. Following Puck's failure criterion (Puck and Schürmann, 2002), which identifies fibre failure and inter-fibre failure in a unidirectional composite, the following three criteria have been assigned to the S-layers, indicating crack initiation within the XFEM approach (Lukacevic et al., 2014b),

$$f_{sl,1}(\boldsymbol{\sigma}) \leq \frac{\sigma_L}{\sigma_L^{sl}}, \quad (2.28)$$

$$f_{sl,2}(\boldsymbol{\sigma}) \leq \frac{\sigma_{\parallel}}{\sigma_{\parallel}^{sl}}, \quad \text{and} \quad (2.29)$$

$$f_{sl,3}(\boldsymbol{\sigma}) \leq \left( \frac{\tau_{\parallel\perp}}{\tau_{\parallel\perp}^{sl}} \right)^2 + \left( \frac{\tau_{\parallel L}}{\tau_{\parallel L}^{sl}} \right)^2. \quad (2.30)$$

Equation (2.28) describes Mode I fibre failure in  $L$ -direction, whereas Equations (2.29) and (2.30) both describe inter-fiber failure, leading to a fracture plane with its normal pointing toward the local  $\parallel$ -direction (see Figure 2.6 for definitions of the symbols  $\parallel$  and  $\perp$ , which respectively denote the local parallel and perpendicular directions in the 'numerical' unit cell). The corresponding tensile and shear strength values were chosen in the same way as in Lukacevic et al. (2014b), and are given in Table 2.3.

For strength definition in the LA approach, two different strategies were followed. On one hand, the in-plane failure criteria as used in the XFEM approach, Equations (2.29) to (2.30), were assigned to the S-layers, and on the other hand, a single 2D anisotropic Tsai-Wu yield criterion (Tsai and Wu, 1971) was used, reading

$$f_{sl,TW}(\boldsymbol{\sigma}) = \frac{\sigma_{\perp}^2}{(\sigma_{\perp}^{sl})^2} + \frac{\sigma_{\parallel}^2}{(\sigma_{\parallel}^{sl})^2} + \frac{\tau_{\parallel\perp}^2}{(\tau_{\parallel\perp}^{sl})^2} \leq 1. \quad (2.31)$$

Both sets of failure criteria gave almost identical results, but due to the slightly lower numerical effort of the Tsai-Wu criterion, it is used for all LA simulations presented in this paper. All the criteria from Equations (2.29) to (2.31) can be cast in a general quadratic form according to Equation (2.7), and thus can be expressed as second-order cone constraints, as required for the LA optimisation problems in Equations (2.17) and (2.18).

For the annual ring scale, no experimentally-obtained strength values are available for assessing the computational results. For this reason, all three of the selected methods were also used to obtain effective strength values at the clear wood scale. No extension of the EL approach was necessary to achieve this; only the geometry of the wood unit cell was changed to represent a mean value of earlywood and latewood and, in this manner, directly give approximate failure estimates for clear wood. In accordance with Table 2.2, the parameters defining the 'analytical' unit cell geometry for the clear wood yield  $l_T/l_R = 1.12$ ,  $\alpha = 8.0^\circ$ , and  $t_{cw}/l_R = 0.28$ . This geometry was adapted to comply with the mean mass density,  $\rho_{CW} = 0.53 \text{ g/cm}^3$ , of the investigated clear wood material. The mass densities represented by the wood unit cells at the annual ring scale are  $0.35 \text{ g/cm}^3$  for earlywood and  $0.90 \text{ g/cm}^3$  for latewood, with a mean mass density of the cell wall material of  $1.45 \text{ g/cm}^3$ .

For the numerical approaches at the clear wood scale, a simple unit cell was used as shown in Figure 2.6 (left side). For these analyses, focus was laid on the  $L$ - $R$  plane, the

plane for which experimental biaxial testing results are available. At this scale, both annual ring types (earlywood and latewood) are modelled as homogeneous materials, with properties obtained from the modelling results from the scale below. The effective strength values obtained from the 3D XFEM simulations of the earlywood and latewood unit cells can be used to define multiple 3D Tsai-Wu failure surfaces, describing the failure behaviour of the annual rings at the clear wood scale. Thus, instead of the failure criteria (2.28) to (2.30) within the XFEM approach, multiple Tsai-Wu failure surfaces indicate crack initiation within the annual rings at clear wood scale. All the parameters defining these failure criteria and the corresponding definitions of crack directions can be found in Lukacevic et al. (2014b). In the LA approach at clear wood scale, the strength behaviour of each annual ring type is described by a single 2D Tsai-Wu failure surface, defined through the strength values given in Table 2.4. The radial strengths  $\sigma_R$  for the

<b>earlywood (EW)</b>					
	failure criterion	$\sigma_{L,ten}^{EW}$ [MPa]	$\sigma_{L,comp}^{EW}$ [MPa]	$\sigma_R^{EW}$ [MPa]	$\tau_{LR}^{EW}$ [MPa]
<b>XFEM</b>	mult. Tsai Wu	(60.0)	(35.4)	(5.3)	(8.6)
<b>Limit Analysis</b>	Tsai Wu	60.0	35.4	5.3	8.6
<b>Elastic Limit</b>	Von Mises	$\tau_{ignin} = 14.3$			
<b>latewood (LW)</b>					
	failure criterion	$\sigma_{L,ten}^{LW}$ [MPa]	$\sigma_{L,comp}^{LW}$ [MPa]	$\sigma_R^{LW}$ [MPa]	$\tau_{LR}^{LW}$ [MPa]
<b>XFEM</b>	mult. Tsai Wu	(126.0)	(58.0)	(13.0)	(8.6)
<b>Limit Analysis</b>	Tsai Wu	126.0	58.0	13.0	8.6
<b>Elastic Limit</b>	Von Mises	$\tau_{ignin} = 14.3$			

Table 2.4: Strength values for earlywood and latewood layers at the clear wood scale, for the three different methods.  $\sigma_R^{EW}$  is valid for tension (ten) as well as compression (comp). Indices are explained in Figure 2.6.

earlywood and latewood were taken from the 2D LA calculations for the respective unit cells at the annual ring scale. Since these calculations delivered no strength properties in the  $L$ -direction, those values were taken from the multi-surface failure criteria obtained by XFEM. That is the reason why the XFEM values in Table 2.4 are in parentheses, because they describe points of the multi-surface but are not directly linked to Tsai-Wu failure surface parameters. Again, the 2D Tsai-Wu failure criterion in Equation (2.31) can be cast in a general quadratic form according to Equation (2.7), and thus, the upper and lower bound LA formulations (Equations (2.17) and (2.18)) can also be applied at the clear wood scale.

Finally, each of the three methods described in Section 2.2 delivers predictions of effective strength for two different scales of observation: the annual ring scale and the clear wood scale. Selected results from all these computations will be presented in the following section.

## 2.4 Calculations and results

When the strength parameters as described in the previous section were chosen, particular attention was paid to ensure that the results of the different methods remain comparable, meaning that all three methods still describe the same wooden material. Differences in computational results can then be primarily attributed to the respective method, and a valid performance assessment with respect to wood may be issued. In the following section, selected computational results from all three methods are presented and compared with each other, giving insights into their predictive qualities.

By varying the effective (macroscopic) loading situation applied to the unit cell under consideration, either the honeycomb unit cell at the annual ring scale or the layered unit cell at the clear wood scale (see Figure 2.6), effective failure surfaces  $F(\Sigma)$  for those unit cells can be obtained. Within the XFEM approach, loading is applied through a prescribed displacement field, fulfilling periodicity, at the boundary of the relevant unit cell. The maximum attainable reaction force at the boundary, for a certain load situation, defines the corresponding effective failure stress state  $\Sigma^{XFEM}$ . Within the upper bound LA approach, the effective strain rate tensor  $\dot{\mathbf{E}}$  in Equation (2.17) is varied and effective failure stress states  $\Sigma^{UB}$  are obtained by taking the mean value of the microscopic stresses of the optimal solution. The lower bound LA approach leads to different failure stress states  $\Sigma^{LB}$  through variation of the effective traction  $\mathbf{T}^+$  applied in Equation (2.18). Finally, using the EL approach, effective elastic limit stress states  $\Sigma^{EL}$  can easily be obtained as described in the last paragraph of Section 2.2.3.

### 2.4.1 Annual ring scale

In Figure 2.7 the effective failure surfaces obtained for earlywood in the  $R$ - $T$  plane are shown, together with selected failure modes obtained with upper bound LA and XFEM. The XFEM failure surface consists of six Tsai-Wu criteria fitted to the numerically-obtained effective stress states  $\Sigma^{XFEM}$ . The detailed procedure and definition of the failure surfaces shown here can be found in Lukacevic et al. (2014b). LA provides both lower and upper bound envelopes for the effective strength, with both surfaces based on 86 calculations<sup>2</sup>. Despite the fairly complex structural characteristics of the unit cell, the achieved bound gaps, defined as the difference between the lower and upper bounds, are very small. For the majority of the loading states this gap is less than 1.5%, and even the worst value is just 3.6%.

As would be expected according to the nature and characteristics of the various methods (see Figure 2.3), the LA results enclose the results of the XFEM approach. This difference is larger in tension-dominated regions, because there, the difference between brittle (XFEM) and ductile (LA) failure becomes obvious. Nevertheless, compared with the EL approach, the LA method seems to capture the basic failure characteristics quite well and shows a qualitatively similar effective failure behaviour to that delivered by the XFEM approach. A good agreement is also revealed by comparing the related failure modes of LA and XFEM in Figure 2.7. At this point, it is thus shown for the first time that the application of LA approaches to wood might be reasonable, and taking their great efficiency into account, even very promising. The same cannot be said of the EL

<sup>2</sup> A detailed presentation of all the LA results is beyond the scope of this paper, but is going to be provided in an additional publication.

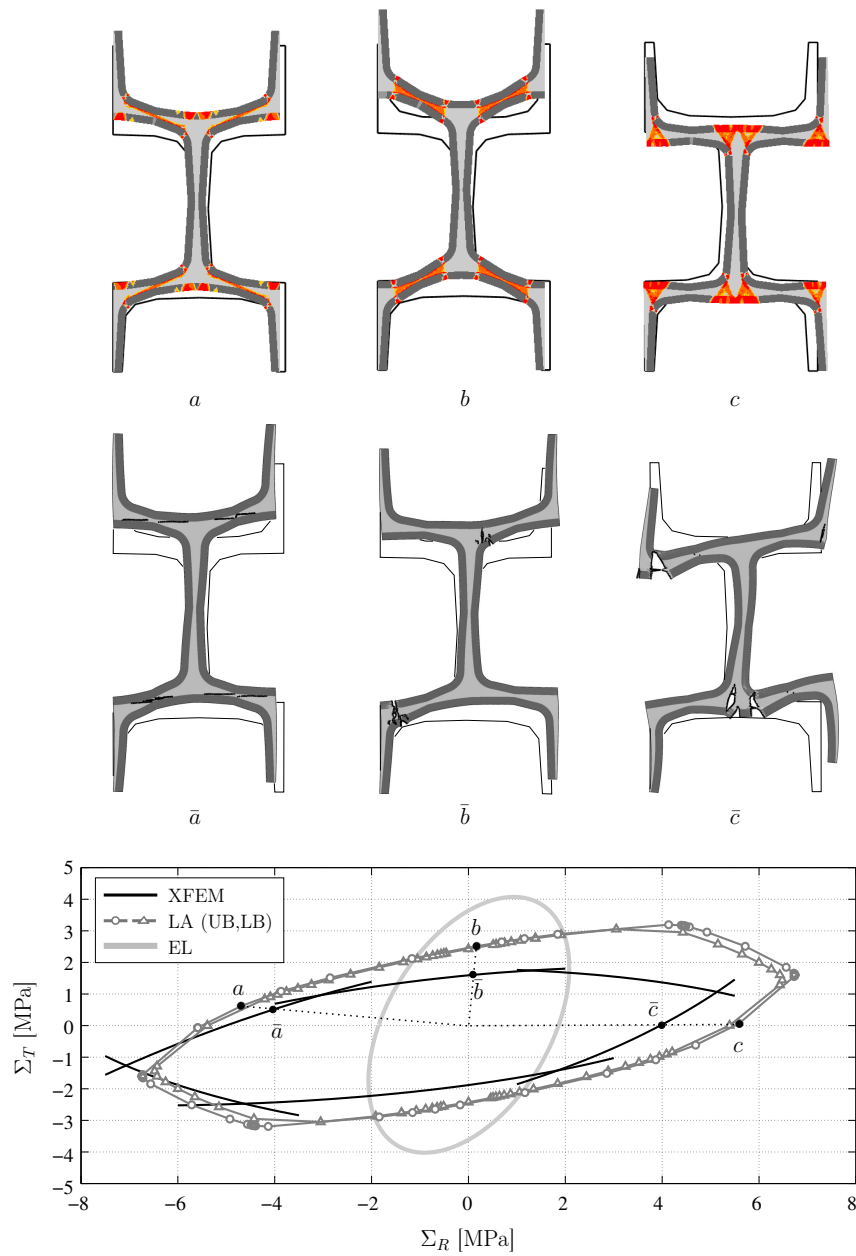


Figure 2.7: Effective failure surfaces for earlywood in the  $R$ - $T$  plane, obtained with the three different methods, and selected failure modes obtained with upper bound LA ( $a$ ,  $b$ , and  $c$ ) and XFEM ( $\bar{a}$ ,  $\bar{b}$ , and  $\bar{c}$ ).

estimates for earlywood, which differ strongly from the XFEM and LA results. The cell wall running in the  $R$ -direction is only slightly inclined, and therefore, structural failure is only achieved when the normal failure stress of the cellulosic fibre-rich S-layers (cf. Table 2.1) is exceeded, and not simply when the lignin-rich middle lamella fails. Since the EL approach used here considers lignin failure as the indication for structural failure, the elastic limit states highly underestimate the strength in the  $R$ -direction. A completely different picture emerges in the  $T$ -direction, where bending and shear loading of the cell wall is predominant, and thus, shear failure of the lignin-rich phases contributes the majority of the dissipated energy at structural failure. In this case, the quadratic strain averages, according to Equations (2.20) and (2.23), probably cannot represent the high strain concentrations at the corners of the wooden cell sufficiently, leading to an overestimation of the strength in this direction. To compensate for these weaknesses, a second effective strain indicating cellulosic fibre failure could be implemented, or higher order effective strain estimates could be envisaged.

The same procedure has been applied to the latewood unit cell, and the resulting effective failure surfaces are shown in Figure 2.8. Again, the obtained gaps between the LA lower and upper bounds are very small, giving reliable strength estimates for ductile failure. Due to the greater thickness of the latewood cell walls, a larger difference between ductile and brittle failure estimates could be expected, which is indeed reflected by comparing the effective failure surfaces obtained from LA and XFEM. Also, the related failure modes do not show such distinct correlations as for the earlywood cell. Nevertheless, the basic shape and orientation of the failure surfaces are still in good agreement. Since the overall volume of solid material in the latewood cell is significantly greater, high strain and stress concentrations in corner regions as well as the strengthening effect of cellulosic fibres play a minor role. For this reason, the effective failure surface obtained with the EL approach fits well into the overall result, predicting structural failure in between brittle and ductile failure, as its characteristics (cf. Figure 2.3) would suggest.

While the results at this observation level seem to be reliable, and give useful insights into the possibilities of the presented methods, they cannot be verified on the basis of experimental data. For this reason, the proposed methods have also been applied to the next higher observation scale, the clear wood scale, as described in Section 3.2. These results are presented in the following section.

### 2.4.2 Clear wood scale

To the knowledge of the authors, the only comprehensive experimental data set for multiaxial failure stress states of spruce wood can be found in Eberhardsteiner (2002), wherein different biaxial loading states in the  $L$ - $R$  plane were applied to clear wood samples. To utilise these experimental results, the proposed computational methods have been used to obtain effective failure surfaces  $F(\Sigma)$  for the same loading states as produced within biaxial testing. The rather complex test specimen and the load application mechanism are shown in Figure 2.9(a). Only clear wood without any growth irregularities and with linear and parallel annual rings was used for the specimens. The loading was applied under displacement control, and the biaxial strength of the sample was assumed to be reached as soon as a peak reaction force in one of the two directions could be identified. Both very brittle as well as ductile failure mechanisms



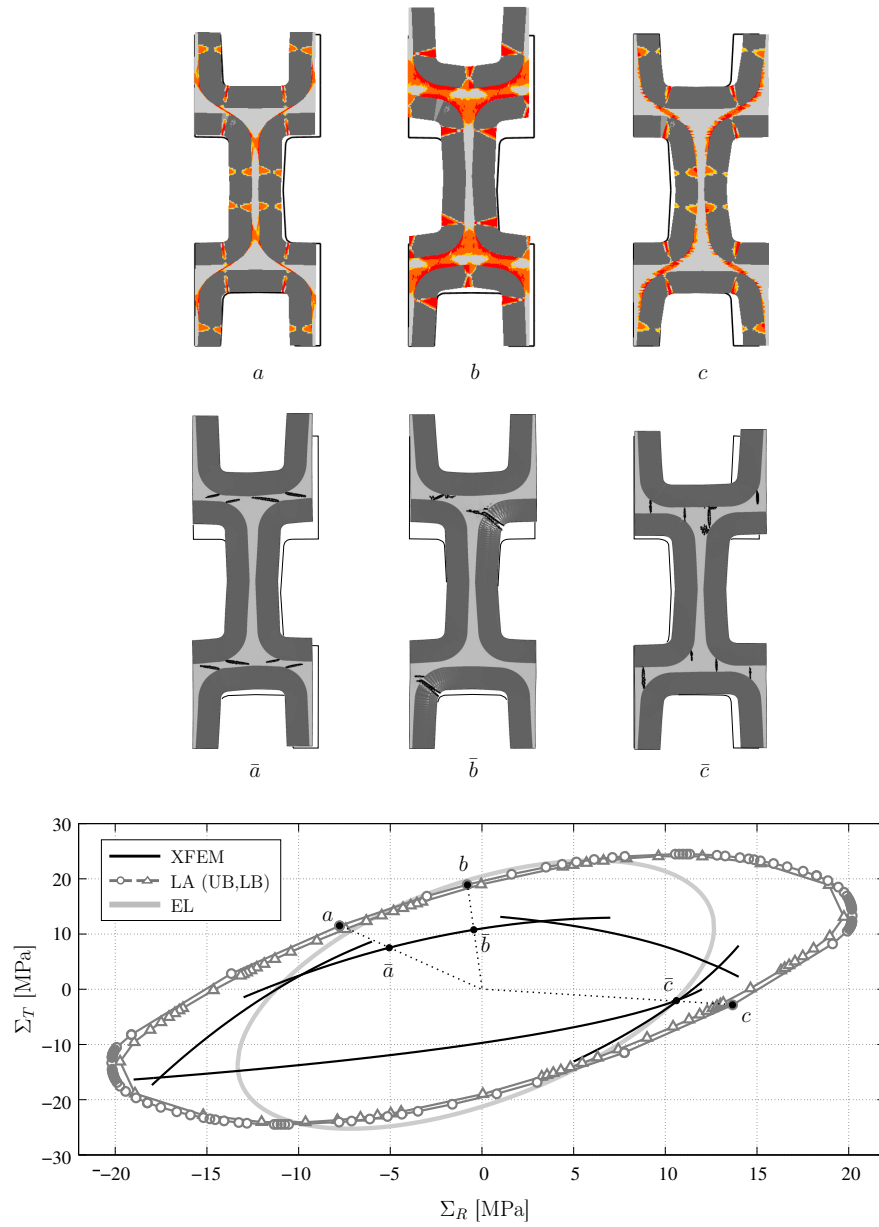


Figure 2.8: Effective failure surfaces for latewood in the  $R$ - $T$  plane, obtained with the three different methods, and selected failure modes obtained with upper bound LA ( $a$ ,  $b$ , and  $c$ ) and XFEM ( $\bar{a}$ ,  $\bar{b}$ , and  $\bar{c}$ ).

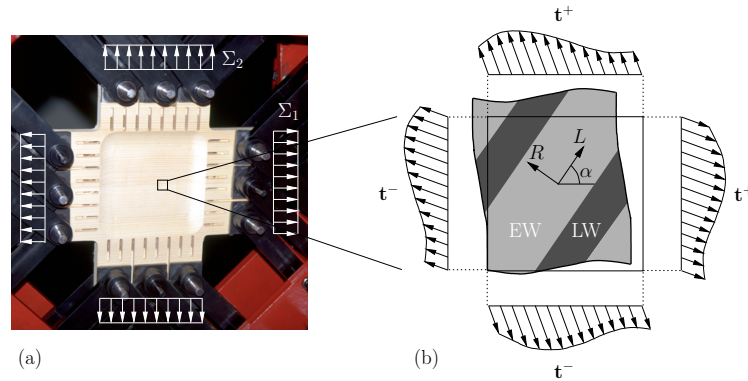


Figure 2.9: (a) Test specimen and load application mechanism for biaxial strength tests in Eberhardsteiner (2002), and (b) clear wood unit cell as used in the XFEM and LA approaches, showing layers of earlywood (EW) and latewood (LW).

were observed, but little hardening, so the experimental failure stress states plotted in Figure 2.10 (circular markers) approximately represent ultimate failure loads, regardless of their nature of failure.

The corresponding unit cell for the numerical approaches, obeying periodic boundary conditions, is schematically illustrated in Figure 2.9(b). When using the LA approach, this unit cell was discretised with about 700 triangular elements as described in Section 2.2.2, and around 800 different loading situations were applied to finally obtain the effective failure surfaces shown in Figure 2.10 (solid and dashed black lines)<sup>3</sup>. Again, the bound gap is satisfactorily small and a visually noticeable difference is only present for grain angles  $\alpha$  between  $7.5^\circ$  and  $30^\circ$ . Together with the small amount of computational effort, which was about 1 hour of computing time per failure surface on a commercial PC with four CPUs, the LA approach represents a remarkably efficient and stable tool for obtaining rigorous effective strength information (for ductile failure).

In contrast, the XFEM calculations at this observation scale have proven to be rather difficult. The homogeneous structure of the unit cell (Figure 2.9(b)) and the resulting smooth stress and strain fields make it difficult to identify a distinct point for crack initiation. Additionally, the hard boundary between earlywood and latewood can cause numerical problems, but its proper consideration is essential to obtain reasonable results. The way in which these problems can be tackled, and how 3D multi-surface failure criteria can be achieved in a similar manner to that proposed in Lukacevic et al. (2014b) for one observation scale below, will be presented in a subsequent work. The effective failure stress states obtained with XFEM shown in Figure 2.10 (bold crosses) represent selected results of this work for the considered  $L$ - $R$  space. Even if not enough results could be obtained to define clear effective failure surfaces, they allow for a qualitative comparison with the other computational methods and the experimental data.

A very satisfactory result is that all methods, without any empirical calibration, are able to predict the correct magnitude and orientation of the experimentally-obtained effective strength regions. The LA results almost perfectly form an outer envelope to these regions. Since no significant hardening effects were encountered during the

<sup>3</sup> Illustrative failure modes and a detailed presentation of all the LA results is beyond the scope of this paper, but is going to be provided in an additional publication.

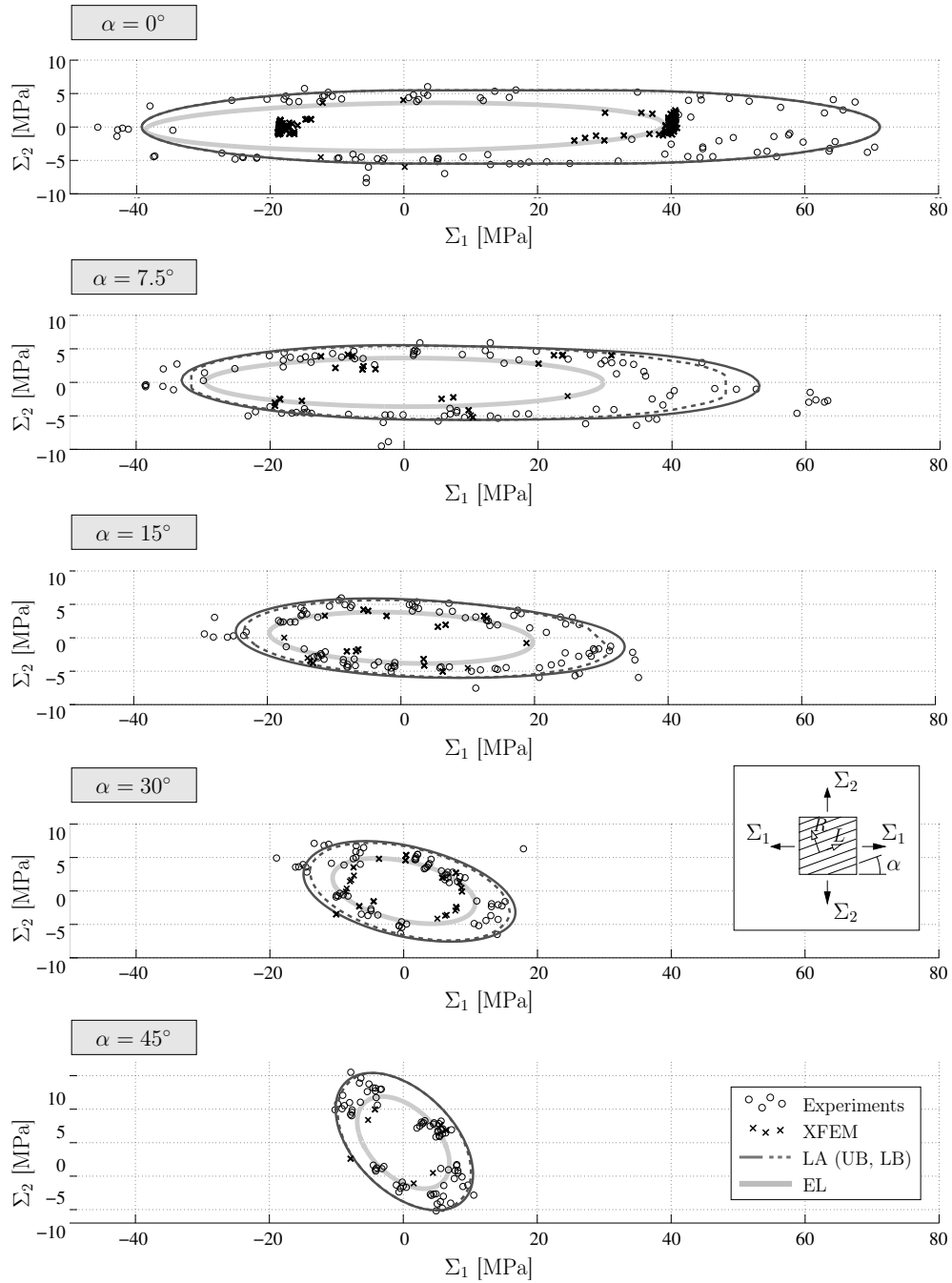


Figure 2.10: Failure stress states of clear wood in the  $L$ - $R$  plane for five different grain angles  $\alpha$ . Comparison of experimental results from Eberhardsteiner (2002) and effective failure surfaces obtained with the three different methods.

experiments, linear-elastic perfectly-plastic failure should lead to the highest effective strength, which exactly corresponds to the underlying assumptions of LA. By means of the LA results, the interpretation of the experimental results can now be extended. As it was stated before, in Section 2.2: ‘A structure does not need to exhibit perfect plasticity for the theoretical plastic collapse load based on the peak yield stress of each component to be approached closely. Rather, it is necessary that, at the point when a collapse mechanism forms under a particular loading, all those regions within the structure which are undergoing straining lie very close to the peak yield stress which they can achieve.’ This statement may help explain the large fluctuation of the experimental strength values in tension-dominated regions. Even if the structural response of wood is known to be quite brittle under tensile loading, it seems that the microstructure of wood has a high capacity to redistribute stresses before ultimate failure. For this reason, the failure loads can (and do) reach values that would be expected for purely ductile failure. This supports the previously made assumption that wood has the ductile potential to ‘activate’ the strength of many points along a potential crack surface before brittle failure occurs. To what extent this potential can be exploited depends on how homogeneous and defect-free the considered specimen is. The natural variation of such defects may then introduce the experimentally-observed scatter of effective strengths.

The effective failure stress states obtained from XFEM are in good agreement with this argument, because they tend to reproduce the lowest strengths achieved in the experiments, and also deliver a larger scatter compared with the LA results. This corresponds well to the nature of brittle failure, where complex discrete cracks trigger the failure load and slightly different crack paths can lead to significantly different effective strength estimates.

Interestingly, the EL estimates deliver a very good inner envelope of the experimental results, and justify their name at this scale of observation. Since the underlying wood unit cell is chosen according to the mean mass density of the investigated clear wood, the strong underestimation of the earlywood strength in the  $R$ -direction (see Figure 2.7) is not observed at this scale. However, it is not accounted for that failure probably occurs mainly in the earlywood, the weaker phase at the clear wood scale, which would again lead to very low strength predictions. Nevertheless, even taking into account these weaknesses, the EL approach has the potential to be an ideally complementary method to the LA approach. And as Figure 2.10 demonstrates, together they could be highly effective tools for predicting the effective strength of wood under multidimensional stress states.

## 2.5 Conclusions

To assess the predictive capabilities of material models and computational approaches is almost impossible without an appropriate set of experimental data for validation. Even then, calibration parameters may shadow potential weaknesses, or inconsistencies may be traced back to the wrong origin. This has motivated the present work, in which three different computational methods have been applied to the same problem: the prediction of effective wooden strength behaviour. An extended finite element method (XFEM) approach able to reproduce brittle failure modes accurately, a newly-developed limit analysis (LA) approach capturing ductile failure modes, and an elastic limit (EL)

approach based on continuum micromechanics, have all been applied to representative earlywood and latewood unit cells as well as clear wood structures. At both scales of observation (annual ring scale and clear wood scale) the geometric models and input parameters to all approaches have been chosen in a consistent way, to make sure that differences appearing in the results can mainly be assigned to the methods themselves.

Based on the results obtained, the three computational methods can be generally evaluated as follows:

- The XFEM approach is by far the most extensive with respect to computational effort and algorithmic implementation. This is not surprising, since this method includes the largest description flexibility, and thus has the potential to reproduce the processes in nature most realistically. It will not, however, be available for quick engineering estimates or for the build-up of material databases for wood species or products in the near future. Nevertheless, as a tool to gain knowledge of the mechanical behaviour of wood, and to serve as a reference for other wood-related models, it is of very great value.
- The LA approach has been successfully applied to wooden unit cell structures at both annual ring scale and clear wood scale. The necessary periodic boundary conditions, as well as anisotropic strength behaviour of certain material phases, were taken into account appropriately. Compared with XFEM, basic characteristics of failure modes and the overall strength behaviour could be captured correctly, both qualitatively and quantitatively. Along with the observed computational efficiency and numerical stability, these results render the LA approach as a very promising tool for this kind of application in the future.
- The continuum micromechanical basis of the EL approach makes it unbeatable with respect to efficiency and the elegance with which material properties of different phases can be linked across several scales of observation. However, when it comes to strength estimates, stress and strain averages over material phases (even if they are consistent with energy considerations) are perhaps not able to capture all failure-triggering processes. In particular, morphological aspects causing high stress or strain gradients may lead to prediction inaccuracies. Nevertheless, the potential of this method is undisputed and due to its efficiency it may become invaluable for rapid strength predictions within engineering design processes.

With respect to wood, a combination of the LA and EL approaches could evolve to an effective bundle of complementary methods, delivering ‘inner’ and ‘outer’ predictions for the natural scatter of wooden strengths. In wood products where brittle failure is prevented by reinforcements, and thus, the ductile potential of wood can be substantially activated, LA approaches may even be able to deliver reliable strength estimates on their own. Finally, reliable 2D and 3D strength information for wooden boards as well as wood-based products could be obtained in an efficient way, which would subsequently help to exploit their full potential in modern engineering structures.

Future work will be devoted to the extension of the LA approach to 3D, and its application to wooden boards and wood-based engineering products. Particularly important topics in this respect are layered wooden structures, as discussed in Gaff et al. (2015), and cross-laminated timber plates in Hochreiner et al. (2013). Preliminary 3D results

agree very well with the 2D results presented within this work, and thus strengthen the statements made. Moreover, stochastic aspects as described in Füssl et al. (2016), Kandler et al. (2015a), very relevant in layered wood-based products, will be taken into account in future works.

## **Acknowledgments**

We gratefully acknowledge the financial support of this work by the Austrian Science Fund (FWF) through the Erwin Schrödinger Fellowship J3748-N30.

Bending strength predictions of  
cross-laminated timber plates  
subjected to concentrated loading  
using 3D finite-element-based limit  
analysis approaches  
(Li et al., 2018d)

Authored by Mingjing Li, Josef Füssl, Markus Lukacevic, Chris M. Martin  
& Josef Eberhardsteiner  
Submitted to *Composite structures*

**Abstract:** Cross-laminated timber (CLT) is an innovative wood product with increasing utilisations. It is well-known that, the orthotropic and inhomogeneous strength properties of wooden boards have a strong influence on the load bearing capacity of CLT plates, especially when the complex wood fibre distribution due to randomly occurring knots is considered. Thus, high safety factors are used in current standards and a generally-accepted numerical tool for the strength prediction of CLT plates is still not available. In this paper, we combine recent advances in 3D numerical limit analysis and a knot reconstruction algorithm, where not only the bending strength of CLT plates under concentrated loading is estimated using the numerical approach, but also the scatter of strength properties resulting from the material's inhomogeneities is investigated using the stochastic approach. For the latter, data collected during the grading process of wooden boards is condensed into so-called strength profiles for single wooden boards. The limit analysis approach then allows a time efficient simulation of a large number of randomly assembled CLT plates. The comparison of the resulting strength predictions to experiments shows good agreement with respect to both the mean load bearing capacity and the statistical scatter of strength.

**Keywords:** cross-laminated timber, orthotropic and inhomogeneous strength proper-

ties, 3D limit analysis, knot reconstruction algorithm, stochastic approach, strength profiles.

### 3.1 Introduction

Wood is undergoing a revival and recapturing market shares from other building materials, reflected in an enormous growth rate of the overall volume consumption. Beside its excellent mechanical and physical properties, wood is well-known as an environmentally sustainable material with a pleasant appearance, and thus, particularly suitable for residential buildings, office buildings, school buildings, and related buildings. The main reasons for this upswing are continuous improvements in building codes throughout Europe on the one hand and the development and application of innovative wood-based products on the other hand.

One of the most aspiring products is cross-laminated timber (CLT), which is a plate-like composite consisting of an odd number of layers with wooden boards placed side-by-side in each layer and stacked crosswise. The basic idea of CLT was developed in Austria and Germany in the early 1990s. From the early 2000s, this innovative wood product has driven global interest and intensive research efforts have been carried out starting from Central Europe and spreading over the world. The utilisation of CLT panels in constructions has sharply increased during the last decade, particularly in mid-rise and high-rise buildings in both Europe and North America. This achievement can be attributed to its outstanding properties regarding in- and out-of-plane bearing capacity, degree of prefabrication, seismic performance, fire resistance, sound insulation, as well as to its environmentally sustainable characteristics (Brandner et al., 2016, Gagnon and Pirvu, 2011).

Despite the increasing demand, the current utilisation of wood-based products with respect to their mechanical properties is far away from their real potential according to Füssl et al. (2012), because dimensioning practice and many existing design rules are still based on empirical observations / background.

Regarding CLT, as reviewed by Hochreiner et al. (2013) and Brandner et al. (2016), a large number of research has been performed on a wide range of topics, but particularly for strength, those research is either limited to the evaluation of failure modes on the surface of CLT elements or only considers the mechanical behaviour within the elastic regime. For this reason, no design method for CLT has been universally accepted at this moment, which is a drawback for the ongoing CLT standardisation (Brandner et al., 2016). For example, the Eurocode 5 (EN 1995-1-1, 2003) design concept for CLT elements is based on the first violation of either bending or rolling shear strength, and the mechanical behaviour beyond the elastic regime is not considered, leaving room for a better utilisation of the material. This could be achieved by efficient and reliable computational methods, providing more information about the mechanical behaviour, especially with respect to failure mechanisms and realistic collapse loads. The main difficulty for the implementation of such computational methods for CLT is inherited from its raw material wood, which, as a typical naturally-grown material, exhibits a very complex hierarchical structure and a significant variety in macroscopic mechanical properties.

However, the application of computational methods to determine the strength of wooden



elements is a rapidly growing area of research and many contributions can be found in the near past. The first group of approaches uses the *mean stress concept*, where averaged stresses over a finite small area are assumed to indicate failure instead of the direct description of failure mechanism (Aicher et al., 2002, Masuda, 1988, Serrano and Gustafsson, 2007, Sjödin and Serrano, 2008, Sjödin et al., 2008). More sophisticated approaches are based on so-called *multi-surface plasticity/failure criteria*, where stress states leading to cracks are determined by orthotropic yield surfaces (Mackenzie-Helnwein et al., 2003, Schmidt and Kaliske, 2006). An extension of this approach is the implementation of *cohesive zone models* to simulate the crack propagation in wood (Schmidt and Kaliske, 2007, 2009). The assumption of a homogeneous fibre orientation is required for such methods, which is normally unrealistic for wood, especially in the presence of knots and other defects. Thus, in recent years, two of the authors (Lukacevic and Füssl, 2016, Lukacevic et al., 2014b, 2017) have established the basis for a crack initiation and propagation criterion in the framework of the *eXtended Finite Element Method* (XFEM). Since microscopic failure mechanisms have significant influence on the macroscopic failure behaviour of wood, in these works, the concepts of plastic failure criteria as well as crack initiation criteria were applied to several length scales to finally obtain a multi-surface failure criterion for wood at the macroscale. With such implementations, a realistic numerical description of failure mechanisms within wooden boards seems to be possible in the near future.

For CLT, because of its laminated structure with wooden lamellas exhibiting variable mechanical properties aligned in an orthogonal manner, numerical modelling becomes even more difficult. Saavedra Flores et. al introduced a promising numerical approach based on a multiscale concept using different homogenisation schemes predicting the stiffness behaviour (Hristov et al., 2017, Saavedra Flores et al., 2016b, 2015) and the rolling shear failure behaviour (Saavedra Flores et al., 2016a). However, their work mainly focuses on stiffness properties and only specific failure mechanism, rolling shear failure, has been studied, and each layer of the CLT plate is defined as homogeneous with no variations between wooden boards. To the authors' knowledge, a numerical approach regarding failure behaviour of CLT with non-homogeneous strength properties of lamellas hasn't been proposed yet.

Additionally, as stated by Hochreiner et al. (2014), the strength properties of wooden boards have a strong influence on the load bearing capacity of CLT, which has rarely been studied in previous research, neither experimentally nor numerically. The variety in mechanical properties between wooden boards can be partly attributed to the varying clear wood properties, e.g. density and moisture content, and more importantly to the presence of knots and fibre deviations around them. As stated by Johansson (2003), in most destructive bending or tension tests, failure is caused either by knots themselves or by cut fibres due to local slope of grain in their vicinities. Lukacevic and Füssl (2014) presented a physically-based structural failure criterion, where it was assumed that in wooden boards with knots, global failure can be related to a stress transfer mechanism, which is identifiable by evaluating averaged stress fields in the vicinity of knots. Complemented by a knot reconstruction algorithm (Kandler et al., 2016a, Lukacevic and Füssl, 2014, Lukacevic et al., 2015), mechanical properties can be predicted for wooden board sections containing knots by using so-called indicating properties (Lukacevic et al., 2015), which are originally used during the strength grading process of such boards. By dividing wooden boards into a reasonable number of

clear wood and knot sections, which are able to represent the distribution of mechanical properties, the global performance of wood-based products can be estimated based on a stochastic approach, as successfully implemented for stiffness estimates of glued laminated timber (GLT) beams by Kandler and Füssl (2017), Kandler et al. (2015a,b). Since the main focus of this work is on strength properties, a similar stochastic approach can be applied to estimate the load bearing capacity of CLT by using above-mentioned strength profiles of wooden boards. For this purpose, comprehensive numerical calculations are required, which must be able to consider highly orthotropic and non-linear material behaviour.

Recently, the *numerical limit analysis* has been implemented by Li et al. (2018c) for strength estimates of wood, providing promising results at different length scales and exhibiting higher time efficiency and a simpler solution procedure compared to conventional finite element based approaches according to Füssl et al. (2017). This numerical approach has been widely used as a powerful prediction tool for load bearing capacities and failure mechanisms of various structures, e.g. reinforced-concrete structures (Domenico et al., 2014), composite laminates (Limam et al., 2011, Pisano et al., 2013) and masonry structures (Milani, 2010, Milani and Burchi, 2010, Milani et al., 2010), in which calculations exhibit high time efficiency and promising performance. Considering these features, the numerical limit analysis is expected to be a suitable alternative tool to estimate the load bearing capacity, especially of CLT, where less brittle and more ductile failure mechanisms are observed in general.

Originally, the objective of limit analysis was the determination of the load bearing capacity of structures exhibiting elastoplastic material response. At collapse, the capacity of structures to store any additional external work as recoverable energy is lost and limit analysis concentrates on the critical energy dissipation rate at structural failure. The problem may be stated as follows: *Find the kinematically admissible velocity field, which minimises the external energy over the set of all statically admissible stress fields, which maximise the internal dissipated energy* according to Ciria et al. (2008). Unfortunately, the so-obtained saddle-point problem can be solved exactly only for simple geometric and loading situations, and for simple material behaviour. For more complex situations, the plastic flow compatibility in the static lower bound principle and the plastic admissibility in the kinematic upper bound principle may be relaxed, providing lower and upper bounds for the load bearing capacity (effective strength) of structures.

The first complete formulations of both lower bound and upper bound theorems were established by Drucker et al. (1951, 1952) as well as Hill (1951), and an early implementation of the finite element method and the optimisation theory into limit analysis was done by Lysmer (1970) for the lower bound problem, and by Anderheggen and Knöpfel (1972) and Maier et al. (1972) for the upper bound problem. In these works, linear three-noded triangular elements were used for discretisation and the underlying optimisation problem could be solved by linear programming, provided that the used failure criteria were linearised.

Thanks to the rapid evolution of computer technology and the development in mathematical programming, more attention has been drawn to numerical limit analysis formulations within past decades. Notable contributions with respect to the non-linear programming have been given in Krabbenhøft and Damkilde (2000), Lyamin and Sloan (2000, 2002a,b), enabling non-linear failure criteria being formulated in their native form. However, local smoothing of yield surfaces with singularities, like the Tresca or

Mohr-Coulomb criteria, were necessary.

In general, the efficiency of the numerical limit analysis method significantly depends on the algorithms for solving the associated optimisation problem. In later studies by Makrodimopoulos and Martin (2006, 2007), Ciria et al. (2008), Füssl et al. (2008), and Portioli et al. (2014), the second-order cone programming (SOCP) has been proven to be an excellent alternative method, with sufficient robustness and efficiency to solve large-scale optimisation problems of limit analysis. This method is also applicable to a large variety of failure criteria, since many commonly-used failure functions can be cast as second-order cones. Therefore, within this work, the SOCP is employed for the proposed numerical limit analysis formulations.

The main objective of this work has been to develop and apply 3D numerical limit analysis formulations to determine the bearing capacity of CLT plates (under bending) and, additionally, considering the strength property variations within wooden lamellas according to several grading classes, which in reality are caused by knots and fibre deviations. In Section 3.2, the complete 3D numerical limit analysis formulations are introduced for both the lower bound and the upper bound approaches. As a validation, these formulations are applied to CLT plate bending tests of three different grading classes to obtain strength estimates in Section 3.3.1. Then, this numerical method is combined with a stochastic approach for the CLT plate bending capacity using strength profiles in Section 3.3.2. Finally, a brief conclusion is given in Section 3.4.

## 3.2 Numerical limit analysis formulations

Limit analysis is based on a plastic bounding theorem requiring the assumptions of perfectly rigid plasticity and pure ductile failure. The main objective is to determine the collapse load multiplier  $\beta$  and corresponding failure modes for a given load situation under certain boundary conditions. The procedure can be briefly summarised as follows: Finding the statically admissible stress field maximising the external load and the kinematically admissible velocity field minimising the internal plastic energy dissipation delivers a lower bound  $\beta^{LB}$  and an upper bound  $\beta^{UB}$  of the exact collapse load multiplier  $\beta^*$ , respectively. The computational error can be easily estimated as

$$err(\%) = (\beta^{UB} - \beta^{LB}) \cdot 100 / (\beta^{UB} + \beta^{LB}) \quad (3.1)$$

In this section, both 3D lower bound and upper bound formulations are introduced in discretised form. More detailed derivations and expressions can be found in related publications from the authors (Li et al., 2018a,c).

### 3.2.1 Lower bound formulation

The lower bound optimisation problem is looking for the maximum external load while the stress field satisfies internal equilibrium, the static boundary conditions, and the plastic failure criteria. It can be formulated as

$$\begin{aligned} \beta^{LB} = \max \quad & \beta \\ \text{s.t.} \quad & \text{div} \boldsymbol{\sigma} = \mathbf{g} \quad \text{in } \Omega \\ & \boldsymbol{\sigma} \cdot \mathbf{n} = \beta \mathbf{t} \quad \text{on } \Gamma_{bc} \\ & f(\boldsymbol{\sigma}) \leq 0 \quad \text{in } \Omega \end{aligned} \quad (3.2)$$

where  $\Omega$  refers to the volume of the structure with  $\Gamma = \partial\Omega$  as the boundary surface,  $\boldsymbol{\sigma} \in \mathfrak{R}^{3 \times 3}$  represents the Cauchy stress field,  $\text{div}$  is the divergence operator for stress tensors,  $\mathbf{g} \in \mathfrak{R}^3$  is the body force field,  $\mathbf{n} \in \mathfrak{R}^3$  is the outward normal vector on the surface part  $\Gamma_{bc} \subset \Gamma$  where a boundary surface traction field  $\mathbf{t} \in \mathfrak{R}^3$  is prescribed, and  $f(\boldsymbol{\sigma}) \leq 0$  indicates the plastic yield function.

For the discretisation of this lower bound formulation, tetrahedron elements with 4 internal stress evaluation nodes (at the 4 vertices) are used. The stress field  $\boldsymbol{\sigma}$  is interpolated within each tetrahedron element using linear shape functions  $N_{\sigma}^{el,i}$ , and the nodal stress vector is expressed in Voigt notation  $\mathbf{q}_{\sigma}^{el,i} \in \mathfrak{R}^6$  ( $\forall el \in \{1, \dots, LE\}$  and  $i \in \{1, \dots, 4\}$ ) with  $LE$  as the total number of elements in the lower bound problem. In the discretised structure, the traction field  $\mathbf{t}$  is enforced to be continuous between elements, but jumps in the stress field  $\boldsymbol{\sigma}$  are allowed across element interfaces. Thus, all elements have their own internal stress evaluation nodes and, at adjacent nodes, stress evaluation nodes from different elements are allowed to share the same position.

### 3.2.1.1 Equilibrium within elements

The first constraint in Eq. (3.2) represents the internal equilibrium within each element  $el$ , which can be formulated in discretised form as

$$\sum_{i=1}^4 \mathbf{L}_{\sigma} N_{\sigma}^{el,i} \mathbf{q}_{\sigma}^{el,i} = \mathbf{q}_g^{el}, \quad \forall e \in \{1, \dots, LE\} \quad (3.3)$$

where  $\mathbf{L}_{\sigma} \in \mathfrak{R}^{3 \times 6}$  represents the divergence operator for the stress vector in Voigt notation and  $\mathbf{q}_g^{el} \in \mathfrak{R}^3$  denotes the elemental body force vector.

### 3.2.1.2 Equilibrium between elements

To enforce continuity of the traction field between elements the following additional constraint is applied:

$$\mathbf{L}_t^{de} \mathbf{q}_{\sigma}^{de,i} - \mathbf{L}_t^{de} \mathbf{q}_{\sigma}^{de,i'} = \mathbf{0}, \quad \forall de \in \{1, \dots, LDE\} \text{ and } i \in \{1, \dots, 3\} \quad (3.4)$$

where  $\mathbf{q}_{\sigma}^{de,i} \in \mathfrak{R}^6$  is the nodal stress vector for each pair of the 3-noded triangular interfaces  $de$ , with  $i$  and  $i'$  indicating the nodal pairs.  $LDE$  is the total number of element interfaces in the lower bound problem and  $\mathbf{L}_t^{de} \in \mathfrak{R}^{3 \times 6}$  represents the stress-traction operator based on the normal vector  $\mathbf{n}^{de} \in \mathfrak{R}^3$  for each element interface  $de$ , pointing from the node  $i$  to the node  $i'$ .

### 3.2.1.3 Static boundary conditions

The traction field on the boundary surface part  $\Gamma_{bc}$  is prescribed through the second constraint in the optimisation problem Eq. (3.2). In the discretised form this constraint is applied to the triangular boundary surfaces, denoted as  $be$ , on  $\Gamma_{bc}$ , reading

$$\mathbf{L}_t^{be} \mathbf{q}_{\sigma}^{be,i} = \beta \mathbf{q}_t^{be,i}, \quad \forall be \in \{1, \dots, LBE\} \text{ and } i \in \{1, \dots, 3\} \quad (3.5)$$

where  $LBE$  is the total number of triangular surfaces on  $\Gamma_{bc}$ ,  $\mathbf{q}_{\sigma}^{be,i}$  is the nodal stress vector of the triangular surface,  $\mathbf{q}_t^{be,i}$  is the surface traction vector, and  $\mathbf{L}_t^{be}$  is the

stress-traction operator for each boundary element based on the corresponding outward normal vector  $\mathbf{n}^{be}$  on  $\Gamma_{bc}^{be} \subset \Gamma_{bc}$ .

### 3.2.1.4 Plastic failure criteria

In the lower bound formulation, the plastic failure criteria are applied at each stress evaluation node to determine the plastic failure state. In this work, the yield function is expressed in a general form as

$$\begin{aligned} \mathbf{q}_{\sigma,loc}^{el,i} &= \mathbf{R}_{\sigma}^{el} \mathbf{q}_{\sigma}^{el,i} \\ f(\mathbf{q}_{\sigma,loc}^{el,i}, k_{\sigma}^{el}) &= \mathbf{q}_{\sigma,loc}^{el,i \top} \mathbf{P}_{\sigma}^{el} \mathbf{q}_{\sigma,loc}^{el,i} + \mathbf{F}_{\sigma}^{el \top} \mathbf{q}_{\sigma,loc}^{el,i} - 1 \leq 0 \\ &, \quad \forall el \in \{1, \dots, LE\} \text{ and } i \in \{1, \dots, 4\} \end{aligned} \quad (3.6)$$

where  $\mathbf{q}_{\sigma,loc}^{el,i} \in \mathfrak{R}^6$  is the nodal local stress vector with respect to the principal material orientation in the element  $el$ ,  $\mathbf{R}_{\sigma}^{el} \in \mathfrak{R}^{6 \times 6}$  is the transformation matrix for stress vectors from the global coordinate basis  $(x - y - z)$  into the material local coordinate basis  $(x' - y' - z')_{mat}^{el}$  for each element. The matrices  $\mathbf{P}_{\sigma}^{el} \in \mathfrak{R}^{6 \times 6}$  and  $\mathbf{F}_{\sigma}^{el} \in \mathfrak{R}^6$  are determined by the type of yield function and the material strength parameters applied to the element  $el$ .

As shown in Eq. (3.2), the nonlinearity of the lower bound optimisation problem is attributed to the nonlinear yield function  $f(\boldsymbol{\sigma}) \leq 0$ . Thus, this nonlinear optimisation problem can be solved efficiently using second-order cone programming (SOCP) as long as the yield function Eq. (3.6) can be formulated as a second-order cone (SOC) constraint, reading

$$\begin{aligned} \mathbf{s}_{\sigma}^{el,i} &= \mathbf{a}_{\sigma}^{el} + \mathbf{B}_{\sigma}^{el} \mathbf{R}_{\sigma}^{el} \mathbf{q}_{\sigma}^{el,i} \\ &, \quad \forall el \in \{1, \dots, LE\} \text{ and } i \in \{1, \dots, 4\} \\ \mathbf{s}_{\sigma}^{el,i} &\in \mathcal{C} \end{aligned} \quad (3.7)$$

where  $\mathbf{s}_{\sigma}^{el,i} \in \mathfrak{R}^8$  represents the SOC expression of the yield function.  $\mathbf{a}_{\sigma}^{el} \in \mathfrak{R}^8$  and  $\mathbf{B}_{\sigma}^{el} \in \mathfrak{R}^{8 \times 6}$  are determined from  $\mathbf{P}_{\sigma}^{el}$  and  $\mathbf{F}_{\sigma}^{el}$ .

### 3.2.1.5 Discretised lower bound optimisation problem

Assembling above constraints, the lower bound optimisation problem Eq. (3.2) can be written in discretised form as

$$\begin{aligned} \beta^{LB} &= \max \quad \beta \\ \text{s.t.} \quad &\mathbf{A}_{\sigma}^{mat} \mathbf{q}_{\sigma} = \mathbf{q}_g \\ &\mathbf{A}_t^{dis} \mathbf{q}_{\sigma} = \mathbf{0} \\ &\mathbf{A}_t^{bc} \mathbf{q}_{\sigma} = \beta \mathbf{q}_t \\ &\mathbf{s}_{\sigma} = \mathbf{a}_{\sigma} + \mathbf{B}_{\sigma} \mathbf{R}_{\sigma} \mathbf{q}_{\sigma} \\ &\mathbf{s}_{\sigma} \in \mathcal{C} \end{aligned} \quad (3.8)$$

where  $\mathbf{q}_\sigma \in \mathfrak{R}^{24LE}$  contains all nodal stress vectors throughout the whole structure,  $\mathbf{q}_g \in \mathfrak{R}^{3LE}$  is the assembled body force vector for all elements,  $\mathbf{q}_t \in \mathfrak{R}^{9LBE}$  is the assembled boundary traction vector,  $\mathbf{s}_\sigma \in \mathfrak{R}^{32LE}$  is the assembled vector for SOC expressions of yield functions at all stress evaluation nodes,  $\mathbf{a}_\sigma \in \mathfrak{R}^{32LE}$  and  $\mathbf{B}_\sigma \in \mathfrak{R}^{32LE \times 24LE}$  are assembled matrices containing material strength parameters from Eq. (3.7).  $\mathbf{A}_\sigma^{mat} \in \mathfrak{R}^{3LE \times 24LE}$ ,  $\mathbf{A}_t^{dis} \in \mathfrak{R}^{9LDE \times 24LE}$ ,  $\mathbf{A}_t^{bc} \in \mathfrak{R}^{9LBE \times 24LE}$  and  $\mathbf{R}_\sigma \in \mathfrak{R}^{24LE \times 24LE}$  are assembled throughout the whole structure from Eqs. (3.3), (3.4), (3.5) and (3.7), respectively.

### 3.2.2 Upper bound formulation

Based on the theorem, the objective of upper bound calculations is looking for the failure mechanism for which the corresponding kinematically admissible velocity field  $\dot{\mathbf{u}} \in \mathfrak{R}^3$  leads to the lowest internal energy dissipation rate  $W_{int}$ .

In this work, as is introduced in Li et al. (2018a,b), velocity jumps  $\Delta \dot{\mathbf{u}} \in \mathfrak{R}^3$  are allowed only across prescribed discontinuities  $\Gamma_{dis}$ , consisting of a surface  $\Gamma_{dis}^+$  with the related velocity field  $\dot{\mathbf{u}}_{dis}^+$  and a surface  $\Gamma_{dis}^-$  with the related velocity field  $\dot{\mathbf{u}}_{dis}^-$ . Such velocity jumps  $\Delta \dot{\mathbf{u}} = (\dot{\mathbf{u}}_{dis}^+ - \dot{\mathbf{u}}_{dis}^-)$  represent additional degrees of freedom for the plastic flow, locally at  $\Gamma_{dis}$ . Then, the internal energy dissipation rate  $W_{int}$  is composed of the plastic energy dissipation rate in the continuum body  $\Omega$  and the dissipation rate due to interface failure across the prescribed discontinuities  $\Gamma_{dis}$ , giving

$$W_{int} = \int_{\Omega} d_p^{mat}(\dot{\boldsymbol{\varepsilon}})dV + \int_{\Gamma_{dis}} d_p^{dis}(\dot{\boldsymbol{\mu}})dA \quad (3.9)$$

with the plastic dissipation functions as

$$\begin{aligned} d_p^{mat} &= \sup_{\boldsymbol{\sigma} \in \mathcal{F}} \boldsymbol{\sigma}^\top \dot{\boldsymbol{\varepsilon}}, \quad \mathcal{F} = \{\boldsymbol{\sigma} | f(\boldsymbol{\sigma}) \leq 0\} \quad \text{in } \Omega \\ d_p^{dis} &= \sup_{\mathbf{t} \in \mathcal{D}} \mathbf{t}^\top \dot{\boldsymbol{\mu}}, \quad \mathcal{D} = \{\mathbf{t} | f(\mathbf{t}) \leq 0\} \quad \text{on } \Gamma_{dis} \end{aligned} \quad (3.10)$$

where  $\dot{\boldsymbol{\mu}} \in \mathfrak{R}^3$  is the local plastic flow related to the velocity-jump field  $\Delta \dot{\mathbf{u}}$  at  $\Gamma_{dis}$ ,  $f(\boldsymbol{\sigma}) \leq 0$  and  $f(\mathbf{t}) \leq 0$  are the stress-based yield function for  $\Omega$  and the traction-based yield function for  $\Gamma_{dis}$ , respectively.

Then, the primal upper bound optimisation problem can be formulated as

$$\begin{aligned} \min \quad & W_{int} \\ \text{s.t.} \quad & \dot{\boldsymbol{\varepsilon}} = \mathbf{L}_{\dot{\mathbf{u}}} \dot{\mathbf{u}} \quad \text{in } \Omega \\ & \dot{\mathbf{u}} = \dot{\mathbf{u}}_{bc} \quad \text{on } \Gamma_{bc} \\ & \dot{\boldsymbol{\varepsilon}} = \dot{\lambda}_\sigma \partial f(\boldsymbol{\sigma}) / \partial \boldsymbol{\sigma} \quad \text{in } \Omega \\ & \dot{\boldsymbol{\mu}} = \dot{\lambda}_t \partial f(\mathbf{t}) / \partial \mathbf{t} \quad \text{on } \Gamma_{dis} \end{aligned} \quad (3.11)$$

in which the four constraints are related to compatibility, kinematic boundary conditions, and associated plastic flow both in  $\Omega$  as well as at  $\Gamma_{dis}$ . In the first constraint,  $\mathbf{L}_{\dot{\mathbf{u}}} \in \mathfrak{R}^{6 \times 3}$  denotes the linear compatibility operator mapping the velocity field  $\dot{\mathbf{u}}$  onto the strain-rate field  $\dot{\boldsymbol{\varepsilon}}$ . In the second constraint,  $\dot{\mathbf{u}}_{bc}$  refers to the prescribed velocity boundary conditions at the boundary surface part  $\Gamma_{bc} \subset \Gamma$ . In the last two constraints,

$\dot{\lambda}_\sigma$  and  $\dot{\lambda}_t$  are the plastic multipliers determining the magnitude of plastic flow within the continuum material  $\Omega$  and at the prescribed velocity discontinuity  $\Gamma_{dis}$ , respectively. The upper bound optimisation problem in Eq. (3.11) can also be formulated in a, mathematically equivalent, dual form, in which the objective function becomes the external work rate  $W_{ext}$ , reading

$$W_{ext} = \int_{\Omega} \dot{\mathbf{u}}^\top \mathbf{g}_0 dV + \int_{\Gamma_{bc}} \dot{\mathbf{u}}^\top \beta \mathbf{t}_{bc} dA \quad (3.12)$$

consisting of the work done by a constant body force field  $\mathbf{g}_0$  in  $\Omega$  and the boundary surface traction field  $\mathbf{t}_{bc}$  on  $\Gamma_{bc}$ . The complete dual upper bound problem can then be formulated as follows

$$\begin{aligned} \max \quad & W_{ext} \\ \text{s.t.} \quad & \int_{\Omega} \dot{\boldsymbol{\varepsilon}}^\top \boldsymbol{\sigma} dV + \int_{\Gamma_{dis}} \dot{\boldsymbol{\mu}}^\top \mathbf{t} dA = \int_{\Omega} \dot{\mathbf{u}}^\top \mathbf{g}_0 dV + \int_{\Gamma_{bc}} \dot{\mathbf{u}}^\top \beta \mathbf{t}_{bc} dA & \text{in } \Omega \\ & f(\boldsymbol{\sigma}) \leq 0 & \text{in } \Omega \\ & f(\mathbf{t}) \leq 0 & \text{on } \Gamma_{dis} \end{aligned} \quad (3.13)$$

where the first constraint refers to the weak form of equilibrium, related to Eq. (3.9) and Eq. (3.12), the second and the third constraints represent the stress-based and traction-based yield functions for the continuum material  $\Omega$  and the velocity discontinuities  $\Gamma_{dis}$ , respectively.

In the following, only this dual optimisation problem is discretised and solved, but complete expressions of discretised primal and dual upper bound formulations can be found in Li et al. (2018a,b). For the discretisation linear strain tetrahedron elements are used with 10 velocity evaluation nodes (4 vertice and 6 middle nodes) and 4 strain-rate evaluation nodes (at the 4 vertices). The velocity field  $\dot{\mathbf{u}}$  is approximated using 3D quadratic shape functions  $N_{\dot{\mathbf{u}}}^{el,i}$  for interpolation between the nodal velocities  $\mathbf{q}_{\dot{\mathbf{u}}}^{el,i} \in \mathfrak{R}^3$  ( $\forall el \in \{1, \dots, UE\}$  and  $i \in \{1, \dots, 10\}$ ) with  $UE$  as the total number of elements; the strain-rate field  $\dot{\boldsymbol{\varepsilon}}$  is approximated using 3D linear shape functions  $N_{\dot{\boldsymbol{\varepsilon}}}^{el,j}$  for the interpolation between the nodal strain-rate vectors  $\mathbf{q}_{\dot{\boldsymbol{\varepsilon}}}^{el,i} \in \mathfrak{R}^6$  ( $\forall el \in \{1, \dots, UE\}$  and  $j \in \{1, \dots, 4\}$ ).

On the boundary surface part  $\Gamma_{bc}$ , each boundary surface element  $be$  contains 6 velocity evaluation nodes (3 vertice and 3 middle nodes). The velocity field  $\dot{\mathbf{u}}$  is approximated using 2D quadratic shape functions  $\bar{N}_{\dot{\mathbf{u}}}^{be,i}$  for interpolation between the nodal velocity vectors  $\mathbf{q}_{\dot{\mathbf{u}}}^{be,i} \in \mathfrak{R}^3$  ( $\forall be \in \{1, \dots, UBE\}$  and  $i \in \{1, \dots, 6\}$ ) within  $\Gamma_{bc}^{be} \subset \Gamma_{bc}$ , where  $UBE$  is the total number of 6-noded boundary elements on  $\Gamma_{bc}$ .

In the discretised upper bound formulation, the strain-rate field  $\dot{\boldsymbol{\varepsilon}}$  varies linearly within each element and is allowed to be discontinuous between elements; velocity jumps  $\Delta \dot{\mathbf{u}}$  are allowed only across prescribed velocity discontinuities  $\Gamma_{dis}$ .

At  $\Gamma_{dis}$ , each triangular discontinuity element  $de$  contains 6 velocity evaluation nodes (3 vertice and 3 middle nodes), where 2D quadratic shape functions  $\bar{N}_{\dot{\mathbf{u}}}^{de,i}$  are used to interpolate between 6 pairs of nodal velocity vectors  $\mathbf{q}_{\dot{\mathbf{u}}}^{de+,j}$  and  $\mathbf{q}_{\dot{\mathbf{u}}}^{de-,j}$  ( $\forall de \in \{1, \dots, UDE\}$  and  $i \in \{1, \dots, 6\}$ ) with  $UDE$  as the total number of discontinuity elements on  $\Gamma_{dis}$ . To guarantee consistence of plastic flow throughout the whole structure, it is straightforward to enforce the localised plastic flow  $\dot{\boldsymbol{\mu}}$  to be linear at each discontinuity element  $\Gamma_{dis}^{de} \subset \Gamma_{de}$ , where 3 internal evaluation nodes (at the 3 vertices) are used

to interpolate the localised plastic flow  $\dot{\boldsymbol{\mu}}$  using 2D linear shape functions  $\bar{N}_{\dot{\boldsymbol{\mu}}}^{de,i}$  to interpolate between the nodal plastic flow vectors  $\mathbf{q}_{\dot{\boldsymbol{\mu}}}^{de,j} \in \mathfrak{R}^3$  ( $\forall de \in \{1, \dots, UDE\}$  and  $j \in \{1, \dots, 3\}$ ).

### 3.2.2.1 Weak equilibrium

Strictly speaking, as stated by Makrodimopoulos (2010), the upper bound problem is based on the kinematic theorem, in which only the velocity field  $\dot{\mathbf{u}}$  and the strain-rate field  $\dot{\boldsymbol{\varepsilon}}$  are to be considered. Thus, the forces appearing in the upper bound formulations, partly due to exploiting duality, not necessarily represent physically accurate interpretable quantities. They can rather be interpreted as stress-like quantities  $\hat{\boldsymbol{\sigma}}^{el}$  and traction-like quantities  $\hat{\mathbf{t}}^{de}$ , defined as follows

$$\hat{\boldsymbol{\sigma}}^{el} = \sum_{i=1}^4 \frac{\int_{\Omega^{el}} N_{\dot{\boldsymbol{\varepsilon}}}^{el,i} \boldsymbol{\sigma} dV}{\int_{\Omega^{el}} N_{\dot{\boldsymbol{\varepsilon}}}^{el,i} dV}, \quad \forall el \in \{1, \dots, UE\} \quad (3.14a)$$

$$\hat{\mathbf{t}}^{de} = \sum_{j=1}^3 \frac{\int_{\Gamma_{dis}^{de}} \bar{N}_{\dot{\boldsymbol{\mu}}}^{de,j} \mathbf{t} dA}{\int_{\Gamma_{dis}^{de}} \bar{N}_{\dot{\boldsymbol{\mu}}}^{de,j} dA}, \quad \forall de \in \{1, \dots, UDE\} \quad (3.14b)$$

where both evaluation nodes and shape functions are shared with the strain-rate field  $\dot{\boldsymbol{\varepsilon}}$  in each solid element  $\Omega^{el} \subset \Omega$  and the localised plastic flow  $\dot{\boldsymbol{\mu}}$  at each discontinuity element  $\Gamma_{dis}^{de}$ , respectively.

The internal energy dissipation rate Eq. (3.9), consisting of the plastic dissipation in both the material as well as at the interface, can then be discretised as follows

$$\begin{aligned} W_{int} &= \sum_{el=1}^{UE} \int_{\Omega^{el}} \dot{\boldsymbol{\varepsilon}}^{\top} \hat{\boldsymbol{\sigma}}^{el} dV + \sum_{de=1}^{UDE} \int_{\Gamma_{dis}^{de}} \dot{\boldsymbol{\mu}}^{\top} \hat{\mathbf{t}}^{de} dA \\ &= \sum_{el=1}^{UE} \sum_{i=1}^4 \sum_{j=1}^4 \mathbf{q}_{\dot{\boldsymbol{\varepsilon}}}^{el,i\top} \hat{\mathbf{q}}_{\boldsymbol{\sigma}}^{el,j} \int_{\Omega^{el}} N_{\dot{\boldsymbol{\varepsilon}}}^{el,i} N_{\dot{\boldsymbol{\varepsilon}}}^{el,j} dV + \sum_{de=1}^{UDE} \sum_{k=1}^3 \sum_{l=1}^3 \mathbf{q}_{\dot{\boldsymbol{\mu}}}^{de,k\top} \hat{\mathbf{q}}_t^{de,l} \int_{\Gamma_{dis}^{de}} \bar{N}_{\dot{\boldsymbol{\mu}}}^{de,k} \bar{N}_{\dot{\boldsymbol{\mu}}}^{de,l} dV \end{aligned} \quad (3.15)$$

where  $\hat{\mathbf{q}}_{\boldsymbol{\sigma}}^{el,i} \in \mathfrak{R}^6$  denotes the nodal stress-like vector in  $\Omega^{el}$  and  $\hat{\mathbf{q}}_t^{de,i} \in \mathfrak{R}^3$  the nodal traction-like vector at  $\Gamma_{dis}^{de}$ .

The compatibility constraint for each solid element in  $\Omega^{el}$  in discretised form reads

$$\sum_{i=1}^4 \mathbf{N}_{\dot{\boldsymbol{\varepsilon}}}^{el,i} \mathbf{q}_{\dot{\boldsymbol{\varepsilon}}}^{el,i} = \mathbf{L}_{\dot{\mathbf{u}}} \sum_{j=1}^{10} \mathbf{N}_{\dot{\mathbf{u}}}^{el,j} \mathbf{q}_{\dot{\mathbf{u}}}^{el,j}, \quad \forall el \in \{1, \dots, UE\} \quad (3.16)$$

indicating the relation between the nodal strain-rate vectors  $\mathbf{q}_{\dot{\boldsymbol{\varepsilon}}}^{el,i}$  and the nodal velocity vectors  $\mathbf{q}_{\dot{\mathbf{u}}}^{el,j}$ ; the compatibility constraint for each discontinuity element at  $\Gamma_{dis}^{de}$  reads

$$\sum_{i=1}^3 \mathbf{q}_{\dot{\boldsymbol{\mu}}}^{de,i} = \sum_{j=1}^6 (\mathbf{q}_{\dot{\mathbf{u}}}^{de+,j} - \mathbf{q}_{\dot{\mathbf{u}}}^{de-,j}), \quad \forall de \in \{1, \dots, UDE\} \quad (3.17)$$

indicating the relation between the nodal localised plastic flow vector  $\mathbf{q}_{\dot{\boldsymbol{\mu}}}^{de,i}$  and the pairs of nodal velocity vectors  $\mathbf{q}_{\dot{\mathbf{u}}}^{de+,j}$  and  $\mathbf{q}_{\dot{\mathbf{u}}}^{de-,j}$ .



In this work, the body force is not considered, giving  $\mathbf{g} = \mathbf{0}$ . According to Eq. (3.12), the discretised form of the external work rate can then be expressed as

$$\begin{aligned} W_{ext} &= \sum_{be=1}^{UBE} \int_{\Gamma_{bc}^{be}} \dot{\mathbf{u}}^\top \beta \mathbf{t}_{bc} dA \\ &= \sum_{be=1}^{UBE} \sum_{i=1}^6 \sum_{j=1}^{n_t} \beta \mathbf{q}_i^{be,i\top} \mathbf{q}_{t_{bc}}^{be,j} \int_{\Gamma_{bc}^{be}} \bar{N}_{\dot{u}}^{be,i} \bar{N}_{t_{bc}}^{be,j} dA \end{aligned} \quad (3.18)$$

where the nodal traction vectors  $\mathbf{q}_{t_{bc}}^{be,i}$  are prescribed at  $n_t$  evaluation nodes at each boundary surface element on  $\Gamma_{bc}^{be}$ , interpolated by the 2D shape functions  $\bar{N}_{t_{bc}}^{be,j}$  for the traction field  $\mathbf{t}_{bc}$ . Note that, since the boundary traction field  $\mathbf{t}_{bc}$  is prescribed directly to each evaluation node on  $\Gamma_p$ ,  $\mathbf{q}_{t_{bc}}^{be,i}$  can be expressed directly in the exact form.

### 3.2.2.2 Plastic yield function

The dual upper bound problem Eq. (3.13) consists of the stress-based yield functions  $f(\boldsymbol{\sigma}) \leq 0$  for the continuum material  $\Omega$  and the traction-based yield functions  $f(\mathbf{t}) \leq 0$  for the prescribed velocity discontinuities  $\Gamma_{dis}$ . In order to guarantee consistent strength behaviour throughout the whole structure, an algorithm has been introduced by the authors to project the stress-based yield function  $f(\boldsymbol{\sigma}) \leq 0$  onto a locally equivalent traction-based yield function  $f(\mathbf{t}) \leq 0$  with respect to  $\Gamma_{dis}$  (Li et al., 2018a,b).

Since both the stress-like quantities  $\hat{\boldsymbol{\sigma}}^{el}$  and the traction-like quantities  $\hat{\mathbf{t}}^{de}$  are interpolated linearly within corresponding elements, it is sufficient to evaluate yield functions only at vertices of the elements. As introduced in Eq. (3.7), both yield functions can be formulated in SOC form, giving

$$\hat{\mathbf{s}}_\sigma^{el,i} = \hat{\mathbf{a}}_\sigma^{el} + \hat{\mathbf{B}}_\sigma^{el} \mathbf{R}_\sigma^{el} \hat{\mathbf{q}}_\sigma^{el,i}, \quad \forall el \in \{1, \dots, UE\} \text{ and } i \in \{1, \dots, 4\} \quad (3.19a)$$

$$\hat{\mathbf{s}}_\sigma^{el,i} \in \mathcal{C}$$

$$\hat{\mathbf{s}}_t^{de,j} = \hat{\mathbf{a}}_t^{de} + \hat{\mathbf{B}}_t^{de} \mathbf{R}_t^{de} \hat{\mathbf{q}}_t^{de,j}, \quad \forall de \in \{1, \dots, UDE\} \text{ and } j \in \{1, \dots, 3\} \quad (3.19b)$$

$$\hat{\mathbf{s}}_t^{de,j} \in \mathcal{C}$$

where  $\mathbf{R}_t^{de}$  represents the transformation matrix for traction vectors from the global coordinate basis  $(x - y - z)$  to the local coordinate basis  $(x' - y' - z')^{de}_{dis}$  for velocity discontinuities,  $\hat{\mathbf{s}}_\sigma^{el,i} \in \mathfrak{R}^8$  and  $\hat{\mathbf{s}}_t^{de,j} \in \mathfrak{R}^5$  are the SOC expressions of the yield functions,  $\hat{\mathbf{a}}_\sigma^{el,i} \in \mathfrak{R}^8$ ,  $\hat{\mathbf{B}}_\sigma^{el,i} \in \mathfrak{R}^{8 \times 6}$  and  $\hat{\mathbf{a}}_t^{de,j} \in \mathfrak{R}^5$ ,  $\hat{\mathbf{B}}_t^{de,j} \in \mathfrak{R}^{5 \times 3}$  contain material strength parameters. In Eq. (3.19), the yield functions are formulated in terms of the weighted averaged expressions according to Eq. (3.14). As stated by Makrodimopoulos (2010), only when the material strength properties are constant within each element, the weighted averaged quantities equal the exact nodal quantities and all hat symbols can be ignored in Eqs. (3.15), (3.14) and (3.19).

### 3.2.2.3 Assembly

Finally, the discretised formulation of the dual upper bound optimisation problem, Eq. (3.13), can be formulated as

$$\begin{aligned}
& \max W_{ext} \\
& \text{s.t.} \quad \mathbf{A}_{UB}^{mat\top} \hat{\mathbf{q}}_\sigma^{mat} + \mathbf{A}_{UB}^{dis} \hat{\mathbf{q}}_t^{dis} = \beta \mathbf{A}_{UB}^{bc} \mathbf{q}_t^{bc} \\
& \quad \hat{\mathbf{s}}_\sigma^{mat} = \hat{\mathbf{a}}_\sigma^{mat} + \hat{\mathbf{B}}_\sigma^{mat} \mathbf{R}_\sigma^{mat} \hat{\mathbf{q}}_\sigma^{mat} \\
& \quad \hat{\mathbf{s}}_\sigma^{mat} \in \mathcal{C} \\
& \quad \hat{\mathbf{s}}_t^{dis} = \hat{\mathbf{a}}_t^{dis} + \hat{\mathbf{B}}_t^{dis} \mathbf{R}_t^{dis} \hat{\mathbf{q}}_t^{dis} \\
& \quad \hat{\mathbf{s}}_t^{dis} \in \mathcal{C}
\end{aligned} \tag{3.20}$$

where  $\mathbf{A}_{UB}^{mat} \in \mathfrak{R}^{3UN \times 24UE}$  and  $\mathbf{A}_{UB}^{dis} \in \mathfrak{R}^{3UN \times 9UD}$  are assembled from Eqs. (3.15), (3.16) and (3.17) with  $UN$  as the total number of velocity evaluation nodes;  $\mathbf{q}_t^{bc} \in \mathfrak{R}^{3UN}$  and  $\mathbf{A}_{UB}^{bc} \in \mathfrak{R}^{3UN \times 3n_t UBC}$  are assembled from Eq. (3.18);  $\hat{\mathbf{s}}_\sigma^{mat} \in \mathfrak{R}^{32UE}$ ,  $\hat{\mathbf{a}}_\sigma^{mat} \in \mathfrak{R}^{32UE}$ ,  $\hat{\mathbf{B}}_\sigma^{mat} \in \mathfrak{R}^{32UE \times 24UE}$ ,  $\mathbf{R}_\sigma^{mat} \in \mathfrak{R}^{24UE \times 24UE}$  and  $\hat{\mathbf{s}}_t^{dis} \in \mathfrak{R}^{15UD}$ ,  $\hat{\mathbf{a}}_t^{dis} \in \mathfrak{R}^{15UD}$ ,  $\hat{\mathbf{B}}_t^{dis} \in \mathfrak{R}^{15UD \times 9UD}$ ,  $\mathbf{R}_t^{dis} \in \mathfrak{R}^{9UD \times 9UD}$  are assembled from Eq. (3.19);  $\hat{\mathbf{q}}_\sigma^{mat} \in \mathfrak{R}^{24UE}$  and  $\hat{\mathbf{q}}_t^{dis} \in \mathfrak{R}^{9UD}$  are the assembly of weighted average vectors for nodal stress vectors in  $\Omega$  and nodal traction vectors on  $\Gamma_{dis}$ , respectively.

## 3.3 Application to CLT plates

In this section, the proposed numerical limit analysis formulations are applied to estimate the bending bearing capacities of CLT plates. The CLT plates are implemented as layer laminated structures consisting of wooden boards aligned parallelly in each layer and perpendicularly over adjacent layers. For each wooden board, anisotropic failure behaviour is considered using the Tsai-Wu failure criterion. All CLT plates are discretised by above-mentioned tetrahedron elements. Strength parameters are prescribed for each element, by which, the distribution of strength properties along wooden boards can be considered easily by prescribed strength profiles.

### 3.3.1 CLT plate bending test

The first task is applying the numerical method to estimate the CLT plate bending capacity for several grading classes and comparing the numerical results with experimental observations from Hochreiner et al. (2014). In the experimental setup, CLT plates were assembled using wooden boards from 3 different strength classes (C18, C24, and C35) according to the European code EN338, where each plate consisted of wooden boards from the same strength class. Each CLT plate exhibits a 3 layered structure with dimensions of  $1500 \times 1500 \times 57$  mm and each layer consisted of 15 parallelly-aligned wooden boards with a dimension of  $1500 \times 100 \times 19$  mm.

As shown in Figure 3.1a, the CLT plate was mounted on a vertically oriented steel frame and a concentrated loading was applied horizontally. Against the loading direction, the plate was supported by 4 pre-assembled tubes on the loaded front surface as line constraints, shown in Figure 3.1b. The loading was applied by a hydraulic punch device

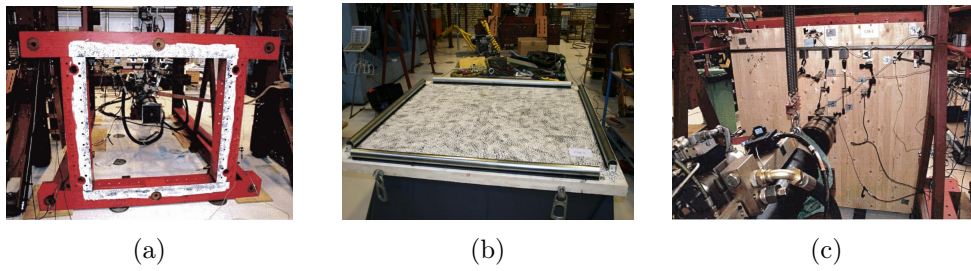


Figure 3.1: Illustration of the experimental set-up: (a) vertically oriented supporting steel frame with horizontal loading; (b) four pre-assembled tubes as the supporting structure on loaded front surface of CLT plates; (c) hydraulic punch device as the concentrated loading on the center of loaded back surface (Hochreiner et al., 2014).

on the centre of the loaded surface with a square loaded area of  $200 \times 200$  mm, shown in Figure 3.1c.

In this way, 8 CLT specimens were tested for each of the 3 strength classes (C18, C24, and C35) and the influence of the wooden board strength properties on the CLT plate load bearing capacities were discussed by Hochreiner et al. (2014).

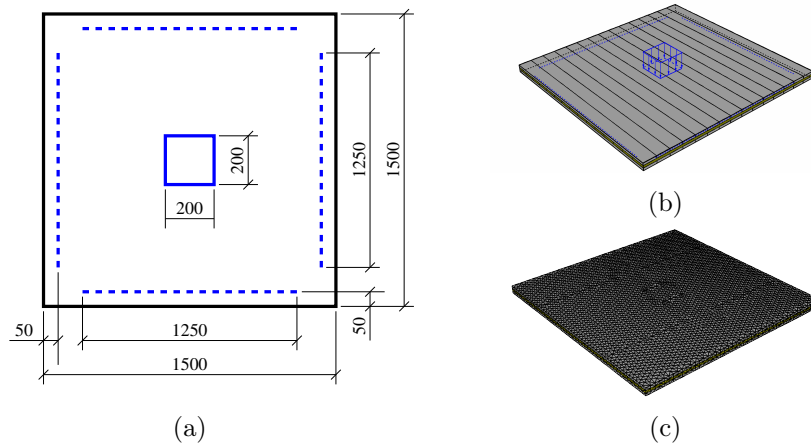


Figure 3.2: Numerical implementation of the CLT plate bending test as: (a) dimensions of the numerical model according to the experiment set-up with the blue square as loading region and the blue dash line as line constraints; (b) assembly of the wooden boards and the prescribed boundary conditions; (c) example of model discretisation.

Dimensions of the numerical models for the CLT plates, shown in Figure 3.2a, are defined according to the experimental setup. Boundary conditions are defined as a concentrated loading on the top surface and the line constraints on the bottom as shown in Figure 3.2b. Each CLT plate is discretised using approximately 40,000 tetrahedral elements (see Figure 3.2c for an example). An orthotropic Tsai-Wu yield function is applied to each element with respect to the local coordinate basis determined from the alignment of the corresponding wooden board.

As a validation, the numerical approaches are expected to provide reliable estimates on the load bearing capacities of CLT plates compared to experimental results. For this purpose, the differences in strength properties between the strength classes have

strength class	strength properties (N/mm <sup>2</sup> )				
	$f_{t,0}$	$f_{t,90}$	$f_{c,0}$	$f_{c,90}$	$f_{\tau}$
C18	11	0.4	18	2.2	3.4
C24	14	0.4	21	2.5	4
C35	21	0.4	25	2.8	4

Table 3.1: Strength properties for different strength classes of wooden boards according to European Code EN338, including tension parallel  $f_{t,0}$ , tension perpendicular  $f_{t,90}$ , compression parallel  $f_{c,0}$ , compression perpendicular  $f_{c,90}$  and Shear  $f_{\tau}$ .

to be considered, and it is straightforward to determine strength parameters according to EN338 as shown in Table (3.1). Note that, these code strength values represent the characteristic 5%-fractile-strengths, but for the comparison with experimental results it is more meaningful to use mean strength values, which can be determined from characteristic values as introduced by Jenkel et al. (2015). Then, the strength parameters for the Tsai-Wu yield function Eq. (3.6) can be determined by

$$\begin{aligned}
 F_{\sigma,1} &= \frac{1}{f_{t,0}} - \frac{1}{f_{c,0}}, & F_{\sigma,2} = F_{\sigma,3} &= \frac{1}{f_{t,90}} - \frac{1}{f_{c,90}}, \\
 P_{\sigma,11} &= \frac{1}{f_{t,0}f_{c,0}}, & P_{\sigma,22} = P_{\sigma,33} &= \frac{1}{f_{t,90}f_{c,90}}, \\
 P_{\sigma,55} &= \frac{1}{(f_{\tau}/3)^2}, \text{ and } P_{\sigma,44} = P_{\sigma,66} &= \frac{1}{f_{\tau}^2},
 \end{aligned} \tag{3.21}$$

where the material is considered as transversely isotropic, such that the strength values are identical in radial ( $R$ ) and tangential direction ( $T$ ), and the rolling shear strength is considered as one-third of the shear strength value in Table (3.1). As a result of using strength values obtained from codes, in the perpendicular-to-grain directions, the tensile strength  $f_{t,90}$  is much smaller than the compressive strength  $f_{c,90}$ . In addition, the definition of the failure criterion with the components of Eq. (3.21) leads to an ellipsoidal failure surface, where the intersections of the ellipsoid with the coordinate axis conform with the chosen strength values. But the transformation of the failure surface towards the perpendicular-to-grain compressive stress region leads to unrealistically high maximum strength values in the parallel-to-grain direction, which are much larger than the desired, chosen strength values, in this direction. Thus, interaction parameters for the Tsai-Wu yield function ( $P_{\sigma,12}$ ,  $P_{\sigma,23}$  and  $P_{\sigma,13}$ ) are determined by an optimisation algorithm, which introduces rotations to the failure surface without violating the normal and shear strengths in Table 3.1.

With the proposed numerical limit analysis approach, the bending bearing capacities of CLT plates are estimated for all three strength classes and the results are compared to the experimental data. In the experiments, 8 CLT plates were tested for each strength class, and the collapse load from each test is plotted in Figure 3.3 with black crosses. Due to the uncertainty of the wooden board strength properties, the collapse loads from experiments for each strength class are distributed with certain scatter as discussed by Hochreiner et al. (2014). In numerical calculations, where constant strength parameters are used for wooden boards from the same strength class, the numerical results are plotted as blue lines in Figure 3.3, indicating one collapse load for each strength

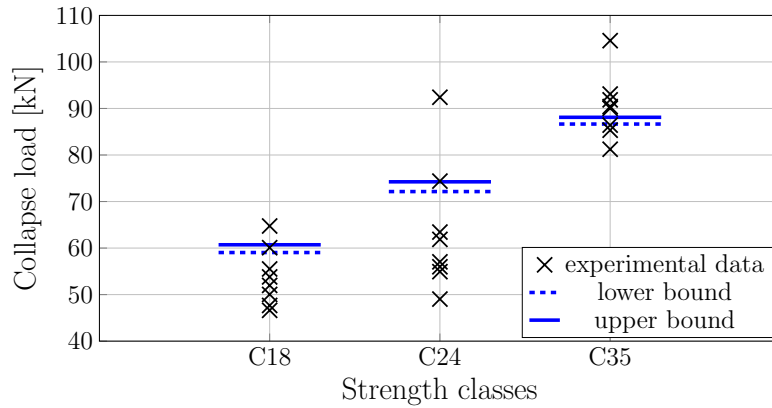


Figure 3.3: Numerical and experimental ultimate bending capacity of CLT plates using wooden boards from different strength classes.

class. Small bound gaps between lower bound and upper bound results are observed for each strength configuration, which indicates small computational errors, which can be determined according to Eq. (3.1) as 1.39% for C18, 1.43% for C24 and 0.83% for C35, suggesting an accurate approximation of the exact solution. Regarding the collapse load, the numerical results (blue lines) are close to the mean of the scatter of the experimental data points (black crosses) for the strength class C35, but the numerical calculations tend to overestimate the collapse load for the other 2 strength classes, C18 and C24. Since limit analysis considers only ductile failure, this agrees well with the experimental observation in Hochreiner et al. (2014) that, the structural collapse in CLT plates of C35 is dominated by ductile rolling shear failure but brittle failure mechanisms also play an important role in the weaker CLT plates of C18 and C24.

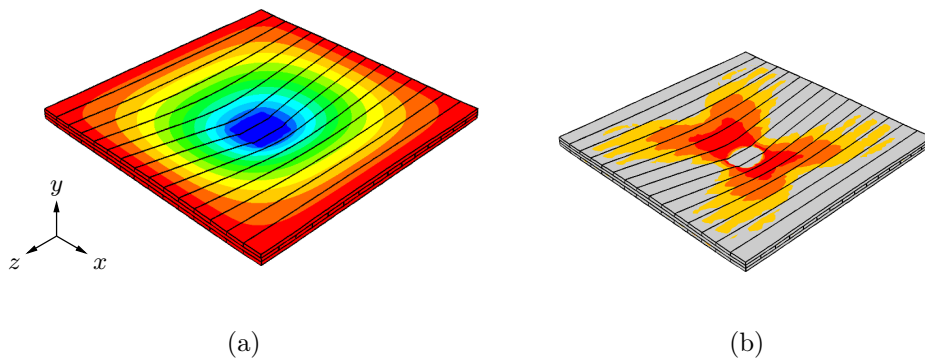


Figure 3.4: Illustrative example for numerical upper bound results using wooden boards from strength class C24 as: (a) the velocity field in the  $y$  direction; (b) the failure mode with a threshold of  $[-0.00024, -0.00016, -0.00008, 0]$ .

Beside the collapse load, a velocity field and an effective failure mode are obtained from each upper bound calculation, with illustrative examples for strength class C24, shown in Figures 3.4a and 3.4b, respectively. In the failure mode of Figure 3.4b, the velocity field at the point of structural failure is plotted on the deformed plate, and the failure region is marked by colours (from yellow to red) with red colours indicating the most critical failure.

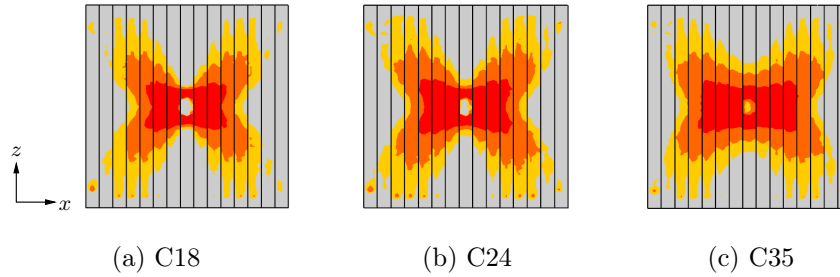


Figure 3.5: Comparison of upper bound failure modes observed on the loaded surface ( $y^+$  surface in Figure 3.4a) for strength classes: (a) C18 with a threshold  $[-0.00042, -0.00028, -0.00014, 0]$ ; (b) C24 with a threshold  $[-0.00024, -0.00016, -0.00008, 0]$ ; (c) C35 with a threshold  $[-0.0002, -0.00013, -0.00006, 0]$ .

The failure modes of CLT plates for different strength classes are compared in Figure 3.5, showing the loaded surface ( $y^+$  surface in Figure 3.4a). For all 3 strength classes, the plastic failure is initiated at the red region mainly due to kink-bending failure, and propagates sequentially through the orange and yellow regions due to a mixed mode of compressive and in-plane shear failures. In comparison, the failure region of the C18 plate is more localised, and in opposite, is more dispersed for the C35 plate. This agrees well with the experimental observation in Hochreiner et al. (2014), that, at structural collapse, the failure region only covers 40% of the total plate width for C18 and 76% for C35. The reason for this behaviour is that, by using stronger wooden boards, higher tensile loads can be carried in grain direction and the rolling shear strength is reached first in the middle layer close to the interface between other layers. Thus, the propagation of rolling shear failure in the middle layer leads to a stress redistribution and more wooden boards are activated to carry the bending load.

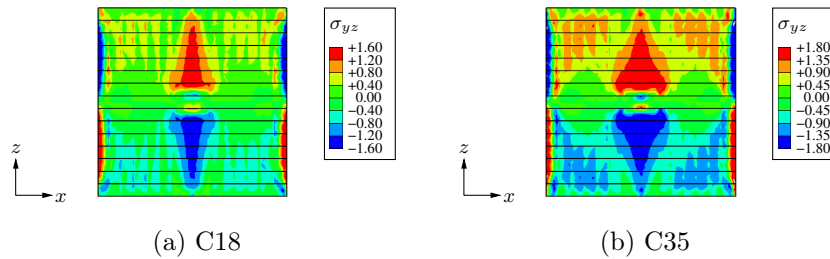


Figure 3.6: Comparison of the rolling shear stress fields in the middle layer of CLT plates for two different strength classes.

To verify this hypothesis, the shear stress fields  $\sigma_{yz}$  on the interface between the middle layer and the top layer of CLT plates, considered as the rolling shear stress field for the middle layer, are compared in Figure 3.6 for C18 and C35. It can be noticed that high rolling shear stress regions cover larger areas of the surface of the CLT plate with stronger wooden boards, i.e. of the higher grading class, which agrees well with above-mentioned experimental observations and conclusions.

Beside reliable estimates, the time efficiency of the numerical method is also remarkable. With a mesh of 40,000 tetrahedral elements, the total CPU time for each approximation

is around 40 min, including a lower bound and an upper bound calculation. Taking advantage of the high time efficiency, this numerical method provides the basis for a stochastic approach targeting a closer look into the failure mechanism of CLT plates with the consideration of property varieties and inhomogeneities of wooden boards by simulating a large number of models.

### 3.3.2 Application using strength profiles

To study the impact of inhomogeneities, in our case of knots, on the bending strength of CLT plates, we use a database of so-called strength profiles of real wooden boards. For this database, a total of 350 Norway spruce boards of strength grades LS15 (T14) and LS22 (T22) were, first, virtually reconstructed and, then, by using so-called indicating properties section-wise evaluated to obtain strength profiles of the longitudinal strength component for each board. The respective procedure is described in detail in Kandler et al. (2017) and summarised subsequently.

All boards were inspected using a tracheid effect-based laser scanning device, resulting in grid-like fibre orientation information available on all four board surfaces. In addition, photographs of the cross sections on both ends of the board allow for an estimation of pith locations. The fully automated approach described in Kandler et al. (2016a) is used to obtain a geometrical description of the knot morphology. Therein, fibre angle measurements are used to estimate knot areas on the board's surfaces. This information in combination with the pith location is used to fit rotationally symmetric cones representing knots into the board. Here, the reconstruction error is minimised by employing a so-called simulated-annealing optimisation scheme, which reduces the difference between actual knot areas and knot areas obtained from intersecting the reconstructed cones with the board. Figure 3.7a-e shows the results for an exemplary board. In Figure 3.7c, all recognised knots are displayed, whereas in Figure 3.7d only the significant knot groups according to a modified version of the criterion presented in Kandler et al. (2016b) are shown. Here, significance is defined by using a size measure for the knots. Knots with a visible knot area above the 70%-quantile are considered to be large knots and, thus, to have a significant influence on the board's mechanical behaviour. In addition, the mutual distance between adjacent large knots is checked and those with longitudinal distances below 200 mm are grouped together. All other (small) knots are now disregarded unless they lie in close vicinity of larger knots, defined as a maximum distance of 100 mm. The reason for this approach is that small knots are considered to be of small mechanical significance if by themselves, but they might have an influence on sections, where interacting multiple knots lead to variations in fiber deviations and, thus, influences on failure mechanisms. The board is now divided into so-called knot sections, with maximum lengths of 300 mm, and interjacent clear-wood sections without knots. Each knot section is then subjected to a set of indicating properties, which are based on a study presented in Lukacevic et al. (2015) and are combinations of the following parameters:

- knot area ratio (KAR), which is the ratio of the projected knot areas to the cross-section area,
- knot area, which refers to the visible knot areas on the board's surfaces,

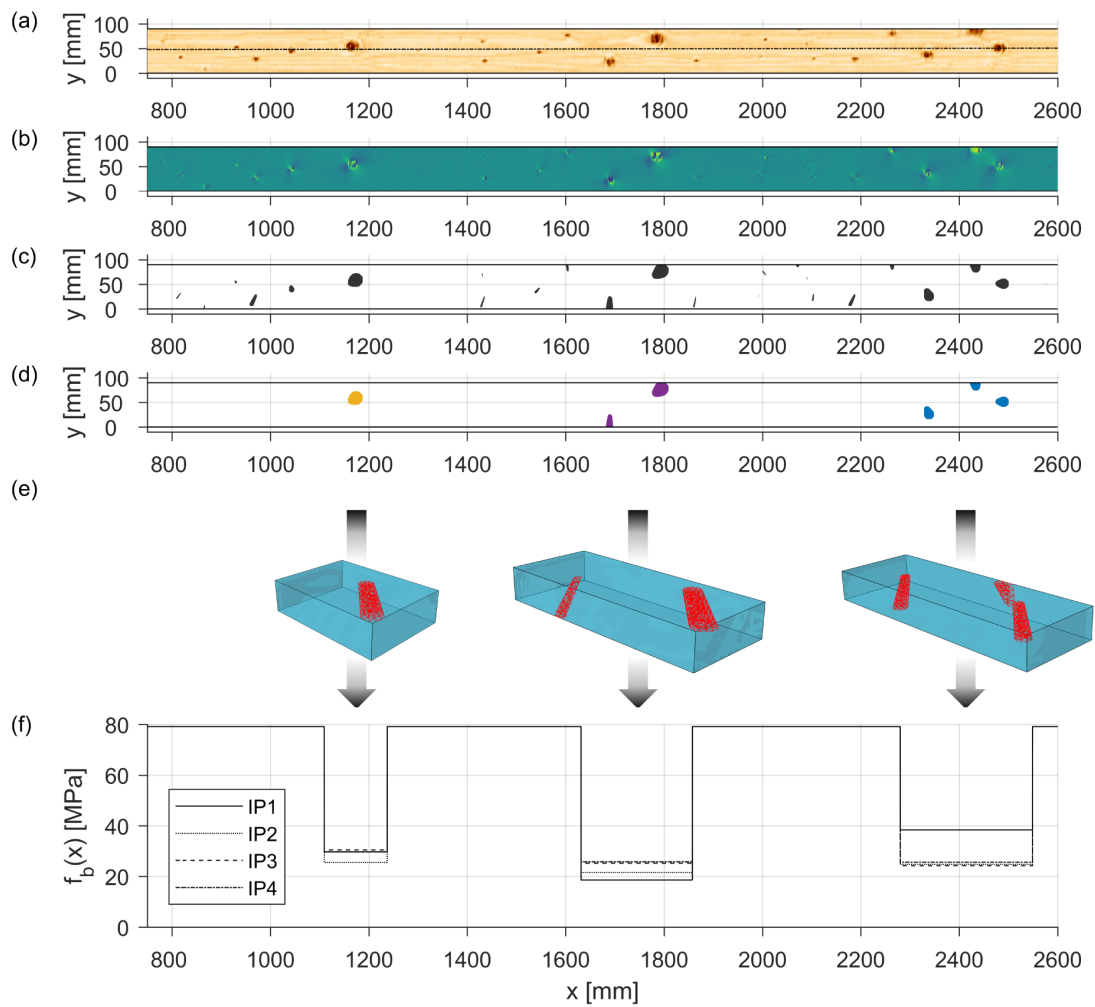


Figure 3.7: From board to strength profiles. (a) For a regular board, (b) based on laser scanning data (c) the knot fitting algorithm (Kandler et al., 2016a) automatically reconstructs the 3D knot geometry. (d) After the regrouping procedure has been applied, only the most important knot groups are retained in the model (Kandler et al., 2016b). These knot groups, displayed in (e), are investigated using indicating properties (IPs). In (f), different strength profiles according to IPs 1 to 4 are displayed. (modified from Kandler et al. (2017))



- weighted knot area, further distinguishes between knot areas on top/bottom and left/right surfaces,
- knot volume,
- interface areas, between knots and surrounding clear-wood, and
- Foley area ratio (FAR), which, in analogy to the KAR value, describes the ratio of the projected fiber deviation area to the cross section area.

These parameters were combined to a total of four indicating properties:

1. IP1: KAR, weighted knot area, knot volume, interface areas, FAR
2. IP2: KAR, knot area, knot volume, interface
3. IP3: KAR
4. IP4: KAR, knot area, knot volume

For the clear-wood sections, the longitudinal tensile strength is computed following the approach in Hackspiel et al. (2014), which is based on scaling experimentally obtained strength values according to density-dependent results obtained by a micromechanical model for elastic behavior. The resulting strength profiles for the exemplary wooden board can be seen in Figure 3.7f. Such profiles of alternating defect-free and knot sections are referred to as weak zone models and are in accordance to Fink et al. (2015), Källsner (1994), Källsner et al. (1997).

The database of strength profiles provides the basis for a stochastic study on how wooden board properties influence the overall CLT capacities. In the experiments (Hochreiner et al., 2014), wooden boards were graded into the bending-based strength classes, C18, C24, and C35, defined in EN 338 (2009); for the strength profile database, wooden boards were graded into the tensile-based strength classes, LS15 and LS22, defined in EN 14081-4 (2009). As mentioned in Bacher and Krzosek (2014), by comparing the tensile strengths, the strength classes LS15 and LS22 can be considered as equivalent to C24 and C35, respectively. Thus, the application of numerical limit analysis using existing strength profiles to obtain CLT bending capacity estimates can also be validated using the experimental results for C24 and C35 shown in Figure 3.3.

In this work, the strength profile group IP4 is used in the calculations, as it has been proven to be reliable for strength estimates in Kandler et al. (2017). From the strength profile database, both densities and longitudinal tensile strengths are available for knot sections and clear wood sections. In order to define the Tsai-Wu failure surfaces, all strength parameters have to be determined as shown in Eq. (3.21) which requires more strength components beside the longitudinal tensile strengths. For each clear wood section, all 9 strength components ( $f_{t,L}$ ,  $f_{t,R}$ ,  $f_{t,T}$ ,  $f_{c,L}$ ,  $f_{c,R}$ ,  $f_{c,T}$ ,  $f_{\tau,LR}$ ,  $f_{\tau,RT}$  and  $f_{\tau,LT}$ ) are determined by its density according to the strength-density correlation discussed in Hackspiel et al. (2014). For knot sections, no reliable data for strength properties is available due to the lack of knowledge about failure mechanisms in the vicinity of knots, thus, in this work, the strength components are determined by the longitudinal tensile strengths using similar correlations as applied for the clear wood sections.

For each grading class, data for a total of 140 individual boards was available. During the assembly of the CLT plate models, for each simulation run, unique boards were randomly chosen from the database according to the studied grading class. The single boards were then divided into several knot and clear-wood sections with assigned strength parameters determined by the board’s strength profile information. By re-running the random board selection process, for both strength classes, a big number of different CLT plates can be assembled using wooden boards with different strength profiles, and their failure behaviour under bending can be predicted using numerical limit analysis.

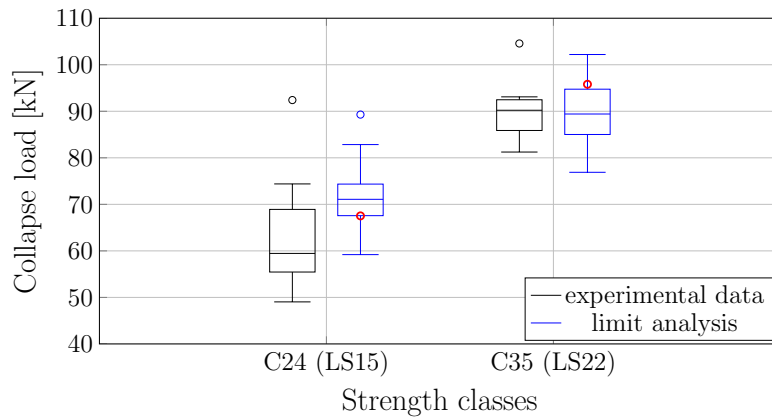


Figure 3.8: Comparison of numerical and experimental collapse loads of CLT plates under bending load using wooden boards from different strength classes (the red marked points denote the results of the exemplary CLT boards of Figures 3.10 and 3.12).

type	C24(LS15)			C35(LS22)		
	$\bar{x}$	$s$	$COV$	$\bar{x}$	$s$	$COV$
experiment	63.64	13.82	0.2172	90.37	6.93	0.0767
limit analysis	71.17	6.02	0.0846	89.59	6.21	0.0693

Table 3.2: Resulting mean value  $\bar{x}$  [kN], standard deviation  $s$  [kN] and coefficient of variation  $COV$  for both experimental and numerical results corresponding to different strength classes.

For each of the two strength classes, LS15 and LS22, 50 CLT plate models were generated. The collapse loads of all CLT plates from numerical limit analysis calculations are plotted in Figure (3.8) compared with the experimental results for strength classes C24 and C35. For strength class C35, the scatter for numerically-obtained collapse loads matches well to the experimental data points and the mean value  $\bar{x}$  as well as the standard deviation  $s$  for both numerical and experimental results agree well to each other shown in Table (3.2), indicating that the numerical estimates are reliable for this strength class in a stochastic manner. For the strength class C24, the scatter for the numerical results covers about 75% of the distribution of experiment data points in the higher end with higher mean value  $\bar{x}$  for the numerical estimates. For an explanation it can be referred to the discussion in Section (3.3.1), that the numerical limit analysis is able to predict the ductile failure mechanisms of the CLT plates, as the dominant failure for C35, but leads to an overestimation of collapse loads when brittle failure

mechanisms cannot be ignored, as for C24. Since failure mechanisms of CLT plates for C24 can be considered as a mixed mode of ductile and brittle responses, in Table (3.2), the standard deviation  $s$  is higher for experimental results than for numerical results where only ductile response is considered.

Assessing all failure modes from the comprehensive numerical upper bound limit analysis calculations for both strength classes, basically two categories of failure modes are identified and the impact of wooden board strength profiles is discussed in the following.

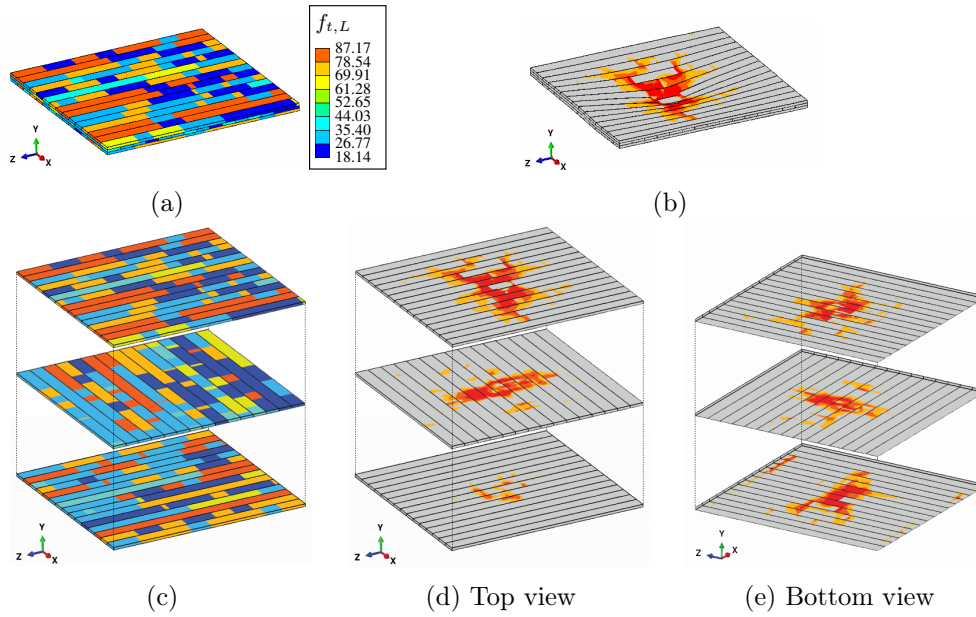


Figure 3.9: Selected upper bound results for the localised failure mode plotted as: (a) the longitudinal tensile strength profiles assigned in the 3-layer CLT plate; (b) the failure mode of this plate as the coloured region and the velocity field as the deformation; (c) the exploded view for strength profiles; (d) the exploded view for the failure mode from top; (e) the exploded view for the failure mode from bottom.

The first category is identified mainly in CLT plates for strength class C24, for which a selected example from one upper bound calculation is illustrated in Figure (3.9). The strength profiles, indicated by the longitudinal tensile strength, are illustrated for the whole plate in Figure (3.9a) and for each layer in the exploded view Figure (3.9c), where weaker clear wood sections and a higher number of knot sections are present. The failure mode of the plate is plotted in Figure (3.9b), and, in order to have a complete image of failure pattern over the whole plate, exploded views from top and bottom are shown in Figure (3.9d) and Figure (3.9e), respectively. It is observed that the dominant failure locates in the top layer, especially on the top surface (the loaded surface). The selected failure mode on the top surface is plotted in Figure 3.10a, where a localised plastic failure mechanism is observed. When the loading is applied, plastic failure is initiated due to the local instabilities around the loaded region (marked by the blue square) known as the kink-bending failure on the top wooden board layer as shown in the sectional view ①. Then the failure propagates through wooden boards perpendicularly mainly due to the longitudinal compressive failure, as shown in the sectional view ②, leading to the final structural collapse. In order to discuss the impact of wooden board inhomogeneities on

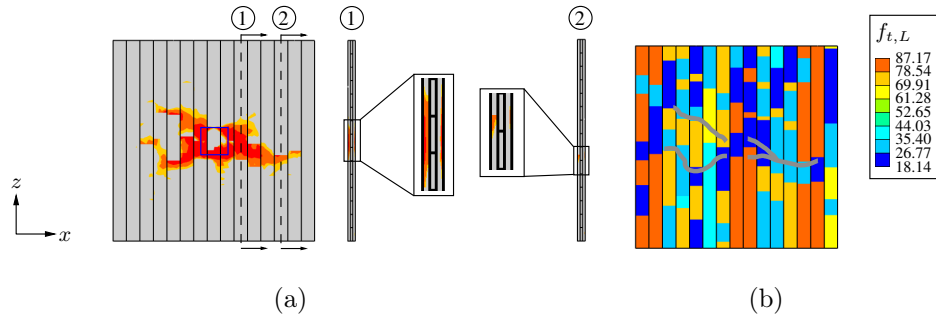


Figure 3.10: Illustration of the identified dominant failure mechanisms from the selected localised failure mode as: (a) the failure mode observed on the loaded surface (blue square indicates loaded region) as well as 2 view cuts ① and ② with zone-in views for the kink-bending failure and the longitudinal compressive failure, respectively; (b) the longitudinal tensile strength profiles assigned to wooden boards in the upper layer and the identified failure pattern (grey curves) according to the failure mode.

the failure mode, the longitudinal tensile strength profiles are plotted and the failure mechanism identified in Figure 3.10a are indicated by grey curves in Figure 3.10b. It is obvious that, after the kink-bending failure initiated around the loaded region, the longitudinal compressive failure always propagates through wooden boards in the weak zones, normally knot sections, without plastic failure in surrounding clear wood sections. In this case, the failure mechanisms are mainly determined by the distributions of the knot sections leading to an insufficient utilisation of the strength properties of clear wood sections since they are not activated to carry loads during structural collapse.

The second category of failure modes is identified in CLT plates with stronger wooden boards, in this case from strength class C35, for which strength profiles of a selected example are plotted for the whole plate in Figure (3.11a) and for each layer in Figure (3.11c). Since less knot sections are present, the localised failure cannot propagate through the whole plate and dispersed failure mechanisms are observed as shown in Figure (3.11b) as well as in the exploded views Figure (3.11d) and Figure (3.11e), where the dominant failure is still observed on the top surface shown in Figure (3.12a). Compared to the first category, the main difference is that, instead of the localised failure region perpendicular to the wooden board orientation, the dispersed failure mechanism is observed in this case with the tip of the failure region aligning parallel to the wooden boards. This difference is attributed to the rolling shear failure in the middle layer prior to the structural collapse, shown in the view cut ① and ②, which results in the stress redistribution in the top layer. Plotting failure patterns, identified in Figure 3.12a as grey curves in the strength profiles Figure 3.12b, the failure mechanisms of the CLT plate can be summarised in sequence as: 1) the plastic failure is initiated due to the kink-bending failure and propagates through the knot sections of wooden boards; 2) further propagation of the localised longitudinal compressive failure is interrupted due to the presence of strong clear wood sections; 3) the rolling shear failure occurs in the middle layer; 4) the strong wooden boards are activated to carry the load whose bending failure leads to the structural collapse.

The dominant failure mechanisms in above numerically-obtained failure modes are the longitudinal compressive failure, for the first category, and the rolling shear failure as

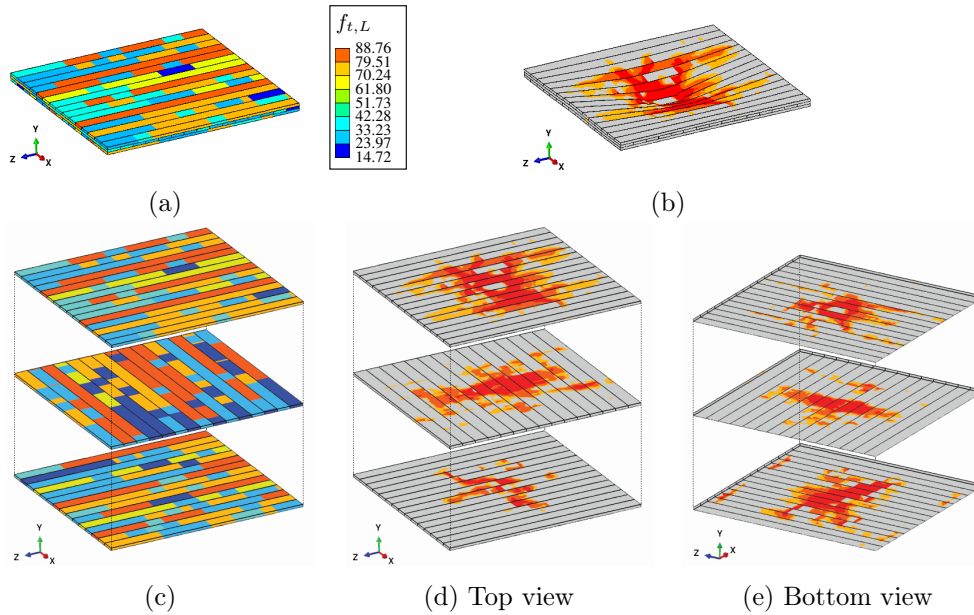


Figure 3.11: Selected upper bound results for the dispersed failure mode plotted as: (a) the longitudinal tensile strength profiles assigned in the 3-layer CLT plate; (b) the failure mode of this plate as the coloured region and the velocity field as the deformation; (c) the exploded view for strength profiles; (d) the exploded view for the failure mode from top; (e) the exploded view for the failure mode from bottom.

well as the bending failure, for the second category, which agrees to the experimental observations in Hochreiner et al. (2013). Additionally, similar conclusions can be drawn as mentioned in the experimental study of Hochreiner et al. (2014) that, by using stronger wooden boards in CLT plates, the increase in bending capacity is achieved not only because of the higher strength properties of wooden boards, but, more importantly, related to a more efficient utilisation, as more wooden boards are involved to carry the load.

### 3.4 Summary and conclusions

In this paper, 3D numerical limit analysis formulations were implemented for strength estimates of CLT plates for which, to the authors' knowledge, no sophisticated numerical method is available in timber engineering. In this method, the anisotropic Tsai-Wu failure criterion was employed to measure the material failure behaviour in wooden boards with respect to the local principal material orientations, and the strength parameters were determined from either code values in Eurocode 5 or a strength profile database. By using code values, the main focus was laid on the validation of the numerical method using experimental results and the influence of wooden board strengths on the CLT plate bending capacities; by using strength profiles, the main focus was laid on the impact of section-wise varying strength values, caused by inhomogeneities like knots, on the CLT plate failure mechanisms. Based on the obtained results, the main finding of this work can be summarised as:

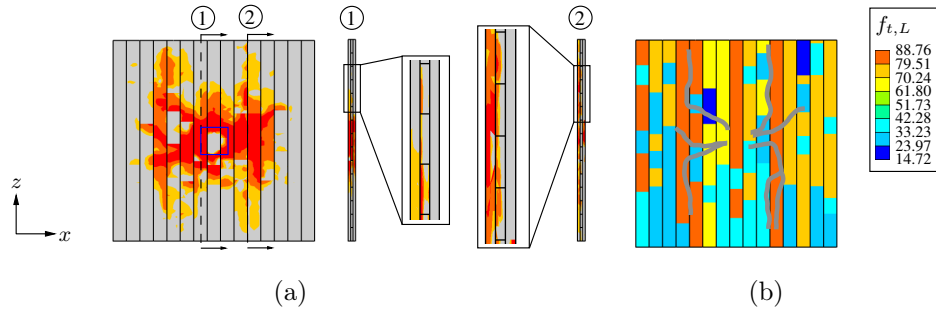


Figure 3.12: Illustration of the identified dominant failure mechanisms from the selected dispersed failure mode as: (a) the failure mode observed on the loaded surface (blue square indicates loaded region) as well as 2 view cuts ① and ② with zone-in views for the kink-bending failure and the longitudinal compressive failure, respectively; (b) the longitudinal tensile strength profiles assigned to wooden boards in the upper layer and the identified failure pattern (red curves) according to the failure mode.

- A validation of the numerical limit analysis approaches has been introduced using strength values from Eurocode 5 for 3 different strength classes, C18, C24, and C35, as input parameters, and good agreement between numerical and experimental results are observed. The dominant advantages of this numerical method rely on the small computational error, indicated by the small bound gap, and the high time efficiency over the conventional finite element method.
- By using a strength profile database, CLT plates are assembled using wooden boards with arbitrarily-assigned strength profiles, resulting in section-wise varying numerical strength estimates. Performing comprehensive calculations, the numerical upper bound calculations are able to provide reliable strength estimates with similar scatter as found in experimental results for strength classes C24 and C35. Distinct failure modes are obtained for each calculation with arbitrary combinations of strength profiles.
- Due to the high time efficiency of this numerical method, the influence from section-wise varying strength values, caused by inhomogeneities in wooden boards, on the overall CLT plate capacities can be studied in a stochastic approach using a strength profile database. The numerically-obtained failure modes agree well with experimental observations that, 1) when weaker wooden boards (e.g. C24) are used, the failure mechanisms are more localised and propagate through weak links of wooden boards (normally knot sections) and both brittle and ductile responses can be observed at the point of structural collapse; 2) when stronger wooden boards (e.g. C35) are used, the rolling shear failure in the middle layer plays an important role and more wooden boards are activated to carry the bending load and the structural collapse is dominated by ductile response.

Accordingly, one can conclude that, the presented numerical limit analysis is a useful tool to fill the gap in timber engineering for efficient and reliable estimates on CLT plate bending capacities and structural failure mechanisms in which inhomogeneities and strength variants in wooden boards can be considered in a stochastic approach.

Future work is devoted to more sophisticated stochastic studies on the impact of inhomogeneities on the overall strength of CLT plates and the corresponding failure modes. The results are expected to provide more information about CLT plate failure mechanisms and serve as reference for the ongoing development of the wooden board grading process as well as the standardisation of CLT products. Additionally, for further study on the strength profiles, the presented numerical method will be applied for strength estimates of knot sections to predict failure mechanisms in vicinities of knots and surrounding fibre deviations.

## Acknowledgments

Financial support for this work in the framework of the PhD School DokInHolz funded by the Austrian Federal Ministry of Science, Research and Economy and the Austrian Association of Wood Industries is gratefully acknowledged. We also gratefully acknowledge the financial support of this work by the Austrian Science Fund (FWF) through the Erwin Schrödinger Fellowship J3748-N30.

# A numerical upper bound formulation with sensibly-arranged velocity discontinuities and orthotropic material strength behaviour (Li et al., 2018b)

Authored by Mingjing Li, Josef Füssl, Markus Lukacevic, Josef Eberhardsteiner & Chris M. Martin

Published in *Journal of Theoretical and Applied Mechanics*

The final publication is available at:

<http://ptmts.org.pl/jtam/index.php/jtam/article/view/4655>

**Abstract:** Numerical limit analysis allows for fast estimates of the collapse load of structures exhibiting ideal plastic material behaviour. In numerical upper bound formulations, the description of the unknown velocity field can be extended by introducing velocity discontinuities between finite elements. Through these additional degrees of freedom, localised failure modes may be approximated more accurately and better upper bounds can be obtained. In existing formulations, such discontinuities are typically introduced between all elements and the description is restricted to isotropic failure behaviour. In this work, a general 3D upper bound formulation is briefly proposed, allowing the consideration of both isotropic and orthotropic yield functions within finite elements as well as at velocity discontinuities. The concept of “projecting” a stress-based orthotropic yield function onto a certain discontinuity is presented, giving a traction-based yield function which allows for a consistent description of the material strength behaviour across the interface. The formulation is verified by means of two classical examples, the rigid strip footing and the block with asymmetric holes. Furthermore, based on the computation of potential orientations of plastic flow localisation, a simple concept for a sensible arrangement of velocity discontinuities is proposed. It is shown that this concept performs very well for isotropic as well as anisotropic material strength



behaviour. A feature of the present work is that, velocity jumps are allowed only across the prescribed finite element interfaces determined from the sensible discontinuity arrangement. Good upper bounds similar to those in existing works are obtained with far fewer degrees of freedom.

**Keywords:** numerical upper bound formulations, localised failure modes, traction-based yield function, sensible arrangement of velocity discontinuities, orthotropic material strength behaviour.

## 4.1 Introduction

### 4.1.1 Numerical limit analysis

The main objective of limit analysis is the determination of load bearing capacities of structures exhibiting elastoplastic material response. To achieve this, limit analysis concentrates on the critical energy dissipation rate at the time instant of structural failure, and the basic task can be expressed as follows: *Find the kinematically admissible velocity field which minimises energy dissipation over the set of all statically admissible stress fields which maximise the dissipated energy* (Ciria et al., 2008). Statically admissible stress fields are required to be in equilibrium, fulfil the static boundary conditions, and obey a plastic yield criterion at each point of the body. Kinematically admissible velocity fields are subject to compatibility, the kinematic boundary conditions, and fulfil an associated plastic flow rule at each point of the body. Unfortunately, the so-defined saddle-point problem can be solved only for simple geometric and loading situations as well as for simple material behaviours. For more complex situations, the plastic flow compatibility in the so-called static principle or the static equilibrium in the so-called kinematic principle may be relaxed, providing lower and upper bounds on the exact load bearing capacity of a structure according to the bounding theorems by Drucker et al. (1951, 1952).

However, for complex problems, the application of these bounding theorems (in the context of limit analysis) in an analytical way is very limited and often not possible. Thus, finite-element-based formulations were first introduced in the 1970s (Anderheggen and Knöpfel, 1972, Belytschko and Hodge, 1970, Lysmer, 1970, Maier et al., 1972), and gained popularity from then on. The computational efficiency and accuracy of such numerical formulations strongly depend on the mathematical programming method used to solve the underlying optimisation problems. At the early stage, the limit analysis theorems were formulated as linear optimisation problems, by linearising the applied plastic yield functions. At the turn of the millennium, Lyamin and Sloan (2002a,b) proposed more general lower and upper bound formulations allowing for nonlinear yield functions, which were solved using nonlinear programming concepts. However, local smoothing was required for yield functions with singularities, e.g. the Mohr-Coulomb yield function. Subsequently, during the past two decades, second-order cone programming (SOCP) has been proven to be an excellent alternative method by Makrodimopoulos and Martin (2006, 2007) and Ciria and Peraire (2004) for cohesive-frictional materials and Füssl et al. (2008) for composite materials, with sufficient robustness and efficiency to solve large-scale nonlinear optimisation problems of numerical limit analysis. Such implementations allow the applications of many different yield functions in

their native form, since most of the commonly-used yield functions can be formulated as second-order cones. In this work, SOCP is employed to solve the nonlinear optimisation problems arising from the presented limit analysis formulations.

The efficiency and accuracy of such formulations is also strongly influenced by the chosen finite elements and related shape functions. In order to obtain rigorous upper bound solutions, for example, the associated plastic flow rule must be satisfied throughout the whole body. Basically, this can be achieved by using constant strain triangular elements, which are often combined with velocity discontinuities between element boundaries (Bottero et al., 1980, Lyamin and Sloan, 2002b, Sloan and Kleeman, 1995). To improve the quality of upper bound solutions, the use of higher order interpolation functions is desired. Makrodimopoulos and Martin (2007) have shown that the associated plastic flow rule can also be enforced throughout the whole body by using linear strain triangular elements, leading to a better performance than constant strain elements even without discontinuities. As a further development, the meshless method has been implemented for numerical upper bound approaches in Le et al. (2010a), Liu and Zhao (2013), Yu et al. (2016). However, in such implementations with high order shape functions, it is difficult to guarantee both compatibility and satisfaction of the associated plastic flow rule throughout each element.

Additionally or as an alternative to the use of high order elements, velocity discontinuities can be implemented in upper bound formulations to increase their effectiveness. In Chen et al. (2003), Milani and Lourenço (2009), for example, rigid elements were used and plastic dissipation was only allowed between finite elements. Such approaches are highly dependent on the mesh and even adaptive mesh refinement cannot fully compensate for this issue. An approach without using classical finite elements is the so-called discontinuity layout optimisation (DLO), where velocity discontinuities are determined by using a truss layout optimisation algorithm based on a prescribed grid (Hawksbee et al., 2013, Smith and Gilbert, 2007). This approach performs well for 2D problems, but the determination of complex failure mechanisms in 3D bodies requires a fine grid and large computational effort.

For this reason, to the authors' opinion, the most promising approach so far to obtain rigorous upper bound solutions still seems to be the use of solid finite elements with or without velocity discontinuities. In Krabbenhøft et al. (2005) zero-thickness interface elements between constant strain elements are introduced, which perform very well for a large number of applications. Another development can be found in Makrodimopoulos and Martin (2008), where velocity discontinuities are implemented between linear strain elements. In order to increase the efficiency of the upper bound formulations, adaptive mesh refinement was introduced by Ciria and Peraire (2004), Ciria et al. (2008), Martin (2011) However, a targeted arrangement of discontinuities, as will be proposed in this work, has not been introduced until now.

#### 4.1.2 Objective of the paper

In several previous works, e.g. in Füssl et al. (2017), Li et al. (2018c), anisotropic yield functions have been implemented in numerical upper bound formulations. To the authors' knowledge, the combination of anisotropic yield functions and velocity discontinuities has not previously been presented, although it could significantly improve the capability of upper bound approaches in handling localised plastic failure for anisotropic

materials like wood or fibre reinforced composites. In particular, it is beneficial if the alignment of discontinuities is tuned to the direction of localised plastic failure.

Thus, the main objectives of this work can be introduced as follows:

1. The formulation of 3D numerical upper bound approaches with anisotropic yield functions, quadratic shape functions for the velocity fields, and velocity discontinuities.
2. To allow for a consistent description of plastic failure also across velocity discontinuities, the derivation of a traction-based yield function which is in accordance with the stress-based yield function assigned to the solid finite elements / bulk material.
3. Implementation of an initial concept for a sensible introduction and arrangement of velocity discontinuities only in failure regions.

According to these objectives, the paper is structured as follows. A quite general numerical upper bound approach is briefly proposed in Section 4.2, able to consider plastic energy dissipation in both finite elements and discontinuities obeying an anisotropic failure criterion. Furthermore, the process for obtaining the required traction-based yield function for the discontinuities is described. A verification of the implemented upper bound formulations by means of well-known examples can be found in Section 4.3, as well as a discussion about the performance of velocity discontinuities. Finally, a brief summary and concluding comments are given in Section 4.4.

## 4.2 Upper bound approaches

The upper bound theorem focuses exclusively on the kinematically admissible velocity field  $\dot{\mathbf{u}} = (\dot{u}_x, \dot{u}_y, \dot{u}_z)^\top \in \mathfrak{R}^3$ , and by minimising the internal plastic energy dissipation rate  $W_{int}$ , which has to be equal to the work rate of the external loads  $W_{ext}$ , the resulting failure state provides an upper bound for the exact collapse load. A kinematically admissible velocity field  $\dot{\mathbf{u}}$  has to satisfy compatibility, the associated plastic flow rule, and the kinematic boundary conditions at each point of the considered body. Additionally, a velocity-jump field  $\Delta\dot{\mathbf{u}} = (\Delta\dot{u}_x, \Delta\dot{u}_y, \Delta\dot{u}_z)^\top \in \mathfrak{R}^3$  is introduced, describing localised interface plastic failure across a prescribed interior surface.

The internal energy dissipation rate  $W_{int}$  is composed of a part referring to material failure in the continuum body  $\Omega$  and a part related to the energy dissipation at interior surfaces  $\Gamma^{dis}$ , and reads

$$W_{int} = \int_{\Omega} d_p^{mat}(\dot{\boldsymbol{\epsilon}})dV + \int_{\Gamma^{dis}} d_p^{dis}(\Delta\dot{\mathbf{u}})dA \quad (4.1)$$

with the plastic dissipation functions

$$\begin{aligned} d_p^{mat} &= \sup_{\boldsymbol{\sigma} \in \mathcal{F}} \boldsymbol{\sigma}^\top \dot{\boldsymbol{\epsilon}}, & \mathcal{F} &= \{\boldsymbol{\sigma} | f(\boldsymbol{\sigma}) \leq 0\} & \text{in } \Omega \\ d_p^{dis} &= \sup_{\mathbf{t} \in \mathcal{D}} \mathbf{t}^\top \Delta\dot{\mathbf{u}}, & \mathcal{D} &= \{\mathbf{t} | f(\mathbf{t}) \leq 0\} & \text{on } \Gamma^{dis} \end{aligned} \quad (4.2)$$

where  $\dot{\boldsymbol{\epsilon}} = (\dot{\epsilon}_{xx}, \dot{\epsilon}_{yy}, \dot{\epsilon}_{zz}, \dot{\epsilon}_{xy}, \dot{\epsilon}_{yz}, \dot{\epsilon}_{xz})^\top \in \mathfrak{R}^6$  represents the plastic strain-rate field,  $\boldsymbol{\sigma} = (\sigma_{xx}, \sigma_{yy}, \sigma_{zz}, \tau_{xy}, \tau_{yz}, \tau_{xz})^\top \in \mathfrak{R}^6$  the stress field and  $\mathbf{t} = (t_x, t_y, t_z)^\top \in \mathfrak{R}^3$  the surface traction field.  $f(\boldsymbol{\sigma}) \leq 0$  and  $f(\mathbf{t}) \leq 0$  denote the stress-based yield function for  $\Omega$  and the traction-based yield function for  $\Gamma^{dis}$ , respectively.

The upper bound theorem can be formulated as a nonlinear optimisation problem, reading

$$\begin{aligned}
& \min && W_{int} \\
& \text{s.t.} && \dot{\boldsymbol{\epsilon}} = \text{div} \dot{\mathbf{u}} && \text{in } \Omega \\
& && \dot{\mathbf{u}} = \dot{\mathbf{u}}_b && \text{on } \Gamma \\
& && \dot{\boldsymbol{\epsilon}} = \dot{\lambda}_\sigma \partial f(\boldsymbol{\sigma}) / \partial \boldsymbol{\sigma} && \text{in } \Omega \\
& && \Delta \dot{\mathbf{u}} = \dot{\lambda}_t \partial f(\mathbf{t}) / \partial \mathbf{t} && \text{on } \Gamma^{dis}
\end{aligned} \tag{4.3}$$

in which the constraints enforce compatibility between the velocities and the plastic strain-rates, the kinematic boundary conditions, and the associated plastic flow rule both in the continuum  $\Omega$  and at the interior surfaces  $\Gamma^{dis}$ . In the second constraint,  $\dot{\mathbf{u}}_b$  refers to the prescribed velocity boundary conditions defined over the whole surface  $\Gamma = \partial\Omega$  of the continuum body. In the last two constraints,  $\dot{\lambda}_\sigma$  and  $\dot{\lambda}_t$  are plastic multipliers determining the magnitude of plastic flow within the continuum and at the discontinuities, respectively. Note that, these two associated plastic flow constraint in Eq. (4.3) are valid only when the yield function is differentiable everywhere. If singular apex points exist, additional technology is required, and the use of SOCP in this work ensures that such points are handled naturally.

As shown in Makrodimopoulos and Martin (2007), using the duality of nonlinear programming, a mathematically equivalent optimisation problem to Eq. (4.3) can be formulated, reading

$$\begin{aligned}
& \max && W_{ext} \\
& \text{s.t.} && \int_\Omega (\text{div} \dot{\mathbf{u}})^\top \boldsymbol{\sigma} dV + \int_{\Gamma^{dis}} \Delta \dot{\mathbf{u}}^\top \mathbf{t} dA = \int_\Omega \dot{\mathbf{u}}^\top \boldsymbol{\beta} dV + \int_\Gamma \dot{\mathbf{u}}^\top \boldsymbol{\beta} t dA && \text{in } \Omega \\
& && f(\boldsymbol{\sigma}) \leq 0 && \text{in } \Omega \\
& && f(\mathbf{t}) \leq 0 && \text{on } \Gamma^{dis}
\end{aligned} \tag{4.4}$$

in which the first constraint represents weak equilibrium of the dissipated energy, and the objective function is related to the external work rate given as

$$W_{ext} = \int_\Omega \dot{\mathbf{u}}^\top \boldsymbol{\beta} dV + \int_\Gamma \dot{\mathbf{u}}^\top \boldsymbol{\beta} t dA \tag{4.5}$$

where  $\boldsymbol{\beta}$  denotes a load multiplier applied to the surface traction field  $\mathbf{t}$  and the prescribed body force field  $\mathbf{g} \in \mathfrak{R}^3$ .

For the discretisation of the upper bound optimisation problem, tetrahedral linear-strain simplex elements are used, as introduced for 2D upper bound problem under plane strain conditions in Makrodimopoulos and Martin (2007, 2008) and for 3D upper bound problem in Martin and Makrodimopoulos (2008). Thus, the velocity field is approximated using quadratic interpolation functions and the plastic strain-rate field is described by linear shape functions. Worth mentioning is that each finite element has its own strain-rate evaluation nodes, which means that adjacent nodes from different elements share the same coordinates but can have different strain-rate states. The exact representation of this approximation is given in Makrodimopoulos and Martin (2008).

In this work, to assess the capability of the discontinuity arrangement, velocity jumps are allowed only across particularly prescribed finite element interfaces determined by the arrangement, on which adjacent elements have their own velocity evaluation nodes. Finally, as introduced in detail by the authors in Li et al. (2018c), the discretised formulation of the dual upper bound optimisation problem, Eq. (4.4), can be written as

$$\begin{aligned}
& \max W_{ext} \\
& \text{s.t.} \quad \mathbf{A}_{UB}^{mat\top} \hat{\mathbf{q}}_\sigma + \mathbf{A}_{UB}^{dis\top} \hat{\mathbf{q}}_t^{dis} = \beta \mathbf{A}_{UB}^{bc} \hat{\mathbf{q}}_t^{bc} \\
& \quad \hat{\mathbf{s}}_\sigma^{mat,i} = \hat{\mathbf{a}}_\sigma^{mat,i} + \mathbf{B}_\sigma^{mat} \mathbf{R}_\varepsilon^{mat} \hat{\mathbf{q}}_\sigma^{mat,i} \\
& \quad \hat{\mathbf{s}}_\sigma^{mat,i} \in \mathcal{C} \\
& \quad \hat{\mathbf{s}}_t^{dis,j} = \hat{\mathbf{a}}_t^{dis,j} + \mathbf{B}_t^{dis} \mathbf{R}_t^{dis} \hat{\mathbf{q}}_t^{dis,j} \\
& \quad \hat{\mathbf{s}}_t^{dis,j} \in \mathcal{C}
\end{aligned} \tag{4.6}$$

with the matrices  $\mathbf{A}_{UB}$  obtained by applying the linear compatibility operator to the related shape functions of the velocity (or the velocity jump), within the finite elements (*mat*), at the discontinuities between elements (*dis*), and at the boundary (*bc*). The vectors  $\hat{\mathbf{q}}_\sigma$ ,  $\hat{\mathbf{q}}_t^{dis}$ , and  $\hat{\mathbf{q}}_t^{bc}$  collect all nodal degrees of freedom related to stress-like quantities and surface tractions. Note that, for arbitrary vector  $\mathbf{x}$ , the symbol  $\hat{\mathbf{x}} = \int_{\Omega_e} \mathbf{x} dV$  refers to the volume-integrated quantity over each element. The remaining constraints represent a second-order cone formulation of a general quadratic yield function for both the solid material (*mat*) and the discontinuities (*dis*), with  $i$  and  $j$  ranging from 1 to the number of stress and traction evaluation nodes, respectively. Thereby, the matrices  $\hat{\mathbf{a}}$  and  $\mathbf{B}$  contain strength parameters and the matrices  $\mathbf{R}$  represent transformation operators, rotating the stress tensor into the principal material direction and the surface traction vector into the direction of the corresponding discontinuity. The external work rate in discretised form can be written as

$$W_{ext} = \sum_{bc=1}^{UBC} \sum_{i=1}^6 \beta \mathbf{q}_{\hat{u},loc}^{bc,i\top} \hat{\mathbf{q}}_{t,loc}^{bc,i} \tag{4.7}$$

where  $UBC$  denotes the number of 6-noded boundary surface triangular elements with a prescribed local traction field  $\hat{\mathbf{q}}_{t,loc}^{bc}$  and  $\mathbf{q}_{\hat{u},loc}^{bc}$  represents the related velocity degrees of freedom.

In previous upper bound formulations Krabbenhøft et al. (2005), Makrodimopoulos and Martin (2008), Sloan and Kleeman (1995) only isotropic yield functions based on shear failure mechanisms, e.g. the von Mises or the Mohr-Coulomb yield function, were considered, leading to a straightforward definition of failure at the discontinuities between elements. On the contrary, in the upper bound formulation Eq. (4.6) the quite general orthotropic yield function according to Tsai-Wu can be implemented, reading

$$\mathbf{q}^{i\top} \mathbf{P} \mathbf{q}^i + \left(\frac{1}{2} \mathbf{F}^{+\top} \mathbf{q}^i\right)^2 - \left(1 - \frac{1}{2} \mathbf{F}^{-\top} \mathbf{q}^i\right)^2 \leq 0 \tag{4.8}$$

with  $i$  as the evaluation point of  $\mathbf{q}$  either for the stress field (with subscript  $\sigma$ ) in the element or for the traction field (with subscript  $t$ ) at a discontinuity. The vectors  $\mathbf{F}^+$ ,  $\mathbf{F}^-$ , and the matrix  $\mathbf{P}$  are related to the terms in Eq. (4.6) as follower:

$$\mathbf{a} = \begin{pmatrix} 1 \\ \mathbf{0} \end{pmatrix} \quad \text{and} \quad \mathbf{B} = \begin{pmatrix} -\frac{1}{2} \mathbf{F}^{-\top} \\ \mathbf{D} \\ \frac{1}{2} \mathbf{F}^{+\top} \end{pmatrix} \tag{4.9}$$

where  $\mathbf{D}$  is the decomposed product of  $\mathbf{P} = \mathbf{D}^\top \mathbf{D}$ . Note that, the matrix dimensions are  $\mathbf{F}_\sigma^+ \in \mathfrak{R}^6$ ,  $\mathbf{F}_\sigma^- \in \mathfrak{R}^6$ ,  $\mathbf{P}_\sigma \in \mathfrak{R}^{6 \times 6}$ ,  $\mathbf{D}_\sigma \in \mathfrak{R}^{6 \times 6}$  for the stress-based yield function and  $\mathbf{F}_t^+ \in \mathfrak{R}^3$ ,  $\mathbf{F}_t^- \in \mathfrak{R}^3$ ,  $\mathbf{P}_t \in \mathfrak{R}^{3 \times 3}$ ,  $\mathbf{D}_t \in \mathfrak{R}^{3 \times 3}$  for the traction-based yield function.

In the above, it is assumed that there exists a traction-based yield function for the discontinuities which can also be formulated as second-order cone. Additionally, it needs to be consistent with the stress-based Tsai-Wu criterion to allow for the description of a homogeneous strength distribution within a body. Since a surface traction state within a discontinuity cannot directly be related to a unique 3D stress state at a material point, the derivation of such a traction-based yield function is not straightforward. However, according to Wu and Cervera (2014), we can assume a 3D plastic strain-rate state to be localised with respect to a certain discontinuity if the following constraints are satisfied, for orthotropic yield functions which are differentiable everywhere (e.g. Tsai-Wu yield function):

$$\begin{aligned}\Lambda_{mm}^{dis}(\boldsymbol{\sigma}_{loc}^{dis}) &= \dot{\varepsilon}_{mm}/\dot{\lambda}_\sigma = \partial f(\boldsymbol{\sigma}_{loc}^{dis}, \text{strength par.})/\partial \sigma_{mm}^{dis} = 0 \\ \Lambda_{pp}^{dis}(\boldsymbol{\sigma}_{loc}^{dis}) &= \dot{\varepsilon}_{pp}/\dot{\lambda}_\sigma = \partial f(\boldsymbol{\sigma}_{loc}^{dis}, \text{strength par.})/\partial \sigma_{pp}^{dis} = 0 \\ \Lambda_{mp}^{dis}(\boldsymbol{\sigma}_{loc}^{dis}) &= \dot{\varepsilon}_{mp}/\dot{\lambda}_\sigma = \partial f(\boldsymbol{\sigma}_{loc}^{dis}, \text{strength par.})/\partial \tau_{mp}^{dis} = 0\end{aligned}\tag{4.10}$$

where  $\boldsymbol{\sigma}_{loc}^{dis}$  denotes a 3D stress state at a discontinuity with the local coordinate basis  $(n - m - p)$  with the normal vector of the discontinuity pointing in  $n$ -direction. Note that, each of the constraints in Eq. (4.10) can be formulated as a function of the local stress field  $\boldsymbol{\sigma}_{loc}^{dis}$ . By reformulating Eq. (4.10) using the definition of the Cauchy stress tensor, giving  $t_n^{dis} = \sigma_{nn}^{dis}$ ,  $t_m^{dis} = \tau_{nm}^{dis}$ ,  $t_p^{dis} = \tau_{np}^{dis}$ , the three remaining stress tensor components  $\sigma_{mm}^{dis}$ ,  $\sigma_{pp}^{dis}$ , and  $\tau_{mp}^{dis}$  can be expressed as functions, hereafter referred to as  $L^{dis}$ , of  $t_n^{dis}$ ,  $t_m^{dis}$ ,  $t_p^{dis}$ , and certain strength parameters, reading

$$\begin{aligned}\sigma_{mm}^{dis} &= L_{mm}^{dis}(\mathbf{t}_{loc}^{dis}, \text{strength par.}) \\ \sigma_{pp}^{dis} &= L_{pp}^{dis}(\mathbf{t}_{loc}^{dis}, \text{strength par.}) \\ \sigma_{mp}^{dis} &= L_{mp}^{dis}(\mathbf{t}_{loc}^{dis}, \text{strength par.})\end{aligned}\tag{4.11}$$

Therefrom, a relationship between the local stress field and the local traction field on  $\Gamma^{dis}$ ,  $\boldsymbol{\sigma}_{loc}^{dis} = \mathbf{L}_t^{dis} \mathbf{t}_{loc}^{dis}$ , under the condition of plastic strain localisation, can be derived. Finally, by making use of this relationship, it is possible to ‘‘project’’ the stress-based formulation of the Tsai-Wu yield function  $f(\boldsymbol{\sigma}_{loc}^{dis}) \leq 0$  onto a discontinuity, delivering a consistent traction-based yield function  $f(\mathbf{t}_{loc}^{dis}) \leq 0$ .

The main focus of this work is the performance assessment of this approach and to point out how such an approach could be utilised for future concepts of numerical limit analysis. For this reason, in the next section, several numerical examples are presented and discussed in detail.

### 4.3 Numerical results

In this section, numerical results obtained using the proposed upper bound formulation with selectively activated velocity discontinuities are discussed. Two benchmark

problems, with isotropic yield functions, are used for basic verification of the presented approaches. By means of further examples it is demonstrated that orthotropic plastic failure can also be handled appropriately. Moreover, it will be shown that through the introduction of velocity discontinuities across properly-arranged prescribed interfaces, high-quality upper bound results can be obtained with relatively coarse meshes and, thus, very efficiently. Note that, for convenience, the upper bound results obtained using formulations, with and without velocity discontinuities are referred to as continuous and discontinuous upper bound results, respectively.

All computations presented in the following were performed on a Linux desktop machine, with an AMD Phenom(tm) II X6 1090T CPU (6 cores) and 8GB of RAM. The commercial software package Abaqus was used for mesh generation, but all other pre- and post-processing tasks as well as the assembly of the SOCP optimisation problems were carried out by self-written codes in Fortran. The SOCP optimisation problems themselves were solved using the commercial software MOSEK ApS (2017), which is based on the conic interior-point algorithm described in Andersen et al. (2003).

### 4.3.1 Rigid strip footing

The rigid strip footing problem, as illustrated in Figure 4.1a, with a weightless purely cohesive material is a common benchmark for limit analysis approaches. Under the assumption of material failure according to Tresca,  $\tau \leq c$ , the ultimate load can be obtained by the classical Prandtl solution  $N_c^{ref} = P_{lim}/c = 2 + \pi$  Prandtl (1920), where  $N_c$  is the bearing capacity factor,  $P_{lim}$  the collapse load limit,  $\tau$  the principal shear stress, and  $c$  the coefficient of cohesion. Under plane strain conditions, the Tresca yield function is identical to the von Mises yield function  $\sqrt{J_2} \leq c$ , with  $J_2$  as the second deviatoric stress invariant.

Using the yield function formulation according to Eq. (4.8), the von Mises criterion is defined through

$$\mathbf{P}_\sigma^{mat} = \frac{1}{3c^2} \begin{pmatrix} 1 & -0.5 & -0.5 & 0 & 0 & 0 \\ -0.5 & 1 & -0.5 & 0 & 0 & 0 \\ -0.5 & -0.5 & 1 & 0 & 0 & 0 \\ 0 & 0 & 0 & 3 & 0 & 0 \\ 0 & 0 & 0 & 0 & 3 & 0 \\ 0 & 0 & 0 & 0 & 0 & 3 \end{pmatrix} \quad \mathbf{F}_\sigma^{mat,+} = \mathbf{F}_\sigma^{mat,-} = \mathbf{0} \quad (4.12)$$

A consistent traction-based yield function is easily obtained (Makrodimopoulos and Martin, 2008) by applying the shear strength as the tangential strength at discontinuities, giving

$$\mathbf{P}_t^{dis} = \frac{1}{c^2} \begin{pmatrix} 0 & 0 & 0 \\ 0 & 1 & 0 \\ 0 & 0 & 1 \end{pmatrix} \quad \mathbf{F}_t^{dis,+} = \mathbf{F}_t^{dis,-} = \mathbf{0} \quad (4.13)$$

The geometric boundary conditions and loading are given in Figure 4.1a, and an example 3D representation of the model is plotted in Figure 4.1b with respect to the global coordinate basis  $(x - y - z)$  and an illustrative discretisation using 419 tetrahedron

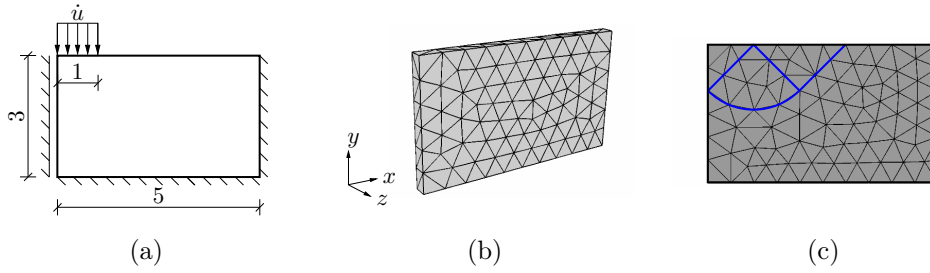


Figure 4.1: Rigid strip footing benchmark example. (a) Geometry and boundary conditions; (b) example 3D model and illustrative discretisation with 419 elements; (c) the prescribed interfaces for velocity jumps according to Prandtl's failure mechanism (445 elements).

elements. By applying symmetric boundary conditions at the  $z^-$  and  $z^+$  boundary surfaces, plane strain conditions are enforced. Thus, in the following, all results will be plotted in the  $x - y$  plane only. The rough footing interface condition is applied by setting the velocities in the  $x$  direction to zero for all nodes in the footing region.

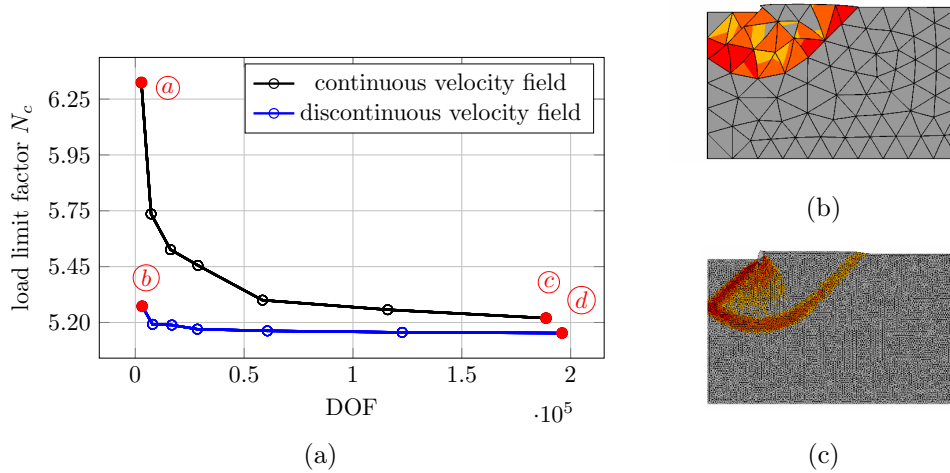


Figure 4.2: Numerical upper bound results for the rigid strip footing problem. (a) Load limit factor  $N_c$ , obtained using continuous and discontinuous velocity fields, as a function of DOF; (b) upper bound failure mode using discontinuities and 445 elements (range of plotted yield function values (robjv)  $[-3 \times 10^{-8} : 0]$ ); (c) upper bound failure mode using continuous velocity field with 31 081 elements (robjv  $[-5 \times 10^{-9} : 0]$ ).

The obtained numerical upper bound results for different fineness of discretisation or degrees of freedom (DOF) are plotted in Figure 4.2a. The black curve represents the results for continuous velocity fields, and shows a clear convergence behaviour. Measuring the difference between the upper bound results and the analytical reference  $N_c^{ref}$ , as  $diff(\%) = (N_c^{ub} - N_c^{ref}) * 100 / (N_c^{ub} + N_c^{ref})$ , a *diff* of 12.92 % (2 790 DOF) for point *a* and 0.95 % for point *c* with 188 685 DOF are obtained. The corresponding CPU times are 2.09 min versus 41.85 min.

In the next step, partitions are introduced into the model according to Prandtl's failure mechanism (Prandtl, 1920), see Figure 4.1c, to allow velocity jumps across prescribed



discontinuities. Since velocity jumps are only allowed through these prescribed interfaces, the number of DOF is not increased significantly. The blue curve in Figure 4.2a shows the related results, again for different numbers of DOF. A *diff* of 1.60 % is obtained for point *b* (3 147 DOF) and 0.13 % for point *d* (196 077 DOF), with corresponding CPU times of 0.56 min and 41.62 min.

With a minimum difference of below 1 % for the obtained best upper bounds compared to the analytical solution, the proposed formulations withstand this basic verification and can be assessed as performing well. Especially when velocity discontinuities are introduced, very good upper bounds can be obtained even with coarse meshes (see point *b* and the related failure mechanism in Figure 4.2b). Of course, this is only possible if the failure mechanism is known in advance and, thus, does not yet represent added value for general calculations. However, the potential of velocity discontinuities to capture very localised failure is evidently huge and, sensibly used, can greatly increase computational efficiency.

### 4.3.2 Block with asymmetric holes

The block with asymmetric holes under tensile loading is a commonly-used benchmark for so-called direct methods (e.g. limit analysis and shakedown analysis) first studied by Zouain et al. (2002), as illustrated in Figure 4.3a. Later on, this problem was studied by Makrodimopoulos and Martin (2007) using an upper bound formulation with a continuous quadratic velocity field and the plane strain Mohr-Coulomb yield function was applied to the material. Their results are used for verification and as reference solution in the following. Moreover, the benefit of using sensibly-arranged velocity discontinuities is further discussed, and a simple strategy to find such arrangements based on preliminary upper bound results is proposed. Geometry, material properties, and boundary conditions (Figure 4.3a) are assigned as in Makrodimopoulos and Martin (2007). The model is built by 3D finite elements with the global coordinate basis ( $x - y - z$ ), similarly to Figure 4.1b, and again symmetric boundary conditions at the  $z-$  and  $z+$  boundary surfaces are applied.

#### 4.3.2.1 Mohr-Coulomb failure criterion

In Makrodimopoulos and Martin (2007), the Mohr-Coulomb yield function was used with a friction angle  $\phi = 30^\circ$ . For our example, the equivalent Drucker-Prager yield function,  $\sqrt{J_2} \leq A - BI_1$ , is assigned to the material, defined by inserting

$$\mathbf{P}_\sigma^{mat} = \frac{1}{3A^2} \begin{pmatrix} 1 & -0.5 & -0.5 & 0 & 0 & 0 \\ -0.5 & 1 & -0.5 & 0 & 0 & 0 \\ -0.5 & -0.5 & 1 & 0 & 0 & 0 \\ 0 & 0 & 0 & 3 & 0 & 0 \\ 0 & 0 & 0 & 0 & 3 & 0 \\ 0 & 0 & 0 & 0 & 0 & 3 \end{pmatrix} \quad \mathbf{F}_\sigma^{mat,+} = \mathbf{0} \quad \mathbf{F}_\sigma^{mat,-} = \frac{1}{A^2} \begin{pmatrix} 2AB \\ 2AB \\ 2AB \\ 0 \\ 0 \\ 0 \end{pmatrix} \quad (4.14)$$

into Eq. (4.8), with the strength parameters  $A = 0.8321c$  and  $B = 0.1601$ . For the consistent traction-based yield function these terms read

$$\mathbf{P}_t^{dis} = \frac{1}{c^2} \begin{pmatrix} -\tan^2 \phi & 0 & 0 \\ 0 & 1 & 0 \\ 0 & 0 & 1 \end{pmatrix} \quad \mathbf{F}_t^{dis,+} = \mathbf{0} \quad \mathbf{F}_t^{dis,-} = \frac{1}{c^2} \begin{pmatrix} 2c \tan \phi \\ 0 \\ 0 \end{pmatrix} \quad (4.15)$$

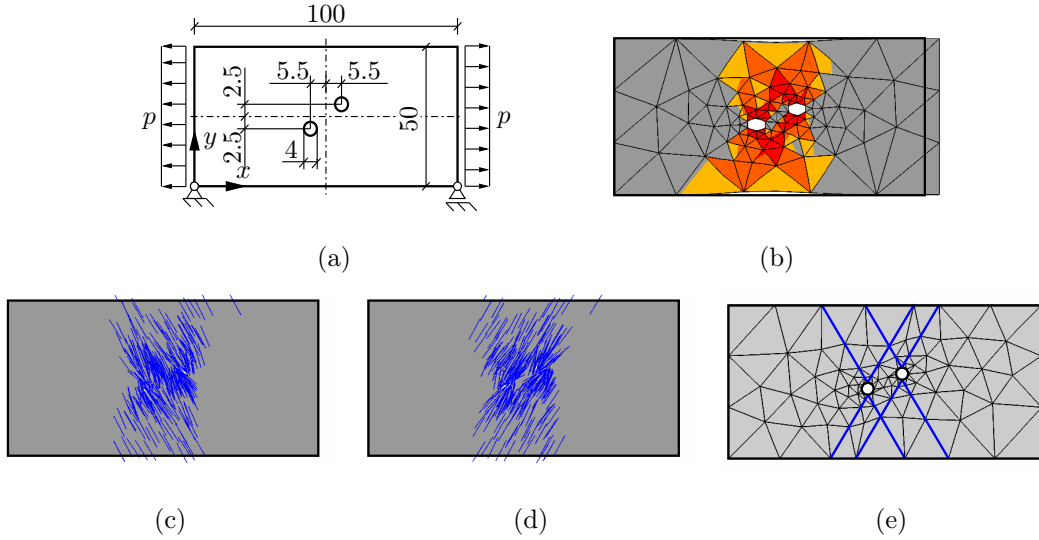


Figure 4.3: Block with asymmetric holes using the Drucker-Prager failure criterion. (a) Geometry and boundary conditions; (b) upper bound failure mode (519 elements, robjv  $[-5 \cdot 10^{-6} : 0]$ ); (c) and (d) potential orientations of plastic strain localisation; (e) prescribed discontinuities based on (c) and (d).

In the previous example, it was shown that velocity discontinuities can improve the upper bound significantly if they are appropriately arranged with respect to potential failure surfaces. For this reason, subsequently, the following strategy is pursued. Based on an upper bound calculation with a continuous velocity field and a relatively coarse mesh, as shown in Figure 4.3b, potential discontinuity directions, where plastic failure could localise, are computed at each integration point where plastic flow takes place according to Eq. (4.10). The resulting orientations are plotted in Figure 4.3c and Figure 4.3d. With respect to the  $x$  axis the mean orientations, obtained by taking the volume average over all orientations, are approximately  $\bar{\theta}_1 = -60^\circ$  and  $\bar{\theta}_2 = 60^\circ$ , as would be expected from the underlying failure criterion. Next, according to these average directions of possible localised plastic failure, and by referring to the points with maximum plastic strain-rates, the partitions (blue lines) shown in Figure 4.3e are implemented into the model. Finally, the model is re-meshed and velocity discontinuities are introduced along the partitions.

This procedure was applied to several models with different level of mesh refinement (DOF) and compared to calculations performed without such discontinuities. The obtained upper bounds for the limit load factor  $N_c$  are plotted in Figure 4.4a. Based on the upper bound result with only 3 327 DOF (point  $a$ ), velocity discontinuities were

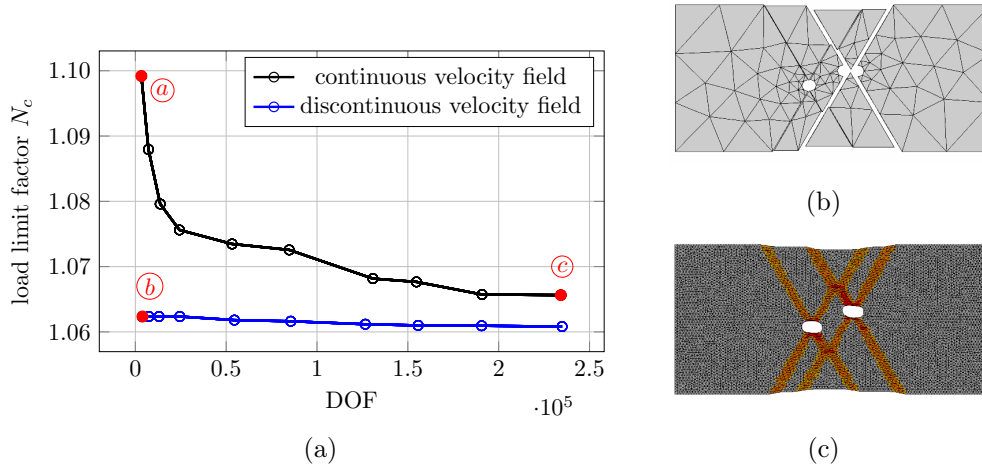


Figure 4.4: Numerical upper bound results for the block with asymmetric holes example using the Drucker-Prager yield function. (a) Load limit factor  $N_c$ , obtained using continuous and discontinuous velocity fields, as a function of DOF; upper bound results (robjv  $[-1 \cdot 10^{-4} : 0]$ ) (b) with discontinuities using 504 elements and (c) with continuous velocity field using 34 875 elements.

introduced into the model, leading to a strong improvement of the upper bound (point *b*) by adding only 585 DOF. The failure mechanism associated with point *b* is shown in Figure 4.4b. To achieve a similarly good upper bound result and related localised failure mechanism without the introduction of discontinuities, the mesh needed to be refined significantly, as shown in Figure 4.4c as the associated failure mechanism to point *c*. The CPU time required to obtain point *c* and the mechanism in Figure 4.4c was 37.87 min, whereas point *b* with the mechanism shown in Figure 4.4b only took 0.38 min. Although an adaptive mesh refinement would probably be more efficient than the uniform mesh refinement performed, the performance of sensibly-arranged discontinuities, even in a coarsely discretised model, is excellent. Comparing the upper bound result of point *b* ( $N_c = 1.062$ ) to the best result in Makrodimitropoulos and Martin (2007) ( $N_c = 1.063$ ) there is almost no difference. However, the upper bound initiated by point *b* was obtained with 3 912 DOF compared to 79 955 DOF in the reference.

In the following, this approach is extended to orthotropic material behaviour, using the Tsai-Wu criterion as the indicator for plastic failure.

### 4.3.2.2 Tsai-Wu failure criterion

The strength parameters used for the example correspond to the typical orthotropic material spruce wood and are taken from Dorn (2012), leading to

$$\mathbf{P}_\sigma^{mat} = \begin{pmatrix} 2.434\text{E-}4 & 0 & 0 & 0 & 0 & 0 \\ 0 & 6.588\text{E-}2 & 0 & 0 & 0 & 0 \\ 0 & 0 & 6.588\text{E-}2 & 0 & 0 & 0 \\ 0 & 0 & 0 & 1.181\text{E-}2 & 0 & 0 \\ 0 & 0 & 0 & 0 & 2.973\text{E-}2 & 0 \\ 0 & 0 & 0 & 0 & 0 & 1.181\text{E-}2 \end{pmatrix} \text{MPa}^{-2}$$

$$\mathbf{F}_\sigma^{mat,+} = \mathbf{F}_\sigma^{mat,-} = (-6.573\text{E-}3 \quad 8.564\text{E-}2 \quad 8.564\text{E-}2 \quad 0 \quad 0 \quad 0)^\top \text{MPa}^{-1} \quad (4.16)$$

inserted into the general yield function in Eq. (4.8), defined with respect to the local coordinate basis ( $L - T - R$ ). Due to the orthotropic characteristics, the consistent traction-based yield function is highly dependent on the orientation of the discontinuity at which it describes plastic failure. Thus, for each introduced discontinuity, a different set of strength parameters had to be computed, determined by the ‘‘projection’’ procedure introduced at the end of Section 4.2. Then, the equivalence between the material strength within elements and the strength behaviour at discontinuities is guaranteed.

In the following, this orthotropic strength behaviour is assigned to the block with asymmetric holes, for two different material orientations, to assess the capability of the presented approach in handling anisotropic strength behaviour.

#### Material orientation 1

In the first case, the longitudinal orientation  $L$  of the material is identical to the  $y$ -direction, as indicated in Figure 4.5a. Moreover, the local material coordinate basis ( $L - T - R$ ) is defined with  $L$  and  $T$  as the in-plane axes and  $R$  as the out-of-plane axis.

The preliminary upper bound calculation, based on which the arrangement of discontinuities will be defined, is carried out using a coarse mesh with 519 elements. The corresponding failure mechanism is displayed in Figure 4.5b, and the computed orientations of potential discontinuities are shown in Figures 4.5c and 4.5d. Averaging over these orientations results in two mean angle values of  $\theta_1 = -84^\circ$  and  $\theta_2 = 84^\circ$  with respect to the  $x$ -axis. According to these mean angles and starting from the points of highest plastic strain-rate (present at the boundaries of the holes), the velocity discontinuities shown in Figure 4.5e are implemented into the model. Subsequently the model is re-meshed and a further upper bound calculation is performed.

The numerical upper bounds on the collapse load for different levels of mesh refinement (DOF) with and without discontinuities are plotted in Figure 4.6. Again, the introduction of velocity discontinuities improves the upper bound significantly, while hardly increasing the DOF. In contrast to the isotropic case before, plastic failure also occurs in the solid finite elements between discontinuities (Figure 4.6b), indicating that the orientation or arrangement of discontinuities could be improved. This can also be seen by looking at the plastic regions in Figure 4.6c, which do not exactly match the defin-

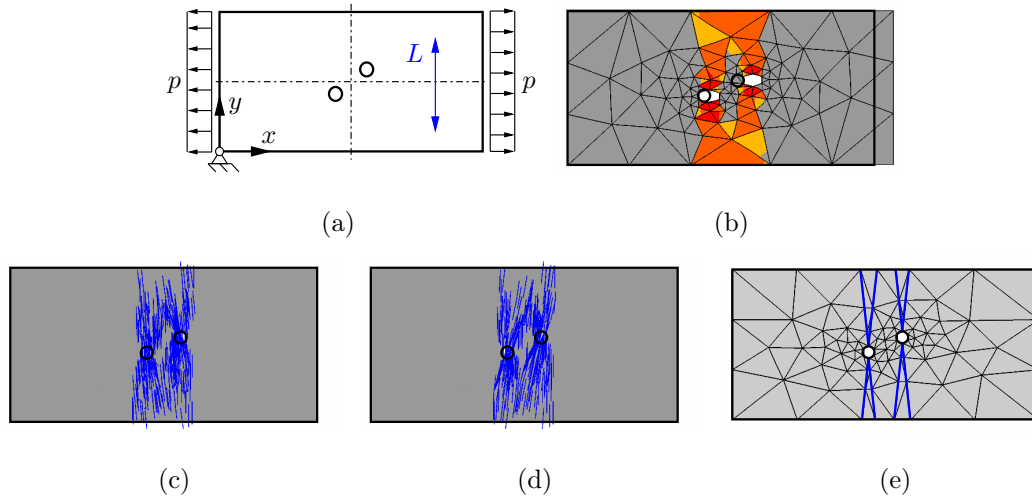


Figure 4.5: Block with asymmetric holes using the Tsai-Wu orthotropic failure criterion. (a) Geometry, boundary conditions, and the principal material orientation indicated by the blue arrow; (b) upper bound result using 519 elements ( $robjv [-1.5 \cdot 10^{-6} : 0]$ ); (c) and (d) potential orientations of plastic strain localisation; (e) prescribed discontinuities based on (c) and (d).

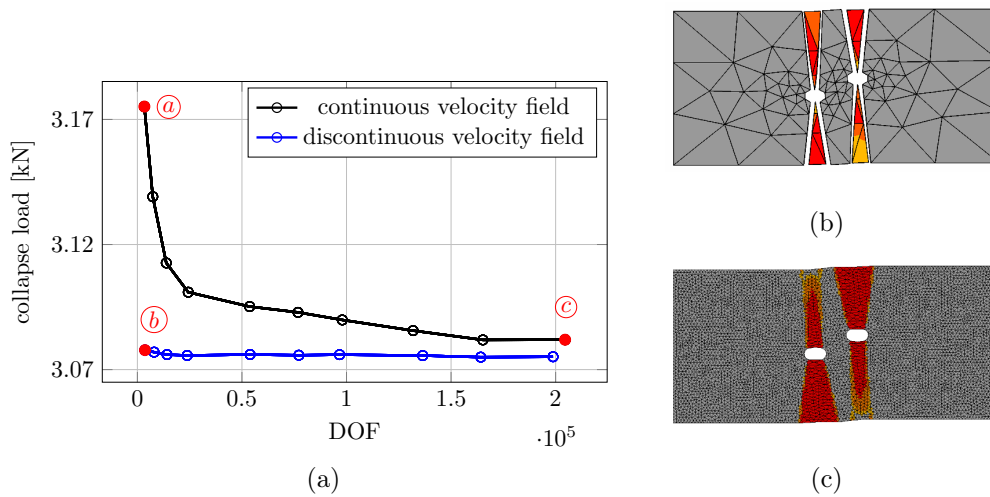


Figure 4.6: Numerical upper bound results for the block with asymmetric holes with the principal material direction as defined in Figure 4.5a. (a) Collapse load using continuous and discontinuous velocity fields as a function of DOF; upper bound failure mode ( $robjv [-9 \cdot 10^{-6} : 0]$ ) using (b) discontinuities within a coarse mesh (486 elements) and (c) a continuous velocity field with a fine mesh (38 537 elements).

ition of discontinuities above. It seems that the arrangement of discontinuities does not necessarily have to be ideal in order to achieve considerable improvement in the numerical upper bound results.

## Material orientation 2

In the second case, the local material orientation basis ( $L - T - R$ ) is rotated by  $30^\circ$  in the  $x - y$  plane, as indicated in Figure 4.7a. Again, based on an efficient preliminary upper bound calculation (Figure 4.7b), possible orientations of discontinuities are computed, resulting in mean angles of  $\bar{\theta}_1 = \pm 80^\circ$  and  $\bar{\theta}_2 = -58^\circ$ . The introduced velocity discontinuities are shown in Figure 4.7e.

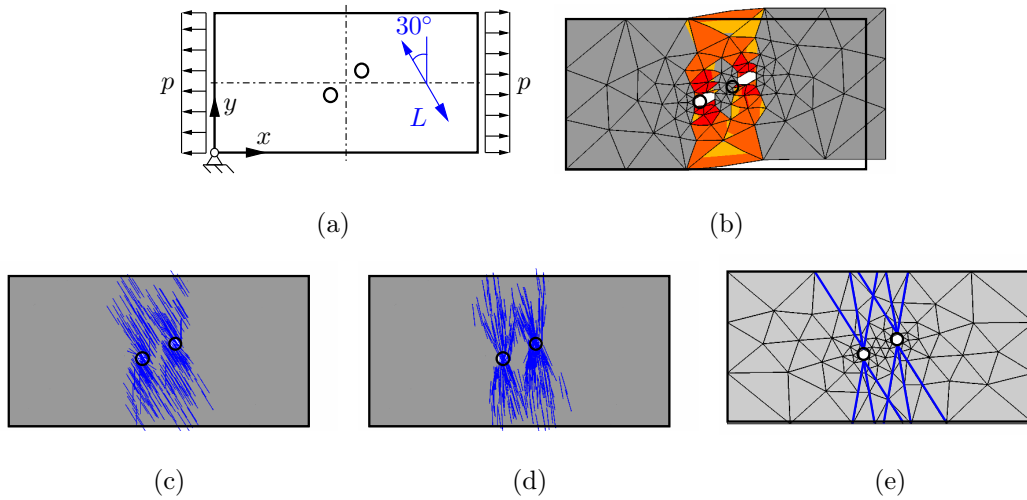


Figure 4.7: Block with asymmetric holes using the Tsai-Wu orthotropic failure criterion. (a) Geometry, boundary conditions, and the principal material orientation indicated by the blue arrow; (b) upper bound result using 519 elements ( $\text{robjv} [-3 \cdot 10^{-6} : 0]$ ); (c) and (d) potential orientations of plastic strain localisation; (e) prescribed discontinuities based on (c) and (d).

As before, all numerical upper bounds are plotted in Figure 4.8, showing the strong performance increase achieved by the selectively introduced discontinuities. Interestingly, the intensity of localisation of plastic failure is slightly different comparing the approaches with (Figure 4.8b) and without (Figure 4.8c) discontinuities. It seems that with discontinuities the real failure mechanism can be better represented, since the main plastic failure direction is well aligned with the principal material direction (wood fibre direction) as expected.

### 4.3.3 Shear test on block

The last example is used to assess the capability of this upper bound formulation regarding localised shear failure in orthotropic materials. The setup of the model is shown in Figure 4.9a and is designed to represent a characteristic as well as often critical loading

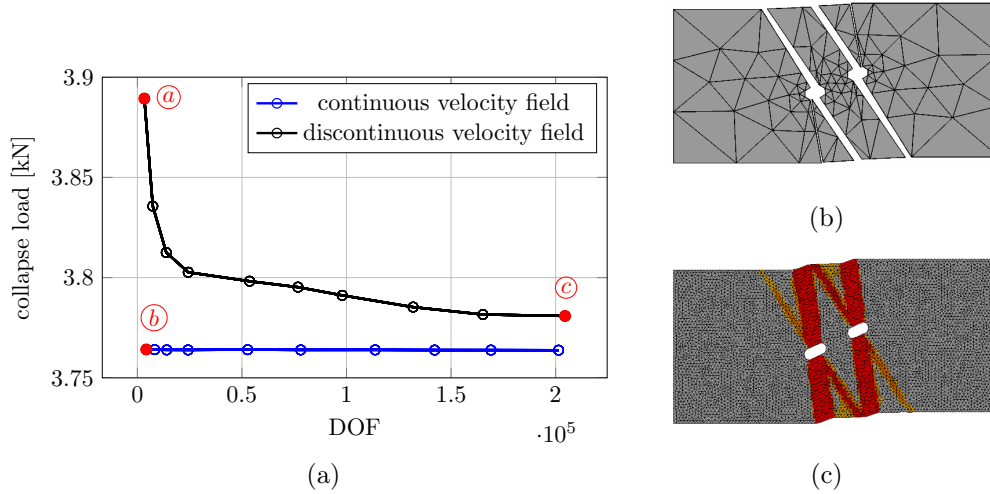


Figure 4.8: Numerical upper bound results for the block with asymmetric holes with the principal material direction as defined in Figure 4.7a. (a) Collapse load using continuous and discontinuous velocity fields as a function of DOF; upper bound failure mode (robjv  $[-2 \cdot 10^{-5} : 0]$ ) using (b) discontinuities within a coarse mesh (524 elements) and (c) a continuous velocity field with a fine mesh (34 875 elements).

state in wood-based products, like glued-laminated timber and cross-laminated timber. As in the previous examples, the boundary conditions are chosen so as to represent plane strain conditions, and the Tsai-Wu failure criterion with strength parameters representing spruce wood is assigned to the material.

Again, based on a preliminary upper bound calculation using a very coarse mesh (Figure 4.9c1), the orientations of possible discontinuities are determined (Figure 4.9c2) and, based on that information, velocity discontinuities are implemented into the model (Figure 4.9c3). The result obtained with this discontinuity arrangement is shown in Figure 4.9d1, where the dominant plastic failure appears within the solid elements between the introduced discontinuities but not at the discontinuities themselves, and, thus, the potential of the velocity discontinuities has not been activated sufficiently. For this reason, a second iteration was carried out, again computing the orientations of possible discontinuities in all plastic regions (Figure 4.9d2). Based on that information a revised discontinuity pattern was implemented as shown in Figure 4.9d3. The corresponding failure mechanism is displayed in Figure 4.10b and it can be seen that, now, localised failure occurs exclusively at the last-introduced discontinuity. The related upper bound (point *b* in Figure 4.10a) is very good in comparison to the preliminary model without discontinuities (point *a*) but uses a similar number of DOF. Moreover, the failure mechanism agrees well with that obtained using a very fine mesh and no discontinuities (Figure 4.10c).

## 4.4 Summary and conclusions

In this work, a 3D numerical upper bound formulation using a quadratic approximation of the velocity field and allowing for the implementation of orthotropic yield functions

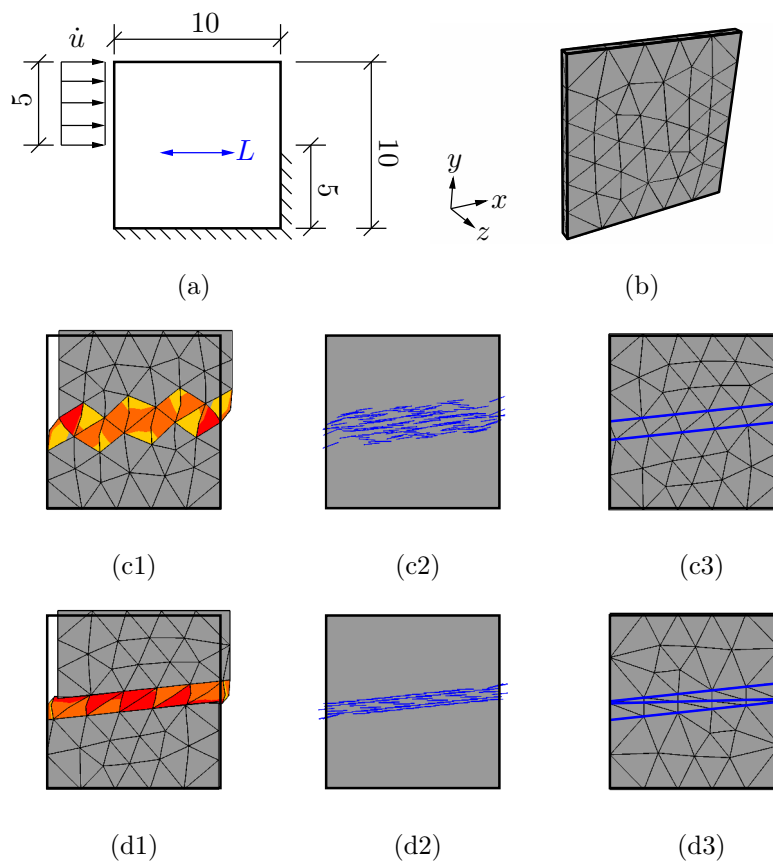


Figure 4.9: Block under shear loading. (a) Geometry, boundary conditions and the principal material orientation indicated by the blue arrow; (b) illustrative 3D model with 222 finite elements; (c) and (d) two iteration steps for the definition of the discontinuities, with (c1) and (d1) as the upper bound result ( $\text{robjv} [-2 \cdot 10^{-9} : 0]$ ), (c2) and (d2) as the potential orientations of plastic strain localisation, and (c3) and (d3) as the prescribed discontinuities based on (c2) and (d2).



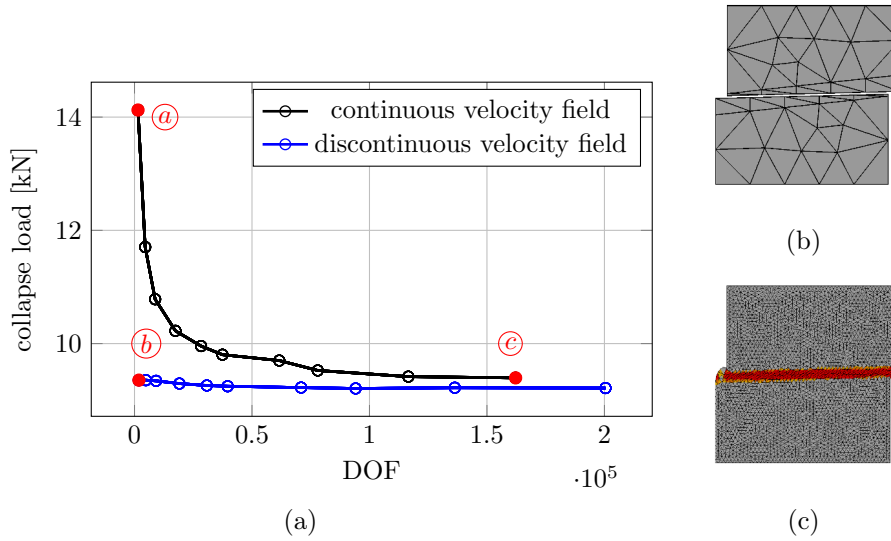


Figure 4.10: Numerical upper bound results for the block under shear loading (a) Collapse load using continuous and discontinuous velocity fields as a function of DOF; upper bound failure mode ( $\text{robjv} [-4 \cdot 10^{-9} : 0]$ ) using (b) discontinuities within a coarse mesh (242 elements) and (c) a continuous velocity field with a fine mesh (32 062 elements).

has been briefly proposed. Furthermore, the implementation of velocity discontinuities into this formulation has been presented, along with the concept of how to derive the necessary traction-based yield functions which guarantees a consistent description of the material strength behaviour across discontinuities. Based on that formulation, compatibility as well as the associated plastic flow rule are fulfilled throughout the whole body and, thus, rigorous upper bounds are obtained.

The formulation has been verified by means of two classical examples, the rigid strip footing and the block with asymmetric holes. Subsequently, based on preliminary upper bound calculations with very coarse meshes, the orientation of potential slip lines where very localised plastic flow may occur could be determined. Based on that information, sensibly-arranged velocity discontinuities were incorporated into the finite element models. In that way, upper bounds could be improved significantly with essentially no increase of degrees of freedom.

It has also been shown that this concept works very well when assigning orthotropic failure behaviour to the material. If the first introduction of discontinuities does not improve the upper bound significantly, which means that most of the plastic dissipation still takes place in solid elements, a second iteration step can improve the situation, as shown by means of the shear test on a block. This may represent an important finding for future developments, which could lead to a general algorithm for an adaptive introduction and re-arrangement of velocity discontinuities, as an efficient alternative to existing adaptive mesh refinement strategies. Especially for laminated structures and orthotropic materials, where plastic failure often occurs in very localised mechanism, as shown for wood at the microscale in Lukacevic and Füssl (2016), Lukacevic et al. (2014b) and at the product scale in Hochreiner et al. (2013, 2014), such an approach could have great value. Moreover, the efficiency of numerical limit analysis in combination with the accuracy of the extended finite element formulations presented in Lukacevic and Füssl

(2016), Lukacevic et al. (2014b) could lead to more flexible engineering design tools, in which the focus can be switched between accuracy and efficiency as needed.

## **Acknowledgments**

Financial support for this work in the framework of the PhD School DokIn' Holz funded by the Austrian Federal Ministry of Science, Research and Economy and the Austrian Association of Wood Industries is gratefully acknowledged. We also gratefully acknowledge the financial support of this work by the Austrian Science Fund (FWF) through the Erwin Schrödinger Fellowship J3748-N30.

# An algorithm for adaptive introduction and arrangement of velocity discontinuities within 3D finite-element-based upper bound limit analysis approaches (Li et al., 2018a)

Authored by Mingjing Li, Josef Füssl, Markus Lukacevic, Josef Eberhardsteiner & Chris M. Martin

Submitted to *Computer Methods in Applied Mechanics and Engineering*

**Abstract:** This paper presents a new adaptive strategy to efficiently exploit velocity discontinuities in 3D finite-element-based upper bound limit analysis formulations. Based on an initial upper bound result, obtained with a conventional approach without velocity discontinuities, possible planes of plastic flow localisation are determined at each strain-rate evaluation node and, subsequently, this information is used to sequentially introduce discontinuities into the considered discretised structure. During a few iterations, by means of introducing new and adjusting existing discontinuities, an optimal velocity discontinuity layout is obtained. For the general 3D case, the geometry of this layout is defined by the well-known level-set method, standardly used to define the geometry of cracks in extended finite element method.

To make this method also applicable for orthotropic strength behaviours, traction-based yield functions defining the plastic flow across discontinuities are derived from their stress-based counterparts. This procedure is outlined in detail and the obtained traction-based yield functions are verified numerically, to guarantee a consistent strength behaviour throughout the whole discretised structure.

By means of three different examples, including isotropic as well as orthotropic yield

functions, the performance of the proposed strategy is investigated and upper bound results as well as failure modes are compared to reference solutions. The proposed approach delivered reliable upper bounds for each example and the majority of plastic flow takes place across the sensibly-arranged discontinuities. For this reason, very good upper bounds can be obtained with a quite coarse finite element mesh and only few introduced velocity discontinuities. This represents an attractive alternative to commonly-used adaptive mesh refinement strategies, where often a huge amount of degrees of freedom needs to be added to capture localised failure.

**Keywords:** adaptive strategy, velocity discontinuities, upper bound limit analysis, level-set method, orthotropic strength behaviours, localised failure.

## 5.1 Introduction

Limit analysis has been proven as a powerful computational method for strength predictions of a wide range of materials used in practical engineering areas, such as soil, masonry, and composite materials (Chen, 2013, Füssl et al., 2008, Milani et al., 2006a, 2010, Nielsen and Hoang, 2016, Sloan, 2013). Originally, the main objective of limit analysis has been determining the ultimate load a structure, exhibiting elastoplastic material response, can resist without structural collapse. Since structures lose the capability to store further external work as recoverable internal energy at structural collapse, limit analysis exclusively focuses on the time instant when the critical plastic dissipation rate is achieved.

This problem can be stated as: *Find the kinematically admissible velocity field which minimises the energy dissipation rate over the set of all statically admissible stress fields which maximise the dissipated energy*, according to Ciria et al. (2008). Based on the assumptions of small deformations, perfectly plastic material behaviour, and associated plastic flow, the plastic bounding theorems by Drucker et al. (1951, 1952) are normally employed, leading to a lower and an upper bound of the collapse load multiplier. The lower bound theorem states that, the highest load supported by a statically admissible stress field, which satisfies equilibrium, the static boundary condition, and a plastic yield criterion, is an optimal lower bound on the exact collapse load. In contrast, the upper bound theorem states that, when the velocity field is kinematically admissible by satisfying compatibility, the kinematic boundary conditions and an associated plastic flow rule, the lowest load determined by equating the external work rate to the internal plastic dissipation rate is an optimal upper bound on the exact collapse load. Note that this paper mainly focuses on the upper bound problem.

Since analytical solutions of limit analysis are normally limited to simple problems, the limit analysis theorems have been successfully implemented in numerical formulations since the early 70s and excellent practical capabilities have been achieved in such numerical approaches, from simple two-dimensional (2D) benchmark examples to complicated three-dimensional (3D) problems. Time efficiency and solution quality of these approaches have also benefited from the rapid development of mathematical programming methods used to solve the underlying optimisation problems.

In early implementations, during the last three decades of the 20th Century, these optimisation problems were solved using linear programming methods by linearising the applied plastic yield functions, as can be found in Anderheggen and Knöpfel (1972),

Belytschko and Hodge (1970), Lysmer (1970), Maier et al. (1972), Sloan (1988, 1989), Sloan and Kleeman (1995). Lyamin and Sloan (2002a,b) and Krabbenhøft and Damkilde (2003) were the pioneers who used nonlinear programming methods to solve numerical limit analysis formulations with nonlinear yield functions formulated in their native form. However, since such implementations require differentiability of the yield surfaces, local smoothening procedures are often necessary. Alternatively, as proposed by Makrodimopoulos and Martin (2006, 2007), Ciria and Peraire (2004), and Krabbenhøft et al. (2007), second-order cone programming (SOCP) has been proven to be a robust and efficient method to solve large-scale nonlinear optimisation problems of numerical limit analysis, allowing most commonly-used yield functions to be formulated in their native form. Also in this work SOCP is employed, since all used yield functions can be formulated as second-order cones, including the isotropic von Mises yield function, the Drucker-Prager yield function, as well as the orthotropic Tsai-Wu yield function.

On the other hand, the performance of numerical limit analysis formulations also heavily depends on the discretisation method and the related shape functions. Since rigorous upper bound solutions require the associated plastic flow rule being satisfied at each point of the structures, it is straightforward to use constant strain elements (Bottero et al., 1980, Ciria and Peraire, 2004, Lyamin and Sloan, 2002b, Sloan, 1989, 2013). To achieve a higher quality of upper bound solutions, the simplex strain element using linear shape functions for the strain-rate field has been introduced by Makrodimopoulos and Martin (2007), Martin and Makrodimopoulos (2008). In their implementations, associated plastic flow can still be guaranteed within each element since the strain-rate is linear and the associated plastic flow rule is evaluated at all vertices. From the numerical point of view, further performance improvements can be expected by using higher order interpolation functions. For this purpose, several different implementations were developed using the element-free Galerkin method by Le et al. (2009, 2010b), the radial point interpolation meshless method by Liu and Zhao (2013), Yu et al. (2016), and the smoothed finite element method by Le et al. (2010c), Nguyen-Xuan and Liu (2015). However, in such implementations, it is difficult to guarantee both compatibility and satisfaction of the associated plastic flow rule in each point of the structure, thus, the so-obtained numerical upper bounds are not necessarily rigorous.

Beside using higher order interpolation functions, velocity discontinuities can be implemented into numerical limit analysis formulations, adding additional degrees of freedom to the discretised structure. In an early implementation by Sloan and Kleeman (1995), velocity discontinuities were introduced in finite-element-based upper bound formulations where linear velocity jumps were allowed between constant strain elements introduced in Sloan (1989). As a development of this approach, zero-thickness interface elements were introduced by Krabbenhøft et al. (2005), allowing the use of general yield criteria. In a contribution by Makrodimopoulos and Martin (2008), velocity discontinuities were introduced between simplex strain elements, defined in Makrodimopoulos and Martin (2007), allowing both linear and quadratic velocity jumps, showing a robust and efficient performance for a large number of applications.

Alternative approaches of numerical upper bound formulations were proposed by Chen et al. (2003) and Milani et al. (2006a,b, 2010), where all solid elements are considered as rigid and plastic failure is only possible across velocity discontinuities between elements. Such implementations exhibit good performance for certain engineering problems, e.g. in masonry engineering, but the strong dependence of the solution quality on the finite

element mesh restricts its application, and even adaptive mesh refinement cannot fully compensate this drawback. For this reason, a sequential linear programming method was applied by Milani and Lourenço (2009), to iteratively adapt the finite element mesh. This approach is able to increase the efficiency of velocity discontinuities, but so far it has been proposed only for 2D problems and the original mesh has to be fine enough to provide a sufficient number of velocity discontinuities, since no additional velocity discontinuity can be introduced during the adaptive iterations. Another interesting approach is the so-called discontinuity layout optimisation, presented by Smith and Gilbert (2007) for 2D and Hawksbee et al. (2013) for 3D problems. Thereby, velocity discontinuities are determined by using a truss layout optimisation algorithm based on a prescribed grid. Although this approach performs well for 2D problems, the determination of complex failure mechanisms in 3D solid bodies requires a very fine grid and large computational effort.

For this reason, in the author's opinion, the most promising approach so far to obtain rigorous upper bounds seems to be the use of solid finite elements with or without velocity discontinuities. Due to the fact that plastic failure often occurs very localised, adaptive mesh refinement has been intensively investigated in Borges et al. (2001), Ciria and Peraire (2004), Ciria et al. (2008), Martin (2011), Muñoz et al. (2009), Nguyen-Xuan and Liu (2015), Nguyen-Xuan et al. (2017). However, such strategies normally lead to very fine meshes in failure regions and, thus, increase the number of degrees of freedom and computational effort significantly.

Recently, an alternative approach has been presented by the authors (Li et al., 2018b), where finite-element-based upper bound formulations with sensibly-arranged velocity discontinuities have been proven reliable and efficient, without the need of intensive mesh refinement in failure regions. Additionally, although the implementation of orthotropic yield functions in numerical upper bound formulations has been presented in several publications (Capsoni et al., 2001a,b, Füssl et al., 2017, Li, 2011, Li et al., 2018c,d), to the authors' knowledge, the combination of orthotropic yield functions and velocity discontinuities was presented by the authors in Li et al. (2018b) for the first time. In order to apply this approach to more general problems, in this paper, a comprehensive introduction on the numerical implementations as well as an adaptive introduction and adjustment strategy on the sensible arrangement of velocity discontinuities will be presented.

Thus, the main objectives of this work can be introduced as follows:

1. The implementation of orthotropic yield functions and velocity discontinuities in 3D finite-element-based upper bound formulations, using simplex strain elements with the plastic flow measured by both the linear strain-rates within solid elements and linear velocity-jumps only across sensibly-arranged velocity discontinuities.
2. The derivation of traction-based yield functions for the velocity discontinuities, taking both their orientation and the orthotropic stress-based yield function assigned to the solid elements into account, in order to guarantee consistent orthotropic strength behaviour throughout the whole discretised structure.
3. The implementation of an adaptive approach to introduce and adjust velocity discontinuities in an efficient and meaningful way at regions where very localised plastic failure can be expected.

With respect to these objectives, the paper is structured as follows: In Section 5.2, upper bound formulations considering orthotropic strength behaviour and velocity discontinuities are introduced analytically. In these formulations, the traction-based yield function applied to velocity discontinuities are guaranteed to represent similar orthotropic strength behaviour as the stress-based yield function applied to solid elements by means of a projection algorithm introduced in Section 5.3. The formulation of associated plastic flow rule both in continuum and across velocity discontinuities are presented in Section 5.4. Then, in Section 5.5, upper bound formulations are given in discretised form, using simplex strain elements and linear velocity discontinuities. The algorithm for introduction and adjustment of velocity discontinuities is presented in Section 5.6. A verification of these implementations by means of two commonly-used benchmark examples under plane strain conditions and a 3D example can be found in Section 5.7. Finally, a brief summary and concluding comments are given in Section 5.8.

## 5.2 Kinematic theorem

Upper bound calculations exclusively focus on the kinematically admissible velocity field  $\dot{\mathbf{u}} = (\dot{u}_x, \dot{u}_y, \dot{u}_z)^\top \in \mathfrak{R}^3$  at the time instant of structural collapse, and search for the failure mechanism leading to the minimum internal plastic energy dissipation rate  $W_{int}$ , which must equal to the external work rate  $W_{ext}$ . Thereby, a velocity field  $\dot{\mathbf{u}}$  is considered to be kinematically admissible when it fulfills compatibility, the plastic flow rule, and the kinematic boundary conditions at each point of the considered structure.

In this work, to be able to consider very localised plastic failure mechanisms more easily, the velocity field  $\dot{\mathbf{u}}$  is not enforced to be continuous, rather velocity-jumps  $\Delta\dot{\mathbf{u}} = (\Delta\dot{u}_x, \Delta\dot{u}_y, \Delta\dot{u}_z)^\top \in \mathfrak{R}^3$  are allowed across prescribed discontinuities  $\Gamma_{dis}$ . These consist of one part denoted as  $\Gamma_{dis}^+$  with the related velocity field  $\dot{\mathbf{u}}_{dis}^+$  and an opposite part  $\Gamma_{dis}^-$  with the related velocity field  $\dot{\mathbf{u}}_{dis}^-$ . Then, diffused plastic failure is measured by the plastic strain-rate field  $\dot{\boldsymbol{\epsilon}} = (\dot{\epsilon}_{xx}, \dot{\epsilon}_{yy}, \dot{\epsilon}_{zz}, 2\dot{\epsilon}_{xy}, 2\dot{\epsilon}_{yz}, 2\dot{\epsilon}_{xz})^\top \in \mathfrak{R}^6$  (in Voigt notation) in the continuum  $\Omega$  and very localised plastic failure is measured by the velocity-jump field  $\Delta\dot{\mathbf{u}} = \dot{\mathbf{u}}_{dis}^+ - \dot{\mathbf{u}}_{dis}^-$  at certain discontinuities  $\Gamma_{dis}$ .

The plastic dissipation functions for these two failure mechanisms can be expressed as

$$d_{mat}(\dot{\boldsymbol{\epsilon}}) = \sup_{\boldsymbol{\sigma} \in \mathcal{F}} \boldsymbol{\sigma}^\top \dot{\boldsymbol{\epsilon}}, \quad \mathcal{F} = \{\boldsymbol{\sigma} | f_{mat}(\boldsymbol{\sigma}) \leq 0\} \quad \text{in } \Omega$$

$$d_{dis}(\Delta\dot{\mathbf{u}}) = \sup_{\mathbf{t} \in \mathcal{D}} \mathbf{t}^\top \Delta\dot{\mathbf{u}}, \quad \mathcal{D} = \{\mathbf{t} | f_{dis}(\mathbf{t}) \leq 0\} \quad \text{on } \Gamma_{dis}$$
(5.1)

where  $\boldsymbol{\sigma} = (\sigma_{xx}, \sigma_{yy}, \sigma_{zz}, \sigma_{xy}, \sigma_{yz}, \sigma_{xz})^\top \in \mathfrak{R}^6$  denotes the stress field,  $\mathbf{t} = (t_x, t_y, t_z)^\top \in \mathfrak{R}^3$  represents the surface traction field,  $f_{mat}(\boldsymbol{\sigma}) \leq 0$  is a stress-based yield function assigned to the continuum  $\Omega$ , and  $f_{dis}(\mathbf{t}) \leq 0$  is a traction-based yield function (depending on  $f_{mat}(\boldsymbol{\sigma}) \leq 0$ ) assigned to the velocity discontinuities  $\Gamma_{dis}$ . Consequently, the internal energy dissipation rate  $W_{int}$  over the whole structure reads

$$W_{int} = \int_{\Omega} d_{mat}(\dot{\boldsymbol{\epsilon}}) dV + \int_{\Gamma_{dis}} d_{dis}(\Delta\dot{\mathbf{u}}) dA = \int_{\Omega} \dot{\boldsymbol{\epsilon}}^\top \boldsymbol{\sigma} dV + \int_{\Gamma_{dis}} \Delta\dot{\mathbf{u}}^\top \mathbf{t} dA \quad (5.2)$$

consisting of the rate of plastic energy dissipated within the continuum as well as at discontinuities.

The upper bound problem can then be formulated as a nonlinear optimisation problem, reading

$$\begin{aligned}
& \min && W_{int} \\
& \text{s.t.} && \dot{\boldsymbol{\varepsilon}} = \mathbf{L}_{\dot{\boldsymbol{\varepsilon}}}\dot{\mathbf{u}} && \text{in } \Omega \\
& && \Delta\dot{\mathbf{u}} = \mathbf{L}_{\Delta\dot{\mathbf{u}}}\dot{\mathbf{u}}_{dis} && \text{on } \Gamma_{dis} \\
& && \dot{\mathbf{u}} = \dot{\mathbf{u}}_{bc} && \text{on } \Gamma \\
& && \dot{\boldsymbol{\varepsilon}} = \dot{\lambda}_{mat}\partial f_{mat}(\boldsymbol{\sigma})/\partial\boldsymbol{\sigma} && \text{in } \Omega \\
& && \Delta\dot{\mathbf{u}} = \dot{\lambda}_{dis}\partial f_{dis}(\mathbf{t})/\partial\mathbf{t} && \text{on } \Gamma_{dis}
\end{aligned} \tag{5.3}$$

where  $\dot{\mathbf{u}}_{dis} = (\dot{\mathbf{u}}_{dis}^+, \dot{\mathbf{u}}_{dis}^-)^\top \in \mathfrak{R}^6$  contains the velocity fields of both surfaces of a discontinuity  $\Gamma_{dis}$ , and

$$\mathbf{L}_{\dot{\boldsymbol{\varepsilon}}} = \begin{pmatrix} \partial/\partial x & 0 & 0 \\ 0 & \partial/\partial y & 0 \\ 0 & 0 & \partial/\partial z \\ \partial/\partial y & 0 & \partial/\partial z \\ \partial/\partial x & \partial/\partial z & 0 \\ 0 & \partial/\partial y & \partial/\partial x \end{pmatrix} \in \mathfrak{R}^{6 \times 3} \quad \text{and} \quad \mathbf{L}_{\Delta\dot{\mathbf{u}}} = (\mathbf{I} \quad -\mathbf{I}) \in \mathfrak{R}^{3 \times 6} \tag{5.4}$$

are the compatibility operators for the continuum  $\Omega$  and the discontinuities  $\Gamma_{dis}$ , respectively.

Through the first constraint of the upper bound formulation in Eq. (5.3) compatibility between the velocity field  $\dot{\mathbf{u}}$  and the strain-rate field  $\dot{\boldsymbol{\varepsilon}}$  is enforced at each point of the continuum  $\Omega$ ; the second constraint enforces compatibility between the velocity-jump field  $\Delta\dot{\mathbf{u}}$  and the velocity field  $\dot{\mathbf{u}}$  across each discontinuity  $\Gamma_{dis}$ ; the third constraint represents the kinematic boundary conditions, prescribing a velocity field  $\dot{\mathbf{u}}_{bc}$  on the surface  $\Gamma = \partial\Omega$ . The last two constraints ensure associated plastic flow in  $\Omega$  as well as across  $\Gamma_{dis}$ , where  $\dot{\lambda}_{mat}$  and  $\dot{\lambda}_{dis}$  denote the corresponding plastic multiplier rates, determining the magnitude of plastic flow.

According to duality in nonlinear programming, the primal form of the upper bound problem in Eq. (5.3) can also be formulated in dual form, reading

$$\begin{aligned}
& \max && W_{ext} \\
& \text{s.t.} && \int_{\Omega} \dot{\boldsymbol{\varepsilon}}^\top \boldsymbol{\sigma} dV + \int_{\Gamma_{dis}} \dot{\boldsymbol{\mu}}^\top \mathbf{t} dA = \int_{\Omega} \dot{\mathbf{u}}^\top \beta \mathbf{g}_u dV + \int_{\Omega} \dot{\mathbf{u}}^\top \mathbf{g}_f dV + \int_{\Gamma_u} \dot{\mathbf{u}}^\top \beta \mathbf{t}_u dA + \int_{\Gamma_f} \dot{\mathbf{u}}^\top \mathbf{t}_f dA \\
& && f_{mat}(\boldsymbol{\sigma}) \leq 0 \quad \text{in } \Omega \\
& && f(\mathbf{t})_{dis} \leq 0 \quad \text{on } \Gamma_{dis}
\end{aligned} \tag{5.5}$$

where the first constraint represents a weak form of equilibrium for the whole structure, with  $\beta$  as an unknown collapse limit load multiplier. The objective function becomes the maximum external work rate in the dual formulation, which can be written as

$$W_{ext} = \int_{\Omega} \dot{\mathbf{u}}^\top \beta \mathbf{g}_u dV + \int_{\Gamma_u} \dot{\mathbf{u}}^\top \beta \mathbf{t}_u dA + \int_{\Omega} \dot{\mathbf{u}}^\top \mathbf{g}_f dV + \int_{\Gamma_f} \dot{\mathbf{u}}^\top \mathbf{t}_f dA \tag{5.6}$$

containing contributions from the unknown body force field  $\mathbf{g}_u = (g_{u,x}, g_{u,y}, g_{u,z})^\top \in \mathfrak{R}^3$  and the fixed body force field  $\mathbf{g}_f = (g_{f,x}, g_{f,y}, g_{f,z})^\top \in \mathfrak{R}^3$  in the continuum  $\Omega$ , as well as from the unknown traction field  $\mathbf{t}_u$  on the boundary surface part  $\Gamma_u$  and the fixed traction field  $\mathbf{t}_f$  on the boundary surface part  $\Gamma_f$ , with  $\Gamma = \Gamma_u \cup \Gamma_f$ .



### 5.3 Traction-based plastic yield function

As discussed in several publications (Krabbenhøft et al., 2005, Makrodimopoulos and Martin, 2008, Sloan and Kleeman, 1995), the implementation of velocity discontinuities in finite-element-based upper bound formulations can significantly improve the quality of upper bound results and locking phenomena can often be avoided. The number of unknown variables, however, is greatly increased and, thus, a higher computational effort is required.

In existing finite-element-based upper bound formulations with velocity discontinuities exclusively shear-failure-based isotropic yield functions  $f_{mat}(\boldsymbol{\sigma}) \leq 0$  (e.g. the von Mises yield function, the Mohr-Coulomb yield function and the Drucker-Prager yield function) are assigned to the continuum  $\Omega$ . In this case, the formulation of an equivalent strength behaviour at discontinuities (between finite elements) is straightforward and leads to a function  $f_{dis}(\sigma_m, \tau) \leq 0$  depending on the normal stress  $\sigma_m$  and the shear stress  $\tau$  at the discontinuity. Thus, this failure criterion can easily be linked to and expressed in terms of the traction forces acting at the discontinuity, giving a function  $f_{dis}(\mathbf{t}) \leq 0$ . However, this is only possible for shear-failure-based strength criteria and becomes much more complicated for other types of failure criteria, like e.g. orthotropic strength behaviour.

For this reason, in this section an algorithm is proposed which allows the projection of a quite general stress-based yield function  $f_{mat}(\boldsymbol{\sigma}) \leq 0$  onto an equivalent traction-based yield function  $f_{dis}(\mathbf{t}) \leq 0$  with respect to a certain velocity discontinuity  $\Gamma_{dis}$ . In this way a consistent strength behaviour throughout a structure with discontinuities can be achieved.

#### 5.3.1 Projection algorithm

As stress-based yield function for the continuum  $\Omega$  the following differentiable quadratic form will be considered, formulated with respect to the local coordinate basis of the material  $(x' - y' - z')_{mat}$ :

$$f_{mat}(\boldsymbol{\sigma}_{loc}^{mat}) = \boldsymbol{\sigma}_{loc}^{mat\top} \mathbf{P}_{\sigma}^{mat} \boldsymbol{\sigma}_{loc}^{mat} + (\frac{1}{2} \mathbf{F}_{\sigma}^{mat,+} \boldsymbol{\sigma}_{loc}^{mat})^2 - (1 - \frac{1}{2} \mathbf{F}_{\sigma}^{mat,-} \boldsymbol{\sigma}_{loc}^{mat})^2 \leq 0, \quad \text{in } \Omega \quad (5.7)$$

where  $\boldsymbol{\sigma}_{loc}^{mat} = \mathbf{R}_{\sigma}^{mat} \boldsymbol{\sigma}$  represents a stress state with respect to the local coordinate basis of the material, and the matrices  $\mathbf{P}_{\sigma}^{mat} \in \mathfrak{R}^{6 \times 6}$ ,  $\mathbf{F}_{\sigma}^{mat,+} \in \mathfrak{R}^6$  and  $\mathbf{F}_{\sigma}^{mat,-} \in \mathfrak{R}^6$  determine the type of yield function as well as strength parameters. Of course, when the special case of an isotropic yield function is considered, the introduction of a local coordinate basis for the material is not necessary and  $\boldsymbol{\sigma}_{loc}^{mat} = \boldsymbol{\sigma}$ .

The transformation matrix for stress vectors from the global coordinate basis  $(x - y - z)$  to the material local coordinate basis  $(x' - y' - z')_{mat}$  reads

$$\mathbf{R}_{\sigma}^{mat} = \begin{pmatrix} n_{x'x}^{mat2} & n_{x'y}^{mat2} & n_{x'z}^{mat2} & 2n_{x'x}^{mat} n_{x'y}^{mat} & 2n_{x'y}^{mat} n_{x'z}^{mat} & 2n_{x'x}^{mat} n_{x'z}^{mat} \\ n_{y'x}^{mat2} & n_{y'y}^{mat2} & n_{y'z}^{mat2} & 2n_{y'x}^{mat} n_{y'y}^{mat} & 2n_{y'y}^{mat} n_{y'z}^{mat} & 2n_{y'x}^{mat} n_{y'z}^{mat} \\ n_{z'x}^{mat2} & n_{z'y}^{mat2} & n_{z'z}^{mat2} & 2n_{z'x}^{mat} n_{z'y}^{mat} & 2n_{z'y}^{mat} n_{z'z}^{mat} & 2n_{z'x}^{mat} n_{z'z}^{mat} \\ n_{x'x}^{mat} n_{y'y}^{mat} & n_{x'y}^{mat} n_{y'y}^{mat} & n_{x'z}^{mat} n_{y'y}^{mat} & n_{x'y}^{mat} n_{y'x}^{mat} + n_{x'x}^{mat} n_{y'y}^{mat} & n_{x'y}^{mat} n_{y'z}^{mat} + n_{x'z}^{mat} n_{y'y}^{mat} & n_{x'x}^{mat} n_{y'z}^{mat} + n_{x'z}^{mat} n_{y'x}^{mat} \\ n_{y'x}^{mat} n_{z'z}^{mat} & n_{y'y}^{mat} n_{z'y}^{mat} & n_{y'z}^{mat} n_{z'z}^{mat} & n_{y'x}^{mat} n_{z'y}^{mat} + n_{y'z}^{mat} n_{z'z}^{mat} & n_{y'y}^{mat} n_{z'z}^{mat} + n_{y'z}^{mat} n_{z'y}^{mat} & n_{y'x}^{mat} n_{z'z}^{mat} + n_{y'z}^{mat} n_{z'y}^{mat} \\ n_{z'x}^{mat} n_{z'z}^{mat} & n_{z'y}^{mat} n_{z'y}^{mat} & n_{z'z}^{mat} n_{z'z}^{mat} & n_{z'x}^{mat} n_{z'y}^{mat} + n_{z'y}^{mat} n_{z'z}^{mat} & n_{z'y}^{mat} n_{z'z}^{mat} + n_{z'z}^{mat} n_{z'y}^{mat} & n_{z'x}^{mat} n_{z'z}^{mat} + n_{z'z}^{mat} n_{z'y}^{mat} \end{pmatrix} \quad (5.8)$$

with  $\mathbf{n}_{x'}^{mat} = (n_{x'x}^{mat}, n_{x'y}^{mat}, n_{x'z}^{mat})^\top \in \mathfrak{R}^3$ ,  $\mathbf{n}_{y'}^{mat} = (n_{y'x}^{mat}, n_{y'y}^{mat}, n_{y'z}^{mat})^\top \in \mathfrak{R}^3$  and  $\mathbf{n}_{z'}^{mat} = (n_{z'x}^{mat}, n_{z'y}^{mat}, n_{z'z}^{mat})^\top \in \mathfrak{R}^3$  as the three normal vectors of the material local coordinate basis.

In order to derive a traction-based yield function for velocity discontinuities based on Eq. (5.7), the first step is the transformation of this yield function from the material local coordinate basis  $(x' - y' - z')_{mat}$  into the discontinuity local coordinate basis  $(n - m - p)_{dis}$ , reading

$$f_{mat}(\boldsymbol{\sigma}_{loc}^{dis}) = \boldsymbol{\sigma}_{loc}^{dis\top} \mathbf{P}_\sigma^{dis} \boldsymbol{\sigma}_{dis}^{dis} + \left(\frac{1}{2} \mathbf{F}_\sigma^{dis,+} \boldsymbol{\sigma}_{loc}^{dis}\right)^2 - \left(1 - \frac{1}{2} \mathbf{F}_\sigma^{dis,-} \boldsymbol{\sigma}_{loc}^{dis}\right)^2 \leq 0, \quad \text{on } \Gamma_{dis} \quad (5.9)$$

where  $\boldsymbol{\sigma}_{loc}^{dis} = \mathbf{R}_\sigma^{dis} \boldsymbol{\sigma}$  denotes a local stress state at the discontinuity with respect to the discontinuity local coordinate basis.  $\mathbf{R}_\sigma^{dis}$  is the related transformation matrix equally defined as the matrix in Eq. (5.8), with  $\mathbf{n}_n^{dis} = (n_{nx}^{dis}, n_{ny}^{dis}, n_{nz}^{dis})^\top \in \mathfrak{R}^3$ ,  $\mathbf{n}_m^{dis} = (n_{mx}^{dis}, n_{my}^{dis}, n_{mz}^{dis})^\top \in \mathfrak{R}^3$  and  $\mathbf{n}_p^{dis} = (n_{px}^{dis}, n_{py}^{dis}, n_{pz}^{dis})^\top \in \mathfrak{R}^3$  as the normal vectors of the local coordinate basis  $(n - m - p)_{dis}$  (with  $\mathbf{n}_n^{dis}$  as the out of plane normal vector and  $\mathbf{n}_m^{dis}$  and  $\mathbf{n}_p^{dis}$  as the in plane normal vectors). According to these definitions,  $\boldsymbol{\sigma}_{loc}^{mat}$  (Eq. (5.7)) and  $\boldsymbol{\sigma}_{loc}^{dis}$  (Eq. (5.9)) are connected as follows:  $\boldsymbol{\sigma}_{loc}^{mat} = \mathbf{R}_\sigma^{mat} (\mathbf{R}_\sigma^{dis})^{-1} \boldsymbol{\sigma}_{loc}^{dis}$ . The yield function matrices in Eq. (5.9) can then be determined as

$$\begin{aligned} \mathbf{P}_\sigma^{dis} &= (\mathbf{R}_\sigma^{mat} (\mathbf{R}_\sigma^{dis})^{-1})^\top \mathbf{P}_\sigma^{mat} (\mathbf{R}_\sigma^{mat} (\mathbf{R}_\sigma^{dis})^{-1}) \in \mathfrak{R}^{6 \times 6} \\ \mathbf{F}_\sigma^{dis,+} &= (\mathbf{R}_\sigma^{mat} (\mathbf{R}_\sigma^{dis})^{-1})^\top \mathbf{F}_\sigma^{mat,+} \in \mathfrak{R}^6 \\ \mathbf{F}_\sigma^{dis,-} &= (\mathbf{R}_\sigma^{mat} (\mathbf{R}_\sigma^{dis})^{-1})^\top \mathbf{F}_\sigma^{mat,-} \in \mathfrak{R}^6 \end{aligned} \quad (5.10)$$

Next, the local stress field at discontinuities  $\boldsymbol{\sigma}_{loc}^{dis}$  is linked to the corresponding traction field  $\mathbf{t}_{loc}^{dis}$  simply by

$$\mathbf{t}_{loc}^{dis} = \mathbf{L}_\sigma^{dis} \boldsymbol{\sigma}_{loc}^{dis}, \quad \text{on } \Gamma_{dis} \quad (5.11)$$

with

$$\mathbf{L}_\sigma^{dis} = \begin{pmatrix} 1 & 0 & 0 & 0 & 0 & 0 \\ 0 & 0 & 0 & 1 & 0 & 0 \\ 0 & 0 & 0 & 0 & 0 & 1 \end{pmatrix} \in \mathfrak{R}^{3 \times 6} \quad (5.12)$$

as the projection operator. Thereby, the local traction field is obtained by  $\mathbf{t}_{loc}^{dis} = \mathbf{R}_t^{dis} \mathbf{t}$ , with the transformation matrix

$$\mathbf{R}_t^{dis} = \begin{pmatrix} n_{nx}^{dis} & n_{ny}^{dis} & n_{nz}^{dis} \\ n_{mx}^{dis} & n_{my}^{dis} & n_{mz}^{dis} \\ n_{px}^{dis} & n_{py}^{dis} & n_{pz}^{dis} \end{pmatrix} \in \mathfrak{R}^{3 \times 3} \quad (5.13)$$

According to Eq. (5.11), it is obvious that, from a critical stress state, the corresponding critical traction forces at a discontinuity can easily be evaluated. However, the reverse way, evaluating whether a traction force state is critical or not with respect to the stress-based yield function in Eq. (5.9), is not possible without further conditions, because the local traction field  $\mathbf{t}_{loc}^{dis}$  only defines three stress components  $(\sigma_{nn}^{dis}, \sigma_{nm}^{dis}, \sigma_{np}^{dis})$  of the related local 3D stress state. For this reason, three additional constraints are needed to ensure that the finally derived traction-based yield function  $f_{dis}(\mathbf{t}) \leq 0$  is only triggered

for traction force states which in any case lead to plastic failure. This can be achieved by adding the following three constraints:

$$\begin{aligned}\dot{\varepsilon}_{mm}^{dis} &= \Lambda_{mm}^{dis}(\boldsymbol{\sigma}_{loc}^{dis}) = \dot{\lambda}_{\dot{\varepsilon}}^{dis} \partial f_{mat}(\boldsymbol{\sigma}_{loc}^{dis}) / \partial \sigma_{mm}^{dis} = 0 \\ \dot{\varepsilon}_{pp}^{dis} &= \Lambda_{pp}^{dis}(\boldsymbol{\sigma}_{loc}^{dis}) = \dot{\lambda}_{\dot{\varepsilon}}^{dis} \partial f_{mat}(\boldsymbol{\sigma}_{loc}^{dis}) / \partial \sigma_{pp}^{dis} = 0 \\ \dot{\varepsilon}_{mp}^{dis} &= \Lambda_{mp}^{dis}(\boldsymbol{\sigma}_{loc}^{dis}) = \dot{\lambda}_{\dot{\varepsilon}}^{dis} \partial f_{mat}(\boldsymbol{\sigma}_{loc}^{dis}) / \partial \sigma_{mp}^{dis} = 0\end{aligned}\quad (5.14)$$

enforcing the plastic strain-rate field  $\dot{\boldsymbol{\varepsilon}}_{loc}^{dis}$  to be localised with respect to the discontinuity  $\Gamma_{dis}$  ( $(n-m-p)_{dis}$ ), as introduced by Wu and Cervera (2014). Thereby,  $\Lambda_{mm}^{dis}$ ,  $\Lambda_{pp}^{dis}$  and  $\Lambda_{mp}^{dis}$  represent the partial derivative expressions of the yield function Eq. (5.9) with respect to the three stress components  $\sigma_{mm}^{dis}$ ,  $\sigma_{pp}^{dis}$  and  $\sigma_{mp}^{dis}$ , irrelevant to the interface plane of  $\Gamma_{dis}$ .

Substituting the stress components  $\sigma_{nn}^{dis}$ ,  $\sigma_{nm}^{dis}$  and  $\sigma_{np}^{dis}$  in Eq. (5.14) with the local traction components  $t_n^{dis}$ ,  $t_m^{dis}$  and  $t_p^{dis}$  according to Eqs. (5.11) and (5.12), the remaining stress components can be expressed as functions  $L$  of the local traction vector  $\mathbf{t}_{loc}^{dis}$ , reading

$$\begin{aligned}\sigma_{mm}^{dis} &= L_{mm}^{dis}(\mathbf{t}_{loc}^{dis}) \\ \sigma_{pp}^{dis} &= L_{pp}^{dis}(\mathbf{t}_{loc}^{dis}) \\ \sigma_{mp}^{dis} &= L_{mp}^{dis}(\mathbf{t}_{loc}^{dis})\end{aligned}\quad (5.15)$$

Now, each local traction force state  $\mathbf{t}_{loc}^{dis}$  can be linked to a unique 3D local stress state  $\boldsymbol{\sigma}_{loc}^{dis}$ , reading

$$\boldsymbol{\sigma}_{loc}^{dis} = \mathbf{L}_t^{dis} \mathbf{t}_{loc}^{dis}, \quad \text{on } \Gamma_{dis} \quad (5.16)$$

where  $\mathbf{L}_t^{dis} \in \mathfrak{R}^{6 \times 3}$  represents the projection operator determined from Eqs. (5.11) and (5.15) with respect to  $\Gamma_{dis}$ .

Finally, by inserting Eq. (5.16) into Eq. (5.9), the stress-based yield function  $f_{mat}(\boldsymbol{\sigma}_{loc}^{dis}) \leq 0$  in  $\Omega$  can be projected onto a traction-based yield function  $f_{dis}(\mathbf{t}_{loc}^{dis}) \leq 0$  locally on  $\Gamma_{dis}$ , which reads

$$f_{mat}(\boldsymbol{\sigma}_{loc}^{dis}) = \boldsymbol{\sigma}_{loc}^{dis \top} \mathbf{P}_\sigma^{dis} \boldsymbol{\sigma}_{loc}^{dis} + \left(\frac{1}{2} \mathbf{F}_\sigma^{dis, +\top} \boldsymbol{\sigma}_{loc}^{dis}\right)^2 - \left(1 - \frac{1}{2} \mathbf{F}_\sigma^{dis, -\top} \boldsymbol{\sigma}_{loc}^{dis}\right)^2 \quad (5.17a)$$

$$= (\mathbf{L}_t^{dis} \mathbf{t}_{loc}^{dis})^\top \mathbf{P}_\sigma^{dis} (\mathbf{L}_t^{dis} \mathbf{t}_{loc}^{dis}) + \left(\frac{1}{2} \mathbf{F}_\sigma^{dis, +\top} (\mathbf{L}_t^{dis} \mathbf{t}_{loc}^{dis})\right)^2 - \left(1 - \frac{1}{2} \mathbf{F}_\sigma^{dis, -\top} (\mathbf{L}_t^{dis} \mathbf{t}_{loc}^{dis})\right)^2 \quad (5.17b)$$

$$= \mathbf{t}_{loc}^{dis \top} \mathbf{P}_t^{dis} \mathbf{t}_{loc}^{dis} + \left(\frac{1}{2} \mathbf{F}_t^{dis, +\top} \mathbf{t}_{loc}^{dis}\right)^2 - \left(1 - \frac{1}{2} \mathbf{F}_t^{dis, -\top} \mathbf{t}_{loc}^{dis}\right)^2 = f_{dis}(\mathbf{t}_{loc}^{dis}) \quad (5.17c)$$

where  $\mathbf{P}_t^{dis} = \mathbf{L}_t^{dis \top} \mathbf{P}_\sigma^{dis} \mathbf{L}_t^{dis} \in \mathfrak{R}^{3 \times 3}$ ,  $\mathbf{F}_t^{dis, +} = \mathbf{L}_t^{dis \top} \mathbf{F}_\sigma^{dis, +} \in \mathfrak{R}^3$  and  $\mathbf{F}_t^{dis, -} = \mathbf{L}_t^{dis \top} \mathbf{F}_\sigma^{dis, -} \in \mathfrak{R}^3$  are the matrices containing strength parameters for the traction-based yield function.

### 5.3.2 Numerical verification

In the following, the presented transition (Eq. (5.17)) from a stress-based yield function into a traction-based yield function is numerically verified. Assuming the material local

coordinate basis as identical to the global coordinate basis, arbitrary Tsai-Wu strength parameters for the stress-based yield function (Eq. (5.7)) are chosen as

$$\mathbf{F}_\sigma^{mat} = \begin{pmatrix} 0.0750 \\ 0.7500 \\ 0.1905 \\ 0 \\ 0 \\ 0 \end{pmatrix} \quad \mathbf{P}_\sigma^{mat} = \begin{pmatrix} 0.0250 & 0 & 0 & 0 & 0 & 0 \\ 0 & 0.2500 & 0 & 0 & 0 & 0 \\ 0 & 0 & 0.0476 & 0 & 0 & 0 \\ 0 & 0 & 0 & 0.1111 & 0 & 0 \\ 0 & 0 & 0 & 0 & 0.2500 & 0 \\ 0 & 0 & 0 & 0 & 0 & 0.0400 \end{pmatrix} \quad (5.18)$$

Then, a set of failure stress states  $\boldsymbol{\sigma}^i$  ( $i \in \{1, \dots, n_f\}$ ) with respect to the global coordinate basis ( $x-y-z$ ) can be determined by inserting the parameters in Eq. (5.18) into the general form of the yield function in Eq. (5.7), where  $n_f$  represents the number of selected failure stress states.

Considering two different and arbitrarily selected planes (discontinuities)  $\Gamma_1$  and  $\Gamma_2$  defined by their normal vectors

$$\begin{aligned} \mathbf{n}_1 &= (0.1826, 0.9129, 0.3651)^\top && \text{for } \Gamma_1 \\ \mathbf{n}_2 &= (-0.8018, 0.5345, -0.2673)^\top && \text{for } \Gamma_2 \end{aligned} \quad (5.19)$$

two sets of local traction force states  $\mathbf{t}_{\sigma,1}^{dis,i}$  and  $\mathbf{t}_{\sigma,2}^{dis,i}$  ( $i \in \{1, \dots, n_\sigma\}$ ) can be determined as

$$\mathbf{t}_{\sigma,j}^{dis,i} = \mathbf{L}_\sigma^{dis} \mathbf{R}_{\sigma,j}^{dis} \boldsymbol{\sigma}^i \quad \forall i \in \{1, \dots, n_\sigma\} \text{ and } j \in \{1, 2\} \quad (5.20)$$

with respect to their local coordinate bases  $(n-m-p)_1$  and  $(n-m-p)_2$ , respectively. In Eq. (5.20),  $\mathbf{L}_\sigma^{dis}$  denotes the operator projecting the stress state into the traction force state defined in Eq. (5.12), and  $\mathbf{R}_{\sigma,1}^{dis}$  and  $\mathbf{R}_{\sigma,2}^{dis}$  are the transformation matrices similar to Eq. (5.8) based on the axial normal vectors  $\mathbf{n}_{n,1} = (0.1826, 0.9129, 0.3651)^\top$ ,  $\mathbf{n}_{m,1} = (-0.9806, 0.1961, 0.0000)^\top$ ,  $\mathbf{n}_{p,1} = (-0.0716, -0.3581, 0.9309)^\top$  for  $(n-m-p)_1$  and  $\mathbf{n}_{n,2} = (-0.8018, 0.5345, -0.2673)^\top$ ,  $\mathbf{n}_{m,2} = (0.5547, 0.8321, 0.0000)^\top$ ,  $\mathbf{n}_{p,2} = (0.2224, -0.1483, -0.9636)^\top$  for  $(n-m-p)_2$ , respectively.

Although all failure stress states  $\boldsymbol{\sigma}^i$  naturally lie on a continuous surface, as defined through the stress-based yield function in Eq. (5.7), the corresponding traction force failure stress states  $\mathbf{t}_{\sigma,1}^{dis,i}$  and  $\mathbf{t}_{\sigma,2}^{dis,i}$ , obtained through Eq. (5.20) are not necessarily located on such. They rather represent point clouds whose shapes heavily depend on the orientation of the planes  $\Gamma_1$  and  $\Gamma_2$ , as illustrated in Figure 5.1. However, a clear ellipsoidal outer envelope can be observed, meaning that every traction force state lying outside this envelope is for sure related to a failure stress state according to Eq. (5.7).

According to Eq. (5.17), the stress-based yield function using the strength parameters in Eq. (5.18) can be projected into the traction-based yield functions with respect to the local coordinate basis  $(n-m-p)_1$  and  $(n-m-p)_2$  for which the strength parameters

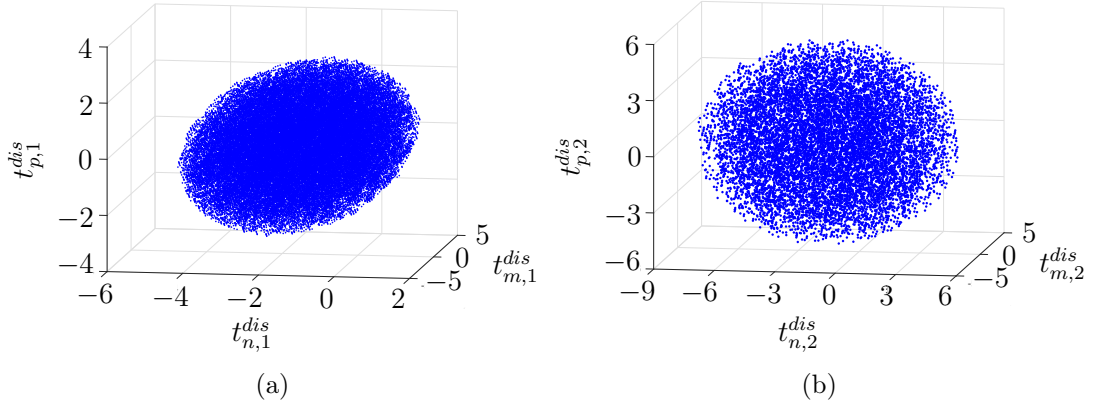


Figure 5.1: Local traction point clouds determined by projecting the set of global failure stress state  $\sigma^i$  into two sets of local traction states (a)  $\mathbf{t}_{loc,1}^{dis,i}$  on the plane  $\Gamma_1$  with respect to  $(n - m - p)_1$  and (b)  $\mathbf{t}_{loc,2}^{dis,i}$  on the plane  $\Gamma_2$  with respect to  $(n - m - p)_2$  where  $(i \in \{1, \dots, n_f\})$ .

are determined as

$$\mathbf{F}_{t,1}^{dis} = \begin{pmatrix} 0.4584 \\ 0.1290 \\ -0.1012 \end{pmatrix} \quad \mathbf{P}_{t,1}^{dis} = \begin{pmatrix} 0.1515 & 0.0424 & -0.0485 \\ 0.0424 & 0.0780 & -0.0111 \\ -0.0485 & -0.0111 & 0.1488 \end{pmatrix} \quad \text{for } \Gamma_1 \quad (5.21a)$$

$$\mathbf{F}_{t,2}^{dis} = \begin{pmatrix} 0.0899 \\ 0.0791 \\ -0.0020 \end{pmatrix} \quad \mathbf{P}_{t,2}^{dis} = \begin{pmatrix} 0.0296 & 0.0260 & -0.0037 \\ 0.0260 & 0.0782 & -0.0033 \\ -0.0037 & -0.0033 & 0.0356 \end{pmatrix} \quad \text{for } \Gamma_2 \quad (5.21b)$$

Inserting these strength parameters into the general form of the traction-based yield function in Eq. (5.17c) leads to yield functions for the two planes  $\Gamma_1$  and  $\Gamma_2$ , respectively.

For each plane, a set of traction force failure states  $\mathbf{t}_{t,j}^{dis,i}$  ( $i \in \{1, \dots, n_t\}$  and  $j \in \{1, \dots, 2\}$ ) is evaluated and plotted in Figure 5.2 as red point cloud ( $n_t$  is the number of selected failure traction states based on the traction-based yield function), where the blue point cloud is identical to Figure 5.1. It can be seen that, for each example plane, the red point cloud spans a continuous surface identical to the outer envelope of the blue point cloud. This proves that the presented traction-based yield function in Eq. (5.17c) represents a suitable criterion to indicate whether a traction force state at a discontinuity should exhibit plastic deformation or not. Of course, there are plenty of traction force states which could lead to failure but do not violate the traction-based yield function. In these cases plastic deformation takes place in the adjacent solid finite elements, and the upper bound theorem itself will never be violated. Thus, to exploit the performance of discontinuities in this kind of formulation, they should be aligned according to planes where strain localisation takes place. This requires an adaptive implementation, which will be presented and discussed in Section 6.

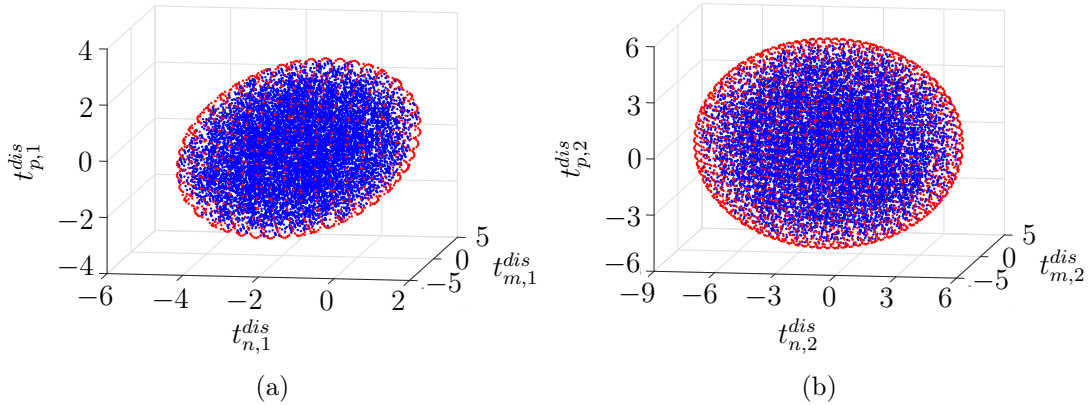


Figure 5.2: Verification of the projection in Eq. (5.17) by means of two example planes (a)  $\Gamma_1$  and (b)  $\Gamma_2$ , where the blue point clouds indicate all possible traction states,  $\mathbf{t}_{\sigma,1}^{dis,i}$  and  $\mathbf{t}_{\sigma,2}^{dis,i}$ , related to the yield stress states  $\boldsymbol{\sigma}^i$  determined by the stress-based yield function with the parameters in Eq. (5.18) ( $i \in \{1, \dots, n_\sigma\}$ ). The red point clouds indicate the yield traction states  $\mathbf{t}_{t,1}^{dis,j}$  and  $\mathbf{t}_{t,2}^{dis,j}$  according to the traction-based yield function with the parameters in Eq. (5.21) ( $j \in \{1, \dots, n_t\}$ ).

## 5.4 Associated plastic flow rule

In both the primal and dual form of the upper bound problem in Eqs. (5.3) and (5.5), all nonlinear constraints are related to the yield functions and their associated plastic flow rule. As stated by Makrodimopoulos and Martin (2007) and Ciria et al. (2008), for 3D problems, most commonly used failure criteria are smooth and can be formulated into second-order cone constraints (e.g. the von Mises failure criterion, the Drucker-Prager failure criterion and the Tsai-Wu failure criterion), thus, the nonlinear optimisation problems in Eqs. (5.3) and (5.5) can be solved efficiently by using SOCP. The widely-used 3D Mohr-Coulomb failure criterion is non-smooth and, thus, cannot be formulated into a second-order cone. Using semidefinite programming instead of second-order cone programming, as introduced by Martin and Makrodimopoulos (2008) and Krabbenhøft et al. (2008), this problem can be overcome. In the following, only formulations of smooth yield functions and their associated plastic flow rule are considered and their reformulation as second-order cone constraints is described.

### Associated plastic flow rule in the continuum

In the continuum  $\Omega$  the plastic flow is measured by the strain-rate field and the associated plastic flow rule reads

$$\dot{\boldsymbol{\varepsilon}}_{loc}^{mat} = \dot{\lambda}_\varepsilon^{mat} \partial f_{mat}(\boldsymbol{\sigma}_{loc}^{mat}) / \partial \boldsymbol{\sigma}_{loc}^{mat} \quad (5.22)$$

where  $\dot{\boldsymbol{\varepsilon}}_{loc}^{mat}$  represents the strain-rate field with respect to the material local coordinate basis  $(x' - y' - z')_{mat}$  and  $\dot{\lambda}_{loc}^{mat}$  is the corresponding plastic multiplier rate.

If the stress-based yield functions can be formulated according to Eq. (5.7) and the parametric matrix  $\mathbf{P}_\sigma^{mat}$  is either positive definite or positive semidefinite, so that it can be decomposed as  $\mathbf{P}_\sigma^{mat} = \mathbf{D}_\sigma^{mat\top} \mathbf{D}_\sigma^{mat}$  with  $\mathbf{D}_\sigma^{mat} \in \mathfrak{R}^{6 \times 6}$ , the yield function

$f_{mat}(\boldsymbol{\sigma}_{loc}^{mat}) \leq 0$  can be reformulated as

$$\begin{aligned}\mathbf{s}_{\sigma}^{mat} &= \mathbf{a}_{\sigma}^{mat} + \mathbf{B}_{\sigma}^{mat} \boldsymbol{\sigma}_{loc}^{mat} \\ \mathbf{s}_{\sigma}^{mat} &\in \mathcal{C}\end{aligned}\quad (5.23)$$

where  $\mathbf{s}_{\sigma}^{mat} \in \mathfrak{R}^8$  is the second-order cone expression of the stress-based yield function Eq. (5.7),  $\mathcal{C}$  refers to the quadratic cone, and the parametric matrices are composed as follows

$$\mathbf{a}_{\sigma}^{mat} = \begin{pmatrix} 1 \\ \mathbf{0} \end{pmatrix} \in \mathfrak{R}^8 \quad \text{and} \quad \mathbf{B}_{\sigma}^{mat} = \begin{pmatrix} -\frac{1}{2} \mathbf{F}_{\sigma}^{mat, -\top} \\ \mathbf{D}_{\sigma}^{mat} \\ \frac{1}{2} \mathbf{F}_{\sigma}^{mat, +\top} \end{pmatrix} \in \mathfrak{R}^{8 \times 6} \quad (5.24)$$

according to the definition of second-order cones (Eq. (5.60)).

As applied by Makrodimopoulos and Martin (2007) and Li et al. (2018c), if the yield function can be formulated as second-order cone constraint (Eq. (5.23)), the corresponding associated plastic flow rule Eq. (5.22) can be formulated as

$$\begin{aligned}\dot{\boldsymbol{\varepsilon}}_{loc}^{mat} &= -\mathbf{B}_{\sigma}^{mat \top} \dot{\boldsymbol{\varepsilon}}_{\varepsilon}^{mat} \\ \dot{\boldsymbol{\varepsilon}}_{\varepsilon}^{mat} &\in \mathcal{C}^*\end{aligned}\quad (5.25)$$

where  $\dot{\boldsymbol{\varepsilon}}_{\varepsilon}^{mat} \in \mathfrak{R}^8$  represents the second-order cone expression of the associated plastic flow rule and  $\mathcal{C}^*$  is the dual cone of the primal quadratic cone  $\mathcal{C}$  of Eq. (5.23).

### Associated plastic flow rule at velocity discontinuities

As introduced in Section 5.2, velocity-jumps  $\Delta \dot{\mathbf{u}}$  are employed in the primal upper bound problem Eq. (5.3) as additional degrees of freedom beside the strain-rate field  $\dot{\boldsymbol{\varepsilon}}$  measuring the localised plastic flow. At velocity discontinuities  $\Gamma_{dis}$  plastic flow occurs when the traction-based yield function according to Eq. (5.17c) is violated. Then, a velocity jump field between the surfaces  $\Gamma_{dis}^+$  and  $\Gamma_{dis}^-$  appears, given by

$$\Delta \dot{\mathbf{u}}_{loc}^{dis} = \dot{\lambda}_{loc}^{dis} \partial f_{dis}(\mathbf{t}_{loc}^{dis}) / \partial \mathbf{t}_{loc}^{dis} \quad (5.26)$$

where  $\Delta \dot{\mathbf{u}}_{loc}^{dis} = \mathbf{R}_{\Delta \dot{\mathbf{u}}}^{dis} \Delta \dot{\mathbf{u}}$  is the local velocity discontinuity field with respect to  $(n - m - p)_{dis}$ ,  $\mathbf{R}_{\Delta \dot{\mathbf{u}}}^{dis} = \mathbf{R}_t^{dis}$  is the transformation matrix with similar definition as in Eq. (5.13), and  $\dot{\lambda}_{loc}^{dis}$  denotes the corresponding plastic multiplier rate.

As indicated in Eq. (5.17), the traction-based yield function exhibits a similar structure as the stress-based yield function and, thus, can also be formulated as second-order cone constraint, reading

$$\begin{aligned}\mathbf{s}_t^{dis} &= \mathbf{a}_t^{dis} + \mathbf{B}_t^{dis} \mathbf{t}_{loc}^{dis} \\ \mathbf{s}_t^{dis} &\in \mathcal{C}\end{aligned}\quad (5.27)$$

where  $\mathbf{s}_t^{dis} \in \mathfrak{R}^5$  is the second-order cone expression of the traction-based yield function Eq. (5.17c) and the parametric matrices are composed as follows

$$\mathbf{a}_t^{dis} = \begin{pmatrix} 1 \\ \mathbf{0} \end{pmatrix} \in \mathfrak{R}^5 \quad \text{and} \quad \mathbf{B}_t^{dis} = \begin{pmatrix} -\frac{1}{2} \mathbf{F}_t^{dis, -\top} \\ \mathbf{D}_t^{dis} \\ \frac{1}{2} \mathbf{F}_t^{dis, +\top} \end{pmatrix} \in \mathfrak{R}^{5 \times 3} \quad (5.28)$$

with  $\mathbf{D}_t^{dis} \in \mathfrak{R}^{3 \times 3}$  as the decomposed matrix of  $\mathbf{P}_t^{dis} = \mathbf{D}_t^{dis \top} \mathbf{D}_t^{dis}$ .

Furthermore, similar to Eq. (5.25), the associated plastic flow rule at  $\Gamma_{dis}$  can be formulated as the dual cone constraint of Eq. (5.27), reading

$$\begin{aligned} \Delta \dot{\mathbf{u}}_{loc}^{dis} &= -\mathbf{B}_t^{dis \top} \dot{\mathbf{e}}_{\Delta \dot{\mathbf{u}}}^{dis} \\ \dot{\mathbf{e}}_{\Delta \dot{\mathbf{u}}}^{dis} &\in \mathcal{C}^* \end{aligned} \quad (5.29)$$

where  $\dot{\mathbf{e}}_{\Delta \dot{\mathbf{u}}}^{dis} \in \mathfrak{R}^5$  is the second-order cone expression of Eq. (5.26).

## 5.5 Finite-element-based upper bound formulation

In this work, 10-noded simplex strain tetrahedral elements are used for discretisation, which are capable of providing more accurate upper bound results compared to the often used 4-noded (constant strain rate) elements (Makrodimopoulos and Martin, 2007, Martin and Makrodimopoulos, 2008). In each element  $el$ , the strain-rate field  $\dot{\boldsymbol{\varepsilon}}$  is obtained through interpolation between nodal strain-rate vectors  $\mathbf{q}_{\dot{\boldsymbol{\varepsilon}}}^{el,i} = (q_{\dot{\boldsymbol{\varepsilon}},xx}^{el,i}, q_{\dot{\boldsymbol{\varepsilon}},yy}^{el,i}, q_{\dot{\boldsymbol{\varepsilon}},zz}^{el,i}, q_{\dot{\boldsymbol{\varepsilon}},xy}^{el,i}, q_{\dot{\boldsymbol{\varepsilon}},yz}^{el,i}, q_{\dot{\boldsymbol{\varepsilon}},xz}^{el,i})^\top \in \mathfrak{R}^6$  at 4 evaluation nodes (4 vertices) using 3D linear interpolation functions  $N_{\dot{\boldsymbol{\varepsilon}}}^{el,i}(\mathbf{x})$  ( $\forall el \in \{1, \dots, UE\}$  and  $i \in \{1, \dots, 4\}$ ) and the velocity field  $\dot{\mathbf{u}}$  is obtained through interpolation between nodal velocity vectors  $\mathbf{q}_{\dot{\mathbf{u}}}^{el,j} = (q_{\dot{\mathbf{u}},x}^{el,j}, q_{\dot{\mathbf{u}},y}^{el,j}, q_{\dot{\mathbf{u}},z}^{el,j})^\top \in \mathfrak{R}^3$  at 10 evaluation nodes (4 vertices and 6 edge middle nodes) using 3D quadratic interpolation functions  $N_{\dot{\mathbf{u}}}^{el,j}(\mathbf{x})$  ( $\forall el \in \{1, \dots, UE\}$  and  $j \in \{1, \dots, 10\}$ ) with  $UE$  as the total number of elements in the upper bound problem. Here,  $\mathbf{x} = (x_x, x_y, x_z)^\top \in \mathfrak{R}^3$  represents an arbitrary position vector inside each element. In the discretised structure, the strain-rate field  $\dot{\boldsymbol{\varepsilon}}$  is piecewise linear within each element and allowed to be discontinuous between elements, thus, each element has its own internal strain-rate evaluation nodes but adjacent nodes from different elements can share the same coordinate.

Consequently, each boundary surface of an element  $be$  is triangular with 6 velocity evaluation nodes (3 vertices and 3 edge middle nodes), and the velocity field  $\dot{\mathbf{u}}$  is obtained through interpolation between nodal velocity vectors  $\mathbf{q}_{\dot{\mathbf{u}}}^{be,k}$  using 2D quadratic interpolation functions  $\bar{N}_{\dot{\mathbf{u}}}^{be,k}(\mathbf{x})$  ( $\forall be \in \{1, \dots, UBE\}$  and  $k \in \{1, \dots, 6\}$ ) with  $UBE$  as the total number of 6-noded boundary elements on  $\Gamma$ .

As mentioned above, velocity jumps  $\Delta \dot{\mathbf{u}}$  are only allowed at prescribed discontinuities  $\Gamma_{dis}$ , where each surface pair  $\Gamma_{dis}^+$  and  $\Gamma_{dis}^-$  has its own set of internal velocity evaluation nodes with different nodal velocity vectors  $\mathbf{q}_{\dot{\mathbf{u}}}^{de+,i}$  and  $\mathbf{q}_{\dot{\mathbf{u}}}^{de-,j}$  ( $\forall de \in \{1, \dots, UDE\}$  and  $i, j \in \{1, \dots, 6\}$ ). Each triangular surface at a discontinuity  $de$ , located on the interface part  $\Gamma_{dis}^{de} \subset \Gamma_{dis}$ , has 6 velocity evaluation nodes with corresponding 2D quadratic interpolation functions  $\bar{N}_{\dot{\mathbf{u}}}^{de,i}(\mathbf{x})$ . Here  $UDE$  represents the total number of velocity discontinuity elements on  $\Gamma_{dis}$ .

### 5.5.1 Primal formulations

The discretised form of each constraint in the primal upper bound problem (Eq. (5.3)) is introduced in the following.



### Compatibility within elements

Based on the assumptions of small strains and straight element edges, all changes in geometry of the considered structure during collapse are negligible, and the discretised form of the first constraint in Eq. (5.3) can be written as

$$\sum_{i=1}^4 N_{\dot{\epsilon}}^{el,i}(\mathbf{x}) \mathbf{q}_{\dot{\epsilon}}^{el,i} = \mathbf{L}_{\dot{\epsilon}} \sum_{j=1}^{10} N_{\dot{u}}^{el,j}(\mathbf{x}) \mathbf{q}_{\dot{u}}^{el,j}, \quad \forall el \in \{1, \dots, UDE\} \quad (5.30)$$

enforcing compatibility between the velocity field and the strain-rate field within each solid element  $\Omega^{el} \subset \Omega$ .

### Compatibility across velocity discontinuities

Since the strain-rate field  $\dot{\epsilon}$  is linear within each solid element  $\Omega^{el}$ , to guarantee consistency of plastic flow, it is straightforward to enforce the velocity jump  $\Delta \dot{\mathbf{u}}$  to be linear across each velocity discontinuity  $\Gamma_{dis}^{de}$ , where  $\Delta \dot{\mathbf{u}}$  is obtained through interpolation between the nodal velocity jumps  $\mathbf{q}_{\Delta \dot{u}}^{de,i} = (q_{\Delta \dot{u},x}^{de,i}, q_{\Delta \dot{u},y}^{de,i}, q_{\Delta \dot{u},z}^{de,i})^T \in \mathfrak{R}^3$  at 3 evaluation nodes (3 vertices) using 2D linear interpolation functions  $\bar{N}_{\Delta \dot{u}}^{de,i}(\mathbf{x})$  ( $\forall de \in \{1, \dots, UDE\}$  and  $i \in \{1, \dots, 3\}$ ).

Then, the second constraint in Eq. (5.3) reads in discretised form as follows:

$$\sum_{i=1}^3 \bar{N}_{\Delta \dot{u}}^{de,i}(\mathbf{x}) \mathbf{q}_{\Delta \dot{u}}^{de,i} = \sum_{j=1}^6 \mathbf{L}_{\Delta \dot{u}} \bar{N}_{\dot{u}}^{de,j}(\mathbf{x}) \mathbf{q}_{\dot{u}}^{de,j}, \quad \forall de \in \{1, \dots, UDE\} \quad (5.31)$$

with  $\mathbf{L}_{\Delta \dot{u}}$  as defined in Eq. (5.4) and  $\mathbf{q}_{\dot{u}}^{de,j} = (\mathbf{q}_{\dot{u}}^{de+,j}, \mathbf{q}_{\dot{u}}^{de-,j})^T \in \mathfrak{R}^{3 \times 6}$  is a vector containing each pair of nodal velocities across the discontinuity  $\Gamma_{dis}^{de}$ . Additional constraints are applied reading

$$\begin{aligned} \mathbf{L}_{\Delta \dot{u}} \mathbf{q}_{\dot{u}}^{de,4} &= \frac{1}{2} (\mathbf{L}_{\Delta \dot{u}} \mathbf{q}_{\dot{u}}^{de,1} + \mathbf{L}_{\Delta \dot{u}} \mathbf{q}_{\dot{u}}^{de,2}) \\ \mathbf{L}_{\Delta \dot{u}} \mathbf{q}_{\dot{u}}^{de,5} &= \frac{1}{2} (\mathbf{L}_{\Delta \dot{u}} \mathbf{q}_{\dot{u}}^{de,2} + \mathbf{L}_{\Delta \dot{u}} \mathbf{q}_{\dot{u}}^{de,3}), \quad \forall de \in \{1, \dots, UDE\} \\ \mathbf{L}_{\Delta \dot{u}} \mathbf{q}_{\dot{u}}^{de,6} &= \frac{1}{2} (\mathbf{L}_{\Delta \dot{u}} \mathbf{q}_{\dot{u}}^{de,1} + \mathbf{L}_{\Delta \dot{u}} \mathbf{q}_{\dot{u}}^{de,3}) \end{aligned} \quad (5.32)$$

in order to enforce a linear velocity jump distribution across each discontinuity.

### Kinematic boundary conditions

The kinematic boundary conditions are applied as

$$\mathbf{q}_{\dot{u}}^{be,i} = \mathbf{q}_{\dot{u}_{bc}}^{be,i}, \quad \forall be \in \{1, \dots, UBE\} \text{ and } i \in \{1, \dots, 6\} \quad (5.33)$$

where  $\mathbf{q}_{\dot{u}_{bc}}^{be,i}$  is the prescribed nodal velocity vector at each velocity evaluation node on the boundary surface  $\Gamma$ .

### Associated plastic flow rule

In each solid element  $\Omega^{el}$ , the associated plastic flow rule is enforced at each strain-rate evaluation node, using the discretised form derived from Eq. (5.25), reading

$$\begin{aligned} \mathbf{R}_{\dot{\boldsymbol{\varepsilon}}}^{el} \mathbf{q}_{\dot{\boldsymbol{\varepsilon}}}^{el,i} &= -\mathbf{B}_{\sigma}^{el\top} \dot{\mathbf{e}}_{\dot{\boldsymbol{\varepsilon}}}^{el,i} \\ &, \quad \forall el \in \{1, \dots, UE\} \text{ and } i \in \{1, \dots, 4\} \\ \dot{\mathbf{e}}_{\dot{\boldsymbol{\varepsilon}}}^{el,i} &\in \mathcal{C}^* \end{aligned} \quad (5.34)$$

in which  $\mathbf{q}_{\dot{\boldsymbol{\varepsilon}},loc}^{el,i}$  is the local nodal strain-rate vector determined from the transformation matrix  $\mathbf{R}_{\dot{\boldsymbol{\varepsilon}}}^{el}$  with similar shape as Eq. (5.8) based on the axial normal vectors  $\mathbf{n}_{x'}^{el}$ ,  $\mathbf{n}_{y'}^{el}$ ,  $\mathbf{n}_{z'}^{el}$  of the material local coordinate basis  $(x' - y' - z')_{mat}^{el}$  of the element,  $\dot{\mathbf{e}}_{\dot{\boldsymbol{\varepsilon}}}^{el,i} \in \mathfrak{R}^8$  is the nodal vector for the associated plastic flow rule Eq. (5.22) in the second-order cone expression and  $\mathbf{B}_{\sigma}^{el} \in \mathfrak{R}^{8 \times 6}$  is the parametric matrix defined in Eq. (5.24). Note that, in this paper the strength behaviours are considered as constant within one element.

Similarly, across each velocity discontinuity  $\Gamma_{dis}^{de}$ , the discretised associated plastic flow rule is derived from Eq. (5.29), reading

$$\begin{aligned} \mathbf{R}_{\Delta \dot{\mathbf{u}}}^{de} \mathbf{q}_{\Delta \dot{\mathbf{u}}}^{de,i} &= -\mathbf{B}_t^{de\top} \dot{\mathbf{e}}_{\Delta \dot{\mathbf{u}}}^{de,i} \\ &, \quad \forall de \in \{1, \dots, UDE\} \text{ and } i \in \{1, \dots, 3\} \\ \dot{\mathbf{e}}_{\Delta \dot{\mathbf{u}}}^{de,i} &\in \mathcal{C}^* \end{aligned} \quad (5.35)$$

where  $\mathbf{q}_{\Delta \dot{\mathbf{u}},loc}^{de,i} \in \mathfrak{R}^3$  is the local nodal velocity-jump vector,  $\mathbf{R}_{\Delta \dot{\mathbf{u}}}^{de}$  is the transformation matrix, defined similar as in Eq. (5.13), from the global coordinate basis  $(x - y - z)$  into the local coordinate basis  $(n - m - p)_{dis}^{de}$  for  $\Gamma_{dis}^{de}$ ,  $\dot{\mathbf{e}}_{\Delta \dot{\mathbf{u}}}^{de,i}$  is the nodal second-order expression of the associated plastic flow rule Eq. (5.26) and  $\mathbf{B}_t^{de} \in \mathfrak{R}^{5 \times 3}$  is the parametric matrix defined in Eq. (5.29).

### Internal dissipation rate

Inserting Eqs. (5.30) and (5.31), the internal plastic dissipation rate Eq. (5.2) can be formulated numerically as

$$\begin{aligned} W_{int} &= \sum_{el=1}^{UE} \int_{\Omega^{el}} \dot{\boldsymbol{\varepsilon}}^{el\top} \boldsymbol{\sigma}^{el} dV + \sum_{de=1}^{UDE} \int_{\Gamma_{dis}^{de}} \Delta \dot{\mathbf{u}}_{loc}^{de\top} \mathbf{t}_{loc}^{de} dA \\ &= \sum_{el=1}^{UE} \int_{\Omega^{el}} (\mathbf{L}_{\dot{\boldsymbol{\varepsilon}}} \sum_{i=1}^{10} N_{\dot{\mathbf{u}}}^{el,i}(\mathbf{x}) \mathbf{q}_{\dot{\mathbf{u}}}^{el,i})^{\top} (\sum_{j=1}^4 N_{\dot{\boldsymbol{\varepsilon}}}^{el,j}(\mathbf{x}) \mathbf{q}_{\boldsymbol{\sigma}}^{el,j}) dV \\ &\quad + \sum_{de=1}^{UDE} \int_{\Gamma_{dis}^{de}} (\mathbf{L}_{\Delta \dot{\mathbf{u}}} \sum_{i=1}^6 \bar{N}_{\dot{\mathbf{u}}}^{de,i}(\mathbf{x}) \mathbf{q}_{\dot{\mathbf{u}}}^{de,i})^{\top} (\sum_{j=1}^3 \bar{N}_{\Delta \dot{\mathbf{u}}}^{de,j}(\mathbf{x}) \hat{\mathbf{q}}_t^{de,j}) dA \\ &= \sum_{el=1}^{UE} \sum_{i=1}^{10} \sum_{j=1}^4 \mathbf{q}_{\dot{\mathbf{u}}}^{el,i\top} \mathbf{G}_{\dot{\boldsymbol{\varepsilon}}}^{el,i,j} \hat{\mathbf{q}}_{\boldsymbol{\sigma}}^{el,j} + \sum_{de=1}^{UDE} \sum_{i=1}^6 \sum_{j=1}^3 \mathbf{q}_{\dot{\mathbf{u}}}^{de,i\top} \bar{\mathbf{G}}_{\Delta \dot{\mathbf{u}}}^{de,i,j} \hat{\mathbf{q}}_t^{de,j} \end{aligned} \quad (5.36)$$

where the numerical integration operators over each solid element  $\Omega^{el}$  and discontinuity  $\Gamma_{dis}^{de}$  are defined as

$$\begin{aligned}\mathbf{G}_{\dot{\varepsilon}}^{el,i,j} &= \int_{\Omega^{el}} \mathbf{L}_{\dot{\varepsilon}}^{\top} N_{\dot{u}}^{el,i}(\mathbf{x}) N_{\dot{\varepsilon}}^{el,j}(\mathbf{x}) dV \in \mathfrak{R}^{3 \times 6} \\ \bar{\mathbf{G}}_{\Delta \dot{u}}^{de,k,l} &= \int_{\Gamma_{dis}^{de}} \mathbf{L}_{\Delta \dot{u}}^{\top} \bar{N}_{\dot{u}}^{de,k}(\mathbf{x}) \bar{N}_{\Delta \dot{u}}^{de,l}(\mathbf{x}) dA \in \mathfrak{R}^{6 \times 3}\end{aligned}\quad (5.37)$$

with  $\forall el \in \{1, \dots, UE\}$ ,  $\forall de \in \{1, \dots, UDE\}$ ,  $i \in \{1, \dots, 10\}$ ,  $j \in \{1, \dots, 4\}$ ,  $k \in \{1, \dots, 6\}$  and  $l \in \{1, \dots, 3\}$ .

As stated by Makrodimitropoulos (2010), since the upper bound problem is based on the kinematic theorem the stress field  $\boldsymbol{\sigma}^{el}$  in each solid element  $\Omega^{el}$  and the traction field  $\mathbf{t}_{loc}^{de}$  at each discontinuity  $\Gamma_{dis}^{de}$  can not be numerically interpolated. Instead, nodal weighted-average stress and traction vectors are obtained, reading

$$\begin{aligned}\hat{\mathbf{q}}_{\sigma}^{el,i} &= \int_{\Omega^{el}} N_{\dot{\varepsilon}}^{el,i}(\mathbf{x}) \boldsymbol{\sigma}^{el} dV / \int_{\Omega^{el}} N_{\dot{\varepsilon}}^{el,i}(\mathbf{x}) dV, \quad \forall el \in \{1, \dots, UE\} \text{ and } i \in \{1, \dots, 4\} \\ \hat{\mathbf{q}}_{t,loc}^{de,j} &= \int_{\Gamma_{dis}^{de}} \bar{N}_{\Delta \dot{u}}^{de,j}(\mathbf{x}) \mathbf{t}_{loc}^{de} dA / \int_{\Gamma_{dis}^{de}} \bar{N}_{\Delta \dot{u}}^{de,j}(\mathbf{x}) dA, \quad \forall de \in \{1, \dots, UDE\} \text{ and } j \in \{1, \dots, 3\}\end{aligned}\quad (5.38)$$

at the strain-rate evaluation nodes, with the interpolation function for the strain-rate  $N_{\dot{\varepsilon}}^{el,i}(\mathbf{x})$  and the traction evaluation nodes with the interpolation function for velocity-jump  $\bar{N}_{\Delta \dot{u}}^{de,j}(\mathbf{x})$ , respectively.

## Assembly

Assembling above constraints, the primal upper bound problem Eq. (5.3) in discretised form reads

$$\begin{aligned}\min \quad & W_{int} \\ \text{s.t.} \quad & \mathbf{A}_{\dot{\varepsilon}}^{com} \mathbf{q}_{\dot{u}} = \mathbf{q}_{\dot{\varepsilon}} \\ & \mathbf{A}_{\Delta \dot{u}}^{com} \mathbf{q}_{\dot{u}} = \mathbf{q}_{\Delta \dot{u}} \\ & \mathbf{A}_{\Delta \dot{u}}^{lin} \mathbf{q}_{\dot{u}} = \mathbf{0} \\ & \mathbf{q}_{\dot{u}} = \mathbf{q}_{\dot{u}_{bc}} \\ & \mathbf{R}_{\dot{\varepsilon}}^{el} \mathbf{q}_{\dot{\varepsilon}}^{el,i} = -\mathbf{B}_{\sigma}^{el\top} \dot{\mathbf{e}}_{\dot{\varepsilon}}^{el,i} \\ & \dot{\mathbf{e}}_{\dot{\varepsilon}}^{el,i} \in \mathcal{C}^* \\ & \mathbf{R}_{\Delta \dot{u}}^{de} \mathbf{q}_{\Delta \dot{u}}^{de,j} = -\mathbf{B}_t^{de\top} \dot{\mathbf{e}}_{\Delta \dot{u}}^{de,j} \\ & \dot{\mathbf{e}}_{\Delta \dot{u}}^{de,j} \in \mathcal{C}^*\end{aligned}\quad (5.39)$$

with  $el \in \{1, \dots, UE\}$ ,  $de \in \{1, \dots, UDE\}$ ,  $i \in \{1, \dots, 4\}$  and  $j \in \{1, \dots, 3\}$ . In the formulation Eq. (5.39),  $\mathbf{q}_{\Delta \dot{u}} \in \mathfrak{R}^{3UN}$ ,  $\mathbf{q}_{\dot{\varepsilon}} \in \mathfrak{R}^{24UE}$  and  $\mathbf{q}_{\Delta \dot{u}} \in \mathfrak{R}^{9UDE}$  are the assembly of all nodal velocity vectors, nodal strain-rate vectors and nodal velocity-jump vectors over the whole structure with respect to the global coordinate basis ( $x - y - z$ ). Here,  $UN$  is the total number of velocity evaluation nodes in the upper bound formulations. The assembled matrices are introduced as the compatibility operator in solid elements  $\mathbf{A}_{\dot{\varepsilon}}^{com} \in \mathfrak{R}^{24UE \times 3UN}$  from Eq. (5.30), the compatibility operator on velocity discontinuities  $\mathbf{A}_{\Delta \dot{u}}^{com} \in \mathfrak{R}^{9UDE \times 3UN}$  from Eq. (5.31), the operator enforcing

linear velocity jumps across velocity discontinuities  $\mathbf{A}_{\Delta\dot{u}}^{lin} \in \mathfrak{R}^{9UDE \times 3UN}$  from Eq. (5.32) and the prescribed kinematic boundary conditions  $\mathbf{q}_{\dot{u}bc} \in \mathfrak{R}^{3UN}$  from Eq. (5.33).

### 5.5.2 Dual formulations

The dual upper bound problem Eq. (5.5) is based on the stress field  $\boldsymbol{\sigma}$  and is mathematically equivalent to the primal problem Eq. (5.3). As mentioned above, in the finite-element-based formulations, the numerical interpolation and integration can only be directly applied to the velocity field and the strain-rate field, thus, in the dual formulations the stress field and the traction field are interpolated using the nodal weighted-average vectors defined in Eq. (5.38) at evaluation nodes for the strain-rate field and the velocity field, respectively.

#### External work rate

The external work rate Eq. (5.6) in discretised form reads

$$W_{ext} = \sum_{i=1}^{UN} (\mathbf{q}_u^{i\top} \beta \mathbf{q}_{p_u}^i + \mathbf{q}_u^{i\top} \mathbf{q}_{p_f}^i) \quad (5.40)$$

where  $\mathbf{q}_u^i$  is the nodal velocity field,  $\mathbf{q}_{p_u}^i = (q_{p_u,x}^i, q_{p_u,y}^i, q_{p_u,z}^i)^\top \in \mathfrak{R}^3$  is the unknown nodal force at each velocity evaluation node determined from the unknown body force field  $\mathbf{g}_u$  in  $\Omega$  and the unknown traction field  $\mathbf{t}_u$  on  $\Gamma_u$ , and  $\mathbf{q}_{p_f}^i = (q_{p_f,x}^i, q_{p_f,y}^i, q_{p_f,z}^i)^\top \in \mathfrak{R}^3$  is the fixed nodal force determined from the fixed body force field  $\mathbf{g}_f$  in  $\Omega$  and the fixed traction field  $\mathbf{t}_f$  on  $\Gamma_f$ .

#### Weak form of equilibrium

The weak form of equilibrium refers to the equality between the total internal energy dissipation rate and the total work rate done by external loads. Considering Eqs. (5.36) and (5.40), the discretised form can be expressed as

$$\sum_{el=1}^{UE} \sum_{i=1}^{10} \sum_{j=1}^4 \mathbf{q}_u^{el,i\top} \mathbf{G}_{\dot{\varepsilon}}^{el,i,j} \hat{\mathbf{q}}_{\sigma}^{el,j} + \sum_{de=1}^{UDE} \sum_{i=1}^6 \sum_{j=1}^3 \mathbf{q}_u^{de,i\top} \bar{\mathbf{G}}_{\Delta\dot{u}}^{de,i,j} \hat{\mathbf{q}}_t^{de,j} = \sum_{i=1}^{UN} \mathbf{q}_u^{i\top} (\beta \mathbf{q}_{p_u}^i + \mathbf{q}_{p_f}^i) \quad (5.41)$$

where it is obvious that the velocity vector at both sides can be eliminated in the assembly.

#### Plastic yield function

Since in the discretised formulations the stress field and the traction field are obtained as weighted-average vectors defined in Eq. (5.38), the second-order cone expressions of

yield functions Eqs. (5.23) and (5.27) are formulated as

$$\begin{aligned} \hat{\mathbf{s}}_{\sigma}^{el,i} &= \mathbf{a}_{\sigma}^{el} + \mathbf{B}_{\sigma}^{el} \mathbf{R}_{\sigma}^{el} \hat{\mathbf{q}}_{\sigma}^{el,i} \\ \hat{\mathbf{s}}_{\sigma}^{el,i} &\in \mathcal{C} \end{aligned}, \quad \forall el \in \{1, \dots, UE\} \text{ and } i \in \{1, \dots, 4\} \quad (5.42a)$$

$$\begin{aligned} \hat{\mathbf{s}}_t^{de,j} &= \mathbf{a}_t^{de} + \mathbf{B}_t^{de} \mathbf{R}_t^{de} \hat{\mathbf{q}}_t^{de,j} \\ \hat{\mathbf{s}}_t^{de,j} &\in \mathcal{C} \end{aligned}, \quad \forall de \in \{1, \dots, UD\} \text{ and } j \in \{1, \dots, 3\} \quad (5.42b)$$

where  $\mathbf{R}_{\sigma}^{el} = \mathbf{R}_{\dot{\varepsilon}}^{el}$ ,  $\mathbf{R}_t^{de} = \mathbf{R}_{\Delta \dot{u}}^{de}$ , and  $\hat{\mathbf{s}}_{\sigma}^{el,i} \in \mathfrak{R}^8$  and  $\hat{\mathbf{s}}_t^{de,j} \in \mathfrak{R}^5$  are the weighted-average vectors for the second-order cone expressions of the stress-based and traction-based yield functions, respectively.

### Assembly

The discretised formulation of the dual upper bound problem Eq. (5.5) can be expressed as

$$\begin{aligned} \max \quad & W_{ext} \\ \text{s.t.} \quad & \mathbf{G}_{\dot{\varepsilon}} \hat{\mathbf{q}}_{\sigma} + \bar{\mathbf{G}}_{\Delta \dot{u}} \hat{\mathbf{q}}_t + \mathbf{A}_{\Delta \dot{u}}^{lin \top} \mathbf{r} = \beta \mathbf{q}_{p_u} + \mathbf{q}_{p_f} \\ & \hat{\mathbf{s}}_{\sigma}^{el,i} = \mathbf{a}_{\sigma}^{el} + \mathbf{B}_{\sigma}^{el} \mathbf{R}_{\sigma}^{el} \hat{\mathbf{q}}_{\sigma}^{el,i} \\ & \hat{\mathbf{s}}_{\sigma}^{el,i} \in \mathcal{C} \\ & \hat{\mathbf{s}}_t^{de,j} = \mathbf{a}_t^{de} + \mathbf{B}_t^{de} \mathbf{R}_t^{de} \hat{\mathbf{q}}_t^{de,j} \\ & \hat{\mathbf{s}}_t^{de,j} \in \mathcal{C} \end{aligned} \quad (5.43)$$

with  $el \in \{1, \dots, UE\}$ ,  $de \in \{1, \dots, UDE\}$ ,  $i \in \{1, \dots, 4\}$  and  $j \in \{1, \dots, 3\}$ . In the dual upper bound formulation Eq. (5.43),  $\hat{\mathbf{q}}_{\sigma} \in \mathfrak{R}^{24UE}$  and  $\hat{\mathbf{q}}_t \in \mathfrak{R}^{9UDE}$  are the assembly of the nodal weighted-average stress vectors in all solid element  $\Omega^{el}$  and the nodal weighted-average traction vectors at all discontinuities  $\Gamma_{dis}^{de}$ ,  $\mathbf{q}_{p_u} \in \mathfrak{R}^{3UN}$  and  $\mathbf{q}_{p_f} \in \mathfrak{R}^{3UN}$  are the assembly of unknown and fixed nodal force vectors at all velocity evaluation nodes, and  $\mathbf{G}_{\dot{\varepsilon}} \in \mathfrak{R}^{3UN \times 24UE}$  and  $\bar{\mathbf{G}}_{\Delta \dot{u}} \in \mathfrak{R}^{3UN \times 9UDE}$  are the assembled matrices for integration operators from Eq. (5.37). The auxiliary term  $\mathbf{A}_{\Delta \dot{u}}^{lin \top} \mathbf{r}$  in the first constraint is derived from the third constraint of the primal assembled formulation Eq. (5.39) due to the duality and is vanished in the internal energy expression Eq. (5.41) since  $\mathbf{A}_{\Delta \dot{u}} \mathbf{q}_{\dot{u}} = \mathbf{0}$  where  $\mathbf{r} \in \mathfrak{R}^{3UN}$  is an auxiliary vector.

## 5.6 Adaptive arrangement of the velocity discontinuity

In existing finite-element-based upper bound approaches, velocity discontinuities are often introduced between all finite elements with their orientation only depending on the finite element mesh. However, in most cases significant velocity jumps occur only at very few discontinuities, in regions where very localised plastic failure modes can be identified (Ciria et al., 2008, Krabbenhøft et al., 2005, Makrodimopoulos and Martin, 2008, Sloan and Kleeman, 1995). Thus, in many parts of a discretised body the additional degrees of freedom introduced by discontinuities are not well invested and, additionally, an in general arbitrary orientation of discontinuities prevents them to capture localised plastic

flow efficiently. Subsequently, strong mesh refinements are necessary to further improve upper bound results, even if adaptive mesh refinement strategies are used.

However, as shown by the authors in Li et al. (2018b), if discontinuities are only introduced in regions with large plastic flow and arranged/oriented in view of potential directions of plastic flow localisation, very good upper bounds can be obtained (even for orthotropic material strength behaviour) using relatively coarse finite element meshes. In this way, only as many as useful discontinuities are implemented and, due to a sensibly arrangement, they are on average much better utilised.

Naturally, the performance of this approach relies heavily on the algorithm for the adaptive introduction and adjustment of velocity discontinuities, and its applicability to arbitrary problems. Such an algorithm will be proposed within the next sections.

### 5.6.1 Determination of planes of plastic flow localisation

As introduced in Section 5.3, plastic flow (a velocity jump) across a discontinuity will only happen when the strain-rate localisation conditions in Eq. (5.14) are fulfilled. Thus, these conditions can also be used to find a meaningful orientation of a discontinuity. The task of a related algorithm can be formulated as: *for a given strain-rate state find the critical plane on which the two tangential components and the in-plane shear component of the local strain-rate vector equal zero*. In particular, for a given 3D strain-rate state  $\dot{\boldsymbol{\epsilon}} = (\dot{\epsilon}_{xx}, \dot{\epsilon}_{yy}, \dot{\epsilon}_{zz}, 2\dot{\epsilon}_{xy}, 2\dot{\epsilon}_{yz}, 2\dot{\epsilon}_{xz})^\top \in \mathfrak{R}^6$  the critical plane  $\Gamma_{crit}$  on which the local strain-rate state reads  $\dot{\boldsymbol{\epsilon}}_{crit} = (\dot{\epsilon}_{nm}, 0, 0, 2\dot{\epsilon}_{nm}, 0, 2\dot{\epsilon}_{np})^\top \in \mathfrak{R}^6$  with respect to the local coordinate basis  $(n - m - p)_{crit}$  needs to be found.

The strain-rate state can be represented by three Mohr's circles based on the three principal strain-rates  $\dot{\epsilon}_1$ ,  $\dot{\epsilon}_2$  and  $\dot{\epsilon}_3$  ( $\dot{\epsilon}_1 \geq \dot{\epsilon}_2 \geq \dot{\epsilon}_3$ ). Denoting the eigenvectors of the the strain-rate tensor as  $\mathbf{v}_1 \in \mathfrak{R}^3$ ,  $\mathbf{v}_2 \in \mathfrak{R}^3$  and  $\mathbf{v}_3 \in \mathfrak{R}^3$ , the transformation matrix from the global coordinate basis  $(x - y - z)$  into the principal coordinate basis  $(1 - 2 - 3)$  reads  $\mathbf{R}_v = (\mathbf{v}_1, \mathbf{v}_2, \mathbf{v}_3)^\top \in \mathfrak{R}^{3 \times 3}$ .

The corresponding strain-rate invariants then read

$$\dot{I}_1 = \dot{\epsilon}_1 + \dot{\epsilon}_2 + \dot{\epsilon}_3 = \dot{\epsilon}_{nn} \quad (5.44a)$$

$$\dot{I}_2 = \dot{\epsilon}_1\dot{\epsilon}_2 + \dot{\epsilon}_2\dot{\epsilon}_3 + \dot{\epsilon}_1\dot{\epsilon}_3 = -\dot{\epsilon}_{nm}^2 - \dot{\epsilon}_{np}^2 \quad (5.44b)$$

$$\dot{I}_3 = \dot{\epsilon}_1\dot{\epsilon}_2\dot{\epsilon}_3 = 0 \quad (5.44c)$$

Eqs. (5.44b) and (5.44c) are only ever met when the following conditions are satisfied

$$\dot{\epsilon}_1 \geq 0 \quad \text{and} \quad \dot{\epsilon}_2 = 0 \quad \text{and} \quad \dot{\epsilon}_3 \leq 0 \quad (5.45)$$

That means, if strain-rate states can be found fulfilling Eq. (5.45), ideal orientations for a discontinuity can be easily calculated at which plastic flow will happen very localised, as will be shown in the following.

The Mohr's circles for the strain-rate state  $\dot{\boldsymbol{\epsilon}}$  are plotted in Figure 5.3 as  $C_1$  for the 2 - 3 plane,  $C_2$  for the 1 - 3 plane and  $C_3$  for the 1 - 2 plane. According to Eq. (5.45) (since  $\dot{\epsilon}_1 \geq 0$ ) the vertical axis must form a tangent to  $C_1$  and  $C_3$  and  $C_2$  must intersect with the vertical axis since  $\dot{\epsilon}_1 \geq 0$  and  $\dot{\epsilon}_3 \leq 0$ . Note that, in a 3D coordinate basis

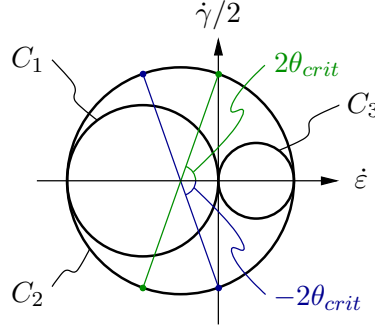


Figure 5.3: Mohr's circles for the given strain-rate state  $\dot{\epsilon}$  and the two critical orientations  $\pm\theta_{crit}$  in the 1 – 3 plane, where the tangential strain-rate components equal zero.

an arbitrary plane intersects with two coordinate planes if it passes through the origin  $(0, 0, 0)$ . Thus, the critical plane  $\Gamma_{crit}$  for the strain-rate state  $\dot{\epsilon}$  can be determined from its two intersecting lines with different coordinate planes along with the tangential strain-rate component equals zero.

By means of Mohr's circles in Figure 5.3, since both  $C_1$  and  $C_3$  conform to the vertical axis, the first intersecting line runs parallel to axis 2 and its orientation is given by the normal vector  $\mathbf{n}_{(123)}^{line,1} = (0, 1, 0)^\top \in \mathfrak{R}^3$  with respect to the principal coordinate basis  $(1 - 2 - 3)$ ; since  $C_2$  intersects with the vertical axis, the second intersecting line can be determined in the 1 – 3 plane. Introducing  $\theta_{crit}$  as the angle between the intersecting line and axis 1 in the 1 – 3 plane, based on the strain-rate transformation Eq. (5.8), the tangential strain-rate component along this line can be expressed as

$$\dot{\epsilon}_1(\cos(\theta_{crit}))^2 + \dot{\epsilon}_3(\cos(\theta_{crit}))^2 = 0 \quad (5.46)$$

resulting in

$$\theta_{crit} = \pm \text{atan}(\sqrt{-\dot{\epsilon}_1/\dot{\epsilon}_3}) \quad (5.47)$$

Thus, the second intersecting line can be determined in the 1 – 3 plane and exhibits two possibilities, with the normal vectors reading  $\mathbf{n}_{(123)}^{line,2\pm} = (\cos(\theta_{crit}), 0, \pm \sin(\theta_{crit}))^\top \in \mathfrak{R}^3$ . Obviously, these two lines coincide with each other if  $\dot{\epsilon}_1 > 0$ ,  $\dot{\epsilon}_3 = 0$  then  $\mathbf{n}_{(123)}^{line,2+} = \mathbf{n}_{(123)}^{line,2-} = (0, 0, 1)^\top$  and  $\dot{\epsilon}_1 = 0$ ,  $\dot{\epsilon}_3 < 0$  then  $\mathbf{n}_{(123)}^{line,2+} = \mathbf{n}_{(123)}^{line,2-} = (1, 0, 0)^\top$ .

Finally, the out-of-plane normal vectors for the two possible critical planes, with respect to the global coordinate basis  $(x - y - z)$ , are determined as

$$\mathbf{n}_{(xyz)}^{surf,\pm} = \mathbf{R}_v^{-1} \mathbf{n}_{(123)}^{surf,\pm} = \mathbf{R}_v^{-1} (\mathbf{n}_{(123)}^{line,1} \times \mathbf{n}_{(123)}^{line,2\pm}) \in \mathfrak{R}^3 \quad (5.48)$$

where  $\mathbf{n}_{(123)}^{surf,\pm} \in \mathfrak{R}^3$  represent the normal vectors for the critical planes with respect to the principal coordinate basis  $(1 - 2 - 3)$  and  $\mathfrak{R}_v$  is the transformation matrix from  $(x - y - z)$  to  $(1 - 2 - 3)$ .

### 5.6.2 Adaptive introduction and adjustment of velocity discontinuities

Based on the determination of critical planes, where localised plastic failure will occur, an adaptive strategy for the introduction and adjustment of velocity discontinuities  $\Gamma_{dis}$  is presented in the following. The procedure of this adaptive strategy is roughly illustrated in the flowchart Figure 5.4.

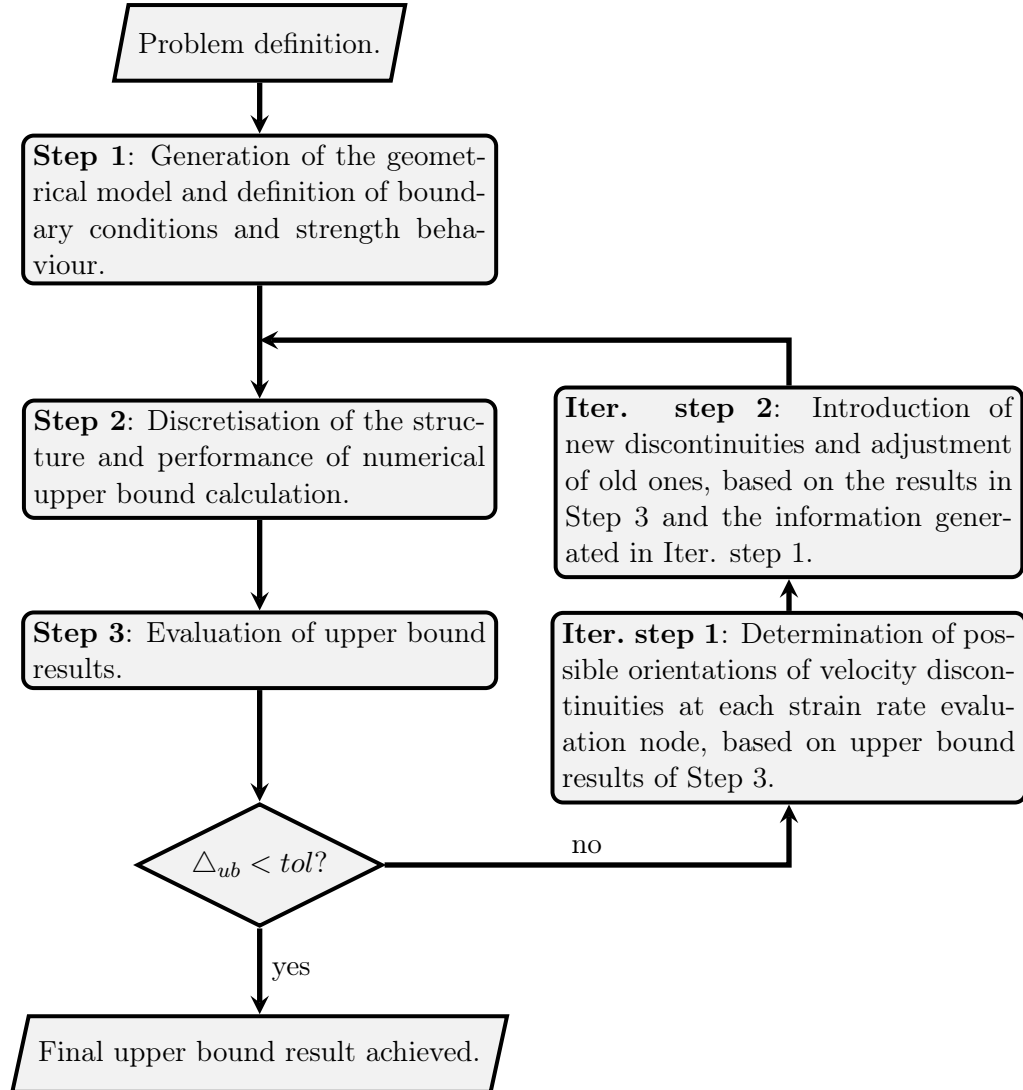


Figure 5.4: Flowchart introducing the adaptive strategy, where in each iteration the introduction and adjustment of velocity discontinuity (**Iter. step 1-2**) are based on the upper bound calculations (**Step 2-3**).

At first, an upper bound calculation without any velocity discontinuity using a relatively coarse mesh is performed. Based on this result, at each strain rate evaluation node (of the solid elements) the normal vectors  $\mathbf{n}_{(xyz)}^{surf,+}$ ,  $\mathbf{n}_{(xyz)}^{surf,-}$ , indicating the two possible critical planes of plastic flow localisation, are determined. Then, the node with the highest plastic multiplier rate serves as starting point for the first introduced discontinuity. From the two possible orientations,  $\mathbf{n}_{(xyz)}^{surf,+}$  and  $\mathbf{n}_{(xyz)}^{surf,-}$ , the one is selected



which points into the region with higher plastic multiplier rates. All subsequent discontinuities are introduced in a repetitive sequence, starting always at the previous end node of the last introduced discontinuity and oriented along the critical plane with the lower deviation angle to the existing discontinuity. As will be introduced in the following, the length of each discontinuity is of the same magnitude as the characteristic mesh size and defined by a straight line for problems under plane strain conditions and as an interior surface cutting through the corresponding solid element for 3D problems, respectively. In the first iteration, since a quite coarse mesh is used, the so-obtained layout for the velocity discontinuities is normally not able to capture localised failure sufficiently, and thus, adjustments through further iterations are needed, as sketched in Figure 5.4.

In every further iteration, the structure is discretised again, taking the introduced discontinuities into account. The improvement in the upper bound result is measured by  $\Delta_{ub}(\%) = (\beta_{UB}^i - \beta_{UB}^{i-1})/\beta_{UB}^{i-1} \times 100$ , as the percentage reduction of the collapse load multiplier from the previous iteration  $\beta_{UB}^{i-1}$  to the current iteration  $\beta_{UB}^i$ . As soon as the discontinuity layout is sufficiently arranged with respect to the appearing failure mode, only small improvements will be obtained from further iterations, and the iteration is ended as soon as  $\Delta_{ub}$  is smaller than the prescribed threshold value *tol*.

In the following, the introduction of discontinuities is explained in more detail, separately for the plane strain case and the general 3D case.

### Plane strain case

The first method is applied for problems under plane strain conditions, in which the introduction of discontinuities can be defined by lines on a 2D plane. Thereby, the  $y$  axis represents the out-of-plane direction and, then, if the conditions in Eq. (5.45) are satisfied, one principal axis coincides with the  $y$  axis and the principal strain rates  $\dot{\epsilon}_1, \dot{\epsilon}_3$  can be found in the  $x - z$  plane.

Based on an upper bound calculation, the plastic multiplier rate  $\dot{\lambda}_{mat}$  and the two normal vectors  $\mathbf{n}_{(xyz)}^{surf,\pm}$  according to Eq. (5.48), defining the critical discontinuities  $\Gamma_{crit}$ , are determined at each strain rate evaluation node. Through linear interpolation between the plastic multiplier rates and nearest neighbour interpolation between the normal vectors, the fields  $\dot{\lambda}_{mat}(\hat{\mathbf{x}})$  and  $\mathbf{n}_{(xyz)}^{surf,\pm}(\hat{\mathbf{x}})$  are defined, where  $\hat{\mathbf{x}}$  refers to an arbitrary node in the  $x - z$  plane.

The subsequent determination of discontinuities is demonstrated in Figure 5.5, where the abandoned critical planes are plotted as dashed lines and the dot-dashed curves indicate contours of the plastic multiplier rate field. As illustrated in Figure 5.5a, the starting point of the first discontinuity is automatically chosen as the boundary node  $\hat{\mathbf{x}}_0$  with the highest plastic multiplier rate  $\dot{\lambda}_{mat}(\hat{\mathbf{x}}_0)$ . The end point  $\hat{\mathbf{x}}_1$  is defined by the characteristic length of the mesh and the orientation given by the normal vectors  $\mathbf{n}_{(xyz)}^{surf,\pm}(\hat{\mathbf{x}}_0)$ , where the orientation is selected leading to the higher plastic multiplier rate at the end point. Any further discontinuity always starts at the end node of the previous one  $\hat{\mathbf{x}}_{i-1}$  and the normal vector  $\mathbf{n}_{(xyz)}^{surf,i}$  is determined as the one with the smaller angle to the previous normal vector, indicated as  $\hat{\theta}_1 < \hat{\theta}_2$  in Figure 5.5a, where  $i \in \{2, \dots, n_p\}$  and  $n_p$  is the total number of introduced discontinuities in this iteration. This sequence of introducing discontinuities is terminated as soon as the end node of the last line  $\hat{\mathbf{x}}_i$

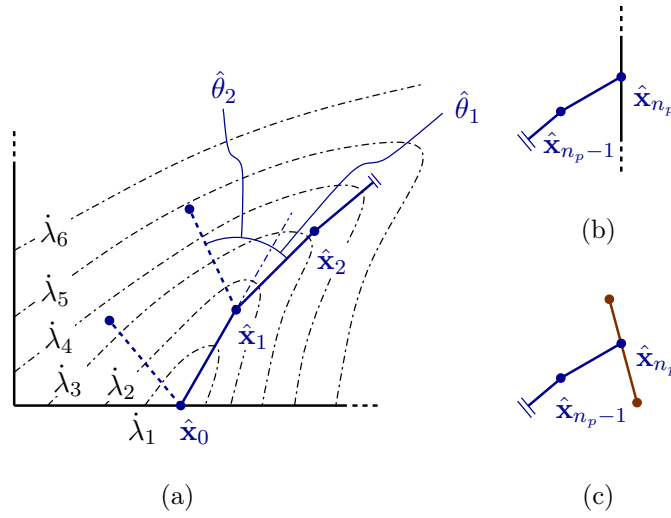


Figure 5.5: Illustrative example for the introduction of velocity discontinuities under plane strain conditions. (a) First and second discontinuity; (b) the last discontinuity in an iteration step in case it intersects with the boundary of the structure; (c) the last discontinuity of an iteration step in case it intersects with an existing discontinuity.

intersects with either the boundary of the 2D plane, as shown in Figure 5.5b, or an existing discontinuity, as shown in Figure 5.5c.

### General 3D case

Instead of lines, as for the plane strain case, in 3D, discontinuities are determined and defined through surfaces. Thus, a slightly different approach is required to introduce them into a 3D body. For this reason, piecewise planar surfaces are introduced, which cut through the tetrahedral elements. To track the evolution of surfaces, the level-set method is employed (Moës et al., 2002, Osher and Sethian, 1988). Thereby, for each element, which is cut by a surface, all nodes have nonzero  $\phi$ -values, such that  $\phi(\mathbf{x}) = 0$  clearly defines the partition surface. Analogously to the plane strain case, first, the element with the highest plastic multiplier rate  $\dot{\lambda}_{mat}(\hat{\mathbf{x}}_0)$  on one of the boundary surfaces is chosen as the starting point of the partitioning algorithm. A first partition (in this element) with the normal vector  $\mathbf{n}_{(xyz)}^{surf,1}$  is determined from the two possibilities  $\mathbf{n}_{(xyz)}^{surf,\pm}(\hat{\mathbf{x}}_0)$ , where the one is selected leading to end nodes on the interface of the adjacent element with higher plastic multiplier rate.

To ensure a continuous surface, the next partition is introduced in the current element following the algorithm demonstrated in Figure 5.6, where the blue surface indicates the determined partition surface in the adjacent element with end nodes marked in blue. Thus, three of the four  $\phi$ -values ( $\phi_1^i, \phi_2^i, \phi_3^i$ ) for the current element are already predetermined by the neighbouring element and only the last one ( $\phi_4^i$ ) has to be calculated. The partition with the normal vector  $\mathbf{n}_{(xyz)}^{surf,i}$ , as the one with the smallest angle to the normal vector  $\mathbf{n}_{(xyz)}^{surf,i-1}$  of the partition in the adjacent element, is chosen out of the two possible normal vectors  $\mathbf{n}_{(xyz)}^{surf,\pm}(\hat{\mathbf{x}}_{i-1})$  and the resulting fourth  $\phi$ -value is calculated.

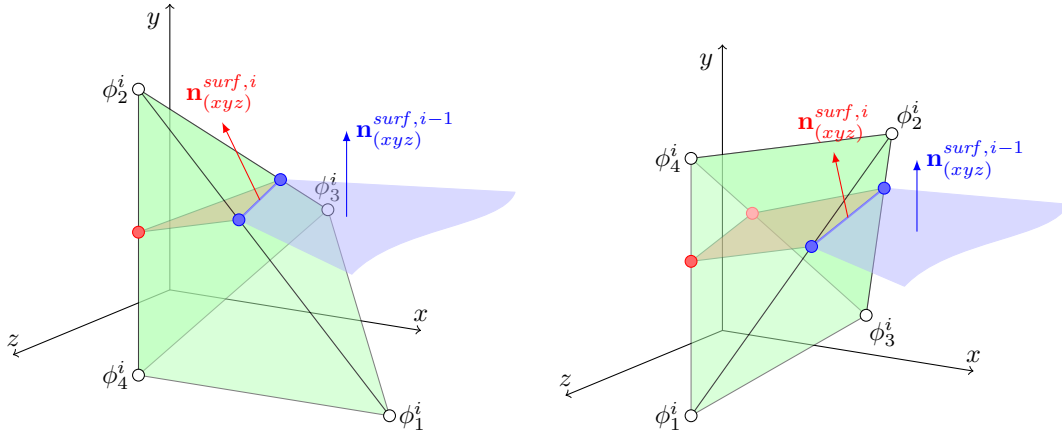


Figure 5.6: Two examples of an element  $i$  (green) with a possible partition/discontinuity and normal vector  $\mathbf{n}_{(xyz)}^{surf,i}$  (red), which is adjacent to an element  $i - 1$  with already determined partition/discontinuity surface and normal vector  $\mathbf{n}_{(xyz)}^{surf,i-1}$  (blue), obtained in a previous step of the algorithm. The partition surface is tracked by using the level-set method, where the iso-zero level set  $\phi(\mathbf{x}) = 0$  defines the surface location.

It can also be noticed that the resulting iso-zero level set, and, therefore, the partition surface, inside a tetrahedron is either a triangle or a quadrilateral.

This step is then repeated until no more partitioning candidates are found, which means that the piecewise planar partition has reached a boundary surface on all sides and the model can be separated into two parts, where all nodal  $\phi$ -values on one side of the partition have the same sign. The resulting iso-zero level set surface, which is built up of planar triangles and quadrilaterals, is then used to partition the model. Next, the partitioned model is re-meshed with a similar mesh size as the original version and the simulation is rerun with velocity discontinuities introduced between the two model parts.

## 5.7 Numerical results

In this section, the performance of the proposed upper bound formulations with adaptive introduction of velocity discontinuities is assessed by means of several examples. Two often used benchmark problems (under the plane strain condition) with isotropic strength behaviour are discussed and the results are compared with reference solutions, providing a basic verification of the proposed approach. Subsequently, these two examples are extended by orthotropic strength behaviour, showing that both the traction-based yield functions as well as the adaptive arrangement of velocity discontinuities also work for such cases. Finally, the full potential of the presented approach is shown by means of an example 3D problem.

It should be noted that the main goal of this section is to assess the performance of the adaptive arrangement of velocity discontinuities with respect to reliability and efficiency whereas the chosen examples themselves have no special significance. Thus, focus is laid on comparisons between upper bound results with velocity discontinuities (referred to as discontinuous upper bound results) and reference solutions obtained without any

discontinuities (referred to as continuous upper bound results).

The computations were performed on a Linux desktop machine with an AMD FX(tm)-8350 processor (8 cores) and 16 GB of RAM. All pre- and post-processing tasks as well as the assembly of SOCP optimisation problems were carried out by self-written codes in Fortran. The mesh generation and introduction of velocity discontinuities into the discretised structure were done by the commercial software package ABAQUS controlled via self-written Python scripts. The SOCP optimisation problems themselves were solved using the commercial software MOSEK ApS (2017), which is based on the conic interior-point algorithm described in Andersen et al. (2002). The adaptive approach introduced in Section 5.6 runs fully automated, realised by only a Python script for the plane strain problems and in combination with a Matlab script for general 3D problems.

### 5.7.1 Block with thin symmetric notches

In this benchmark problem, double-sided uniform tensile load is applied on a square block with zero-thickness symmetric notches under plane strain conditions. This example has already been extensively studied in Christiansen and Andersen (1999), Christiansen and Pedersen (2001), Ciria et al. (2008), Krabbenhøft and Damkilde (2003), Makrodimopoulos and Martin (2006), Nguyen-Xuan and Liu (2015), Nguyen-Xuan et al. (2017), where very good lower as well as upper bound predictions could be obtained. An exact solution is not available for the collapse limit load multiplier  $\beta$ , thus, the solutions obtained based on Richardson extrapolation (Christiansen and Andersen, 1999, Christiansen and Pedersen, 2001) are considered as reference value  $\beta^*$ , with the difference between the obtained results and this reference value measured by  $err(\%) = (\beta - \beta^*)/\beta^* \times 100$ .

For the upper bound calculation, only a quarter of the square is considered, with geometry and boundary conditions as shown in Figure 5.7a.  $L$  is the length of each side,  $a$  is the length of the notch, and  $p$  refers to the uniform tensile loading. Note that, in this paper all calculations are carried out by 3D finite-element-based upper bound formulations. An example mesh with 592 tetrahedral elements is shown in Figure 5.7b. The plane strain condition is enforced with respect to the  $x-y$  plane by applying symmetric boundary conditions on the  $z-$  and  $z+$  boundary surfaces. Thus, in the following, all results will be plotted only in the  $x-y$  plane.

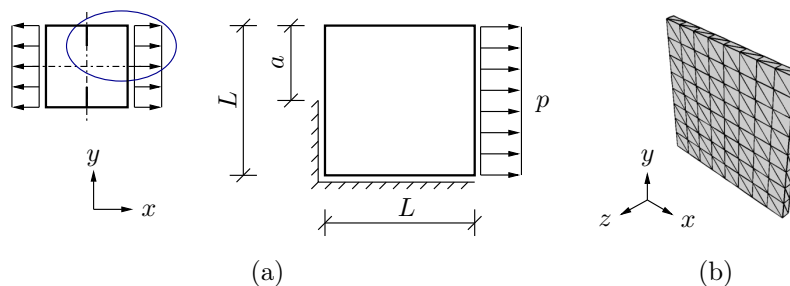


Figure 5.7: Example square block with symmetric notches under uniform tensile loading: (a) geometry and boundary conditions; (b) example discretisation with 592 tetrahedron elements.

Isotropic strength behaviour is defined using the von Mises yield function  $\sqrt{J_2} \leq c$ , with  $J_2$  as the second deviatoric stress invariant and  $c$  as the coefficient of cohesion. With respect to the general form of yield function in Eq. (5.7), the von Mises criterion is recovered by

$$\mathbf{P}_\sigma^{mat} = \frac{1}{3c^2} \begin{pmatrix} 1 & -0.5 & -0.5 & 0 & 0 & 0 \\ -0.5 & 1 & -0.5 & 0 & 0 & 0 \\ -0.5 & -0.5 & 1 & 0 & 0 & 0 \\ 0 & 0 & 0 & 3 & 0 & 0 \\ 0 & 0 & 0 & 0 & 3 & 0 \\ 0 & 0 & 0 & 0 & 0 & 3 \end{pmatrix} \quad \mathbf{F}_\sigma^{mat,+} = \mathbf{F}_\sigma^{mat,-} = \mathbf{0} \quad (5.49)$$

The traction-based yield function for velocity discontinuities is determined using the projection algorithm introduced in Section 5.3 and is, because of the isotropic strength behaviour, independent on the orientation of the discontinuities. The matrices according to Eq. (5.17c) then read

$$\mathbf{P}_t^{dis} = \frac{1}{c^2} \begin{pmatrix} 0 & 0 & 0 \\ 0 & 1 & 0 \\ 0 & 0 & 1 \end{pmatrix} \quad \mathbf{F}_t^{dis,+} = \mathbf{F}_t^{dis,-} = \mathbf{0} \quad (5.50)$$

By means of an example with a notch length of  $a = L/2$ , the performance of the adaptive introduction and arrangement of discontinuities is shown in the following. Thereby, in each iteration the improvement of the upper bound and the related failure mechanism is discussed. An upper bound value of  $\lambda^* = 1.1316$  according to Christiansen and Pedersen (2001) is chosen as reference.

**Initial step** In an initial step, an upper bound calculation is performed using a relatively coarse mesh and no velocity discontinuities, as shown in Figure 5.8a1. The resulting failure mode (deformed configuration and plastic multiplier rate field) is plotted in Figure 5.8b1, where it can be observed that plastic failure is very dominant in regions close to the notch tip as well as at the corner between the loaded surface and the symmetric surface. In general, due to the coarse mesh in combination with the continuous velocity field, the plastic failure is distributed over several elements and no obvious failure/slip lines can be identified. However, based on that results, according to the algorithm presented in Section 5.6, a first layout of velocity discontinuities is determined. The CPU time for this iteration step was 12.8 s.

**First iteration** A first layout of velocity discontinuities is introduced into the structure as a sequence of partitions as shown in Figure 5.8a2. After re-meshing, the failure mode in Figure 5.8b2 is obtained, showing significant interface shear failure across the introduced discontinuities and, simultaneously, a reduction of plastic dissipation within adjacent elements, especially within those close to the notch tip. Since the characteristic length of the introduced discontinuities is of the same size as the characteristic initial mesh size, the fineness of discretisation remains almost the same, and only a minor amount of degrees of freedom is added through the velocity discontinuities. From the initial step to this first iteration, the total

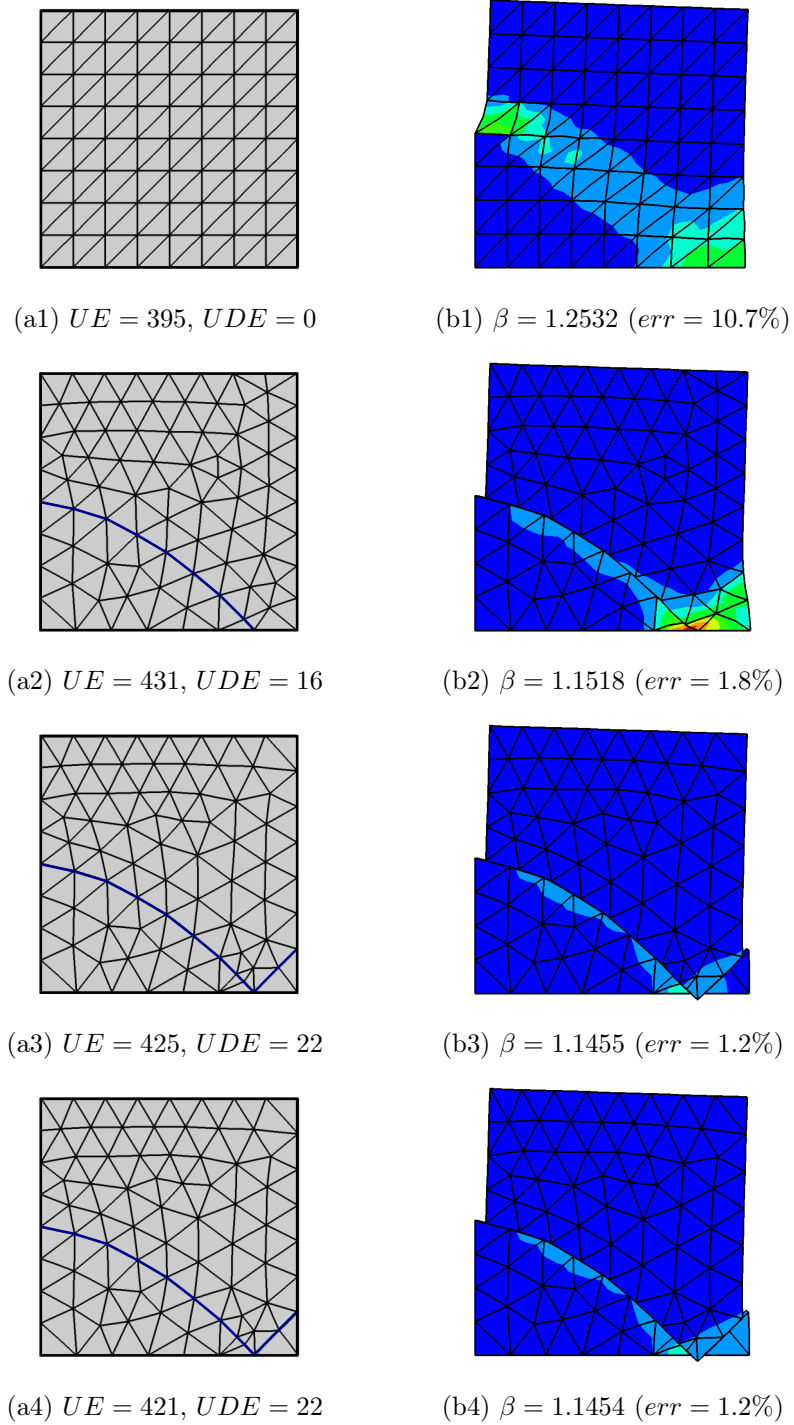


Figure 5.8: Example notched block under uniform tensile loading with  $a = L/2$ . The adaptive introduction of velocity discontinuities through three iteration steps. (a1)-(a4) The initial mesh and the meshes for each iteration with the introduced velocity discontinuities in blue; (b1)-(b4) the related upper bound failure modes with the plastic multiplier rate  $\dot{\lambda}_{\varepsilon}^{mat}$  distribution plotted in the range  $[0 : 3.7 \times 10^{-1}]$ .

number of degrees of freedom increases slightly from 2646 to 2985 but leads to an improvement of the upper bound from 10.7 % error to 1.8 % error. However, very high dissipation within elements can still be observed in the right bottom corner (Figure 5.8b2), suggesting further introduction of discontinuities. The CPU time for this iteration was 16.3 s.

**Second iteration** A second iteration of the presented algorithm leads to the introduction of additional discontinuities in the right bottom corner, as illustrated in Figure 5.8a3. Finally, only small plastic dissipation is observed within elements and the dominant failure takes place at the introduced discontinuities. A further improvement of the collapse load multiplier from  $\beta = 1.1518$  to  $\beta = 1.1455$  is achieved, resulting in an error with respect to the reference solution of only  $err = 1.2\%$ . The CPU time of this iteration was 18.7 s.

**Third iteration** In a third iteration the velocity discontinuities in the bottom right corner are slightly adjusted, see Figure 5.8a4, which doesn't significantly change the result, indicating that the velocity discontinuities are already well arranged and further iterations wouldn't improve the upper bound significantly. The CPU time for this last iteration was 20.0 s.

This adaptive approach runs fully automated with the iteration sequence controlled by a self-written Python code, based on the strategy outlined in Figure 5.4. The total CPU time for this example was 74.7 s.

Additionally, also for two other notch lengths very good results were obtained: for  $a = L/3$ ,  $\beta = 0.9361$  with  $err = 1.3\%$  ( $\beta^* = 0.9241$ ) obtained after three iterations with a CPU time of 82.8 s, and for  $a = 2L/3$ ,  $\beta = 1.4024$  with  $err = 1.4\%$  ( $\beta^* = 1.3833$ ) obtained after three iterations in a CPU time of 92.4 s. The corresponding failure modes are plotted in Figure 5.9, again showing almost no plastic dissipation within elements.

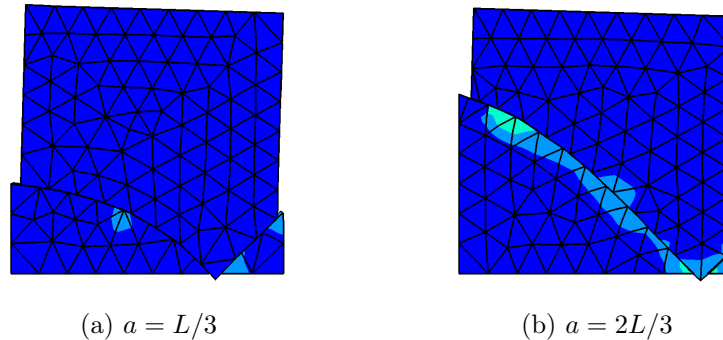


Figure 5.9: Example notched block under uniform tensile loading. (a)  $a = L/3$  with  $UE = 581$ ,  $UDE = 22$  and  $\dot{\lambda}_{\epsilon}^{mat}$  in the range  $[0 : 0.0045]$ ; (b)  $a = 2L/3$  with  $UE = 578$ ,  $UDE = 24$  and  $\dot{\lambda}_{\epsilon}^{mat}$  in the range  $[0 : 6.2 \times 10^{-3}]$ .

The obtained failure modes of the presented three examples agree very well to the ones obtained in Christiansen and Pedersen (2001), Ciria et al. (2008), Nguyen-Xuan and Liu (2015), Nguyen-Xuan et al. (2017). However, in the referenced works adaptive mesh refinement is extensively used, leading to a large increase in degrees of freedom. Although the proposed results are slightly less accurate than some references (error

between 1 to 2 %), due to the quite rough discretisation and few iteration steps these upper bounds could be obtained very efficient.

### 5.7.2 Block with symmetric rectangular holes

As second benchmark example the square block with symmetric rectangular holes under uniform load is considered. This example has also been investigated in Ciria and Peraire (2004), Nguyen-Xuan and Liu (2015), where numerical limit analysis formulations with adaptive mesh refinement led to reliable and very good results. However, in these references only purely cohesive material behaviour under uniform tensile load has been considered. A more interesting problem is the failure behaviour of the block under uniform compressive load with cohesive frictional strength behaviour, as stated in Makrodimopoulos and Martin (2008).

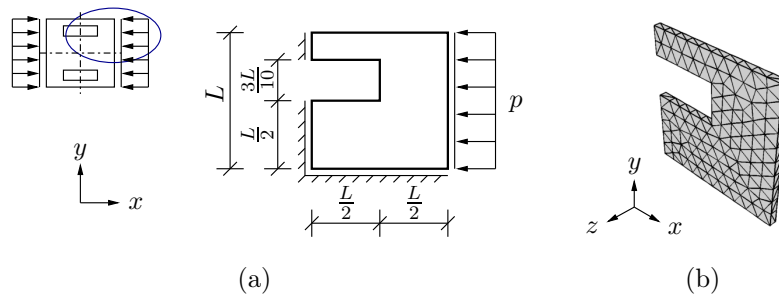


Figure 5.10: Example square block with symmetric rectangular holes under uniform compressive loading. (a) Geometry and boundary conditions; (b) Exemplary mesh with 618 tetrahedron elements.

The considered geometry and boundary conditions are plotted in Figure 5.10a, and an exemplary 3D mesh of the model with 618 tetrahedral elements is shown in Figure 5.10b, where symmetric boundary conditions are prescribed on the  $z-$  and  $z+$  boundary surfaces. A cohesive frictional strength behaviour is defined through the Drucker-Prager yield function  $\sqrt{J_2} = A - BI_1$ , with  $I_1$  as the first stress invariant. Since the Drucker-Prager yield function and the Mohr-Coulomb yield function are equivalent to each other under plane strain conditions, the strength parameters are determined for two different friction angles  $\phi$ , reading

$$\begin{aligned} A = c & & B = 0 & & \text{for } \phi = 0^\circ \\ A = 0.8321c & & B = 0.1601 & & \text{for } \phi = 30^\circ \end{aligned} \quad (5.51)$$

For  $\phi = 0^\circ$  the Drucker-Prager yield function reduces to the von Mises yield function and the strength parameters according to Eq. (5.49) and Eq. (5.7), respectively, are



used. For  $\phi = 30^\circ$  the matrices defining the yield functions become

$$\mathbf{P}_\sigma^{mat} = \frac{1}{3A^2} \begin{pmatrix} 1 & -0.5 & -0.5 & 0 & 0 & 0 \\ -0.5 & 1 & -0.5 & 0 & 0 & 0 \\ -0.5 & -0.5 & 1 & 0 & 0 & 0 \\ 0 & 0 & 0 & 3 & 0 & 0 \\ 0 & 0 & 0 & 0 & 3 & 0 \\ 0 & 0 & 0 & 0 & 0 & 3 \end{pmatrix} \quad \mathbf{F}_\sigma^{mat,+} = \mathbf{0} \quad \mathbf{F}_\sigma^{mat,-} = \frac{B}{A} \begin{pmatrix} 1 \\ 1 \\ 1 \\ 0 \\ 0 \\ 0 \end{pmatrix} \quad (5.52)$$

for the stress-based yield function according to Eq. (5.7) and

$$\mathbf{P}_t^{dis} = \frac{(1 - 12B^2)}{A^2} \begin{pmatrix} 0 & 0 & 0 \\ 0 & 1 & 0 \\ 0 & 0 & 1 \end{pmatrix} \quad \mathbf{F}_t^{dis,+} = \mathbf{0} \quad \mathbf{F}_t^{dis,-} = \frac{B}{A} \begin{pmatrix} 1 \\ 0 \\ 0 \end{pmatrix} \quad (5.53)$$

for the traction-based yield function according to Eq. (5.17c).

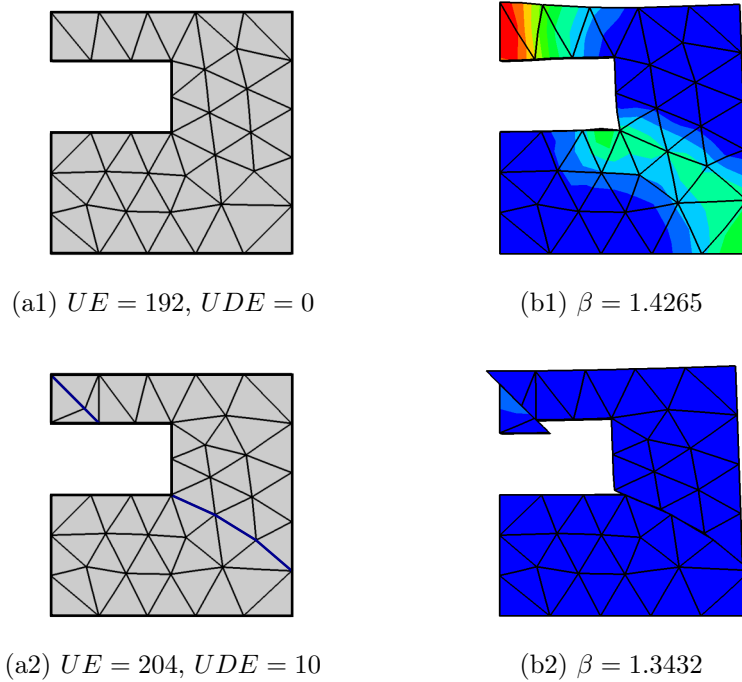


Figure 5.11: Example block with symmetric rectangular holes under uniform compressive loading, considering purely cohesive strength behaviour. (a1) Discretised structure for the initial calculation; (a2) discretised structure with velocity discontinuities (blue), determined through three iterations; (b1) and (b2) related failure modes with  $\lambda_{\dot{\epsilon}}^{mat}$  plotted in the range  $[0 : 1.05 \times 10^{-2}]$ .

For this example, in the following only the upper bound results of the initial step and of the last iteration are discussed. For purely cohesive strength behaviour,  $\phi = 0^\circ$ , an initial calculation is performed using a mesh with only 192 elements, as plotted in Figure 5.11a1. The corresponding failure mode is shown in Figure 5.11b1, where two

separated regions with high plastic dissipation can be identified. Based on that initial result, after three iterations and the introduction of 10 discontinuities a final layout of velocity discontinuities was obtained, shown in Figure 5.11a2. The total number of degrees of freedom increased from 1344 to 1509. The final failure mode, illustrated in Figure 5.11b2, again shows that plastic dissipation can be captured very localised by the introduced discontinuities. During the three iterations, the upper bound collapse multiplier  $\beta$  reduced from 1.4265 to 1.3432 and the total CPU time was 58.3 s.

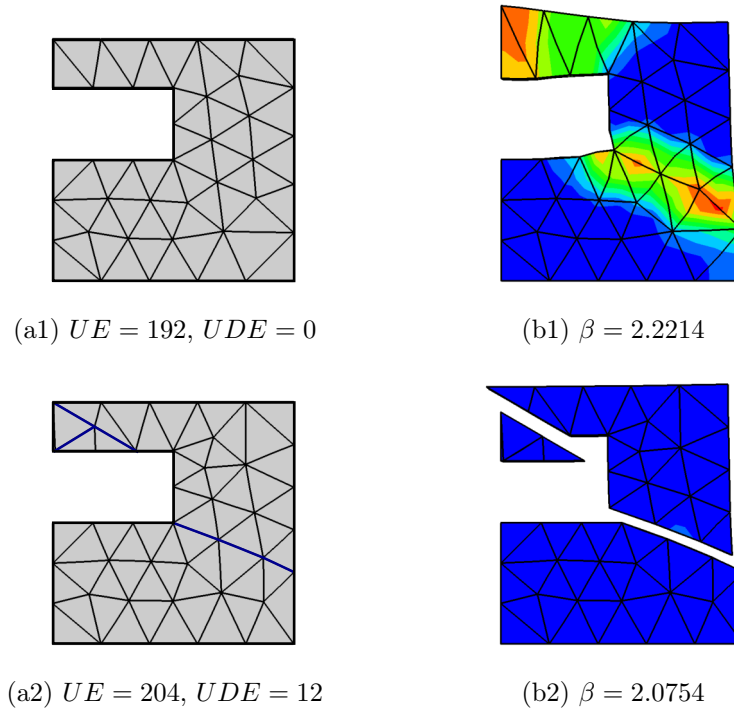


Figure 5.12: Example block with symmetric rectangular holes under uniform compressive loading, considering cohesive-frictional strength behaviour,  $\phi = 30^\circ$ . (a1) Discretised structure for the initial calculation; (a2) discretised structure with velocity discontinuities (blue), determined through four iterations; (b1) and (b2) related failure modes with  $\lambda_{\epsilon}^{mat}$  plotted in the range  $[0 : 1.1 \times 10^{-2}]$ .

For cohesive-frictional strength behaviour,  $\phi = 30^\circ$ , the discretised structures and the corresponding results are shown in Figure 5.12. Again, through the introduction of only a few velocity discontinuities the very localised failure could be captured appropriately. Since cohesive-frictional strength behaviour is considered, not only shear failure but also normal velocity jumps across discontinuities can be observed. In this way, the upper bound collapse multiplier  $\beta$  was improved from 2.2214 to 2.0754, at a total CPU time of 69.3 s.

Since no exact solution is available for this problem, the collapse load multiplier  $\beta$  obtained from our calculations are compared with those available in references listed in Table 5.1. Note that for this example, when purely cohesive strength behaviour is considered,  $\phi = 0^\circ$ , the collapse limit load multipliers  $\beta$  obtained from uniform tensile load (Ciria et al., 2008, Nguyen-Xuan and Liu, 2015) and compressive load (Makrodimopoulos and Martin (2008) and present work) are equivalent to each other. Table 5.1

Authors	LB/UB	UE	$\beta$ ( $\phi = 0^\circ$ )	$\beta$ ( $\phi = 30^\circ$ )
Ciria et al. (2008)	LB	4788	1.3219	-
	UB	4788	1.3342	-
Makrodimitropoulos and Martin (2008)	LB	34000	1.3221	2.0605
	UB	4788	1.3290	2.0840
	UB	34000	1.3260	2.0705
Nguyen-Xuan and Liu (2015)	UB	4208	1.3247	-
present	UB	204	1.3432	2.0754

Table 5.1: Comparison of obtained (present) collapse limit load multiplier  $\beta$  with reference solutions, including the number of elements (UE).

shows that the present upper bound approach is able to provide quite good strength predictions by using much less elements compared to the reference solutions, even though 3D tetrahedral elements are used in our calculation versus 2D triangular elements used in references.

### 5.7.3 Examples with orthotropic strength behaviours

In the following, the performance of the presented approach including orthotropic strength behaviour is assessed by means of the two examples above. Therefore, a Tsai-Wu yield function is assigned to the material, defined by inserting

$$\mathbf{P}_\sigma^{mat} = \begin{pmatrix} P_{11} & P_{12} & P_{13} & 0 & 0 & 0 \\ P_{12} & P_{22} & P_{23} & 0 & 0 & 0 \\ P_{13} & P_{23} & P_{33} & 0 & 0 & 0 \\ 0 & 0 & 0 & P_{44} & 0 & 0 \\ 0 & 0 & 0 & 0 & P_{55} & 0 \\ 0 & 0 & 0 & 0 & 0 & P_{66} \end{pmatrix} \quad \mathbf{F}_\sigma^{mat,+} = \mathbf{F}_\sigma^{mat,-} = \begin{pmatrix} F_1 \\ F_2 \\ F_3 \\ 0 \\ 0 \\ 0 \end{pmatrix} \quad (5.54)$$

into the general stress-based yield function in Eq. 5.7.

The strength parameters are chosen in a way that they represent the behaviour of Norway spruce clear wood, a classical orthotropic material, as introduced in Dorn (2012), giving

$$\mathbf{P}_\sigma^{mat} = \begin{pmatrix} 0.0002 & 0 & 0 & 0 & 0 & 0 \\ 0 & 0.0659 & 0 & 0 & 0 & 0 \\ 0 & 0 & 0.0659 & 0 & 0 & 0 \\ 0 & 0 & 0 & 0.0473 & 0 & 0 \\ 0 & 0 & 0 & 0 & 0.1189 & 0 \\ 0 & 0 & 0 & 0 & 0 & 0.0473 \end{pmatrix} \quad \mathbf{F}_\sigma^{mat,+} = \mathbf{F}_\sigma^{mat,-} = \begin{pmatrix} -0.0066 \\ 0.0856 \\ 0.0856 \\ 0 \\ 0 \\ 0 \end{pmatrix} \quad (5.55)$$

with respect to the material local coordinate basis ( $L - R - T$ ). The traction-based yield function for each velocity discontinuity is determined according to the projection algorithm introduced in Section 5.3.

Firstly, the example illustrated in Figure 5.7a with a notch length of  $a = L/2$  is investigated. The arbitrary chosen longitudinal direction  $L$  is defined in Figure 5.13a1, also

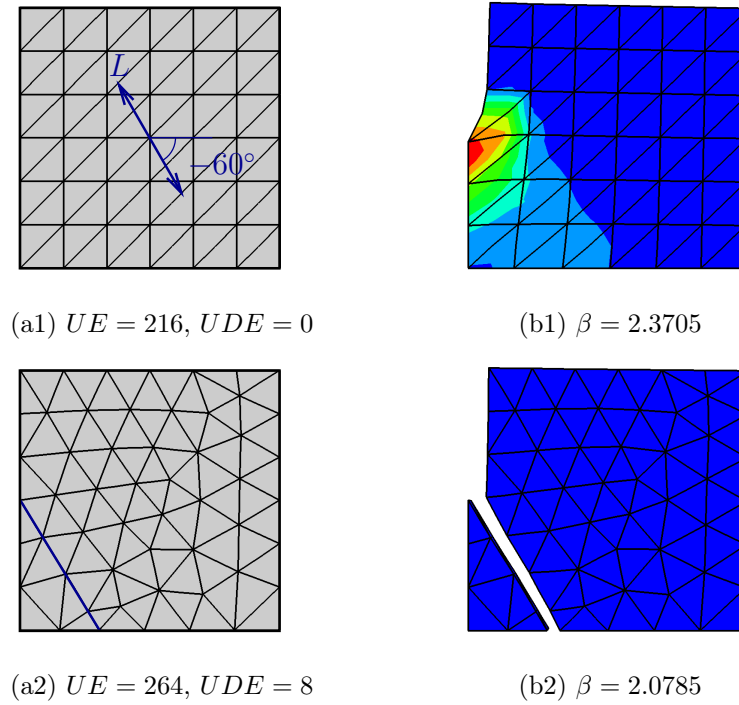


Figure 5.13: Example block with symmetric notches ( $a = L/2$ ) under uniform tensile loading considering orthotropic strength behaviour. (a1) Discretised structure for the initial calculation and the prescribed longitudinal direction  $L$  (blue arrow); (a2) discretised structure with velocity discontinuities (blue), determined through two iterations; (b1) and (b2) related failure modes with  $\dot{\lambda}_{\varepsilon}^{mat}$  plotted in the range  $[0 : 4 \times 10^{-2}]$ .

showing the mesh for the initial calculation. The corresponding failure mode is given in Figure 5.13b1, showing a concentration of plastic dissipation rate around the notch tip, but no distinct failure surface / slip line can be identified. In the course of two iterations 8 velocity discontinuities were introduced (see Figure 5.13a2), almost parallel to the longitudinal direction  $L$ , increasing the total number of degrees of freedom from 1521 to 1857 and the number of elements from 216 to 264. The final failure mechanism is shown in Figure 5.13b2, where almost all plastic failure occurs across discontinuities. Through the whole iteration process, the upper bound collapse load multiplier  $\beta$  decreases from 2.3705 to 2.0785, within a CPU time of 47.5 s.

Since neither an exact solution nor a reference value is available for this example, the obtained upper bounds are compared to a solution without velocity discontinuities but with a very fine mesh consisting of 55571 tetrahedral elements, shown in Figure 5.15a. Additionally, the 3D lower bound formulations proposed by the authors in Li et al. (2018d) was applied to enclose the exact collapse load multiplier  $\beta^*$ , giving

$$1.7855 < \beta^* < 2.0878 \quad (5.56)$$

The total CUP time for the upper bound as well as lower bound calculation with the fine mesh were 10.6 min and 18.6 min, respectively. The upper bound obtained with velocity discontinuities,  $\beta = 2.0785$ , can thus be considered as reliable, since it is located within the bound gap given in Eq. (5.56). It is even slightly better than the upper bound obtained using the very fine mesh.

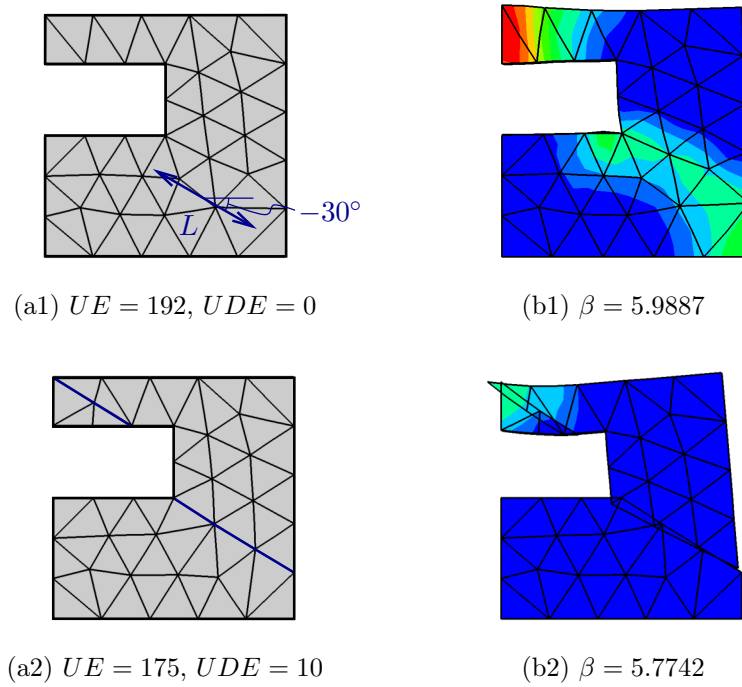


Figure 5.14: Example block with symmetric rectangular holes under uniform compressive loading considering orthotropic strength behaviour. (a1) Discretised structure for the initial calculation and the prescribed longitudinal direction  $L$  (blue arrow); (a2) discretised structure with velocity discontinuities (blue), determined through three iterations; (b1) and (b2) related failure modes with  $\lambda_{\dot{\epsilon}}^{mat}$  plotted in the range  $[0 : 6 \times 10^{-2}]$ .

Secondly, the orthotropic strength behaviour is applied to the example defined in Figure 5.10a, with the longitudinal direction  $L$  defined in Figure 5.14a1. The discontinuity layout shown in Figure 5.14a2 was obtained after three iterations, the introduction of 10 discontinuities, and an increase of the total number of degrees of freedom from 1344 to 1383. The collapse load multiplier decreased from 5.9887 to 5.7742 within a CPU time of 71.8 s. Note that, in this example, the number of elements even decreases from 192 to 175, being an output of the proposed algorithm without any manual influence.

Again, the result is compared to upper and lower bounds obtained with an approach without velocity discontinuities but a very fine mesh with 56894 tetrahedral elements, as displayed in Figure 5.15b, giving

$$5.6681 < \beta^* < 5.7981 \quad (5.57)$$

in a CPU time of 12.5 min and 24.0 min, respectively. Also for this example, the upper bound obtained with a discontinuous velocity field and a very rough mesh represents a reliable solution and the best upper bound. Comparing the failure modes of these two approaches, Figure 5.15b versus Figure 5.14b2, it becomes obvious that velocity discontinuities can only unfold their full potential if there is really localised failure, as in the lower right part of this example. In case of distributed plastic collapse, as in the upper left region of this example, discontinuities are, clearly, not able to take over plastic dissipation. Thus, there is still plastic dissipation within solid elements after the last iteration, as can be seen in Figure 5.14b2. Nevertheless, both examples show

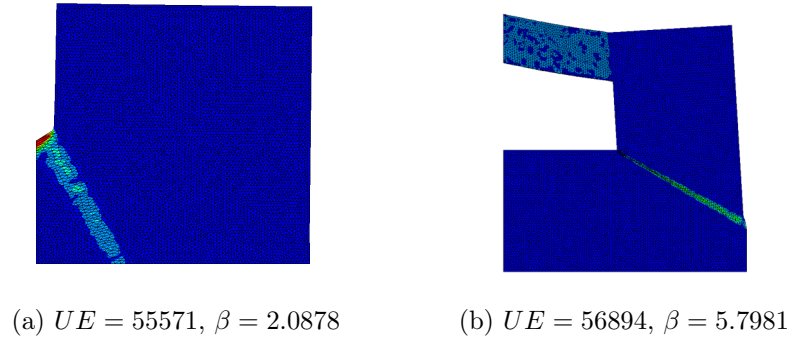


Figure 5.15: Upper bound failure modes for the two examples with orthotropic strength behaviour using a fine mesh and no velocity discontinuities. (a) block with symmetric notches under uniform tensile loading with  $\dot{\lambda}_{\epsilon}^{mat}$  plotted in the range  $[0 : 0.0015]$ ; (b) Block with symmetric rectangular holes under uniform compressive loading with  $\dot{\lambda}_{\epsilon}^{mat}$  plotted in the range  $[0 : 1 \times 10^{-3}]$ .

that the presented approach works also very reliable and efficient for problems with orthotropic strength behaviour.

### 5.7.4 3D cylinder with central circular notch

As final example a 3D cylinder with central circular notch is considered, applying the algorithm presented for the general 3D case instead of the plane strain case. Thus, the introduced discontinuities not necessarily form a plane surface.

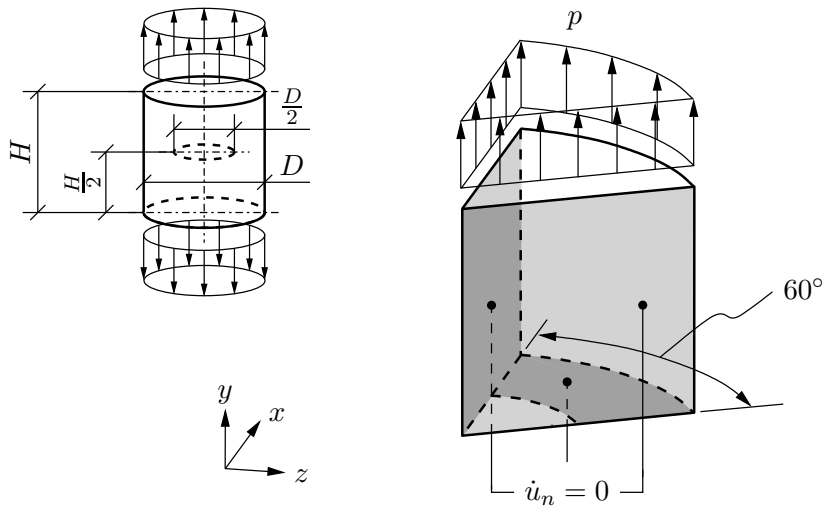


Figure 5.16: Example cylinder ( $H = D$ ) with central circular notch under uniform tensile loading  $p$ , and  $60^\circ$  slice used for upper bound calculations.

The geometry and boundary conditions are defined in Figure 5.16. For the upper bound calculation, a  $60^\circ$  slice of the upper-half of the cylinder is considered. Cohesive-frictional isotropic strength behaviour is assigned using the Drucker-Prager yield function accord-

ing to Eq. (5.52), with the parameters  $A = 0.9219c$  and  $B = 0.1118$ . Again, according to the projection algorithm in Section 5.3, the traction-based yield function for the strength behaviour across velocity discontinuities is determined according to Eq. (5.53), which is identical for all orientations due to the isotropic strength behaviour.

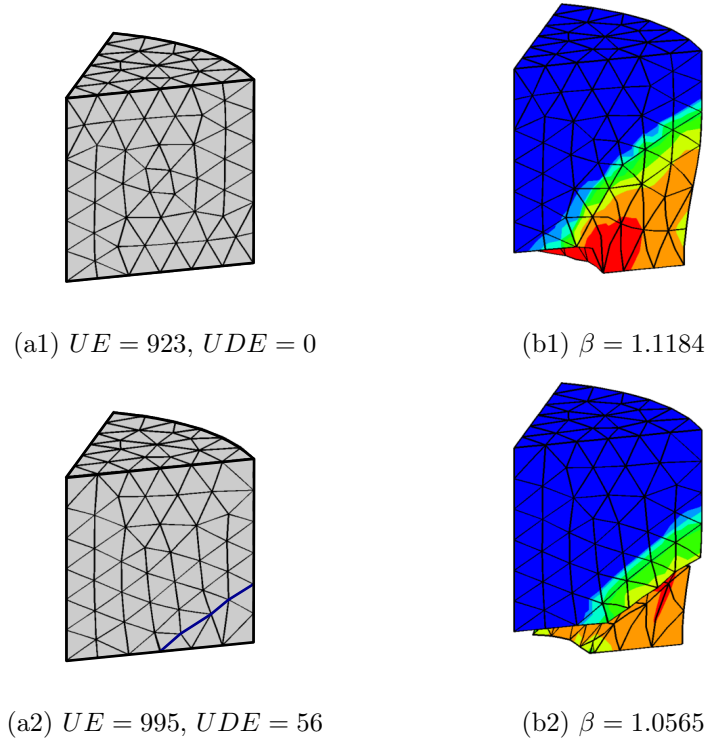


Figure 5.17: Example cylinder with central circular notch under uniform tensile loading, considering cohesive-frictional isotropic strength behaviour. (a1) Discretised structure used in the initial calculation; (a2) discretised structure with velocity discontinuities (blue); (b1) and (b2) related failure modes with  $\dot{\lambda}_{\epsilon}^{mat}$  plotted in the range  $[1 \times 10^{-6} : 3.3 \times 10^{-3}]$ .

Similar to the previous examples, an initial upper bound calculation is performed using a coarse mesh with 923 tetrahedral elements, as shown in Figure 5.17a1. The corresponding failure mode is displayed in Figure 5.17b1, leading to an upper bound of the collapse load multiplier of  $\beta = 1.1184$ . A very high plastic dissipation rate can be observed around the notch tip, but a distinct localised failure region can hardly be identified.

Based on this initial result, the algorithm proposed in Section 5.6 for the general 3D case was applied, making use of the level-set method as illustrated in Figure 5.6 to define the geometry of discontinuities to be introduced. By applying this algorithm, a sequence of continuous discontinuities, plotted in Figure 5.18a, are determined, cutting through the tetrahedral elements. Since the so-obtained discontinuities are either triangular or quadrilateral plane surfaces in various sizes, it is not ideal to use the resulting surface directly for re-meshing the whole structure. For this reason, the **Face from mesh** feature in ABAQUS/CAE is used for smoothing, resulting in the surface shown in Figure 5.18b. Since this smoothed surface can be discretised using triangular elements

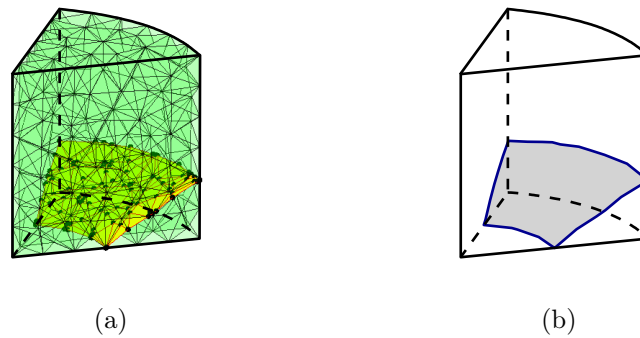


Figure 5.18: Example cylinder with central circular notch under uniform tensile loading. (a) Continuous partitions cutting through tetrahedral elements defined by the level-set method introduced in Figure 5.6; (b) resulting smooth surface determined from the piecewise plane partition surfaces using the **Face from mesh** feature in ABAQUS/CAE.

of uniform size, it is guaranteed that the new mesh created for the next iteration is balanced and of similar mesh size as the initial mesh. Performing only one iteration, 56 discontinuities were introduced and the structure was re-meshed with 995 tetrahedral elements, as shown in Figure 5.17a2. The total number of degrees of freedom is 5190.

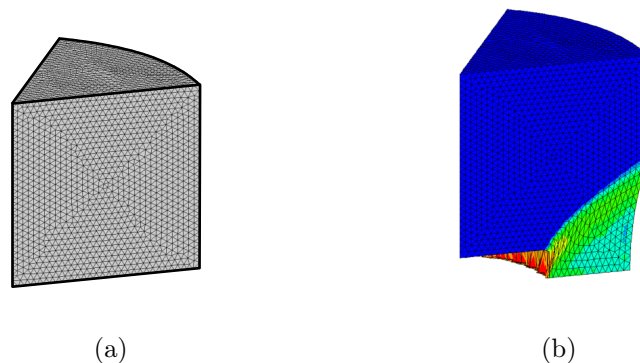


Figure 5.19: Example cylinder with central circular notch under uniform tensile loading. (a) Fine mesh with 88798 tetrahedral elements and without velocity discontinuities, and (b) the corresponding continuous upper bound failure mode with the collapse load multiplier  $\beta = 1.0547$ .

Finally, a distinct plastic flow across the introduced velocity discontinuities is obtained (Figure 5.17b2), and the plastic dissipation rate within the solid elements around the notch tip is reduced significantly. A continuous upper bound calculation with 88798 tetrahedral elements (379593 degrees of freedom) was performed to obtain a reference solution. The mesh as well as the corresponding failure mode is shown in Figure 5.19a and Figure 5.19b, respectively. The failure modes agree very well and the collapse load multiplier of the discontinuous upper bound approach,  $\beta = 1.0565$ , is only slightly larger than the one of the continuous approach,  $\beta = 1.0547$ . However, the total CPU time of the continuous approach was 131.7 min, whereas the discontinuous approach only took



131.0 s. 41.0 s for the initial upper bound calculation, 44.1 s for the introduction of velocity discontinuities, and 45.9 s for the discontinuous upper bound calculation.

Note that, in the discontinuous failure mode in Figure 5.17b2, the high plastic dissipation rate (red and orange regions) within tetrahedral elements beneath velocity discontinuities indicates a mixed mode of shear and tensile failure which is rather dispersed, as also observed in the continuous failure mode in Figure 5.19b. It is also worth mentioning that, in this paper, only one iteration is used for the introduction of velocity discontinuities for general 3D problems and no further adjustment is included. This is because the introduction of velocity discontinuities is based on the framework of the level-set method, and the adjustment of an introduced discontinuity as well as the intersection between a new discontinuity with an existing one has not yet been implemented and is considered as a difficulty to be overcome in future work.

## 5.8 Summary and conclusions

In this paper, a new implementation of finite-element-based upper bound formulations including the possibility to consider orthotropic strength behaviour is proposed, where velocity discontinuities are introduced iteratively in a sensible way based on an adaptive introduction and adjustment algorithm.

With respect to the objectives specified in Section 5.1, the main findings of this paper can be summarised as follows:

1. Finite-element-based upper bound formulations have been implemented taking orthotropic strength behaviour into account and allowing velocity-jumps across sensibly-arranged discontinuities. In the discretised dual upper bound formulation, both the used stress-based yield functions assigned to solid elements and the related traction-based yield functions, describing plastic failure across velocity discontinuities, could be formulated in the form of second-order cone constraints. Thus, the resulting optimisation problems could be solved efficiently by SOCP. The obtained velocity discontinuity layouts were able to capture localised failure modes very efficiently and the obtained upper bounds agree very well with reference solutions or values obtained without discontinuities but a very fine discretisation. In this way, plastic dissipation within solid elements could be reduced significantly, making any kind of adaptive mesh refinement in failure regions obsolete.
2. The required projection of an orthotropic stress-based yield function into a locally-equivalent traction-based yield function, with respect to the orientation of an arbitrary plane, could be shown successfully and is described in detail. This algorithm has been verified numerically, showing that the failure surface in the traction basis represents a perfect envelope to the critical traction point cloud determined from critical stress states on the corresponding plane. Thus, under the assumption that plastic strain localisation with respect to a plane can occur, consistent strength behaviour throughout the whole discretised body can be guaranteed.
3. An adaptive algorithm has been implemented to iteratively introduce and arrange velocity discontinuities. At each iteration, based on the plastic multiplier rate in

each strain-rate evaluation node, two critical orientations of plastic strain-rate localisation are determined. Starting from the node with the highest plastic multiplier rate, a sequence of line segments for the plane strain case and plane surfaces for the general 3D case is then generated, defining the velocity discontinuities to introduce. The so-obtained discontinuity layouts played a dominant role in the final failure mode at all investigated examples, and reliable upper bounds were obtained using relatively coarse meshes and only a limited number of velocity discontinuities.

The present approach provides an alternative method to the commonly-used numerical upper bound approaches with adaptive mesh refinement. Especially for problems where plastic failure through the body occur very localised, efficient and good upper bound solutions can be expected with a minimum number of degrees of freedom. This also applies to materials exhibiting orthotropic strength behaviour, which can be of great value for practical applications, since plastic failure in laminated structures and orthotropic materials often takes place very localised. An example would be wood at the microscale (Lukacevic and Füssl, 2016, Lukacevic et al., 2014b) as well as at the product scale (Hochreiner et al., 2013, 2014).

Note that the main goal of this paper has been to propose this new concept as a further development of existing numerical upper bound formulations. The capabilities of this new approach have been assessed by means of several examples, showing high efficiency with respect to computational cost and good solution qualities. However, it is also necessary to mention that several difficulties needs to be overcome in future work. Firstly, for general 3D problems, velocity discontinuities are introduced in the discretised structures as partitions cutting through tetrahedron elements determined by means of the level-set method introduced in Section 5.6. When a set of partitions have been determined in the first iteration, the adjustment of existing partitions and the introduction of additional partitions in further iterations would require more advanced and comprehensive algorithms, such as the multiphase level set method, which have not yet implemented in the present approach. Secondly, for the algorithm introduced in Section 5.6, critical orientations can only be determined from the strain-rate states satisfying the condition in Eq. (5.45), derived from the assumption of strain localisation formulated in Eq. (5.14). This condition is fulfilled for shear-based yield functions, such as von Mises or Drucker-Prager, but seems to be too strict for other yield functions, such as the Tsai-Wu orthotropic yield function. Thus, a further development of the present algorithms is still necessary to allow a feasible and stable application for any engineering problem.

## 5.A Second-order cone programming

The definition of the cone set  $\mathcal{C}$  is that,

$$\forall \mathbf{x} \in \mathcal{C} \text{ and } \lambda \geq 0 \iff \lambda \mathbf{x} \in \mathcal{C} \quad (5.58)$$

and then its dual cone  $\mathcal{C}^*$  can be defined as,

$$\mathbf{x}^\top \mathbf{y} \geq 0, \forall \mathbf{x} \in \mathcal{C} \iff \mathbf{y} \in \mathcal{C}^* \quad (5.59)$$

where  $\mathbf{x} \in \mathfrak{R}^n$  and  $\mathbf{y} \in \mathfrak{R}^n$ . If  $\mathcal{C} = \mathcal{C}^*$  holds, the cone is considered as self-dual.

The most common second-order cones is the quadratic cone  $\mathcal{C}$ ,

$$\mathcal{C} = \{\mathbf{x} : x_1 \geq \|\mathbf{x}_{2:d}\|, x_1 \geq 0\} \quad (5.60)$$

and the rotated quadratic cone,

$$\mathcal{C} = \{\mathbf{x} : 2x_1x_2 \geq \|\mathbf{x}_{3:d}\|, x_1 \geq 0, x_2 \geq 0\} \quad (5.61)$$

where  $\mathbf{x}_{m:n} = [x_m \dots x_n]^\top \in \mathfrak{R}^{n-m}$ , and both the two second-order cones are self-dual.

Then the optimization problem of the second-order cone programming (SOCP) can be expressed as

$$\begin{aligned} \min \quad & \mathbf{c}^\top \mathbf{x} \\ \text{s.t.} \quad & \mathbf{A}\mathbf{x} = \mathbf{b} \\ & \mathbf{x} \in \mathcal{C} \end{aligned} \quad (5.62)$$

where  $\mathbf{b} \in \mathfrak{R}^m$ ,  $\mathbf{c} \in \mathfrak{R}^n$ ,  $\mathbf{A} \in \mathfrak{R}^{m \times n}$  and  $\mathcal{C}$  is the second-order cone.

The dual optimization problem is

$$\begin{aligned} \max \quad & \mathbf{b}^\top \mathbf{z} \\ \text{s.t.} \quad & \mathbf{A}^\top \mathbf{z} + \mathbf{y} = \mathbf{c} \\ & \mathbf{y} \in \mathcal{C}^*. \end{aligned} \quad (5.63)$$

where  $\mathbf{z} \in \mathfrak{R}^m$  and  $\mathcal{C}^*$  is the dual cone of  $\mathcal{C}$ .

SOCP can be regarded as a generalization of classical linear programming where the linear constraints are supplemented by specialised nonlinear constraints in the form of the cone constraints. The resulting optimization problem can be solved efficiently with primal-dual algorithms based on the interior-point method.

## Acknowledgments

Financial support for this work in the framework of the PhDSchool DokInHolz funded by the Austrian Federal Ministry of Science, Research and Economy and the Austrian Association of Wood Industries is gratefully acknowledged. We also gratefully acknowledge the financial support of this work by the Austrian Science Fund (FWF) through the Erwin Schrödinger Fellowship J3748-N30.

# Conclusions and outlook

The first part of this thesis is dedicated to a pioneer study on the application of numerical limit analysis approaches for strength predictions of wood and wood-based products and the assessment of their performances. The contributions of this part can be summarised as follows:

- The efficient and promising performance of the proposed numerical limit analysis approaches for strength predictions of clear wood has been assessed and compared with other computational methods. Due to its satisfying capabilities, this numerical tool can potentially play an important role in investigating failure mechanisms of wood at different scales of observation.
- Numerical limit analysis has been found to be an efficient and reliable tool for stochastic studies on load bearing capacities of cross-laminated timber plates, to compensate the intrinsic uncertainties (e.g. strength variations in clear wood) and imperfections (e.g. knots and wood fibre deviations) of the material. This new numerical tool can be expected to provide fast and promising strength predictions, serving as reference for the ongoing development of the wooden board grading process as well as the standardisation of cross-laminated timber products.
- Finite-element-based limit analysis formulations have been implemented through self-written code in Fortran and the interface between the Fortran code and the commercial finite element software ABAQUS has been built up. Thus, the present numerical limit analysis approaches can easily be applied for rapid strength predictions of materials and safety assessments of structures in engineering practice.

Specific and detailed conclusions on the main findings of this part of research work have been drawn in the related publications, and in the following a brief summary is presented with respect to the publications.

In **Publication 1**, numerical limit analysis approaches were applied for the first time to microstructures of wood. Both orthotropic failure criteria and periodic boundary conditions were implemented into two-dimensional finite-element-based limit analysis formulations under plane strain conditions. Periodic boundary conditions were implemented as anti-periodic traction fields and periodic velocity fields in lower bound and upper bound formulations, respectively. The orthotropic Tsai-Wu yield function was reformulated as a second-order cone constraint and, thus, large-scale optimisation problems could be solved efficiently using second-order cone programming. The proposed limit analysis approaches were successfully applied to unit cell models at the annual ring scale and the clear wood scale. Effective failure surfaces as well as failure modes

were obtained very efficiently and robustly at both scales, and only small differences between lower bound and upper bound results were obtained for all calculations. A basic validation was performed by comparing the numerically obtained effective failure surfaces at the clear wood scale with the experimental results from biaxial testing of Norway spruce clear wood.

In **Publication 2**, in order to compare the predictive capabilities, the proposed numerical limit analysis and two other computational methods, the extended finite element method and an elastic limit approach, were applied to the same problem: the prediction of effective wooden strength behaviours. All these three methods were applied to the same unit cell models at both the annual ring scale and the clear wood scale, and similar input strength parameters were chosen in a consistent way. The extended finite element method is the most powerful method, delivering a very realistic description of strength-governing processes, but widespread use of this method in the engineering field is still restricted due to its demand for a complex solution procedure and high computational effort. Due to the continuum micromechanical basis and analytical solution procedure, the elastic limit approach exhibited unbeatable advantage with respect to time efficiency as well as the elegance with which material properties of different phases can be linked across several observation scales, but it is difficult to capture all failure-triggering processes due to stress and strain averages over material phases. The present numerical limit analysis approach is able to correctly capture basic characteristics of failure modes and the overall strength behaviours compared to the extended finite element method, and exhibits sufficient computational efficiency and numerical stability compared to the elastic limit approach. Thus, this new computational method can be expected to serve as a promising tool for rapid strength predictions and the build-up of material databases for wood and wood-based products within timber engineering design processes in the future.

In **Publication 3**, based on numerical limit analysis and a stochastic approach, a new computational concept was developed to fill the gap in timber engineering for efficient and reliable predictions on load bearing capacities of cross-laminated timber plates. For this purpose, the orthotropic Tsai-Wu yield function was implemented in three-dimensional finite-element-based limit analysis formulations to indicate plastic failure within wooden boards, and the strength parameters were determined from either code values in Eurocode 5 or a strength profile database. By using strength values for three different strength classes according to Eurocode 5, a validation using experimental results rendered the numerical limit analysis approaches as a promising tool with small computational error and high time efficiency with respect to the prediction of cross-laminated timber plate bending capacities. By using a strength profile database, cross-laminated plate models were assembled using wooden boards with arbitrarily-assigned strength profiles, resulting in section-wise varying strength properties within each plate. Performing comprehensive calculations, numerical upper bound calculations were able to provide reliable strength predictions in a stochastic manner with similar scatter as found in experimental results for strength classes C24 and C35. Distinct failure modes were obtained from each calculation with an arbitrary combination of strength profiles, providing a valuable basis to study structural failure mechanisms of cross-laminated timber plates.

The second part of the thesis mainly focuses on the development simpler and more efficient numerical upper bound approaches, as compared to commonly-used adaptive

mesh refinement, to capture localised plastic failure mechanisms. The contributions of this part can be summarised as follows:

- A combination of orthotropic yield functions and velocity discontinuities have been implemented for the first time in finite-element-based upper bound formulations. A concept for a sensible arrangement of velocity discontinuities has been presented, allowing for an efficient description of localised plastic failure modes.
- An adaptive strategy has been developed to efficiently arrange velocity discontinuities in a sensible way with respect to localised failure modes. The interface failure across so-determined velocity discontinuities plays a dominant role in all obtained structural failure modes. All required algorithms have been implemented through self-written code either in Fortran or in Python, which are compatible with the Fortran code for numerical limit analysis formulations and allow for an automated determination of velocity discontinuities.

In the following, the main findings are briefly summarised with respect to the related publications:

In **Publication 4**, velocity discontinuities, allowing for linear velocity jumps, were implemented into three-dimensional finite-element-based upper bound formulations, discretised using simplex strain elements. A concept of how to derive the necessary traction-based yield function has been briefly introduced which guarantees a consistent description of the orthotropic material strength behaviours across discontinuities and within solid elements. Accordingly, compatibility as well as the associated plastic flow rule are fulfilled throughout the whole body and, thus, rigorous upper bound solutions are obtained. Additionally, a simple concept has been presented to manually determine sensible arrangements of velocity discontinuities for given problems based on preliminary upper bound calculations using a very coarse mesh and a continuous velocity field. In this way, significantly better upper bound solutions were obtained with almost no increase in degrees of freedom, since it is sufficient to allow velocity jumps only across sensibly-arranged velocity discontinuities.

In **Publication 5**, an automated determination of velocity discontinuities has been introduced as a further development of the numerical approach presented in Publication 4. For this purpose, an adaptive algorithm has been implemented to iteratively introduce and arrange velocity discontinuities into the optimal layout. In each iteration, possible planes of plastic flow localisation were determined at each strain-rate evaluation node using numerical upper bound results from the previous iteration. For the plane strain case, velocity discontinuities were introduced into the discretised structures as a sequence of line segments. For the general three-dimensional case, discontinuities were introduced as plane surfaces cutting through tetrahedral elements based on a level-set method. To guarantee a consistent strength behaviour throughout the whole discretised body, the required algorithm projecting the orthotropic stress-based yield function into a locally-equivalent traction-based yield function, with respect to the orientation of each velocity discontinuity, was introduced in detail and verified numerically. By means of selected examples, the adaptively-arranged velocity discontinuities were able to capture localised failure modes very efficient and so-obtained upper bound results agreed very well to reference solutions, either employed from literature or obtained without discontinuities but a very fine discretisation. In this way, plastic dissipation within solid

elements could be reduced significantly and localised failure mechanisms are mainly measured by velocity discontinuities, making any kind of adaptive mesh refinement in failure region obsolete.

## Perspectives and future research studies

In this thesis, a rigorous study on the implementation of numerical limit analysis approaches and the assessment of their strength prediction capabilities have been presented. Although the tasks originally proposed have been largely accomplished, following tasks can be recommended as potential developments or applications of proposed numerical approaches for future research.

- For strength predictions of wood, the strengths and weaknesses of three computational methods have been discussed in Publication 2. Taking benefit from the efficiency, a combination of the numerical limit analysis and the elastic limit approach could evolve to an effective bundle of complementary methods, delivering ‘inner’ and ‘outer’ predictions for the natural scatter of wooden strength. Another possibility might be a combination of the efficiency of the numerical upper bound and the accuracy of the extended finite element method leading to more flexible engineering design tools, in which the focus can be switched between accuracy and efficiency as needed.
- The numerical limit analysis approaches have been proven a promising prediction tool for load bearing capacities of cross-laminated timber plates in Publication 3. The scatter of experimentally-observed bending capacities has been properly captured using strength profiles in individual wooden boards. In a next step, potential research effort could be invested for more sophisticated stochastic studies on the impact of inhomogeneities on the overall strengths of cross-laminated timber plates and the corresponding failure modes. The results would be of great value for a deeper understanding of the structural failure mechanisms and more efficient utilisations of wooden boards in cross-laminated timber plates.
- The strength behaviours of wooden boards is strongly influenced by knots and the surrounding fibre deviations. A more sophisticated and realistic strength prediction for knot sections by means of computational methods would be desirable. However, according to previous research work, the application of conventional finite element methods tends to be very difficult due to the present of arbitrarily-oriented knots and the complex distributed fibres around them. Due to the efficiency and simplicity of the numerical limit analysis approaches proposed in this thesis, this numerical method is expected to deliver rapid strength predictions of knot sections and provide useful information to complement more sophisticated computational methods.
- In Publication 4 and 5, a numerical upper bound approach with adaptively-arranged velocity discontinuities has been presented. The performance of this new numerical approach is satisfying with respect to efficiency and simplicity. However, several difficulties are worth mentioning in this approach and expected to be overcome in future work. First, for general three-dimensional problems, the

---

introduction of velocity discontinuities into the discretised structure is based on the level-set method. When a first set of discontinuities has been determined, the introduction of new discontinuities and adjustment of existing ones in further iterations would require more advanced and comprehensive algorithms, such as the multiphase level set method, which have not yet implemented. Second, the ‘projection’ algorithm determining the traction-based yield functions for velocity discontinuities and the algorithm determining potential planes of plastic flow localisation are based on a strain localisation assumption which seems to be too strict for some yield functions. Thus, in future work, more generally feasible algorithms are expected to be developed from current ones for more flexible and stable applications.



# Bibliography

- Aicher, S., Gustafsson, P. J., Haller, P., and Petersson, H. (2002). Fracture mechanics models for strength analysis of timber beams with a hole or a notch - A report of RILEM TC-133. Technical report, Structural Mechanics.
- Anderheggen, E. and Knöpfel, H. (1972). Finite element limit analysis using linear programming. *International Journal of Solids and Structures*, 8(12):1413–1431.
- Andersen, E., Roos, C., and Terlaky, T. (2002). Notes on duality in second order and p-order cone optimization. *Optimization*, 51:627–643.
- Andersen, E., Roos, C., and Terlaky, T. (2003). On implementing a primal-dual interior-point method for conic quadratic optimization. *Mathematical Programming*, 95(2):249–277.
- Bacher, M. and Krzosek, S. (2014). Bending and tension strength classes in European standards. *Forestry and Wood Technology*, 88:14–22.
- Bader, T. K., Hofstetter, K., Hellmich, C., and Eberhardsteiner, J. (2010). Poromechanical scale transitions of failure stresses in wood: from the lignin to the spruce level. *Journal of Applied Mathematics and Mechanics*, 90(10-11):750–767.
- Bader, T. K., Hofstetter, K., Hellmich, C., and Eberhardsteiner, J. (2011). The poroelastic role of water in cell walls of the hierarchical composite softwood. *Acta mechanica*, 217(1-2):75–100.
- Belytschko, T. and Black, T. (1999). Elastic crack growth in finite elements with minimal remeshing. *International Journal for Numerical Methods in Engineering*, 45(5):601–620.
- Belytschko, T. and Hodge, P. G. (1970). Plane stress limit analysis by finite elements. *Journal of the Engineering Mechanics Division*, 96(6):931–944.
- Benveniste, Y. (1987). A new approach to the application of Mori-Tanaka’s theory in composite materials. *Mechanics of Materials*, 6(2):147–157.
- Böhm, H. J. (2004). *A Short Introduction to Continuum Micromechanics*, pages 1–40. Springer Vienna, Vienna.
- Borges, L., Zouain, N., Costa, C., and Feijóo, R. (2001). An adaptive approach to limit analysis. *International Journal of Solids and Structures*, 38(10):1707–1720.

- Bottero, A., Negre, R., Pastor, J., and Turgeman, S. (1980). Finite element method and limit analysis theory for soil mechanics problems. *Computer Methods in Applied Mechanics and Engineering*, 22(1):131–149.
- Brandner, R., Flatscher, G., Ringhofer, A., Schickhofer, G., and Thiel, A. (2016). Cross laminated timber (CLT): overview and development. *European Journal of Wood and Wood Products*, 74:331–351.
- Capsoni, A., Corradi, L., and Vena, P. (2001a). Limit analysis of anisotropic structures based on the kinematic theorem. *International Journal of Plasticity*, 17(11):1531–1549.
- Capsoni, A., Corradi, L., and Vena, P. (2001b). Limit analysis of orthotropic structures based on hill's yield condition. *International Journal of Solids and Structures*, 38(22-23):3945–3963.
- Chen, J., Yin, J.-H., and Lee, C. (2003). Upper bound limit analysis of slope stability using rigid finite elements and nonlinear programming. *Canadian Geotechnical Journal*, 40:742–752.
- Chen, W. (2013). *Limit analysis and Soil plasticity*. Elsevier, Amsterdam.
- Christiansen, E. and Andersen, K. D. (1999). Computation of collapse states with von mises type yield condition. *International Journal for Numerical Methods in Engineering*, 46(8):1185–1202.
- Christiansen, E. and Pedersen, O. S. (2001). Automatic mesh refinement in limit analysis. *International Journal for Numerical Methods in Engineering*, 50(6):1331–1346.
- Ciria, H. and Peraire, J. (2004). Computation of upper and lower bounds in limit analysis using second-order cone programming and mesh adaptivity. In *9th ASCE Specialty Conference on Probabilistic Mechanics and Structural Reliability*.
- Ciria, H., Peraire, J., and Bonet, J. (2008). Mesh adaptive computation of upper and lower bounds in limit analysis. *International Journal for Numerical Methods in Engineering*, 75(8):899–944.
- Corradi, L., Luzzi, L., and Vena, P. (2006). Finite element limit analysis of anisotropic structures. *Computer Methods in Applied Mechanics and Engineering*, 195(41-43):5422–5436.
- Danielsson, H. and Gustafsson, P. J. (2014). Fracture analysis of glued laminated timber beams with a hole using a 3D cohesive zone model. *Engineering Fracture Mechanics*, 124-125:182–195.
- Denton, S. R. and Morley, C. T. (2000). Limit analysis and strain-softening structures. *International Journal of Mechanical Sciences*, 42(3):503–522.
- Domenico, D. D., Pisano, A., and Fuschi, P. (2014). A FE-based limit analysis approach for concrete elements reinforced with FRP bars. *Composite Structures*, 107:594–603.
- Dorn, M. (2012). *Investigations on the serviceability limit state of dowel-type timber connections*. PhD thesis, Vienna University of Technology.

- Drucker, D. C., Greenberg, H. J., and Prager, W. (1951). The safety factor of an elastic-plastic body in plane strain. *Journal of Applied Mechanics*, 18:371–378.
- Drucker, D. C., Prager, W., and Greenberg, H. J. (1952). Extended limit design theorems for continuous media. *Quarterly of Applied Mathematics*, 9:381–389.
- Eberhardsteiner, J. (1995). Biaxial testing of orthotropic materials using electronic speckle pattern interferometry. *Measurement*, 16(3):139–148.
- Eberhardsteiner, J. (2002). *Experimentelle Bestimmung der biaxialen Festigkeitseigenschaften (in German)*. Springer-Verlag Wien.
- EN 14081-4 (2009). Timber structures - Strength graded structural timber with rectangular cross section - Part 4: Machine Grading - Grading machine settings for machine controlled systems. *European Committee for Standardization, Brussels*.
- EN 1995-1-1 (2003). Eurocode 5 - Design of timber structures - Part 1-1: General rules and rules for buildings. Technical report, Comité Européen de Normalisation. Bruxelles, Belgium.
- EN 338 (2009). Structural timber - Strength classes. *European Committee for Standardization, Brussels*.
- Eshelby, J. D. (1957). The determination of the elastic field of an ellipsoidal inclusion, and related problems. *Proceedings of the Royal Society of London A: Mathematical, Physical and Engineering Sciences*, 241(1226):376–396.
- Fengel, D. and Wegener, G. (1983). *WOOD Chemistry, Ultrastructure, Reactions*. Verlag Kessel.
- Fink, G., Frangi, A., and Kohler, J. (2015). Bending tests on GLT beams having well-known local material properties. *Materials and Structures*, 48(11):3571–3584.
- Francescato, P. and Pastor, J. (1997). Limit analysis and homogenization: Predicting limit loads of periodic heterogeneous materials. *European Journal of Mechanics - A/Solids*, 16:235–253.
- Füssl, J., Bader, T., and Eberhardsteiner, J. (2012). Computational mechanics for advanced timber engineering - from material modeling to structural applications. *IACM Expressions*, 32:6–11.
- Füssl, J., Kandler, G., and Eberhardsteiner, J. (2016). Application of stochastic finite element approaches to wood-based products. *Archive of Applied Mechanics*, 86(1-2):89–110.
- Füssl, J., Lackner, R., Eberhardsteiner, J., and Mang, H. (2008). Failure modes and effective strength of two-phase materials determined by means of numerical limit analysis. *Acta Mechanica*, 1-4(195):185–202.
- Füssl, J., Li, M., Lukacevic, M., Eberhardsteiner, J., and Martin, C. M. (2017). Comparison of unit cell-based computational methods for predicting the strength of wood. *Engineering Structures*, 141:427–443.

- Gaff, M., Gašparík, M., Borůvka, V., and Haviarová, E. (2015). Stress simulation in layered wood-based materials under mechanical loading. *Materials & Design*, 87:1065–1071.
- Gagnon, S. and Pirvu, C. (2011). *CLT Handbook: cross-laminated timber*. FPInnovations, Canadian edition.
- Ghosh, S., Lee, K., and Raghavan, P. (2001). A multi-level computational model for multi-scale damage analysis in composite and porous materials. *International Journal of Solids and Structures*, 38(14):2335–2385.
- Gindl, W., Gupta, H., Lichtenegger, T. S. H., and Fratzl, P. (2004). Mechanical properties of spruce wood cell walls by nanoindentation. *Applied Physics A: Materials Science & Processing*, 79:2069–2073.
- Gindl, W. and Teischinger, A. (2002). Axial compression strength of norway spruce related to structural variability and lignin content. *Composites Part A: Applied Science and Manufacturing*, 33(12):1623–1628.
- Gloimüller, S., Borst, K., Bader, T., and Eberhardsteiner, J. (2012). Determination of the linear elastic stiffness and hygroexpansion of softwood by a multilayered unit cell using poromechanics. *Interaction and Multiscale Mechanics*, 5(3):229–265.
- Gravouil, A., Moës, N., and Belytschko, T. (2002). Non-planar 3D crack growth by the extended finite element and level sets - Part II: Level set update. *International Journal for Numerical Methods in Engineering*, 53(11):2569–2586.
- Guindos, P. (2011). *Three-dimensional finite element models to simulate the behavior of wood with presence of knots, applying the flow-grain analogy and validation with close range photogrammetry*. PhD thesis, University of Santiago de Compostela, Department of Agroforestry Engineering.
- Hackspiel, C., De Borst, K., and Lukacevic, M. (2014). A numerical simulation tool for wood grading model development. 48(3):633–649.
- Hansbo, A. and Hansbo, P. (2004). A finite element method for the simulation of strong and weak discontinuities in solid mechanics. *Computer Methods in Applied Mechanics and Engineering*, 193(33):3523–3540.
- Hautefeuille, M., Colliat, J.-B., Ibrahimbegovic, A., Matthies, H., and Villon, P. (2012). A multi-scale approach to model localized failure with softening. *Computers & Structures*, 94–95:83–95.
- Hawksbee, S., Smith, C., and Gilbert, M. (2013). Application of discontinuity layout optimization to three-dimensional plasticity problems. *Proceedings of the Royal Society of London A: Mathematical, Physical and Engineering Sciences*, 469(2155).
- Hill, R. (1951). On the state of stress in a plastic-rigid body at the yield point. *Philosophical Magazine*, 42:868–875.
- Hochreiner, G., Füssl, J., and Eberhardsteiner, J. (2013). Cross-laminated timber plates subjected to concentrated loading - Experimental identification of failure mechanisms. *Strain*, 50(1):68–81.

- Hochreiner, G., Füssl, J., Serrano, E., and Eberhardsteiner, J. (2014). Influence of wooden board strength class on the performance of cross-laminated timber plates investigated by means of full-field deformation measurements. *Strain*, 50(2):161–173.
- Hofstetter, K., Hellmich, C., and Eberhardsteiner, J. (2005). Development and experimental validation of a continuum micromechanics model for the elasticity of wood. *European Journal of Mechanics - A/Solids*, 24(6):1030–1053.
- Hofstetter, K., Hellmich, C., and Eberhardsteiner, J. (2007). Micromechanical modeling of solid-type and plate-type deformation patterns within softwood materials. A review and an improved approach. *Holzforschung*, 61(4):343–351.
- Hofstetter, K., Hellmich, C., Eberhardsteiner, J., and Mang, H. A. (2008). Micromechanical estimates for elastic limit states in wood materials, revealing nanostructural failure mechanisms. *Mechanics of Advanced Materials and Structures*, 15(6-7):474–484.
- Hristov, P., DiazDelaO, F., Flores, E. S., Guzmán, C., and Farooq, U. (2017). Probabilistic sensitivity analysis to understand the influence of micromechanical properties of wood on its macroscopic response. *Composite Structures*, 181:229–239.
- Jenkel, C. and Kaliske, M. (2014). Finite element analysis of timber containing branches - An approach to model the grain course and the influence on the structural behaviour. *Engineering Structures*, 75:237–247.
- Jenkel, C., Leichsenring, F., Graf, W., and Kaliske, M. (2015). Stochastic modelling of uncertainty in timber engineering. *Engineering Structures*, 99:296–310.
- Johansson, C.-J. (2003). *Grading of Timber with Respect to Mechanical Properties*, chapter 3, pages 23–43. Wiley.
- Källsner, B. (1994). Lengthwise bending strength variation of structural timber.
- Källsner, B., Ditlevsen, O., and Salmela, K. (1997). Experimental verification of a weak zone model for timber in bending. In *IUFRO S*, volume 5, pages 18–20.
- Kandler, G. and Füssl, J. (2017). A probabilistic approach for the linear behaviour of glued laminated timber. *Engineering Structures*, 148:673–685.
- Kandler, G., Füssl, J., and Eberhardsteiner, J. (2015a). Stochastic finite element approaches for wood-based products: theoretical framework and review of methods. *Wood Science and Technology*, 49(5):1055–1097.
- Kandler, G., Füssl, J., Serrano, E., and Eberhardsteiner, J. (2015b). Effective stiffness prediction of GLT beams based on stiffness distributions of individual lamellas. *Wood Science and Technology*, 49(6):1101–1121.
- Kandler, G., Lukacevic, M., and Füssl, J. (2016a). An algorithm for the geometric reconstruction of knots within timber boards based on fibre angle measurements. *Construction and Building Materials*, 124:945–960.
- Kandler, G., Lukacevic, M., and Füssl, J. (2016b). From the knot morphology of individual timber boards to the mechanical properties of glued laminated timber. In *WCTE 2016 - World Conference on Timber Engineering*.

- Kandler, G., Lukacevic, M., Füssl, J., Zechmeister, C., and Wolff, S. (2017). A stochastic engineering framework for timber structural elements. submitted for publication.
- Kollmann, F. (1951). *Technologie des Holzes und der Holzwerkstoffe*. Springer-Verlag Berlin Heidelberg.
- Krabbenhøft, K. and Damkilde, L. (2000). *Limit Analysis Based On Lower-Bound Solutions And Nonlinear Yield Criteria*, pages 117–129. Civil-Comp Press.
- Krabbenhøft, K. and Damkilde, L. (2003). A general non-linear optimization algorithm for lower bound limit analysis. *International Journal for Numerical Methods in Biomedical Engineering*, 56:165–187.
- Krabbenhøft, K., Lyamin, A., and Sloan, S. (2007). Formulation and solution of some plasticity problems as conic programs. *International Journal of Solids and Structures*, 44(5):1533–1549.
- Krabbenhøft, K., Lyamin, A., and Sloan, S. (2008). Three-dimensional Mohr–Coulomb limit analysis using semidefinite programming. *Communications in Numerical Methods in Engineering*, 24:1107–1119.
- Krabbenhøft, K., Lyamin, A. V., Hija, M., and Sloan, S. W. (2005). A new discontinuous upper bound limit analysis formulation. *International Journal for Numerical Methods in Engineering*, 63(7):1069–1088.
- Landelius, J. (1989). Finit area metoden. en bra metod för beräkning av uppfläckningsbrott? Student Paper.
- Laws, N. (1977). The determination of stress and strain concentrations at an ellipsoidal inclusion in an anisotropic material. *Journal of Elasticity*, 7(1):91–97.
- Le, C. V., Askes, H., and Gilbert, M. (2010a). Adaptive element-free Galerkin method applied to the limit analysis of plates. *Computer Methods in Applied Mechanics and Engineering*, 199(37):2487–2496.
- Le, C. V., Gilbert, M., and Askes, H. (2009). Limit analysis of plates using the EFG method and second-order cone programming. *International Journal for Numerical Methods in Engineering*, 78(13):1532–1552.
- Le, C. V., Gilbert, M., and Askes, H. (2010b). Limit analysis of plates and slabs using a meshless equilibrium formulation. *International Journal for Numerical Methods in Engineering*, 83:1739–1758.
- Le, C. V., Nguyen-Xuan, H., Askes, H., Bordas, S. P. A., Rabczuk, T., and Nguyen-Vinh, H. (2010c). A cell-based smoothed finite element method for kinematic limit analysis. *International Journal for Numerical Methods in Engineering*, 83(12):1651–1674.
- Li, H. (2011). Limit analysis of composite materials with anisotropic microstructures: A homogenization approach. *Mechanics of Materials*, 43(10):574–585.
- Li, M., Füssl, J., Lukacevic, M., Eberhardsteiner, J., and Martin, C. M. (2018a). An algorithm for adaptive introduction and arrangement of velocity discontinuities within finite-element-based upper bound approaches. To be submitted in 2018.

- Li, M., Füssl, J., Lukacevic, M., Eberhardsteiner, J., and Martin, C. M. (2018b). A numerical upper bound formulation with sensible-arranged velocity discontinuities and orthotropic material strength behaviour. *Journal of Theoretical and Applied Mechanics*.
- Li, M., Füssl, J., Lukacevic, M., Eberhardsteiner, J., and Martin, C. M. (2018c). Strength predictions of clear wood at multiple scales using numerical limit analysis approaches. *Computers & Structures*, 196:200–216.
- Li, M., Füssl, J., Lukacevic, M., Martin, C. M., and Eberhardsteiner, J. (2018d). Bending strength predictions of cross-laminated timber plates subjected to concentrated loading using 3D finite-element-based limit analysis approaches. *Composite Structures*.
- Limam, O., Foret, G., and Zenzri, H. (2011). Ultimate strength of pin-loaded composite laminates: A limit analysis approach. *Composite Structures*, 93(4):1217–1224.
- Liu, F. and Zhao, J. (2013). Upper bound limit analysis using radial point interpolation meshless method and nonlinear programming. *International Journal of Mechanical Sciences*, 70:26–38.
- Lubliner, J. (1990). *Plasticity Theory*. Pearson Education, Inc.
- Lukacevic, M. and Füssl, J. (2014). Numerical simulation tool for wooden boards with a physically based approach to identify structural failure. *European Journal of Wood and Wood Products*, 72(4):497–508.
- Lukacevic, M. and Füssl, J. (2016). Application of a multisurface discrete crack model for clear wood taking into account the inherent microstructural characteristics of wood cells. *Holzforschung*, 70(9):845–853.
- Lukacevic, M., Füssl, J., and Eberhardsteiner, J. (2015). Discussion of common and new indicating properties for the strength grading of wooden boards. *Wood Science and Technology*, 49(3):551–576.
- Lukacevic, M., Füssl, J., Griessner, M., and Eberhardsteiner, J. (2014a). Performance assessment of a numerical simulation tool for wooden boards with knots by means of full-field deformation measurements. *Strain*, 50(4):301–317.
- Lukacevic, M., Füssl, J., and Lampert, R. (2014b). Failure mechanisms of clear wood identified at wood cell level by an approach based on the extended finite element method. *Engineering Fracture Mechanics*, 144:158–175.
- Lukacevic, M., Lederer, W., and Füssl, J. (2017). A microstructure-based multisurface failure criterion for the description of brittle and ductile failure mechanisms of clear-wood. *Engineering Fracture Mechanics*, 176:83–99.
- Lyamin, A. and Sloan, S. (2000). *Upper Bound Limit Analysis using Linear Finite Elements and Nonlinear Programming*, pages 131–145. Civil-Comp Press.
- Lyamin, A. V. and Sloan, S. W. (2002a). Lower bound limit analysis using nonlinear programming. *International Journal for Numerical Methods in Engineering*, 55(5):573–611.

- Lyamin, A. V. and Sloan, S. W. (2002b). Upper bound limit analysis using linear finite elements and non-linear programming. *International Journal for Numerical and Analytical Methods in Geomechanics*2, 26(2):181–216.
- Lysmer, J. (1970). Limit analysis of plane problems in soil mechanics. *Journal of the Soil Mechanics and Foundations Division*, 96(4):1311–1334.
- Mackenzie-Helnwein, P., Eberhardsteiner, J., and Mang, H. A. (2003). A multi-surface plasticity model for clear wood and its application to the finite element analysis of structural details. *Computational Mechanics*, 31(1-2):204–218.
- Maier, G., Zavelani-Rossi, A., and Benedetti, D. (1972). A finite element approach to optimal design of plastic structures in plane stress. *International Journal for Numerical Methods in Engineering*, 4(4):455–473.
- Makrodimopoulos, A. (2010). Remarks on some properties of conic yield restrictions in limit analysis. *International Journal for Numerical Methods in Biomedical Engineering*, 26(11):1449–1461.
- Makrodimopoulos, A. and Martin, C. (2005a). Limit analysis using large-scale SOCP optimization. In *Proc. 13th Nat Conf. of UK Association for Computational Mechanics in Engineering*, pages 21–24, Sheffield.
- Makrodimopoulos, A. and Martin, C. (2005b). A novel formulation of upper bound limit analysis as a second-order cone programming problem. In *Proc. 8th International Conference on Computational Plasticity*, pages 1083–1086, Barcelona.
- Makrodimopoulos, A. and Martin, C. M. (2006). Lower bound limit analysis of cohesive-frictional materials using second-order cone programming. *International Journal for Numerical Methods in Engineering*, 66(4):604–634.
- Makrodimopoulos, A. and Martin, C. M. (2007). Upper bound limit analysis using simplex strain elements and second-order cone programming. *International Journal for Numerical and Analytical Methods in Geomechanics*, 31(6):835–865.
- Makrodimopoulos, A. and Martin, C. M. (2008). Upper bound limit analysis using discontinuous quadratic displacement fields. *Communications in Numerical Methods in Engineering*, 24(11):911–927.
- Martin, C. (2011). The use of adaptive finite-element limit analysis to reveal slip-line fields. *Géotechnique Letters*, 1(2):23–29.
- Martin, C. and Makrodimopoulos, A. (2008). Finite-element limit analysis of Mohr-Coulomb materials in 3D using semidefinite programming. *Journal of Engineering Mechanics*, 134(4):339–347.
- Martin, C. and White, D. (2012). Limit analysis of the undrained bearing capacity of offshore pipelines. *Géotechnique*, 62(9):847–863.
- Masuda, M. (1988). Theoretical consideration on fracture criteria of wood - proposal of finite small area theory. In *Proceedings of the 1988 International Conference on Timber Engineering*, volume 2, pages 584–595, Seattle.



- Melenk, J. and Babuška, I. (1996). The partition of unity finite element method: Basic theory and applications. *Computer Methods in Applied Mechanics and Engineering*, 139(1):289–314.
- Michel, J., Moulinec, H., and Suquet, P. (1999). Effective properties of composite materials with periodic microstructure: a computational approach. *Computer Methods in Applied Mechanics and Engineering*, 172(1):109–143.
- Milani, G. (2010). FE homogenized limit analysis model for masonry strengthened by near surface bed joint FRP bars. *Composite Structures*, 92(2):330–338.
- Milani, G. and Bucchi, A. (2010). Kinematic FE homogenized limit analysis model for masonry curved structures strengthened by near surface mounted FRP bars. *Composite Structures*, 93(1):239–258.
- Milani, G. and Lourenço, P. (2009). A discontinuous quasi-upper bound limit analysis approach with sequential linear programming mesh adaptation. *International Journal of Mechanical Sciences*, 51:89–104.
- Milani, G., Lourenço, P., and Tralli, A. (2006a). Homogenised limit analysis of masonry walls, Part I: Failure surfaces. *Computers & Structures*, 84(3):166–180.
- Milani, G., Lourenço, P., and Tralli, A. (2006b). Homogenised limit analysis of masonry walls, Part II: Structural examples. *Computers & Structures*, 84(3):181–195.
- Milani, G., Milani, E., and Tralli, A. (2010). Approximate limit analysis of full scale FRP-reinforced masonry buildings through a 3D homogenized FE package. *Composite Structures*, 92(4):918–935.
- Moës, N., Gravouil, A., and Belytschko, T. (2002). Non-planar 3D crack growth by the extended finite element and level sets-Part I: Mechanical model. *International Journal for Numerical Methods in Engineering*, 53(11):2549–2568.
- MOSEK ApS (2017). *The MOSEK optimization tools version 8.0*. User’s manual and reference. Available from <http://www.mosek.com> [June 2014].
- Muñoz, J. J., Bonet, J., Huerta, A., and Peraire, J. (2009). Upper and lower bounds in limit analysis: Adaptive meshing strategies and discontinuous loading. *International Journal for Numerical Methods in Engineering*, 77(4):471–501.
- Nguyen-Xuan, H. and Liu, G. (2015). An edge-based finite element method (ES-FEM) with adaptive scaled-bubble functions for plane strain limit analysis. *Computer Methods in Applied Mechanics and Engineering*, 285(Supplement C):877–905.
- Nguyen-Xuan, H., Nguyen-Hoang, S., Rabczuk, T., and Hackl, K. (2017). A polytree-based adaptive approach to limit analysis of cracked structures. *Computer Methods in Applied Mechanics and Engineering*, 313(Supplement C):1006–1039.
- Nielsen, M. and Hoang, L. (2016). *Limit Analysis and Concrete Plasticity*. Boca Raton: CRC Press, 3 edition.
- Osher, S. and Sethian, J. A. (1988). Fronts propagating with curvature-dependent speed: Algorithms based on Hamilton-Jacobi formulations. *Journal of Computational Physics*, 79(1):12–49.

- Pastor, J., Thoré, P., and Pastor, F. (2010). Limit analysis and numerical modeling of spherically porous solids with Coulomb and Drucker-Prager matrices. *Journal of Computational and Applied Mathematics*, 234(7):2162–2174.
- Pisano, A., Fuschi, P., and Domenico, D. D. (2012). A layered limit analysis of pinned-joints composite laminates: Numerical versus experimental findings. *Composites Part B: Engineering*, 43(3):940–952.
- Pisano, A., Fuschi, P., and Domenico, D. D. (2013). Peak load prediction of multi-pin joints FRP laminates by limit analysis. *Composite Structures*, 96:763–772.
- Pisano, A., Fuschi, P., and Domenico, D. D. (2015). Numerical limit analysis of steel-reinforced concrete walls and slabs. *Computers & Structures*, 160:42–55.
- Pisano, A. A. and Fuschi, P. (2007). A numerical approach for limit analysis of orthotropic composite laminates. *International Journal for Numerical Methods in Engineering*, 70(1):71–93.
- Portioli, F., Casapulla, C., Gilbert, M., and Cascini, L. (2014). Limit analysis of 3D masonry block structures with non-associative frictional joints using cone programming. *Computers & Structures*, 143:108–121.
- Prandtl, L. (1920). Über die Härte plastischer Körper. *Nachrichten von der Gesellschaft der Wissenschaften zu Göttingen, Mathematisch-Physikalische Klasse*, 12:74–85.
- Puck, A. and Schürmann, H. (2002). Failure analysis of FRP laminates by means of physically based phenomenological models. *Composites Science and Technology*, 62(12):1633–1662.
- Saavedra Flores, E., Saavedra, K., Hinojosa, J., Chandra, Y., and Das, R. (2016a). Multi-scale modelling of rolling shear failure in cross-laminated timber structures by homogenisation and cohesive zone models. *International Journal of Solids and Structures*, 81:219–232.
- Saavedra Flores, E. I., Ajaj, R., Dayyani, I., Chandra, Y., and Das, R. (2016b). Multi-scale model updating for the mechanical properties of cross-laminated timber. *Computers & Structures*, 177:83–90.
- Saavedra Flores, E. I., Dayyani, I., Ajaj, R., Castro-Triguero, R., DiazDelaO, F., Das, R., and Soto, P. G. (2015). Analysis of cross-laminated timber by computational homogenisation and experimental validation. *Composite Structures*, 121:386–394.
- Salmen, L. and Burgert, I. (2009). Cell wall features with regard to mechanical performance. A review COST Action E35 2004–2008: Wood machining – micromechanics and fracture. *Holzforschung*, 63:121–129.
- Schmidt, J. and Kaliske, M. (2006). Zur dreidimensionalen Materialmodellierung von Fichtenholz mittels eines Mehrflächen-Plastizitätsmodells (in German). *Holz als Roh- und Werkstoff*, 64(5):393–402.
- Schmidt, J. and Kaliske, M. (2007). Simulation of cracks in wood using a coupled material model for interface elements. *Holzforschung*, 61(4):382–389.

- Schmidt, J. and Kaliske, M. (2009). Models for numerical failure analysis of wooden structures. *Engineering Structures*, 31(2):571–579.
- Schwiedrzik, J., Raghavan, R., RÜggeberg, M., Hansen, S., Wehrs, J., Adusumalli, R. B., Zimmermann, T., and Michler, J. (2016). Identification of polymer matrix yield stress in the wood cell wall based on micropillar compression and micromechanical modelling. *Philosophical Magazine*, 96(32-34):3461–3478.
- Serrano, E. and Gustafsson, P. J. (2007). Fracture mechanics in timber engineering - Strength analyses of components and joints. *Materials and Structures*, 40(1):87–96.
- Sinn, G., Reiterer, A., Stanzl-Tschegg, S. E., and Tschegg, E. K. (2001). Determination of strain of thin wood samples using videoextensometry. *Holz als Roh- und Werkstoff*, 59:177–182.
- Sjödin, J. and Serrano, E. (2008). A numerical study of methods to predict the capacity of multiple steel-timber dowel joints. *Holz als Roh- und Werkstoff*, 66(6):447–454.
- Sjödin, J., Serrano, E., and Enquist, B. (2008). An experimental and numerical study of the effect of friction in single dowel joints. *Holz als Roh- und Werkstoff*, 66(5):363–372.
- Sloan, S. (1988). Lower bound limit analysis using finite elements and linear programming. *International Journal for Numerical and Analytical Methods in Geomechanics*, 12(1):61–77.
- Sloan, S. (1989). Upper bound limit analysis using finite elements and linear programming. *International Journal for Numerical and Analytical Methods in Geomechanics*, 13(3):263–282.
- Sloan, S. (2013). Geotechnical stability analysis. *Géotechnique*, 63(7):531–571.
- Sloan, S. and Kleeman, P. (1995). Upper bound limit analysis using discontinuous velocity fields. *Computer Methods in Applied Mechanics and Engineering*, 127(1–4):293–314.
- Smith, C. and Gilbert, M. (2007). Application of discontinuity layout optimization to plane plasticity problems. *Proceedings of the Royal Society A*, 463:2461–2484.
- Song, J.-H., Areias, P. M. A., and Belytschko, T. (2006). A method for dynamic crack and shear band propagation with phantom nodes. *International Journal for Numerical Methods in Engineering*, 67(6):868–893.
- Suquet, P. (1997). *Continuum Micromechanics*. Springer-Verlag New York, Inc., New York, NY, USA.
- Suquet, P. M. (1987). *Homogenization Techniques for Composite Media*, chapter Elements of Homogenization for Inelastic Solid Mechanics, pages 193–278. Springer.
- Tsai, S. W. (1965). Strength characteristics of composite materials. Technical report, NASA.
- Tsai, S. W. and Wu, E. M. (1971). A general theory of strength for anisotropic materials. *Journal of Composite Materials*, 5(1):58–80.

- 
- Wu, J.-Y. and Cervera, M. (2014). On the equivalence between traction- and stress-based approaches for the modeling of localized failure in solids. *Journal of the Mechanics and Physics of Solids*, 82:137–163.
- Yu, S., Zhang, X., and Sloan, S. (2016). A 3D upper bound limit analysis using radial point interpolation meshless method and second-order cone programming. *International Journal for Numerical Methods in Engineering*, 108(13):1686–1704.
- Zaoui, A. (2002). Continuum micromechanics: Survey. *Journal of Engineering Mechanics*, 128(8):808–816.
- Zimmermann, T., Sell, J., and Eckstein, D. (1994). Rasterelektronenmikroskopische Untersuchungen an Zugbruchflächen von Fichtenholz. *Holz als Roh- und Werkstoff*, 52(4):223–229.
- Zouain, N., Borges, L., and Silveira, J. L. (2002). An algorithm for shakedown analysis with nonlinear yield functions. *Computer Methods in Applied Mechanics and Engineering*, 191(23):2463–2481.

# Curriculum Vitae

## Personal Data

Name: **M.Sc. Mingjing Li**  
Date of Birth: 23rd April 1989  
Place of Birth: Guiping, Guangxi, China  
Nationality: Chinese  
Current address: Mooslackengasse 21/509, 1190 Wien, Austria

## Education

06/2014 – 06/2018 Doctoral studies in Civil Engineering at Vienna University of Technology, Vienna, Austria  
10/2011 – 09/2013 Master Studies in Civil Engineering at Dresden University of Technology, Dresden, Germany  
09/2007 – 06/2011 Bachelor Studies in Mechanical Engineering at East China University of Science and Technology, Shanghai, China  
09/2004 – 06/2007 High School Student at Guangdong Beijiang High School, Shaoguan, China

## Work Experience

06/2014 – 06/2018 Research Assistant, Institute for Mechanics of Materials and Structures at Vienna University of Technology, Vienna, Austria  
10/2013 – 02/2014 Student Assistant, Institute of Structural Analysis at Dresden University of Technology, Dresden, Germany

# Publications and Conference Contributions

## Publications in Scientific Journals

Füssl, J., **Li, M.**, Lukacevic, M., Eberhardsteiner, J., and Martin, C.M.:  
Comparison of unit cell-based computational methods for predicting the strength of wood.  
*Engineering Structures* 141 (2017), 427-443.

**Li, M.**, Füssl, J., Lukacevic, M., Eberhardsteiner, J., and Martin, C.M.:  
Strength predictions of clear wood at multiple scales using numerical limit analysis approaches.  
*Computers & Structures*, 196 (2018), 200-216.

**Li, M.**, Füssl, J., Lukacevic, M., Eberhardsteiner, J., and Martin, C.M.:  
A numerical upper bound formulation with sensible-arranged velocity discontinuities for orthotropic material strength behaviour.  
*Journal of Theoretical and Applied Mechanics* 56(2) (2018), 417-433.

**Li, M.**, Füssl, J., Lukacevic, M., Martin, C.M., and Eberhardsteiner, J.:  
Bending strength predictions of cross-laminated timber plates subjected to concentrated loading using 3D finite-element-based limit analysis approaches.  
*Composite Structures*, under review.

**Li, M.**, Füssl, J., Lukacevic, M., Eberhardsteiner, J., and Martin, C.M.:  
An algorithm for adaptive introduction and arrangement of velocity discontinuities within finite-element-based upper bound approaches.  
*Computer Methods in Applied Mechanics and Engineering*, submitted.

## Conference Papers

**Li, M.**, Füssl, J., Lukacevic, M., Eberhardsteiner, J., and Martin, C.M.:  
A numerical limit analysis approach for predicting strength of clear wood.  
In: "CD-ROM Proceedings of the World Conference on Timber Engineering (WCTE

2016)", J. Eberhardsteiner, W. Winter, A. Fadai, M. Pöll (Hrg.); herausgegeben von: Vienna University of Technology; Grafisches Zentrum HTU GmbH, Vienna, 2016, ISBN: 978-3-903039-00-1, Paper-Nr. 90, 10 S.

Füssl, J., **Li, M.**, Lukacevic, M., Eberhardsteiner, J., and Martin, C.M.:  
Three different methods for predicting the strength behavior of clear wood - a performance comparison and basis for a combined approach.  
In: "CD-ROM Proceedings of the World Conference on Timber Engineering (WCTE 2016)", J. Eberhardsteiner, W. Winter, A. Fadai, M. Pöll (Hrg.); herausgegeben von: Vienna University of Technology; Grafisches Zentrum HTU GmbH, Vienna, 2016, ISBN: 978-3-903039-00-1, Paper-Nr. 863, 10 S.

## Conference Presentations

**Li, M.**, Füssl, J., Lukacevic, M., Eberhardsteiner, J., and Martin, C.M.:  
A 3D numerical limit analysis approach for strength predict of cross-laminated timber plates.  
14th U.S. National Congress on Computational Mechanics (USNCCM14), Montreal, Canada; 17.07.2017.

**Li, M.**, Füssl, J., Lukacevic, M., Eberhardsteiner, J., and Martin, C.M.:  
Implementation of numerical limit analysis for strength estimates of wood and wood-based products, at different scales of observation.  
PhD school DokIn Holz final meeting, Vienna, Austria; 28.06.2017.

**Li, M.**, Füssl, J., Lukacevic, M., Eberhardsteiner, J., and Martin, C.M.:  
Implementation of numerical limit analysis for strength estimates of wood and wood-based products, at different scales of observation.  
CompWood 2017, Vienna, Austria; 09.06.2017.

**Li, M.**, Füssl, J., Lukacevic, M., Eberhardsteiner, J., and Martin, C.M.:  
A numerical limit analysis approach for predicting strength of clear wood.  
World Conference on Timber Engineering (WCTE 2016), Vienna, Austria; 23.08.2017.

**Li, M.**, Füssl, J., Lukacevic, M., Eberhardsteiner, J., and Martin, C.M.:  
A numerical limit analysis approach for strength predictions of clear wood taking microstructural characteristics into account.  
European Congress on Computational Methods in Applied Sciences and Engineering (ECCOMAS 2016), Crete Island, Greece; 06.06.2016.

**Li, M.**, Füssl, J., Lukacevic, M., Eberhardsteiner, J., and Martin, C.M.:  
Effective strength of wood cells determined by means of numerical limit analysis.  
5th Workshop on Direct Method 2015, Oxford, UK; 08.09.2015.